

530
DEZ

THESES & DISSERTATION
SECTION
CENTRAL LIBRARY, T.U.

CENTRAL LIBRARY
TEZPUR UNIVERSITY
Accession No. T 261
Date 15/1/13

Synthesis, characterization and study on the magneto-optic effects of ferrofluids

*A thesis submitted in partial fulfillment of the requirements
for the degree of Doctor of Philosophy*

Ms. Manasi Devi
Reg. No. 009 of 2009



**Department of Physics
School of Sciences
Tezpur University
Napaam, Tezpur-784028
Assam, India**

December 2012

**THESES & DISSERTATION
SECTION
CENTRAL LIBRARY, T.U.**

Dedicated to my parents
Ms. Kamala Devi (ma)
And
Mr. Manik Bordoloi (deuta)

Abstract

All the way through history, magnetism has played a vital role in the development of civilization. Both bulk as well as nanoscale magnetic structures form basic building blocks in a number of scientific and technological applications, starting from the electronic recording media, spin transport, medical diagnosis (eg. magnetic resonance imaging) to the magnetic levitating train. Recently, production and use of colloidal nanostructured systems has emerged as an important concept in the development of nanoscience and nanotechnology.^[1-3] With the advent of advanced processing tools/techniques, a colloidal system with narrow size distribution, improved environmental stability, surface functionalization capability etc. can be fabricated. Such a system is capable of exhibiting numerous fascinating properties including unusual optical, optoelectronic and magnetic responses.^[4-5] In particular, magnetic colloidal nanocrystals have received widespread application in various fields.^[6-8]

The magnetic control of flow (properties of a liquid material) is a challenging task. Ferromagnetic materials contain a large number of magnetic domains. The magnetization in each domain direct to any direction with uniform alignment of spins in the absence of an external magnetic field. If there exist only one domain in the material, the material shows a very high magneto static energy.^[9] Materials loose their magnetic properties at temperatures far below their melting points.^[10] On the other hand, molecular liquids e.g. paramagnetic salt solutions require extremely high magnetic fields in the order of several Teslas to influence their magnetic properties.^[11] A ferromagnetic liquid cannot, therefore, be produced by simply melting a ferromagnetic solid. Stable suspensions of small magnetic particles in appropriate carrier liquids have many advantages over the above mentioned problems. This kind of stable suspensions, popularly called ferrofluid, were first identified by Gowan Knight's attempts in 1779 to produce a magnetic fluid by suspending iron filings in water. His attempts failed because particle sedimentation occurred in a short time. Recent methods are based on modified principle

and therefore, more advanced in terms of stability and reproducibility. Typically, a ferrofluid contains magnetic colloids in an appropriate carrier liquid. It can be prepared out of any kind of magnetic particles with size 2-10 nm. Because of the various forces (entropic repulsion, Van der Waals force and magnetic force) acting between the magnetic nanoparticles (MNPs), they tend to agglomerate. This results in loss of stability of the ferrofluid. But the agglomeration can be stopped either by electrically charging or by coating the MNPs with some suitable surfactant. [12] Ferrofluid exhibits common fluid nature as well as some extra ordinary behavior under a magnetic field e.g. magneto-optic and magneto viscous property. Such kind of fluid is highly applicable in magnetic seal, shield, drug targeting etc. [14-15]

This thesis is an extensive attempt to study synthesis and characterization of different ferrofluids. Special emphasis was given on selective surface functionalization (by using surfactants) on MNPs that constitute a major component of ferrofluids. Both magneto-optic as well as magneto-viscous effects have been explored. The influence of typical irradiation process on the MNPs/ferrofluids and its impact on the magneto-optic responses are also highlighted. The whole thesis is comprised of eight chapters.

Chapter 1 is the introductory part. Properties of magnetic material system in general as well as characteristic features in the nanoscale range are discussed in this chapter with relevant references. A preliminary discussion on synthesis and use of conventional ferrofluids is also introduced. Towards the end, the objectives of the thesis are highlighted in sequence.

Typically, the preparation of ferrofluid requires three important systems: magnetic nanoparticles (MNPs), appropriate surfactant for coating nanoparticles and a carrier fluid to disperse the nanoparticles. We have synthesized both conventional and unconventional ferrofluid systems. The first one is iron oxide (magnetite (Fe_3O_4)) based and the second one is rare earth oxide (gadolinium oxide (Gd_2O_3)) based. Fe_3O_4

MNPs were coated separately with *oleic acid* (anionic surfactant) and *tetramethylammonium hydroxide* (TMAH, cationic surfactant). The ferrofluids were prepared from oleic acid coated MNPs and dispersed in different carrier fluid such as water and kerosene. Similarly, in order to study the influence of surfactant, different ferrofluids were also synthesized considering *oleic acid* and TMAH coated Fe₃O₄ MNPs in methanol. On the otherhand, Gd₂O₃ MNPs were coated with *N-Cetyl-N,N,N-trimethylammonium bromide* (CTAB, a cationic surfactant) and dispersed in ethanol so as to prepare a novel ferrofluid. The morphological and spectroscopic characteristics of the as prepared nanoparticles/ ferrofluids were studied by various analytical tools: X-ray diffraction, electron microscopy, dynamic light scattering, Fourier transform infra-red spectroscopy, electron paramagnetic resonance spectroscopy, Raman spectroscopy and photoluminescence spectroscopy. In this regard, the **chapter 2** highlights synthesis protocol of the above mentioned ferrofluids and their characterization features.

The **chapter 3** entitled “effect of static magnetic field on ferrofluids”, describes the variation of optical activity (magneto-optic) and of viscosity (magneto-viscous) of the prepared ferrofluids in response to a static magnetic field. Due to the presence of MNPs, ferrofluids show unusual behaviour in presence of an external magnetic field. In presence of a field, the particles are expected to align themselves linearly and with increasing magnetic field, the structure of the particles transform from chain to bundles of chains due to zippering effect. ^[13,14] A custom made set-up was used to study the magneto-optic effects (Faraday rotation and linear dichroism) of the ferrofluids. The Faraday rotation of the synthesized ferrofluidic feature first increases with the field and then tends to saturate at a relatively higher field strength. This is attributed to the chaining effect of ferrofluids.^[15] In addition to the chaining effect, it was suggested earlier that, a mechanical torque is also developed between the magnetic moment of the particle and the applied field.^[16] The free rotation of the particles is hindered by this torque and thus viscosity of the ferrofluid

changes under a static magnetic field.^[17] We have studied the magneto-viscous properties of the synthesized ferrofluid with varying magnetic field strength upto 100 G and for different applied shear rate.

As an important technological aspect, energetic ion irradiation aspects are being used for modification of structural, optical and magnetic properties of nanoscale materials.^[18-20] In general, the ions with high energy (~ MeV regime) could either lead to particle growth or fragmentation, depending on the host media.^[21-22] Whereas, KeV ion beams are generally used for ion implantation^[23-24] and creation of point defects that can segregate to particle interfaces and grain boundaries. The modification caused by 80-keV Ar ions on the synthesized Fe₃O₄ and Gd₂O₃ nanoparticle/ ferrofluid systems are presented in **chapter 4**. The partial phase transformation of Gd₂O₃ MNPs from *B-type (monoclinic)* to *A-type (cubic)* system is an important outcome of the low energy ion impact. In **chapter 4**, emphasis is also given to the effect in the magneto-optic responses of the respective ferrofluids.

Apart from charged ion irradiation, γ -irradiation could also lead to the modification of nanomaterial system including structural, optical and optoelectronic features.^[25-26] The prepared ferrofluids were irradiated with γ -radiation (~1.25 MeV) at UGC-DAE Consortium for Scientific Research, Kolkata. To be specific, Fe₃O₄ based ferrofluids containing water and kerosene as carriers were irradiated with five different doses:(32 - 2635 Gy) of γ -radiation. A substantial enhancement of the Verdet constant (a maximum of ~70%) was predicted which was ascribed to the γ -irradiation induced defects as well as to the structural modification (growth of particles from ~9 nm to ~48 nm). The **chapter 5** depicts characteristic study of the γ -irradiation induced modification of the ferrofluids and its impact on magneto-optic responses.

Chapter 6 is based on a comparative analysis of different irradiation effect on magneto-optic responses of ferrofluids. As discussed above, both ion irradiation and γ -irradiation on nanomaterial system could lead to surface passivation. The ferrofluid properties get modified by the

creation and annihilation of defects on the MNPs due to irradiation. Nanoscale defects are created/ annihilated at the cost of energy loss of the incident radiation. The radiation-matter interaction process is specific to the type of the radiation and the material surface. Considering different types of radiation into account, a comparative analysis was done for Faraday rotation and linear dichroism responses of a given ferrofluid. The consequences of the specific radiation on magneto-optic effect of different ferrofluids (Fe_3O_4 based systems dispersed in water and kerosene) are also highlighted in this chapter.

The response of a typical ferrofluid lies on its explicit property of chain formation of MNPs. The most significant magneto-optic and magneto-viscous effect of ferrofluid are attributed to chaining effect. There are plentiful experimental as well as theoretical works reporting chain formation of ferrofluids. ^[27-28] We made an alternative effort to justify the structure evolution of ferrofluids. In **chapter 7** of the thesis, the chain formation is dealt analytically with the help of dimensional analysis, which is supported by error calculation. An empirical relation is formulated between the chain length and different measurable parameters involved in magneto-optic and magneto-viscous effect. The error/uncertainty creeps into all experimental data in spite of the adequate care is extended to calibration and data acquisition process. Based on specification of the uncertainty in the various primary experimental measurements, Kline and McClintock proposed a method to estimate the uncertainty in experimental results. ^[29] This method is adopted to yield the uncertainty in our formulated relation of chain length. The maximum uncertainty in four sets of data is found as ~ 0.015 .

Finally, the conclusion and future prospects are highlighted in **chapter 8**. The important observations, outcomes and limitations are discussed in this chapter. Moreover, future scope of advanced application of ferrofluids is also mentioned towards the end of the chapter.

References

- [1] Abraham, A.G.P. et al. Depleted-heterojunction colloidal quantum dot solar cells, *ACS Nano* 4 , 3374–3380, 2010.
- [2] Nel, A. E. et al. Understanding biophysicochemical interactions at the nano–bio interface, *Nat. Mater.* 8, 543 – 557, 2009.
- [3] Baranov, D. Assembly of colloidal semiconductor nanorods in solution by depletion attraction, *Nano Lett.* 10, 743–749, 2010.
- [4] Contescu, C.I. and Putyera, K. (Eds.) Dekker encyclopaedia of nanoscience and nanotechnology, CRC Press, New York, 2009.
- [5] Oron, D. et al. Universal role of discrete Acoustic phonons in the low-temperature optical emission of colloidal quantum dots, *Phys. Rev. Lett.* 102, 177402-177405, 2009.
- [6] Tang, X. F., Yang, Z.G. and Wang, W. J., A simple way of preparing high-concentration and high-purity nano copper colloid for conductive ink in inkjet printing technology, *Colloid. Surface. A* 360, 99–104,2010.
- [7] Mishra, B., Patel, B.B. and Tiwari, S. Colloidal nanocarriers: a review on formulation technology, types and applications toward targeted drug delivery, *Nanomed- Nanotechnol.* 6, 9–24, 2010.
- [8] Dias, A.M.G.C., Hussain, A., Marcos, A.S., Roque, A.C.A. A biotechnological perspective on the application of iron oxide magnetic colloids modified with polysaccharides, *Biotechnol. Adv.* 29, 142–155, 2011.
- [9] Bar'yakhtar, V. G., Wigen, P. E., Lesnik, N. A. (Eds.) *Frontiers in Magnetism of Reduced dimension Systems*, Kluwer Academic Publishers, Netherlands, 1998.
- [10] Stefanita, C-G. *Magnetism basics and Applications*, Springer-Verlag, Berlin Heidelberg, 2012.
- [11] Odenbench, S. Ferrofluids-magnetically controlled suspensions, *Collid. Surface. A* 217, 171-178,2003.
- [12] Odenbach, S. Recent progress in magnetic fluid research, *J.Phys.: Conden. Mat.* 16, R1135- R1150, 2004.

- [13] Laskar, J. M., Philip, J., and Raj, B. Experimental evidence for reversible zippering of chains in magnetic nanofluids under external magnetic fields, *Phys. Rev. E* 80, 041401-041408, 2009.
- [14] Martin, J. E., Odinek, J. and Halsey, T. C. Evolution of structure in a quiescent electrorheological fluid, *Phys. Rev. Lett.* 69, 1524–1527, 1992.
- [15] Rousan, A., Ghanem H. M. E. and Yusuf N. A. Faraday rotation and chain formation in magnetic fluids, *IEEE Trans. Magn.* 25, 3121-3124, 1989.
- [16] Odenbach, S. (Ed.) Magneto-viscous effect of ferrofluids, Springer-Verlag, Berlin Heidelberg, 2002.
- [17] Felderhof, B. U. Entrainment by a rotating magnetic field of a ferrofluid contained in a sphere, *Phys. Rev. E* 84, 046313-04617, 2011.
- [18] Bayan, S., Das, U. And Mohanta, D. Development of Tb-doped ZnO nanorods: Effect of nitrogen ion irradiation on luminescence and structural evolution, *Phys. Stat Sol. A*, 207, 1859-1863, 2010.
- [19] Sakamaki, M. et al. Perpendicular magnetic anisotropy in a Pt/Co/Pt ultrathin film arising from a lattice distortion induced by ion irradiation, *Phys. Rev. B* 6, 024418-024422, 2012.
- [20] Rath, H et al., Structural evolution of TiO₂ nanocrystalline thin films by thermal annealing and swift heavy ion irradiation, *J. Appl. Phys.* 105, 074311 – 074311, 2009.
- [21] Hellborg, R., Whitlow, H.J. and Zhang, Y. (Eds.) Ion beams in nanoscience and technology, Springer-Verlag, Berlin Heidelberg, 2009.
- [22] Rabalais, J.W. Principles and applications of ion scattering spectroscopy: surface chemical and structural analysis; Wiley Inter Science: Hoboken, NJ, 2002.
- [23] Fassbender, J. and McCord, J. Magnetic patterning by means of ion irradiation and implantation, *J. Magn. Magn. Mater.* 320, 579–596, 2008.
- [24] Lucia, R. Nanoscale manipulation of Ge nanowires by ion irradiation, *J. Appl. Phys.* 106, 114316 – 114321, 2009.

- [25] Devi, M., Das. R., Mohanta, D., Saha, A. and Baruah, K.K., Enhanced magneto-optic activity of magnetite-based ferrofluids subjected to gamma irradiation, *Appl. Phys. A*, 106,765-771, 2012.
- [26] Devi, M., Paul, N., Mohanta, D. and Saha, A. Characteristic spectroscopic properties of γ -irradiated rare-earth oxide-based ferrofluids, *J. Exp. Nanosci.*, 7,586-595, 2012.
- [27] Yoon, M. and Tománek, D. Equilibrium structure of ferrofluid Aggregates, *J. Phys.: Cond. Mat.* 22, 455105 -455110, 2010.
- [28] Heinrich, D. et al., Dynamics of the Field-induced formation of hexagonal zipped-chain superstructures in magnetic colloids, *Phys. Rev. Lett.* 106, 208301 -208304, 2011.
- [29] Kline, S. J. and McClintok, F. A., Describing Uncertainties in single sample experiments, *Mech. Eng.*75 ,3-8,1953.

Declaration

I hereby declare that the thesis entitled “**Synthesis, characterization and study on the magneto-optic effects of ferrofluids**”, being submitted to the Department of Physics, Tezpur University, Napaam, Tezpur, Assam (India) in fulfillment of the requirements for the award of the degree of Doctor of Philosophy, has previously not formed the basis for the award of any degree, diploma, associateship, fellowship or any other similar title or recognition.

Napaam, Tezpur

Manasi Devi

(Manasi Devi)

Department of Physics

Tezpur University

Tezpur- 784028

Assam, India



TEZPUR UNIVERSITY


Certificate

This is to certify that the thesis entitled “**Synthesis, characterization and study on the magneto-optic effects of ferrofluids**”, submitted to the School of Sciences, Tezpur University in partial fulfillment for the award of the degree of Doctor of Philosophy in Physics is a record of research work carried out by Ms. Manasi Devi under my supervision and guidance.

All help received by her from various sources have been duly acknowledged.

No part of this thesis has been submitted elsewhere for award of any other degree.

Signature of Supervisor:


(D. Mohanta)

Designation: Associate professor

School: Sciences

Department: Physics

Date: 28/12/12

ACKNOWLEDGEMENTS

In the last six years, I availed the opportunity to associate myself in the exciting areas of research and with persons having true love for science and research. In these years, I have been fortunate to spend my time in Nanoscience and Soft matter group of Dept. of Physics, Tezpur University. I am extremely happy to express my thanks and profound sense of gratitude to my supervisor Dr. D. Mohanta for his valuable suggestions, persistent encouragement, creative criticism and scientific approach throughout the period help me to overcome the challenges of the present work. From him I learned how to discover excitements and fun in every aspect of research, and how to approach the problem in a creative way. His supports and assists from U.S.A. at the end of my Ph. D. work was admirable.

I extend my sincere and hearty grateful to Dr. Abhijit Saha of UGC-DAE Consortium for scientific research, Kolkata for his initiatives, personal involvement and valuable suggestions in performing gamma irradiation experiments.

I am grateful to Prof. A. Choudhury and Dr. P. Deb for their expertise comments and suggestions on my research work during this period. I also extend my gratitude to Dr. Kishor K. Baruah for his assistance in performing the MO experiment.

I would like to give special thanks to my lab mate Nibedita Paul and junior Rupali Das for their direct assistance in various

aspects. I am indebted to my sister my friend Dr. Maumita Chakraborty, Dept. of Energy, who has lot of involvements in my research as well as my personal life.

I am also thankful to Dr. P. Kumar of IUAC, New Delhi for landing his support and help during my ion irradiation experiment. I would also like to take this opportunity to thank the staff of TEM facility of SAIJ, NEHU, Shillong and Prof. R. Dutta of Dept. of Chemical Sciences, Tezpur University for giving me the opportunity to characterize my samples.

I also acknowledge my lab mates: senior Dr. Upamanyu Das, juniors- Sayan Bayan, Manjit Bora, Runjum Sarma, Samiran Hazarika and Rizwin Khanam for their valuable efforts in countless way in times of need and requirements.

I would like to thank Dr. Ankur Gogoi, Dr. Sudhir Roy, Dr. Harekrishna Deka, Sovan, Durga Da, Nimisha, Aradhana, Jina, and Mamta (Ghy) for their help.

Last but not least, I gratefully acknowledge my parents, husband, mother-in-law and my baby Jumki for their constant encouragement and support whenever needed.

Manasi Devi

CONTENTS

DECLARATION	xi
CERTIFICATE	xii
ACKNOWLEDGEMENT	xiii
Abbreviations	xix
List of Figures	xxii
List of Tables	xxviii

Chapter 1

Introduction

1.1. Macroscopic magnetic phenomena	1
1.1.1. Magnetic moment	2
1.1.2. Magnetization	4
1.1.3. The Curie-Weiss law	4
1.2. Nanoscale magnetic materials and its characteristic property	5
1.3. Magnetic fluid (ferrofluid)	14
1.3.1. Stability of ferrofluid	15
1.3.2. Magnetic properties of ferrofluids	19
1.4. An overview of ferrofluid synthesis and application	21
1.5. Objective of the thesis	23
References	24

Chapter 2

Synthesis protocol and characterization features of ferrofluids

2.1. Ferrofluids based on different kinds of MNPs, surfactant and carrier fluids	33
2.1.1. Synthesis of magnetite (Fe ₃ O ₄) based	

ferrofluids (with different carrier fluid)	34
2.1.2. Synthesis of magnetite- based FF with methanol as carrier (for varying surfactants)	37
2.1.3. Synthesis of gadolinium oxide (Gd ₂ O ₃) based ferrofluids	39
2.2. Characterization tools	42
2.2.1. X-Ray Diffraction (XRD)	42
2.2.2. Electron microscopy	47
2.2.3. Dynamic light scattering (DLS)	50
2.2.4. Fourier Transform Infra- Red spectroscopy	53
2.2.5. Raman spectroscopy	59
2.2.6. Electron paramagnetic resonance spectroscopy	62
2.2.7. Photoluminescence spectroscopy	65
2.3. Concluding remarks	66
References	67

Chapter 3

Effect of static magnetic field on ferrofluids

3.1. Effect of static magnetic field on ferrofluids	70
3.2. Magneto-optic effects of ferrofluid	71
3.2.1. Faraday rotation of synthesized ferrofluids	72
3.2.2. Linear dichroism of synthesized ferrofluids	78
3.3. Magneto-rheological property of ferrofluid	83
3.4. Concluding remarks	89
References	90

Chapter 4

Low energy ion irradiated nanoparticle based ferrofluids: spectroscopic and magneto-optic characteristics

4.1. Ion irradiation	96
----------------------	----

4.2.Effect of 80-keV Ar ions on synthesized nanoparticles/FFs	101
4.2.1. X-ray diffraction	101
4.2.2. Transmission electron microscopy	102
4.2.3. FT-IR spectroscopy	104
4.2.4. EPR spectroscopy	107
4.2.5. Raman spectroscopy	113
4.4. Concluding remarks	119
References	119

Chapter 5

γ -irradiation effects on ferrofluids

5.1. Gamma (γ) irradiation	125
5.2. γ -irradiation on ferrofluid (FFW, FFK and FFG) systems	127
5.2.1. Transmission electron microscopy	128
5.2.2. Dynamic light scattering	131
5.2.3. FT-IR spectroscopy	135
5.3. Photoluminescence study	139
5.4. Magneto-optic response of gamma-irradiated ferrofluids	144
5.5. Concluding remarks	151
References	152

Chapter 6

Comparative analysis of magneto-optic characteristics of synthesized ferrofluids

6.1. Comparison of magneto-optic responses	156
6.1.1. Faraday rotation of Fe ₃ O ₄ based ferrofluids	157
6.1.2. Linear dichroism of Fe ₃ O ₄ based ferrofluids	160
6.1.3. Irradiation effect on Faraday rotation of FFW	162

6.2. Concluding remarks	163
References	164
Chapter 7	
Analytical calculation of chain length in ferrofluids	
7.1. Structure transition in ferrofluid	167
7.2. Dimensional analysis	170
7.2.1. Methods of dimensional analysis	170
7.2.2. Error analysis	
7.3. Analytical calculation of chain length in ferrofluid	173
7.4. Concluding remarks	181
Rereferences	181
Chapter 8	
Conclusions and future directions	184
Appendix	189
Publications	193
ADDENDA	

Abbreviations

FF	ferrofluid
RT	room temperature
MNP	magnetic nanoparticle
g	gram
rpm	revolution per minute
XRD	X-ray diffraction
h	hour
W-H	Williamson –Hall
TEM	transmission electron microscopy
HRTEM	high resolution transmission electron microscopy
DLS	dynamic light scattering
FWHM	full width at half maxima
FTIR	Fourier transform infra red
EPR	electron paramagnetic resonance
PL	photoluminescence
MO	magneto-optic
EM	electro magnetic
FR	Faraday rotation
LD	linear dichroism
RE	rare earth
MV	magneto-viscous
P	power
PMA	perpendicular magnetic anisotropy
SHI	swift heavy ion
keV	kilo electron volt
MeV	mega electron volt
LEIBF	low energy ion beam facility
IUAC	inter university accelerator centre

SRIM	stopping and range of ions in matter
SANS	small angle neutron scattering
AFM	atomic force microscopy
PDF	pair distribution function
MRI	magnetic resonance imaging
UV	ultra violet
MRI	magnetic resonance imaging

List of Figures

Chapter 1

Figure No.	Caption	Page No
Fig 1.1	: Magnetic moment of an electron moving in a circular path of radius r with velocity v	02
Fig.1.2	: Spin-orbit interaction showing (a) L-S coupling and (b)j-j coupling	04
Fig.1.3	: Magnetic properties of nanostructured system	06
Fig 1.4	: Schematic diagram of (a): multi domain and (b): single domain magnetic structure	08
Fig.1.5	: Schematic diagram for calculation of magnetic dipole-dipole interaction between two particles in a ferrofluid	17

Chapter 2

Fig. 2.1 .	: Schematic diagram of (top to bottom): anionic, cationic, zwitterionic and non ionic surfactants	33
Fig. 2.2	: Unit cell of magnetite with red, blue and white atom as Fe^{2+} , Fe^{3+} and O^{2-} respectively	34
Fig. 2.3	: Chemical structure of oleic acid	35
Fig. 2.4	: Chemical structure of TMAH	37
Fig. 2.5	: Chemical structure of methanol	38
Fig. 2.6	: Unit cell of (A) cubic and (B) hexagonal Gd_2O_3	39
Fig. 2.7	: Chemical structure of CTAB	40
Fig. 2.8	: Structure of ethanol	40
Fig. 2.9	: (a) XRD pattern and (b) W-H plot of the	43

	synthesized Fe ₃ O ₄ particles	
Fig.2.10	: (a)XRD pattern and (b) W-H plot of oleic acid coated synthesized Fe ₃ O ₄ nanoparticles	44
Fig. 2.11	: (a)XRD pattern and (b) W-H plot of the synthesized Gd ₂ O ₃ particles	46
Fig. 2.12	: TEM micrographs of (a) uncoated single domain magnetite nanoparticle and ferrofluids (b) FF1 and (c) FF2	47
Fig. 2.13	: TEM micrographs of FFW with oleic acid coated Fe ₃ O ₄ MNPs	48
Fig. 2.14	: TEM micrographs of FFK with oleic acid coated Fe ₃ O ₄ MNPs	49
Fig. 2.15	: HRTEM micrograph of a FFG particle with clear lattice fringes	49
Fig. 2.16	: DLS study of uncoated Fe ₃ O ₄ nanoparticles	51
Fig. 2.17	: DLS study of FFW	51
Fig. 2.18	: DLS study of FFK	52
Fig. 2.19	: DLS study of FFG	53
Fig. 2.20	: FT-IR spectra of (a) synthesized Fe ₃ O ₄ nanoparticles, (b) TMAH and (c) FF1	54
Fig. 2.21	: FT-IR spectra of (a) oleic acid and (b) FF2	55
Fig. 2.22	: FT-IR spectra of FFW	56
Fig. 2.23	: FT-IR spectra of FFK	57
Fig. 2.24	: FT-IR spectra of FFG	58
Fig. 2.25	: Raman spectrum of oleic acid coated Fe ₃ O ₄ nanoparticles	59
Fig. 2.26	: Raman spectrum of CTAB coated Gd ₂ O ₃ nanoparticles	61

Fig. 2.27	:	EPR response of Fe_3O_4 system with variation of (a) magnetic field and (b) g - value	63
Fig. 2.28	:	EPR response of Gd_2O_3 system with variation of (a) magnetic field and (b) g value	68
Fig. 2.29	:	PL spectrum of FFG specimen under excitation wavelength $\lambda_{\text{ex}}=270$ nm	65

Chapter 3

Fig 3.1	:	(a) Experimental set up and (b) schematic diagram for Faraday rotation measurement with L: laser, C: plano-convex lens, P: polarizer, SM: specimen, (M1, M2, M3): mirror, A: analyser, D: photodetector	73
Fig 3.1(c)	:	Faraday rotation of milli-Q water	74
Fig 3.2	:	FR response of FFW at two different wavelengths	74
Fig 3.3	:	FR response of FFK	76
Fig 3.4	:	FR response of FFG	77
Fig 3.5	:	(a) LD response of FFW and (b) the parallel and perpendicular component of LD	80
Fig 3.6	:	(a) LD response of FFK and (b) the parallel and perpendicular component of LD	81
Fig 3.7	:	(a) LD response of FFG and (b) the parallel and perpendicular component of LD	82
Fig 3.8	:	Variation of viscosity with shear rate for FF1 and FF2	85
Fig 3.9	:	Variation of viscosity (with shear rate) of (a) FF1 and (b)FF2	87
Fig 3.10	:	Relative change of viscosity with magnetic field at shear rate (a) 225 sec^{-1} and (b) 445 sec^{-1}	88

Chapter 4

Fig.4.1	: XRD pattern of unirradiated and Ar-ion irradiated Fe ₃ O ₄ system	102
Fig.4.2	: TEM micrograph of unirradiated (a) FFW, (c) FFK and (e)FFG(at high resolution). The image (b), (d) and (f) are the ferrofluids FFW, FFK and FFG respectively prepared with Ar-ion irradiated particles.	103
Fig.4.3(a)	: FT-IR spectra of FFW prepared with unirradiated and Ar ion irradiated particles	104
Fig.4.3(b)	: FT-IR spectra of FFK prepared with unirradiated and Ar ion irradiated particles	105
Fig.4.3(c)	: FT-IR spectra of FFG [prepared with (i) unirradiated and (ii) Ar-ion irradiated particles] and (iii) ethanol as reference	105
Fig.4.4(i)	: EPR spectra of unirradiated and irradiated Fe ₃ O ₄ nanoparticles with respect to the variation of (a) magnetic field and (b) g values	108
Fig.4.4 (ii)	: EPR spectra of unirradiated and irradiated Gd ₂ O ₃ nanoparticles with respect to the variation of (a) magnetic field and (b) g values	109
Fig.4.5	: Raman spectra of unirradiated and irradiated (a) Fe ₃ O ₄ and (b) Gd ₂ O ₃ nanoparticles	111
Fig.4.6	: Faraday rotation of (a) FFW and (b) FFK. FFs were prepared with unirradiated and Ar-ion irradiated particles	114
Fig.4.6(c)	: Faraday rotation of FFG prepared with unirradiated and Ar-ion irradiated particles	115
Fig.4.7	: Linear dichroism of (a) FFW and (b) FFK. FFs were prepared with unirradiated and Ar-ion irradiated particles	117
Fig.4.7(c)	: Linear dichroism of FFG prepared with	118

unirradiated and Ar-ion irradiated particles

Chapter 5

Fig.5.1(i)	: TEM micrograph of (a) unirradiated and irradiated FFW with dose (b) 878 Gy, (c) 2.635 kGy	128
Fig.5.1(ii)(a)	: TEM of unirradiated FFK	128
Fig.5.1(ii)	: HRTEM micrograph of (a) unirradiated and irradiated FFG with dose (b) 2.635 kGy. The inset of (b) is the SAED pattern	129
Fig.5.2(i)	: DLS spectra of (a) unirradiated (b) irradiated (dose:878 Gy) FFW	131
Fig.5.2(i)(c)	: DLS spectra of irradiated FFW with dose 2.635 kGy	132
Fig.5.2(ii)(a)	: DLS spectra of unirradiated FFK	132
Fig.5.2(ii)	: DLS spectra of irradiated dose FFK with dose (b) 878 Gy and 2.635 kGy	133
Fig. 5.3(a)	: FT-IR spectra of unirradiated and irradiated FFW	135
Fig.5.3	: FT-IR spectra of unirradiated and irradiated (b) FFK and (c) FFG	136
Fig.5.3(c)	: FT-IR spectra of unirradiated and irradiated FFG	136
Fig.5.4	: (i) PL spectra of unirradiated and irradiated FFG with dose (a) 32 Gy,(b) 97 Gy, (c) 292 Gy, (d) 878 Gy and (e) 2.635 kGy, (ii) Energy level diagram of Gd ³⁺	140

Fig.5.4 (ii)	:	Deconvoluted PL spectra of irradiated FFG with dose (a) 32 Gy,(b) 97Gy, (c) 292 Gy, (d) 878 Gy and (e) 2.635 kGy	141
Fig.5.5	:	Variation of relative intensity and relative symmetry factor vs. dose corresponding to (a) defect related emission, (b) band-to-band emission	143
Fig.5.6	:	FR of unirradiated and irradiated (a) FFW and (b)FFK	145
Fig.5.6(c)	:	FR of unirradiated and irradiated FFW	146
Fig.5.7	:	LD of unirradiated and irradiated (a) FFW and (b) FFK	150
Fig.5.7(c)	:	LD of unirradiated and irradiated (c) FFG	151
 Chapter 6			
Fig 6.1	:	FR of (a) unirradiated and (b) 80-keV Ar-ion irradiated MNPs based FFW and FFK	157
Fig 6.1(c)	:	FR of γ -irradiated FFW and FFK	158
Fig 6.2	:	LD of (a) unirradiated and (b) 80-keV Ar-ion irradiated MNPs based FFW and FFK	161
Fig 6.2(c)	:	LD of γ -irradiated FFW and FFK	162
Fig 6.3	:	FR response of unirradiated, FF prepared with Ar-ion irradiated MNPs and γ -irradiated FFW	173
 Chapter 7			
Fig.7.1	:	Schematic of structural evolution in a FF with increasing magnetic field.	169

List of Tables

Table 1.1	Characteristic length with symbol and typical magnitude	08
Table 2.1	Representative data of the observed Raman peaks and assigned modes of Fe ₃ O ₄ nanoparticles	60
Table 2.2	Representative data of the observed Raman peaks and assigned modes	62
Table 3.1	Different parameters of FF1 and FF2	86
Table 5.1	Analysis of DLS spectra	135
Table 5.2	Verdet constant for unirradiated and irradiated ferrofluids	146
Table 6.1	Verdet constant (deg/G-cm) of FFW and FFK for different conditions	160
Table 7.1	Different parameters obtained from experimental results.	178
Table 7.2	Different initial parameters.	179
Table 7.3	Calculated chain length for different FFs.	179
Table 7.4	Error analysis and overall uncertainty	180

Introduction

The sudden attraction of the metal tip of the staff by a black stone, of an elderly Cretan shepherd named Magnes, in Northern Greece called Magnesia, about 4,000 years ago,^[1] has created a revolutionary impact in the modern world. This is the most popular story behind the discovery of magnet/ magnetism. Magnes was curious about the force and he dug the Earth to find the lodestones (load=lead or attract). The Greeks or Chinese were the first to discover the properties of lodestone. Stories of the magnetic properties of lodestone (magnetite, Fe_3O_4) date back to the first century B.C are found in the writings of Lucretius and Pliny the Elder (23-79 AD Roman). Then, around the 11th Century, the Chinese invented the magnetic compass. This invention was timely and allowed navigation at sea possible. Prior to this, the voyagers were dependent on the sun and the stars, thus cloudy weather was a great problem. With advent of widespread applications of magnetic compass, large scale international trade began to flourish, which was the first step in globalization. The first scientific report on magnetite was written by a soldier, named Peter Peregrinus and then William Gilbert in 1600 who tried to know experimentally the story behind magnetism. The endless journey of magnetism as well as the foundation of modern technology progressed specially with the important contributions of Hans Christian Oersted (1777-1851), Michael Faraday (1791 –1867), James Clerk Maxwell (1831-1879), Pierre Curie (1859 –1906), Pierre-Ernest Weiss (1865 - 1940), Felix Bloch (1905-1983), Lev Davidovich Landau (1908-1968) and Louis Néel (1904–2000).

1.1. Macroscopic magnetic phenomena

The magnetic materials are different from non magnetic materials by their exclusive properties. Magnetism exhibited by a system is basically due to the orbital and the spin motion of the electrons. Thus, magnetic properties of a system will be largely dependent on its electronic

configuration. At high temperature, the spin-alignment of the electrons can be affected by random thermal motion. Therefore, magnetic behaviour of most of the systems also depends on working temperature.

1.1.1. Magnetic moment

The fundamental aspect to the magnetic behaviour lies on the magnetic moments (μ_l) of a given material system. This vector quantity quantifies the strength of the internal magnetic field and the impact of an external magnetic field on it. An electron having an orbital angular momentum l is associated with a magnetic moment given by:

$$\mu_l = -\frac{e}{2m} l = -\mu_B l \quad (1.1)$$

where, m is the electron rest mass and μ_B is called the Bohr magneton. The negative sign comes due to the negative charge of electron.

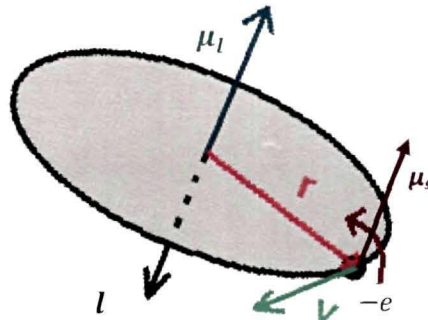


Fig 1.1: Magnetic moment of an electron moving in a circular path of radius r with velocity v

The projection of the magnetic moment along an applied field along z direction is:

$$\mu_{lz} = -m_l \mu_B \quad (1.2)$$

The angular momentum of an electron arises due to two types of motion viz. spin and orbital. The magnetic moment associated with the spin of an electron is called spin magnetic moment. In fact, the electron spin is an intrinsic, quantum mechanical property which has no classical

analogue. Typically, magnetic moments (Fig.1.1) due to spin and orbital motion of an electron are of same order of magnitude. Analogous to orbital moment, the spin magnetic moment of an electron can be expressed by:

$$\mu_s = -\frac{e}{2m} S = -\mu_B S \quad (1.3)$$

Similarly, the projection of the spin magnetic moment along an applied field in the z direction is:

$$\mu_s = -m_s \mu_B \quad (1.4)$$

In atoms, magnetism arises due to presence of unpaired electrons and by virtue of definite spin-orbit interactions. In a light atom, the spins interact collectively and so is the case for orbital moments (L-S coupling). The total orbital angular momentum (L) and spin angular momentum (S) can be defined as:

$$L = \sum_i l_i \quad \text{and} \quad S = \sum_i s_i \quad (1.5)$$

where, the summation extends over all electrons.

The resultant vectors L and S thus formed can be coupled to give rise to the resultant total angular momenta:

$$J = L + S, \quad (1.6)$$

with J can assume values ranging from $J = (L - S)$, $(L - S + 1)$, to $(L + S - 1)$, $(L + S)$. Such a group of levels is called a multiplet. The spin-orbit interaction results in a torque and as a result, L and S would precess around the constant vector J , as shown in Fig.1.2.(a).

In contrast, in heavy atoms, the spin-orbit interaction is stronger than the spin-spin or orbit-orbit ones. The orbital and spin angular momenta of each electron i combine to give the individual total angular momenta (j_i). Finally, the weak electrostatic coupling between the j_i form the resultant total angular momentum (J) as shown in Fig:1.2(b):

$$J = \sum_i j_i = \sum_i (l_i + s_i) \quad (1.7)$$

This is known as jj- coupling. Secondly, the magnetic response of a material system can be determined by its dipole moment, μ given by:

$$\mu = \mu_{tot} \cos \theta = -g_J \mu_B \quad (1.8)$$

Here, g_j is the Landé g -factor expressed as $g_j \approx \frac{3}{2} + \frac{S(S+1) - L(L+1)}{2J(J+1)}$.

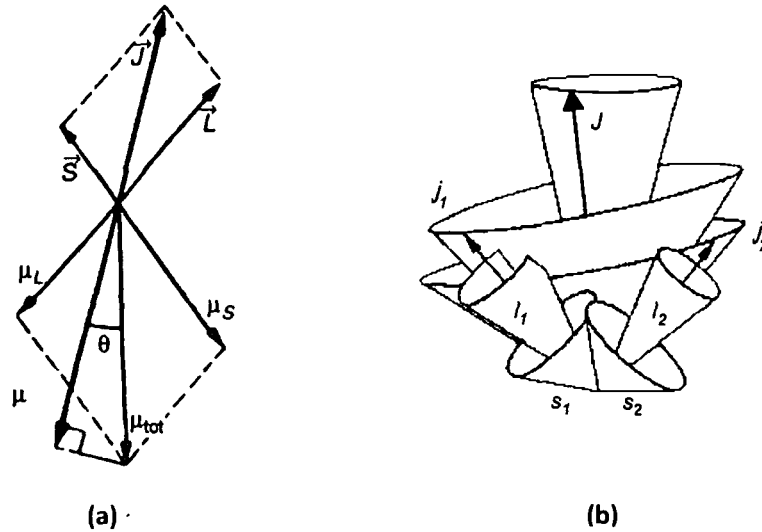


Fig.1.2: Spin-orbit interaction showing (a) L-S coupling and (b)j-j coupling

1.1.2. Magnetization

The response of a magnetic material to an external magnetic field is described by a vector quantity called magnetization. Classically, magnetization is defined as the density of the induced magnetic dipole moment of a material. The net magnetic magnetization results from the field induced as well as the inherent unbalanced magnetic dipole moment of a system. If there are total N atoms in unit volume having magnetic moment μ , then total magnetization will be given by:

$$M = N\mu = Ng_j\mu_B \quad (1.9)$$

1.1.2. The Curie-Weiss law

At a higher temperature, the magnetization of the paramagnetic material is not directly proportional to the applied field. Curie encapsulated that, at a fixed field (H), the magnetization is inversely proportional to the temperature (T):

$$M = C \frac{H}{T} \quad (1.10)$$

Here, C is a material specific constant called Curie constant. The susceptibility of the magnetic material is defined as:

$$\chi = \frac{M}{H} = \frac{C}{T} \quad (1.11)$$

This relation is known as Curie's law.

The ferromagnetic materials (magnetically ordered state) are characterized by spontaneous magnetization which arises due to the quantum-mechanical exchange interaction of the atomic spins. The spontaneous magnetization vanishes at temperature higher than the Curie temperature (T_c) and the system goes to paramagnetic phase. Below T_c the material is in ordered state. Paramagnetic phase is associated with randomly oriented magnetic moment. The Curie-Weiss law describes the magnetic susceptibility of a ferromagnetic specimen above T_c . It can be expressed as:

$$\chi = \frac{C}{T - T_c} \quad (1.12)$$

1.2. Nanoscale magnetic materials and its characteristic property

Recently, research and development of nano dimensional materials (10-100 nm) has received a great deal of interest owing to better means of processability, control, ability and applicability in various fields starting from medicine,^[2,3] energy,^[4,5] semiconductor industry,^[6,7] information and communication^[8,9] to consumer goods.^[10,11] Credit also goes to magnetic nanomaterial for their great contribution in the glorious journey of nanotechnology. The magnetic materials also exhibit tunable properties as the size is reduced to a few atomic clusters. The physical properties become more interesting and extrinsic; due to carrier confinement and quantum size effect.^[12-15] The science and technology of nanomagnetism is comparatively a new revolution, however the evidence of nanomagnetism is much older than human civilization itself. The oldest

paradigm of such evidence was found in a magnetoaerotactic bacterium called *magnetospirillum magneticum* whose age is about two billion years.^[16,17] The bacterium can grow its magnetic particles (upto nanoscale) inside, to passively orient itself in the Earth's magnetic field. They swim towards food in mud by naturally guiding process of orienting themselves through their magnetic property. Magnetic nanoparticle (MNP) is also found in some other living bodies like insects and birds.^[18] MNPs present in many rocks and soils also allow the study of the evolution of the Earth's magnetism and prediction of the age.^[19]

Properties of nanostructured magnetic materials

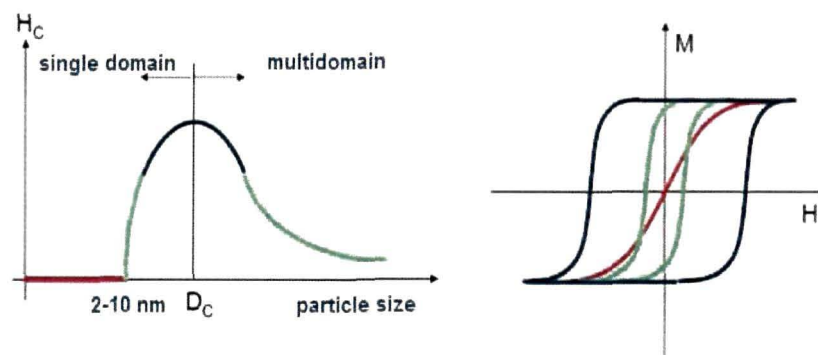


Fig.1.3: Magnetic properties of nanostructured system

Basically, the magnetic nanomaterials differ from their bulk counterparts in many aspects with dimensions comparable to characteristic lengths, such as the limiting size of magnetic domains; broken translation symmetry, with broken exchange bonds and frustration; higher proportion of surface or interface atoms; presence of defects etc.^[20] In general, MNPs are in close contact with other physical substances like capping layer, supporting substrate and encapsulating media (matrices).^[21,22] As a result, their magnetic responses are influenced by these environments. Not only the static properties (e.g. magnetic moment), the dynamic properties (e.g. dynamic susceptibility) also vary in case of

nanomagnetic materials with respect to macroscopic systems.^[23,24] In lower grained size system, time and temperature dependent effects have acquired much importance in recent times.^[25] The phenomenon of superparamagnetism is observed in magnetic nanoparticles if the thermal energy $k_B T$ (k_B : Boltzmann's constant, T : absolute temperature) is of the same order-of-magnitude of the anisotropy energy of the particles, leading to an effectively zero magnetic moment.

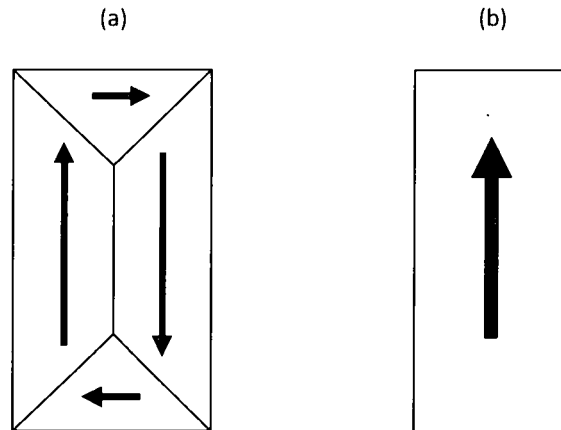
(i) Dimensions and characteristic lengths

There exists a length scale at which materials would exhibit well defined magnetic behaviour. Typically, any observable magnetic response is dependent on the electronic structure of the system of interest. The length scale associated with the microstructure of a polycrystalline material or a composite is an obvious evidence of characteristic length. Due to the slow spatial variation on the scale of the grains of a polycrystalline material, the expression $M=M(H)$ gives adequate information of the responses of the material to an applied field. Here, the magnetization M and field strength H take the average values, calculated over a large volume on the scale of characteristic length. Generally, the length scales are of the order of 10-100 nm. Thus the size regime of characteristic lengths is comparable to nanomaterial system. Some examples of the typical characteristic lengths are given in table 1.1.^[26]

The effect of the characteristic lengths on the magnetic properties is the case of magnetic particles with dimensions smaller than the critical magnetic (single-) domain diameter. In bulk material, more than one domains are packed together [shown schematically in Fig. 1.4 (a)] to minimize the magnetostatic energy of the material. These domain structures are responsible for definite magnetic response of ferromagnetic materials. By lowering down particle dimension, a drastic change in the domain structure occurs. As the particle size decreases, energy of domain wall formation gets enhanced and overcomes the energy due to domain

Table 1.1: Characteristic lengths with symbol and typical magnitude

Length	Symbol	Typical magnitude (nm)
Interatomic distance (for Fe)	d_a	2.5×10^{-1}
Range of exchange interaction	d_{ex}	$\sim 10^{-1} - \sim 1$
Domain size	d_c	$10 - 10^4$
Superparamagnetic critical diameter	D_{cr}^{SPM}	$\sim 1 - \sim 10^2$
Critical single-domain size	D_{cr}	$\sim 10 - \sim 10^3$
Domain wall width	δ_o	$\sim 1 - \sim 10^2$
Exchange length	l_{ex}	$\sim 1 - \sim 10^2$
Spin diffusion length	l_{sd}	$\sim 10 - 10^2$
Electron mean free path	λ_{mfp}	$\sim 1 - 10^2$

**Fig 1.4:** Schematic diagram of (a): multi domain and (b): single domain magnetic structure

formation. Below the critical length (d_c), energy consideration does not support the formation of domain wall and particles can exist with single domain structure. In nano sized particles, the exchange length of the domains converge resulting in single domains [Fig. 1.4(b)].^[26]

(ii) Broken Translational symmetry

Generally, crystal structures are associated with symmetry elements. Point symmetry, translational symmetry and rotational symmetry are few examples of crystal symmetry elements. At the edges, the crystal system has to sacrifice its translational symmetry. In nano dimension, most of the atoms are found in the surface. This leads to a considerable lost or broken up of translation symmetry in nanoparticles. It is considered that the surface of nano material, with broken symmetry, is the most fascinating playground in the age of nanotechnology.^[27] The changes in physical, magnetic properties viz. density of states (DoS), magnetic moment [according to the dimensionality of the sample (0D, 1D or 2D)] are considered as important aspects of the broken symmetry. The drastic change of electron DoS, from continuous state to discrete lines (for bulk and 0D respectively) is related with broken symmetry of nanomatter. Magnetic property such as the Pauli's susceptibility (χ_P) is a direct measurement of DoS of a free electron gas at the Fermi energy (highest occupies quantum state at absolute zero).^[26] It is expressed as:

$$\chi_P = \mu_0 \mu_B^2 D(E_F) \quad (1.13)$$

where, μ_0 is the permeability of free space, μ_B is the Bohr magneton and $D(E_F)$ is the density of state at Fermi energy.

Another significant outcome of the symmetry breaking in nano regime is the change of the coordination of atoms at the interface. The atoms at the surface has less coordination number than the interior atoms. The reduced coordination number of the particles influences both atomic and electronic structure of the particle. Thus the electronic, optical and

magnetic properties of the nanomaterials are no longer same as their bulk counterparts. ^[28]

(iii) The exchange interaction

The long range spin ordering over macroscopic distances are determined by the spin-spin exchange interaction. The quantum mechanical origin depicts the Coulomb coupling between the electrons orbit for the exchange interaction. It also follows Pauli exclusion principle. From the Heisenberg model,^[29] the interaction energy between two localized spins s_i and s_j can be described by a potential energy of the form:

$$V_{ij} = -2Js_i \cdot s_j \quad (1.14)$$

here, J is a quantum mechanical exchange integral. For a ferromagnetic material, J is positive. In semi classical approach, spin matrices are replaced by classical spin angular momentum vectors. It is also assumed that only interactions between nearest neighbour spins are important. Summing over the various lattice sites, the Heisenberg interaction may be expressed in a Taylor series in terms of the gradient of magnetization $m(r) = M(r)/M_s$, giving the expression for exchange energy density.^[30]

$$E_{ex} = A(\nabla m)^2 = A[(\nabla m_1)^2 + (\nabla m_2)^2 + (\nabla m_3)^2] \quad (1.15)$$

where, A is a constant specific for a given material system, called exchange stiffness constant. In general, A is temperature dependent. The above equation describes the change in energy for any deviations from collinear structure of magnetic moments. It does not depend on the magnetization direction and hence isotropic. In nanostructured material, close contacts between two ferromagnetic structures like nanograins or different layers of a thin film multi layer, either directly or through an interposed nonmagnetic body; are very common. These structures can be coupled via the exchange interaction. The interface energy density due to

this type of interaction can be expressed from the generalized Heisenberg interaction:^[31]

$$E_{int} = C_{bl}(1 - \mathbf{m}_1 \cdot \mathbf{m}_2) + C_{bq} [1 - (\mathbf{m}_1 \cdot \mathbf{m}_2)^2] \quad (1.16)$$

Here, m_1 and m_2 are the magnetization vectors at the interface, C_{bl} and C_{bq} are the bilinear and biquadratic coupling constant; respectively.

(iv) Magnetic anisotropy

In a magnetic system, there are always some energetically favoured, definite spatial directions owing to anisotropy effects. In the magnetization process, the work done to bring a ferromagnetic system from a demagnetized state to an ordered magnetic state is stored as potential energy, called the magnetic anisotropy (free) energy. The anisotropy energy is expressed as a volume integral (extended over the magnetic body) of an anisotropy energy density (w_a):^[32]

$$E_a = \int w_a dV \quad (1.17)$$

The anisotropy energy density (w_a) term possesses crystal system-specific expressions.

This anisotropy strongly depends on the direction of magnetization relative to the structural axes of the material. The directions along which the magnetization energy is minimum are called easy magnetization axes.

Crystal anisotropy

Crystal anisotropy is inherent to material system. Crystal symmetry and arrangement of the atoms in the crystal lattice could affect the crystal anisotropy. This anisotropy results from the combined action of spin-orbit and lattice-orbit coupling.^[33]

The anisotropy energy density can be expressed as a function of the direction cosines of the magnetization vector with respect to crystal axes. In a system of cubic symmetry, the anisotropy energy density is expressed as:

$$E_{mca} = K_0 + K_1(m_1^2 m_2^2 + m_1^2 m_3^2 + m_2^2 m_3^2) + K_2 m_1^2 m_2^2 m_3^2 \quad (1.18)$$

The suffices 1, 2, 3 refer to the cubic axes and K_j are anisotropy constants. In polar co-ordinates the equation becomes

$$E_{mca} = (K_1 + K_2 \sin^2 \vartheta) \cos^4 \vartheta \sin^2 \varphi \cos^2 \varphi + K_1 \sin^2 \vartheta \cos^2 \vartheta \quad (1.19)$$

The anisotropy constants are material specific and their values decreases rapidly with increasing order.

Surface anisotropy

Owing to the large surface to volume ratio, low-dimensional materials experience a lower symmetry environment with respect to bulk material. In that case, surface magnetization would contribute to the anisotropy energy. Following Néel's pair interaction model, the surface anisotropy energy density for a structurally isotropic crystal can be expressed as:^[34]

$$E_s = K_s [1 - (\mathbf{m} \cdot \mathbf{n})^2] \quad (1.20)$$

where \mathbf{n} is the normal to the surface and K_s is a constant.

Exchange anisotropy

In general, the hysteresis loop of a non uniform system (eg. a system of ferromagnetic and antiferromagnetic medium), shifts along the field axis.^[35, 36] This type of shifting is due to the exchange anisotropy. The exchange anisotropy is an interfacial effect.

This type of exchange anisotropy has a great technological advantage. It is mainly used in magnetic recording media,^[37] giant magneto-resistance (GMR)^[38] at low saturation field etc.

(v) Dipolar interaction

Magnetic body produces a field by itself or by different macroscopic regions of the body. Conveniently, this type of field is termed as stray-field (H_d). Long range magnetic dipolar interaction contributes magnetic free energy to such field. By definition,^[39] stray field is the magnetostatic field generated by the divergence of the magnetization:

$$\nabla \cdot \mathbf{H}_d = \nabla \cdot \mathbf{M} \quad (1.21)$$

Free magnetic charges can be considered at the origin of the stray field. The stray field energy (E_d) is the potential energy of the magnetic moment in the field (produced by the sample itself), which can be expressed as an integral over the volume of the body:

$$E_d = \frac{1}{2} \mu_0 \int_{\Omega} \mathbf{H}_d^2 dV = -\frac{1}{2} \mu_0 \int_{body} \mathbf{H}_d \cdot \mathbf{M} dV \quad (1.22)$$

with μ_0 as the permeability of the vacuum. The first integral extends over the whole space. The above equation can be solved by considering the magnetic scalar potential (ψ). The demagnetizing field (field inside a magnetic material) is related with the magnetic scalar potential by the relation:

$$\mathbf{H}_d = -\nabla\psi \quad (1.23)$$

The nanostructured materials come with different shapes: rods, cylinders etc. In such case, the demagnetizing factors have to be approximated for each arbitrary shape. Though the magnetization is uniform throughout the body, the demagnetization field varies from point to point within the body.

(vi) Magneto-elastic interaction

When a magnetic material undergoes a magnetic interaction, in order to minimize its energy, it deforms spontaneously. The property of a magnetic material that its physical dimension changes in response to modification in its magnetization is called magnetostriction. External stimuli induced deformation in turn makes certain direction energetically favourable for the magnetization to align with them. Both the stray field energy and the exchange interaction energy are affected by the deformation. The changes occur in stray field energy by deformation is manifested as form effect of magnetostriction and that of exchange interaction energy as volume magnetostriction. The dependence of the magnetic property of a system on a preferred direction is called anisotropy. The spin-orbit interaction and the overlap in wavefunctions

between neighbouring atoms are responsible for the magneto-elastic or magnetostrictive anisotropy.

In a uniformly magnetized crystal system of cubic symmetry, the magneto-elastic interaction energy density may be expressed as:^[40]

$$E_{me}(m_i, \varepsilon_{ij}) = B_1 \sum_i \varepsilon_{ii} (m_i^2 - \frac{1}{3}) + B_2 \sum_{i \neq j} m_i m_j \varepsilon_{ij} \quad (1.24)$$

here, ε_{ij} is the crystal strain tensor ($i, j = x, y, z$), m_i is the direction cosine of M with respect to the cubic cell edges, B_1 and B_2 are the magneto-elastic coupling constants.

In nanomaterials, the large surface atoms have great influence on the magnetostriction coefficients like other energy density terms (surface anisotropy).^[41] In multilayer systems with varying thicknesses, two different regimes namely, coherent and incoherent can be considered.^[42] In coherent regime, lattice mismatch is compensated by the tensile strain (*appendix I*) in one layer and a corresponding compressive strain (*appendix I*) in the adjacent layer. The effective magnetostriction constant depends on the thickness of the concerning layer.

1.3. Magnetic fluid (ferrofluid)

The quest for a magnetic liquid, which can be controlled by an external magnetic field, had been one of the major problems in the scientific community since long back. The first attempt was made by Dr. Gowan Knight In 1779.^[43] He tried to suspend some iron fillings in water. But sedimentation of the fillings marked the failure of his attempt. The ferromagnetic material also cannot fulfill the requirement of magnetic liquid as their Curie temperature is well below the melting point. This type of materials no longer shows ferromagnetism in their melted form. After that the liquid metals gave some ray of hope. In such system, an electric current is applied and the Lorentz forces in strong magnetic field can be used to control the flow of it.^[44] But this concept was also discarded from the technological and application point of view; as only extremely high

magnetic field can significantly change the flow of the liquid metal.^[45]

The malfunction of these entire attempt, gives the hint that only the magnetic body force (Kelvin force) can solve the problem of magnetic control of liquid flow.^[45] For a magnetisable material with susceptibility proportional to the density, the Kelvin force is expressed as:

$$F_K = \mu_0 \int M \nabla H dV \quad (1.25)$$

here, M is the magnetization of the material, ∇H is the magnetic field gradient and μ_0 is the permeability of the vacuum. The integration is carried over the entire volume of the sample. Now the problem is that to make the real use of magnetic body forces, a liquid is required with high magnetization even for small magnetic field strength. However, all the problems were well taken by S. Papell.^[46] He succeeded in this long journey on producing stable colloidal solution of magnetic nanoparticles in appropriate carrier fluid. This type of fluid is commonly termed as ferrofluid.

1.3.1. Stability of ferrofluid

Basically, FF is a colloidal solution of magnetic nanoparticles in an appropriate carrier fluid. For various application purposes, the particles must remain suspended. In other words, stability is the key factor for technological relevance. In a FF, the dispersed particles are in Brownian motion. Their thermal energy plays a major role in the stability factor. In order to get a stable suspension the thermal energy $E_T = k_B T$ of the particles must be high enough so that the particles remain dispersed in the fluid. In a region of magnetic field gradient, the stability of the ferrofluid will be maintained if the dispersed particles can move freely between a region of strong magnetic field and a field free region. The energy of the dispersed particles in the magnetic field region is given by:^[47]

$$|E_H| = \mu_0 m H \quad (1.26)$$

with m being the magnetic moment of the particles. If the spontaneous magnetization of the particles is expressed by M_s and considering the

particles to be spherical with a diameter d , the magnetic moment will be given by:

$$m = M \cdot \frac{\pi}{6} d^3 \quad (1.27)$$

Therefore, the necessary condition for a stable suspension in a magnetic field gradient is $E_T > E_H$ and thus,

$$k_B T > \mu \cdot M \cdot \frac{\pi}{6} d^3 H \quad (1.28)$$

This implies the critical size of the particles to be remained suspended in the carrier fluid in the magnetic field gradient as:

$$d < \left(\frac{6k_B T}{\mu \cdot M \pi H} \right)^{\frac{1}{3}} \quad (1.29)$$

Agglomeration is another point to be considered for a stable ferrofluid. In spite of keeping the size of the particles within the maximum limit, the stability of the FF may be hindered by agglomeration of the particles. Agglomeration increases the active diameters of the particles, thus, causing a destabilization of the fluid by suspension. The magnetic dipole-dipole interaction is the leading force for this type of agglomeration. Again, the counteracting influence of the dipole-dipole interaction is the imbalance in the thermal motion of the particles. So, as for stability argument, the magnetic dipole interaction energy has to be compared with the thermal energy of the interacting particles.^[48] This gives:

$$2k_B T > \frac{\mu \cdot m^2}{2\pi r^3} \quad (1.30)$$

with r as the distance between the two interacting magnetic particles. Now, assuming that the magnetic moments of the particles to be parallel and it aligns with the connecting vector of the interacting particles^[48] (Fig. 1.5) we get:

$$2k_B T > \frac{\mu \cdot \pi M^2}{9} \frac{d^2}{(l+2)^3} \quad (1.31)$$

here, the distance r is replaced by the sum of the diameters of the

particles d and their surface to surface distance δ and it is considered that

$$l = \frac{2\delta}{d}$$

The FF with uncovered magnetic particles is not stable enough despite of satisfying all requisite conditions that make-up the fluid. The attractive interaction due to van der Waals interaction is very strong in the FF which leads to coagulation of the particles. The van der Waals interaction energy for spherical particles with diameter d and separated by a distance δ can be written as:^[48]

$$|E_{vdw}| = \frac{A}{6} \left[\frac{2}{l^2 + 4l} + \frac{2}{(l+2)^2} + \ln \left(\frac{l^2 + 4l}{(l+2)^2} \right) \right] \quad (1.32)$$

Here, A is the Hamaker constant.^[49]

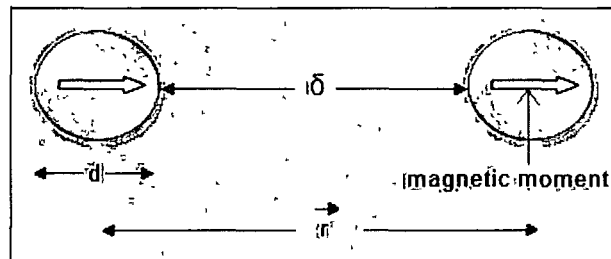


Fig.1.5: Schematic diagram for calculation of magnetic dipole-dipole interaction between two particles in a ferrofluid

To get rid of this problem, the dispersed MNPs have to be coated with a surfactant so that colloidal stability ensures the overall stability of the ferrofluid. Papell^[46] was the first to obtain a stable FF anchored in stearic media. Long chained surfactant molecules were used to get the appropriate steric repulsion. When the particles distance is smaller than two times the thickness of the surfactant layer, it becomes difficult for the surfactant molecules to arrange themselves into a structure. Ultimately, the surfactant molecules exert repulsive interaction energy. For spherical particles, the repulsive interaction energy is of the form,^[48]

$$E_{steric} = \frac{K_B T \pi d^2 \zeta}{2} \left[2 - \frac{l+2}{t} \ln \left(\frac{1+t}{1+l/2} \right) - \frac{l}{t} \right] \quad (1.33)$$

where, ζ denotes the surface density of the surfactant molecules. The surfactant thickness, $t = 2s/d$ with s the thickness of the surfactant layer is normalised to one. Now-a-days, people often prefer this method (steric repulsion) to get a high quality ferrofluid with stable suspension. In general, the MNPs are coated with single layer of surfactant if the carrier fluid is a non-polar solvent (e.g. kerosene). Otherwise, in case of polar solvent (e.g. water) the particles have to be coated with a double layer of surfactant. The role of surfactant on MNP has also created a new field of research. Regmi *et al.*^[50] studied the effect of different fatty acid based surfactants on preparing ferrofluids and its impact on hyperthermia. The excess amount of surfactant is also found to be harmful for maintaining the stability of FFs.^[51,52]

There is another type of FF, where stability against agglomeration of the colloidal system is attained by charging the dispersed MNPs electrically. This type of FF is called ionic ferrofluid. In an ionic ferrofluid, an acid-alkaline reaction between the previously prepared MNPs and the carrier, generates charges on the surface of the nanoparticles.^[53] Particles are charged by transferring protons (H^+) either out from the nanoparticle surface or back to the grains from the acid solvent. pH is also a crucial point in ionic FF. Positively charged MNPs are able to form stable colloids in acidic medium ($pH < 6$) and negatively charged particles yield stable FF in basic medium ($pH > 6$).^[54] As a consequence of the absence of any protecting layer (surfactant coating), ionic FFs are prone to cluster formation in presence of an external field.^[55] In recent years some different FFs, which are ultrastable and often biocompatible, have been developed using a combination of both ionic and surfactant coating methods.^[56,57]

1.3.2. Magnetic properties of ferrofluids

The importance of FFs in both the fields of fundamental research

as well as technology cradles high mainly because of the control on its flow and unusual physical properties induced by an applied magnetic field. The magnetic properties of the FFs in response to external stimuli could bring in new insights for the cause of technological benefit.

(i) Equilibrium magnetization

In general, FF systems are stable colloids in nature, where non interacting spherical particles are suspended. In this regard, the magnetic properties of the FF resembles with non interacting thermally agitated magnetic dipoles. More precisely, FF system can be considered as a paramagnetic system. The magnetization of the fluid follows Langevin equation, described as:

$$M = M_S \left(\coth \alpha - \frac{1}{\alpha} \right) \quad (1.34)$$

$$\alpha = \frac{\mu m H}{k_B T}$$

here, the saturation magnetization: (M_S) is defined as $M_S = \phi M_s$ with ϕ being the volume concentration of the magnetic component and M_s as the spontaneous magnetization of the fluid. For small values of the energy ratio (α), the Langevin function can be approximated as $L_S = \frac{1}{3}\alpha$. So the magnetization of given FF in a small applied field is:

$$M \approx \frac{M_S}{3} \frac{\mu m H}{k_B T}$$

$$= \chi_{in} H \quad (1.35)$$

with initial susceptibility as:

$$\chi_{in} = \frac{M_S}{3} \frac{\mu m}{k_B T} \quad (1.36)$$

In FF system, the initial susceptibility is much higher than a paramagnetic system due to the large magnetic moment (m) interacting with the field in the former case.

The magnetization (M_H) of the fluid along with the eq. (1.34) and (1.36) also provides information regarding the microstructure of the fluid.

In case of very high field, the function $\coth \alpha$ tends to 1 and the eq.(1.34) can be expressed as:

$$M_{(H \rightarrow \infty)} = M_S - \frac{M_S}{\alpha} \quad (1.37)$$

The graph between M versus $\frac{1}{H}$ and extrapolating $\frac{1}{H} = 0$, gives us the value of M_S . Once this value is known, the initial susceptibility eq. (1.36) gives the value of mean diameter of the MNPs.

(ii) Relaxation of magnetization

Since its inception, the ferrofluid-hydrodynamics is found to be imperative for the complete understanding of many amazing phenomena (eg., shear thinning, field driven instability etc.).^[58,59,60] The hydrodynamic theory was derived by Shliomis^[61] and it was based on two essential consideration i.e., relaxation of magnetization M and a torque in the stress tensor. In general, the responses of the magnetization of the FFs, to an applied field, are of two types. In one type, the magnetic moment is fixed with respect to the crystal structure whereas, in the other type it is not fixed with the crystal structure. Conventionally, the particles possess with the first type of relaxation magnetization are called the magnetic hard particles and the other type is the magnetic weak particles. The relaxation of the magnetization of the magnetically hard particles occurs through the rotation of the particles as a whole (Brownian type). On the other hand, the weak particles relax by rotation of the magnetic moment within the particles (Neel type). The thermal energy plays a major role in magnetically weak particles. In actual sense, the excess thermal energy, which is high enough to overcome the crystal anisotropy generated energy barrier, guides the weak particles to relax by a relative rotational motion inside the particles with respect to the crystal structure. Both the relaxation processes are considered with respective characteristic relaxation time. The hard magnetic particles possess the characteristic Brownian relaxation time expressed as:^[62]

$$\tau_B = \frac{3\eta\tilde{V}}{k_B T} \quad (1.38)$$

where \tilde{V} takes the volume of the MNP along with the surfactant layer and η is the dynamic viscosity of the fluid.

Similarly, Néel relaxation time is the characteristic relaxation time for the magnetically weak particles. The expression for the Néel relaxation time is: ^[63]

$$\tau_N = f_s^{-1} \exp \frac{KV}{k_B T} \quad (1.39)$$

This relaxation time is a function of the anisotropy constant K , the Larmour frequency f_s , the volume of the magnetic core V and the thermal energy $k_B T$.

A FF with monodisperse dispersion follows the relaxation process with shorter time. The size of the dispersed particles influences greatly the preferred relaxation time of any FF. The Brownian relaxation time depends linearly on the particles size while the Néel relaxation time changes exponentially with the size of the particles. Thus, smaller particles relax through τ_N with smaller time. At a critical diameter, particles alter its relaxation time from τ_N to τ_B . Near the critical diameter, the particle relaxation time is neither τ_N nor τ_B , rather it follows a combined relaxation time as: ^[64]

$$\tau_{eff} = \frac{\tau_N \tau_B}{\tau_N + \tau_B} \quad (1.40)$$

1.4. An overview of ferrofluid synthesis and application

From its invention till date, people have reported various kinds of FFs. Popell ^[46] started the new era of FF with a magnetite (Fe_3O_4) based FF. Since then, Fe_3O_4 is being considered as one of prime component (MNP) for preparing FF. Different synthesis techniques have been employed to prepare Fe_3O_4 based FFs. The most widely-used synthesis procedure is the synthesis of Fe_3O_4 nanoparticles by co-precipitation

methods and subsequent dispersion in an appropriate carrier fluid.^[65-69] People also follow other wet-chemical methods for synthesizing FFs. Reverse micelle is one such easy, cost effective method adopted for FF synthesis. Ervithayasuporn *et al* have reported the one-pot synthesis of core-shell type nanoparticle based FF in poly (organosilsesquioxane) via reverse micelle route.^[70] There are also reports of different FF systems (other than Fe_3O_4). Maghemite ($\gamma\text{-Fe}_2\text{O}_3$), another type of iron oxide, is also extensively used for ferrofluid synthesis.^[71-73] Further, top-down approach has been opted to produce FFs. This method is preferable for high quality MNPs with minimal impurity (as byproduct). Yang *et al* has reported solid state synthesis of iron oxide based FF which was suitable for magnetic resonance imaging contrast application.^[74] FFs have been prepared synthesizing iron oxide powders by ball milling^[75,76] followed by subsequent dispersion in the carrier fluid.

The magnetization of a FF strongly depends on temperature. In presence of a non-uniform magnetic field, along with a temperature gradient, the viscosity of the fluid undergoes inhomogeneous distribution. To make a temperature sensitive FF for thermo-magnetic energy conversion is still a topic of current interest. Ferrite based ferrofluid e.g. $\text{Mn}_{1-x}\text{Zn}_x\text{Fe}_2\text{O}_4$ (with x varying from 0.1 to 0.5) fulfills the requirement of a thermo-magnetic energy converter.^[77] Co-ferrite (CoFe_2O_4) FF tailors the enhancement of magnetocrystalline anisotropy upto 380 kJ/m^3 .^[78] FF having Ba-ferrite as dispersed nanoparticles, is also being used in technological application for its enhanced anisotropy barrier and heating effect in an ac magnetic field.^[79]

In recent times, magnetic fluids/ferrofluids are extensively used in targeted drug experiments.^[80-83] Thus, FF extends its helping hand in therapeutics especially, in curing cancer patients. Magnetic fluid hyperthermia (MFH) is an advanced treatment that destroys cancer cells by heating a FF-impregnated malignant tissue with an ac magnetic field. The minimal damage caused to the surrounding healthy tissue is the main

advantage of MFH.^[84-86] The magnetic control of FF gives a new direction to magneto-sealing application.^[87,88] Air cooled FF seal is also being used in X-ray tube.^[89] The smart material FF has also been used in Bragg grating. It was reported that the spectral response of the grating reflector inscribed in a microstructured optical fibre has been modified by the application of an a FF.^[90] Optofluidic in-fibre magnetometer, based on a microstructured optical fibre Bragg grating which has been infiltrated using a ferrofluid can measure static magnetic field in the range 740-2200 Gauss.^[91] Ferrofluid based dynamic plug is being used as valve and actuator for aqueous fluid expansion.^[92] In the field of food research, FF is used to modify catalytic activity. FF based biocatalysts are useful for its inexpensive, non toxic and magnetically responsive properties.^[93] Besides its proven applications, research is still open with respect to various aspects of magnetic field orientated structures.^[94,95] To add, some of the fascinating areas of research are magnetic active core and hydrodynamic diameters of MNPs dispersed in FFs,^[96] magnetic field depended viscosity^[97,98] etc.

1.5. Objective of the thesis

This thesis highlights synthesis and characterization of different ferrofluids along with their application in various magneto-optic fields. Special emphasis was given to prepare both conventional and non conventional system based FFs. The selection of an appropriate surfactant as well as carrier is very crucial for a stable FF. Thus, it is also intended to synthesize FF with different types of surfactant-coated nanoparticles and dispersed in diverse carrier fluids. To study morphological, chemical and structural aspects, the synthesized nanoparticles and FFs were characterized by different microscopic and spectroscopic analytical tools: X-ray diffraction, electron microscopy, dynamic light scattering, Fourier transform infra-red spectroscopy, electron

paramagnetic resonance spectroscopy, Raman spectroscopy and photo luminescence spectroscopy.

A FF behaves as a normal liquid in absence of any magnetic stimulus. But the application of an external magnetic field transforms it to a magnetic fluid which is then capable of exhibiting magneto-optic and magneto-viscous effects. To be specific, magneto-optic responses viz. Faraday rotation (FR) and linear dichroism (LD) of the as prepared FFs were studied in a custom made experimental set-up. The magneto-viscous/rheological study was also performed under selective shear flow conditions.

Energetic ion/photon irradiation is a latest topic of interest in advanced nanoscience and technology. Two types of irradiations, namely, low energy (~keV regime) ion irradiation and gamma (γ)-irradiation were considered to irradiate the synthesized nanoparticles/FFs. The subsequent modifications in structural and morphological aspects as well as in magneto-optic responses are presented. A FF undergoes different phases of structural evolution from linear chains to bundles of zipped chains in presence of a magnetic field. Towards the end of the study, it is endeavoured to calculate the length of the linear chains in ferrofluids.

References:

- [1] McGregor, H. *Magnets and Spring*, Windmill Books, NY, 2011.
- [2] Prasad S. et al, Polymer nanoparticles containing tumor lysates as antigen delivery vehicles for dendritic cell-based antitumor immunotherapy” *Nanomedicine* 7, 1-10, 2011.
- [3] Higgins, P. Et al. Nanomedicine: Nanotubes reduce stroke damage, *Nat. Nanotech.* 6, 83-84, 2011.
- [4] Choi, J. J. PbSe Nanocrystal Excitonic Solar Cells, *Nan. Lett.* 9, 3749-3755, 2009.
- [5] Kiebele, A. and Gruner, G. Carbon nanotube based battery architecture, *Appl. Phy. Lett.* 91, 144104-144106, 2007.

- [6] Iniewski, K.(ed.) *Nano Semiconductors, Device and Technology*, CRC Press, Florida, 2012.
- [7] Greet, J., Korkin, A. and Labanowski (eds.) *Nano and Giga challenges in Microelectronics*, Elsevier, The Netherlands, 2003.
- [8] Benjamin, S. C et al., Towards a fullerene-based quantum computer, *J. Phys.: Condens. Matter*, 18, S867–S883, 2006.
- [9] Tseng, R. J. et al. Digital memory device based on tobacco mosaic virus conjugated with nanoparticles, *Nat. Nanotech.* 1,72 – 77, 2006.
- [10] Kim, D.M. and Cho, G.S. Nanofood and Its Materials as Nutrient Delivery System (NDS), *Agri. Chem. Biotech.* 49 (2), 39-47, 2006.
- [11] Dubasa, S. T. et al. Layer-by-layer deposition of antimicrobial silver nanoparticles on textile fibers. *Coll.Surf. A*, 289, 105-109, 2006.
- [12] Lu, L., Li, L., Wang, X. and Li ,G. Understanding of the finite size effects on lattice vibrations and electronic transitions of Nano α -Fe₂O₃. *J. Phys. Chem B* 109, 17151-17156, 2005.
- [13] Kusai, H. et al. Large magnetoresistance in rubrene-Co nano-composites, *Chem. Phy. Lett.* 448, 106–110, 2007.
- [14]Wang, J. et al. Remote manipulation of micronanomachines containing magnetic nanoparticles, *Opt. Lett.* 34, 581-583, 2009.
- [15] Zandrahimi, M. et al. The effect of multi-step milling and annealing treatments on microstructure and magnetic properties of nanostructured Fe–Si powders, *J.Magn.Magn. Mater.* 323, 669–674,201.
- [16] Blakemore R. P., Magnetotactic bacteria, *Ann. Rev. Microbiol.* 36, 217-238, 1982.
- [17] Schüler, D.(ed.) *Magnetoreception and magnetosomes in Bacteria*, Springer-Verlag, Berlin, Heidelberg, 2007.
- [18] Wiltshko, R. and Wiltshko, W., *Magnetic Orientation in Animals*, Springer Verlag, Berlin, Heidelberg, 1995.
-

- [19] Evans, M.E. and Heller, F. *Environmental Magnetism*, Academic Press, San Diego, 2003.
- [20] Nalwa, H. S.(ed.) *Handbook of nanostructured materials and nanotechnology*, Academic Press, London , 2000.
- [21]Chen, B and Fan, Y. Study on the preparation of Fe₃O₄ nanomagnetic fluid for seal, *Adv. Mater. Res.* 139-141, 34-38, 2010.
- [22] Meng, H. and Wang, J. P. Spin transfer in nanomagnetic devices with perpendicular anisotropy, *Appl.Phy.Lett.* 88, 172506-172508, 2006.
- [23] Liu, J.P., Fullerton, E., Gutleish,O. and Sellmyer, D. *Nanoscale Magnetic Materials and applications*, Springer-Dordrecht, Heidelberg, London, NY, 2009.
- [24] Das, M.P.(ed.) *Condensed Matter*, Nova Science Publishers, NY, 2007.
- [25] Himpsel, F.J. et al. Magnetic Nanostructures, *Adv. Phys.*47, 511-597, 1998.
- [26] Guimarães, A. P. *Principles of Nanomagnetism*, Springer-Verlag Berlin Heidelberg, 2009.
- [26] Sellmyer,D. and Skomski, R. (eds.) *Advanced magnetic nanostructure*, Springer--Verlag Berlin Heidelberg, 2006.
- [27] Plummer, E. W. et al. Surfaces: a playground for physics with broken symmetry in reduced dimensionality, *Sur. Sc.* 500, 1–27, 2002.
- [28] Belkacem, M. and Dinh, P. M. (eds.) *Condensed matter Theories*, Nova Science Publishers, New York, 2005.
- [29] Chaikin, P.M. and Lubensky, T.C. (eds.) *Principles of Condensed Matter Physics*, Cambridge University Press, Cambridge, UK, 1995.
- [30]Ogawa, T and Kanemitsu, Y. (eds.) *Optical properties of low dimensional materials*,World Scientific, Singapur, 1995.
-

- [31] C. Kittel and J. K. Galt, *Solid-State Physics*, Academic Press, New York, 1956.
- [32] Sattler, K.D.(ed.) *Handbook of Nanophysics*, CRC Press, NW, 2011.
- [33] Darby, M. and Isaac, E. D. Magnetocrystalline anisotropy of ferro- and ferrimagnetics, *IEEE Trans. Magn.* 1, 259-304, 1974.
- [34] Néel, L. *Compt. Rend. Acad. Sci*, 237, 1468, 1953.
- [35] Meiklejohn, W. H. Exchange Anisotropy-A Review *J. Appl. Phy.* 33,1328-1335, 1962.
- [36] Magaraggia, R. Exchange anisotropy pinning of a standing spin-wave mode, *Phys. Rev. B*, 83, 054405-054411,2011.
- [37] Tang, D. D. and Lee, Y.J. *Magnetic Memory: Fundamentals and Technology*, Cambridge University Press, Cambridge, UK, 2010.
- [38] Garcia, F. et al. Exchange-biased spin valves with perpendicular magnetic anisotropy based on Co/Pt. Multilayers, *J. Appl. Phy.* 93, 8397-8399, 2003.
- [39] Beaurepaire, E., Bulou, H., Scheurer, F. And Kappler, J.P.(eds.) *Magnetism: A synchrotron radiation approach*, Springer –Verlag, Berlin, Heidelberg, NY, 2006.
- [40] Bertotti, G., *Hysteresis in Magnetism*, Academic Press, San Diego, 1998.
- [41] Ozatay, O. et. al., Magnetoresistance and magnetostriction effects in ballistic ferromagnetic nanoconstrictions, *J.App.Phy.* 95, 7315–7317, 2009.
- [42] Jungblut, R. et al. Orientational and structural dependence of magnetic anisotropy of Cu/Ni/Cu sandwiches: Misfit interface anisotropy, *J.App.Phy*, 75, 6424 – 6426, 2009.
-

- [43] Popplewell, J. Technological applications of ferrofluid, *Phys Technol* 15, 150-156, 1984.
- [44] Davidson, P.A. and Thess, A. (eds.) *Lecture Notes on Magnetohydrodynamics*, Springer Verlag, Heidelberg, NY, 2002.
- [45] Landau, L. D. and Lifschitz, E. M. *Lehrbuch der theoretischen Physik: Elektrodynamik der Kontinua*, Akademie, Verlag Berlin, 1985.
- [46] Papell, S. S., *Low viscosity magnetic fluid obtained by the colloidal suspension of magnetic particles*. US Pat. 3 215 572, 1964.
- [47] Rosensweig, R. E. *Ferrohydrodynamics*, Cambridge University Press, Cambridge, New York, 1985.
- [48] Odenbach, S. *Magnetoviscous effects in ferrofluid*, Springer, Tokyo, 2002.
- [49] Butt, H.J., Graf, K. and Kappl, M., *Physics and Chemistry of interfaces*, Willey-VCH, Weinheim, 2003.
- [50] Regmi, R. et al. Effects of fatty acid surfactants on the magnetic and magnetohydrodynamic properties of ferrofluids, *J. Appl. Phys.* 106, 113902- 113910, 2009.
- [51] Petrenko, V.I. et al. Effect of Surfactant Excess in Non-Polar Ferrofluids Probed by Small-Angle Neutron Scattering, *Solid. State. Phen.* 152-153, 198-201, 2009.
- [52] Zhao, Y.X. et al. Study of polydiethylsiloxane-based ferrofluid with excellent frost resistance property, *J Magn. Magn. Mater.* 321, 377-381, 2009.
- [53] Rahn, H., I. et al. Microcomputed tomography analysis of ferrofluids used for cancer treatment, *J. Phys.: Cond. Matter*, 20, 204152-204155, 2008.
- [54] Scherer, S. and Neto, A.M.F. Ferrofluids: properties and applications, *Braz. J.Phys.* 35, 718-727, 2005.

- [55] Qu, F. and Morais, P. C. An Oxide Semiconductor Nanoparticle in an Aqueous Medium: A Surface Charge Density Investigation, *J. Phys. Chem. B*, 104, 5232-5236, 2000.
- [56] Heinrich, D., Goñi, A. R. and Thomsen, C. Dynamics of magnetic-field-induced clustering in ionic ferrofluids from Raman scattering, *J. Chem Phys.* 126, 124701- 124707, 2007.
- [57] Morais, P. C et al. Preparation and characterization of ultra-stable biocompatible magnetic fluids using citrate-coated cobalt ferrite nanoparticles, *Thin Solid Films.* 515, 266 -270, 2006.
- [58] Müller, O., Hahn, D. and Liu, M. Non-Newtonian behaviour in ferrofluids and magnetization relaxation, *J. Phys.: Condens. Matter.* 18, S2623–S2632, 2006.
- [59] Wu, Z. et al, Enhancing the Magnetoviscosity of ferrofluids by the addition of biological nanotubes, *ACS Nano*, 4, 4531–4538, 2010.
- [60] Singh, J. and Bajaj, R. Convective instability in a ferrofluid layer with temperature-modulated rigid boundaries, *Fluid Dyn. Res.* 43, 025502-025526, 2011.
- [61] Shliomis, M.I.. Effective viscosity of magnetic suspensions. *Sov. Phys.- JETP.*34, 1291-1294, 1972.
- [62] Brown, W. F. Thermal fluctuation of single domain particle., *Phy. Rev.* 130,1677-1678, 1963.
- [63] Néel, L., Effects of thermal fluctuations on the magnetization of small particles. *C. R. Acad. Sci. Paris.* 228, 664-668, 1949.
- [64] Martsenyuk, M. A., Raikher, Yu. L. and Shliomis, M. I. On the kinetics of magnetization of suspensions of ferromagnetic particles. *Sov. Phys. JETP.*38, 413-416, 1974.
- [65] Hong R.Y. et al. Magnetic field synthesis of Fe₃O₄ nanoparticles used as a precursor of ferrofluids, *J. Magn. Magn Mater.* 310 ,37-47, 2007.
-

[66] Hong, R.Y. et al. Double-mini-emulsion preparation of Fe₃O₄/poly(methyl methacrylate) magnetic latex, *J. Appl. Poly. Sci.* 112, 89-98, 2009.

[67] Kinnari, P. et al. Magnetic and Rheological Characterization of Fe₃O₄ Ferrofluid: Particle Size Effects, *Hyperfine Interactions*. 160, 211-217, 2005.

[68] Maity, D. and Agrawal, D.C. Synthesis of iron oxide nanoparticles under oxidizing environment and their stabilization in aqueous and non-aqueous media, *J. Magn. Magn. Mater.* 308, 46-55, 2007.

[69] Hernández, E. S. et al. Synthesis of plasticizer-based ferrofluid and its use in the preparation of magnetic PVC nanocomposite, *Mat. Sci. For.* 644, 13-16, 2010.

[70] Ervithayasuporn, V. et al. Synthesis and characterization of core-shell type Fe₃O₄ nanoparticles in poly(organosilsesquioxane), *J. Coll. Inter. Sci.* 332, 389-393, 2009.

[71] Nakamae, S et al., Anisotropy-axis orientation effect on the magnetization of γ -Fe₂O₃ frozen ferrofluid, *J. Phys. D: Appl. Phys.* 43, 474001-474007, 2010.

[72] Hosseini, S. M. et al. Rheological properties of a γ -Fe₂O₃ paraffin-based ferrofluid, *J. Magn. Magn. Mater.* 322, 3792-3796, 2010.

[73] Papaefthymiou, G. C. et al, Gummic acid stabilized γ -Fe₂O₃ aqueous suspensions for biomedical applications, *Hyperfine Interactions*, 190, 59-66, 2009.

[74] Lu, J. et al. Solid-state synthesis of monocrystalline iron oxide nanoparticle based ferrofluid suitable for magnetic resonance imaging contrast application, *Nanotechnol.* 17, 5812-5820, 2006.

[75] Hong, R.Y. et al. Rheological properties of water-based Fe₃O₄ ferrofluids, *Chem. Eng. Sci.* 62, 5912-5924, 2007.

[76] Cui, S. et al. Interaction Mechanism between Fe₃O₄ nanoparticles and sodium 2-dodecylbenzenesulfonate, *Curr. Nanosci.* 7, 366-370, 2011.

[77] Arulmurugan, R. et al. Mn–Zn ferrite nanoparticles for ferrofluid preparation: Study on thermal–magnetic properties, *J. Magn. Magn. Mater.* 298, 83–94, 2006.

[78] Tackett, R. C. et al. Magnetic and optical response of tuning the magnetocrystalline anisotropy in Fe₃O₄ nanoparticle ferrofluids by Co doping, *J. Magn. Magn. Mater.* 320, 2755– 2759, 2008.

[79] Müller, R. et al. Nanocrystalline iron oxide and Ba ferrite particles in the superparamagnetism–ferromagnetism transition range with ferrofluid applications, *J. Phys.: Condens. Matter.* 18, S2527-S2542, 2006.

[80] Munnier, E. S. et al. *Novel method of doxorubicin – SPION reversible association for magnetic drug targeting*, *Int. J. Pharm.* 363, 170-176, 2008.

[81] Ju, D. Y. et al. Fabrication of magnetite nanoparticles and dDrug delivery observation of hydrophobe ferrofluid by spring-8 synchrotron radiation, *Mater. Sci. For.* 614, 229-232, 2009.

[82] Rahn, H. et al. SR μ CT and MRX analysis of ferrofluid accumulation in bovine arteries: a step further in the understanding of magnetic drug targeting, *Phys. Proc.* 9, 258–261, 2010.

[83] Cherry, E.M. et al. Particle size, magnetic field, and blood velocity effects on particle retention in magnetic drug targeting, *Med. Phys.* 37, 175-182, 2010.

[84] Jordan, A. et al. Presentation of a new magnetic field therapy system for the treatment of human solid tumors with magnetic fluid hyperthermia, *J. Magn. Magn. Mater.*, 225, 118-126, 2001.

[85] Zhang, Li-Y. et al. Magnetite ferrofluid with high specific absorption rate for application in hyperthermia, *J. Magn. Magn. Mater.* 311, 228-233, 2007.

[86] Kappiyoor, R. et al. The effects of magnetic nanoparticle properties on magnetic fluid hyperthermia, *J. Appl. Phys.* 108, 094702- 094709, 2010.

[87] Ravaud, R. et al. Magnetic pressure and shape of ferrofluid seals in cylindrical structures, *J. Appl. Phys.* 106, 034911-034919, 2009.

- [88] Ravaud, R. et al. Radial stiffness of a ferrofluid seal, *IEEE Trans.Magn.* 45, 4388-4390, 2009.
- [89] Legall, E. L. et al. Air-cooled ferrofluid seal in an x-ray tube and method of fabricating same, United States Patent 7903787,2011.
- [90] Candiani, A. et al. A spectrally tunable microstructured optical fibre Bragg grating utilizing an infiltrated ferrofluid, *Opt. Exp.* 18, 24654-24660, 2010.
- [91] Candiani, A. et al. A vectorial magnetometer utilising a microstructured optical fibre Bragg grating infiltrated by a ferrofluid, *The European Conference on Lasers and Electro-Optics*, 2011.
- [92]Lok, K. S. et al. Ferrofluid plug as valve and actuator for whole-cell PCR on chip, *Senso. Act. B: Chem.*, 20, 893–897, 2012.
- [93] Safarikova, M. et al. Ferrofluid modified *Saccharomyces cerevisiae* cells for biocatalysis, *Food Res. Inter.*42, 521–524, 2009.
- [94] Sharmah, S. and Mukhopadhyay, G. Shape dependent force between magnetic nanoparticles in a colloidal ferro-fluid, *J. Nanosci.Nanotech.*9, 5448-5450, 2009.
- [95] Ruder, W. C.et al. Biological colloid engineering: Self-assembly of dipolar ferromagnetic chains in a functionalized biogenic ferrofluid, *Appl. Phys. Lett.* 101, 063701-063705, 2012.
- [96] Büttner M. et al. Investigation of magnetic active core sizes and hydrodynamic diameters of a magnetically fractionated ferrofluid, *J. Nanopart Res.* 13,165–173, 2011.
- [97]Ram, P. et al. Effect of magnetic field-dependent viscosity on revolving ferrofluid, *J Magn.Magn. Mater.* 322, 3476–3480, 2010.
- [98] Ramos, J. et al. Steady shear magnetorheology of inverse ferrofluids, *J. Rheol.* 55, 127-252, 2011.

2.1. Ferrofluids based on different kinds of MNPs, surfactant and carrier fluids

Ferrofluid (FF) synthesis is a two step process. First, magnetic nanoparticles of desired dimension are to be synthesized and then, they need to be dispersed in an appropriate carrier fluid. Typically, stable suspensions of magnetic particles in carrier liquids like oil, water or kerosene are desired. To overcome the problem of agglomeration, the particles are coated with a surfactant, made of long-chained molecules chosen in such a way that their dielectric properties match those of the carrier liquid.

The typical thickness of a surfactant layer is about 2-3 nm. This facilitates hydrodynamic interaction with the suspended particles and consequently, on the flow of the carrier liquid. Surfactants used in different FF systems are organic compounds having hydrophobic groups (tails) and hydrophilic groups (heads). A surfactant can be categorized by the presence of formally charged groups in its head as *anionic*, *cationic*, *zwitterionic* and *non-ionic* surfactant. As the name suggests, the head group of an anionic surfactant is negatively charged and that of a cationic surfactant is positively charged whereas, a surfactant having both positive and negative heads is termed as *zwitterionic*. The head group of a non-ionic surfactant is chargeless.

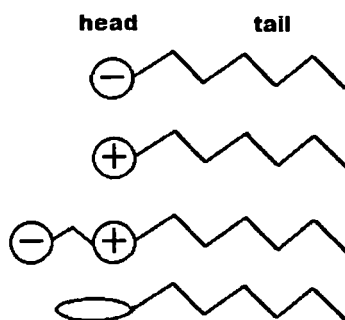


Fig. 2.1: Schematic diagram of (top to bottom): anionic, cationic, zwitterionic and non ionic surfactants

We have synthesized different types of FFs using various kinds of surfactant, carrier fluid and MNPs as described below.

2.1.1. Synthesis of magnetite (Fe_3O_4) based ferrofluids (with different carrier fluid)

(i) Materials

Magnetite

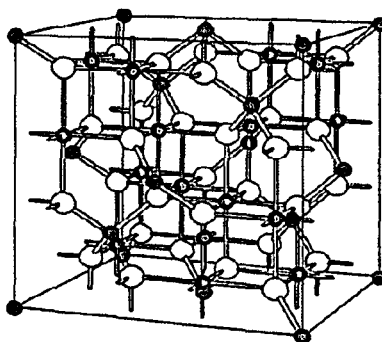


Fig. 2.2: Unit cell of magnetite with red, blue and white atom as Fe^{2+} , Fe^{3+} and O^{2-} respectively

Magnetite is very common among other oxides (eg. maghemite, hematite etc.) of iron. Magnetite crystallizes in inverse spinel structure above 120 K. The inverse spinel structure consists of a cubic close-packed arrangement. The unit cell of Fe_3O_4 contains 32 anions, among them Fe^{2+} ions occupy 1/4 of the octahedral sites, and the Fe^{3+} ions are divided equally between 1/8 of the tetrahedral sites and 1/4 of the octahedral sites. Electron spins of iron (III) ions in octahedral sites are aligned anti-parallel to those in tetrahedral holes; resulting no net magnetization from these ions. The iron (II) ions, however, tend to align their spins parallel with those of iron (III) ions in adjacent octahedral sites, leading to a net magnetization. The reported value of saturation

magnetization of bulk magnetite is ~ 475 kA/m which reduces with decrease of size.^[1,2]

Oleic acid

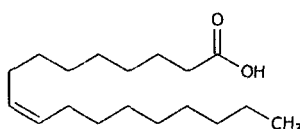


Fig. 2.3: Chemical structure of oleic acid

Oleic acid is a monosaturated omega-9 fatty acid. The molecular formula of oleic acid is $C_{18}H_{34}O_2$. It is an anionic surfactant. Its carboxylic group (-COOH), the head group of oleic acid is exposed to the droplets of surrounding solution forming a binding or a coating layer of surfactant. The physical and chemical properties of oleic acid are detailed in *appendix II*.

Kerosene

It is a combustible hydrocarbon fuel. It is widely used in jet-engined aircraft and some rockets as fuel power. It is obtained from the fractional distillation of petroleum at a temperature between $150^{\circ}C$ and $275^{\circ}C$ and has a density in the range of $0.78-0.81$ g/cm³. Typically, the carbon chains of kerosene are mixed-chains with carbon atoms varying between 6 and 16 per molecule.^[3]

Milli- Q water

It refers to ultra-pure, deionized water. Milli-Q water is free from ions, salts and minerals which are generally abundant in ordinary water. Milli-Q water has been purified and filtered by reverse osmosis process. The purity of such water is scaled in terms of resistivity. Resistance of

value $18 \text{ M}\Omega \text{ cm}^{-1}$ is generally desirable. Higher the resistivity, higher is its purity.

(ii) Magnetite (Fe_3O_4) nanoparticles

We have synthesized Fe_3O_4 nanoparticles by a co-precipitation method following ref [4] except considering extra accumulation of surfactants into account. At constant stirring ($\sim 200 \text{ rpm}$), FeCl_3 and FeCl_2 (in the molar ratio $\text{Fe}^{+2}/\text{Fe}^{+3}=0.5$) were transferred simultaneously to a conical flask containing 25 ml of 0.4 N HCl. Then, 200 μl of oleic acid ($\text{C}_{18}\text{H}_{34}\text{O}_2$, 99% pure, Otto) was mixed with 3 ml of AR-grade acetone and then transferred to the above precursor. The resulting solution was added drop-wise to 250 ml of 1.5N NaOH solution under vigorous stirring. To facilitate the reaction, 100 μl of oleic acid, was added in steps, in 10 min interval. This has resulted in a dark black colouration. In the precursor, the nanoparticle growth was allowed to proceed for 30 min at RT and under constant stirring. Finally, upon cooling down to RT and by performing repeated washing, centrifugation and decantation; we could obtain impurity free single layer surfactant coated magnetite nanopowders.

(iii) Magnetite-based ferrofluid with kerosene as carrier

In order to prepare a suitable FF, $\sim 7 \text{ g}$ of single layer oleic acid coated Fe_3O_4 nanoparticles were added to 40 ml of kerosene under vigorous stirring at 60°C , for 1h. This has resulted in a stable colloidal solution (ferrofluid). The prepared FF is labelled as FFK.

(iv) Magnetite-based ferrofluid with water as carrier

To make Fe_3O_4 based FF with water as a carrier, the magnetic nanoparticles (MNPs) were to be doubly coated by the surfactant. We have taken $\sim 2 \text{ g}$ of oleic acid coated MNPs and added to 40 ml of milli-Q water and then heated to 60°C under vigorous stirring, for 1h.

Simultaneously, a separate solution of oleic acid, milli-Q water and a few drops of NH_4OH was prepared and added to it which yields a stable solution of $\text{pH}=10.2$. The final concentration is $\sim 17.5\%$ (wt/vol). The as-received product was our required FF labelled as FFW.

2.1.2. Synthesis of magnetite- based FF with methanol as carrier (for varying surfactants)

(i) Materials

Two kinds of FFs with methanol as carrier fluid were synthesized. The Fe_3O_4 MNPs used were coated with different surfactants. Two surfactants were considered in the synthesis process, namely oleic acid and tetra methyl ammonium hydroxide.

Tetra methyl ammonium hydroxide

Tetra methylammonium hydroxide (TMAH or TMAOH) is a quaternary ammonium salt. Its molecular formula is $(\text{CH}_3)_4\text{NOH}$. Due to its cationic head group, it comes under cationic surfactants. It is widely used in integrated circuits, liquid crystal displays, printed circuit boards, capacitors, sensors, and many other electronic components as developer and cleaner agent. Its properties are given in *appendix II*.

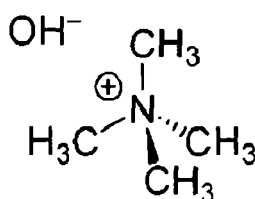


Fig. 2.4: Chemical structure of TMAH

Methanol (CH₃OH)

Now-a-days, methanol fuel is used in speedy bike and racing cars. This fuel has low danger level of firing in contrast to petroleum based fuel.

Along with this, methanol based ferrofluid product e.g. bearing, loud speaker cooling device in music system, etc. might extend their hand in this regard. The detail properties of methanol are given in *appendix II*.

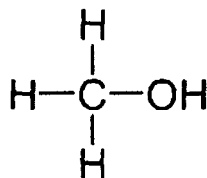


Fig. 2.5: Chemical structure of methanol

(ii) FF-synthesis procedure

For the synthesis of FFs, first Fe_3O_4 MNPs were synthesized by a co-precipitation method as mentioned earlier with some modification. First, FeCl_3 and FeCl_2 were taken in the molar ratio $\text{Fe}^{+2}/\text{Fe}^{+3}=0.5$ and then added simultaneously to the 25 ml of 0.4 N HCl solution with vigorous stirring (~300 rpm). The resulting solution was added drop wise to 250 ml of 1.5 N NaOH solution under magnetic stirring. The *pH* of the solution was maintained at 12. This has resulted in a dark black precipitate. Repeated washing, centrifugation and decantation of the resulting precipitate have provided us with an impurity free magnetite sample. Then 0.01 N HCl was added to the purified particles to stop further oxidation.^[4]

In order to prepare FFs, the MNPs sample was divided into two equal parts and each part was coated with surfactant layer as described in ref [5]. Anionic surfactant oleic acid [$\text{C}_{18}\text{H}_{34}\text{O}_2$, 99% pure, Otto] and a cationic surfactant tetra-methyl ammonium hydroxide [TMAH ($(\text{CH}_3)_4\text{NOH}$), CDH], were used for coating purposes. A few drops (approx. 400 μl) of each of the surfactants were added to each part of the specimen separately under vigorous stirring environment. The surfactant coated particles were finally added to AR-grade methanol resulting in FFs. The concentration of the final FFs was ~ 6.6 % (wt/vol).

The as-prepared FFs containing TMAH and oleic acid coated particles were labelled as FF1, FF2 respectively.

2.1.3. Synthesis of gadolinium oxide (Gd_2O_3) based ferrofluids

(i) Materials

Gadolinium oxide nanoparticles

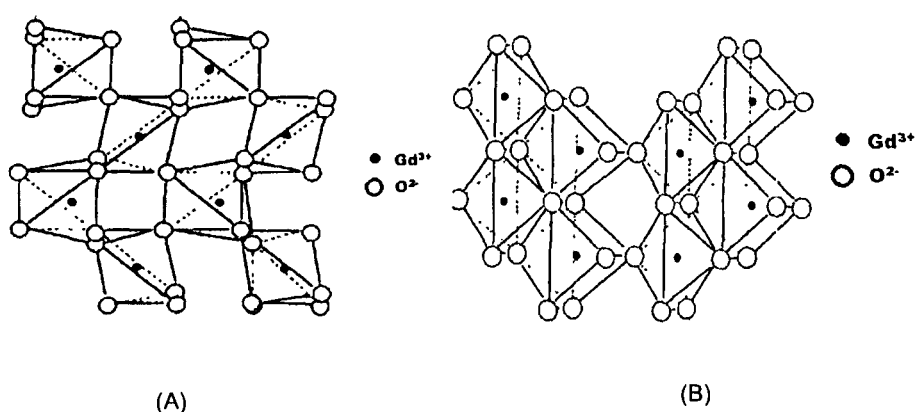


Fig. 2.6: Unit cell of (A) cubic and (B) hexagonal Gd_2O_3

The rare earth element gadolinium is mostly available in the form of gadolinium oxide (Gd_2O_3). It mainly exists in two different crystal structures namely, cubic and monoclinic. The gadolinium atoms in the cubic structure take two sites; both having 6 coordination number, but the geometry of the surrounding oxygen atoms are different in both the sites. Though at room temperature the stable state of Gd_2O_3 is cubic, at higher temperature ($\sim 1200^\circ C$) it exhibits in monoclinic phase.

Nanosized Gd_2O_3 is widely used as contrast agent in magnetic resonance imaging.^[6,7] Gd_2O_3 nanoparticle doped with other rare earth atoms is most promising systems that has immense application in solid-state lasers^[8] and display devices.^[9,10]

N-Cetyl-N,N,N-trimethylammonium bromide

N-Cetyl-N,N,N-trimethylammonium bromide or commonly known as (CTAB) is a widely used cationic surfactant. The molecular formula of CTAB is $C_{19}H_{42}BrN$. Its hexadecyltrimethylammonium of cation has very strong antibacterial effect.^[11] Due to the strong repulsion among its cationic heads (long range electrical force) and attraction among the tails (short range van-der Waals force), CTAB forms micelles in aqueous solution. At 303 K, it reaches critical micelle concentration (cmc) with around 75-120 molecules. From ion selective electrode measurements and conductometry data of Br^- and CTA^+ ions and taking micelle size as $r \sim 3$ nm, the standard constant of Br^- counterion binding to the micelle at 303 K is found as $K^{\circ} \approx 400$.

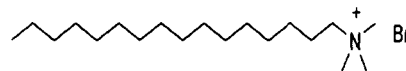


Fig. 2.7: Chemical structure of CTAB

Ethanol

The straight-chain alcohols with molecular formula C_2H_5OH is called ethanol. In ethanol, the carbon of a methyl group (CH_3-) is attached with the carbon atom of a methylene group ($-CH_2-$) and the oxygen of a hydroxyl group ($-OH$) is also attached to the same carbon atom of the ($-CH_2-$) group. The presence of the hydroxyl group and a short carbon chain are the leading factors in determining its physical properties. It is a versatile solvent. It is miscible with water and with many organic solvents, viz. acetic acid, acetone, benzene, carbon tetrachloride, chloroform, toluene etc. The hydrogen bonding of ethanol makes it hygroscopic. Due to the polar hydroxyl group and the nonpolar ends, ethanol dissolves in many ionic compounds and nonpolar substances respectively. Also, various properties are highlighted in *appendix II*.

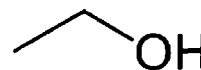


Fig. 2.8: Structure of ethanol

(ii) Synthesis of gadolinium oxide (Gd_2O_3) nanoparticles

The bulk Gd_2O_3 is a very stable RE oxide against high pressure, temperature and with environmental degeneration. It is very difficult to synthesize it in nanoscale form following top down approach. We have followed a low cost physico-chemical route reported by Chen *et al.*^[12] with some modification. In this method, bulk Gd_2O_3 is converted first into a nitrate compound followed by subsequent reductions to obtain hydroxide and oxide products. At first, 100 mmol of bulk Gd_2O_3 (99%, Otto) was added to 50 ml of double distilled water. Then, an appropriate amount of HNO_3 (69% GR, Merck) was mixed with this solution under vigorous stirring until a clear solution of $Gd(NO_3)_3$ is obtained. The solution was diluted to 100 ml in a volumetric conical flask by adding more distilled water and then 3.3 g of N-Cetyl-N,N,N-trimethylammonium bromide (CTAB) was subsequently added at $65^{\circ}C$, resulting in a yellow coloured precursor. After the yellowish solution was cooled down to the room temperature, 10 ml of freshly prepared 0.006 M aqueous NaOH was transferred. As a result, a white precipitate of $Gd(OH)_3$ is formed which is followed by continuous stirring for 30 min, and centrifugation. In order to obtain finest quality precipitate, the as-received product was subjected to repeated washing with hot distilled water and centrifugation. The precipitate was dried in air and then heated at $800^{\circ}C$ for 1h till an off-white powder of Gd_2O_3 is achieved.

(iii) Ferrofluid preparation

In a FF, surfactant coated particles are dispersed in a carrier fluid. CTAB is chemically inert in ethanol and this is one of the reason to choose ethanol as a carrier medium. CTAB-coated Gd_2O_3 nanoscale particles were first transferred to ethanol medium. Magnetic stirring was maintained overnight thus resulting in a uniform dispersion. This ferrofluid is labelled as FFG.

2.2. Characterization tools

A nano-dimensional material is beyond the optical resolution and hence, cannot be resolved by human eye and optical spectroscopy. The prepared nanoparticles as well as the ferrofluids were probed by various sophisticated techniques to extract adequate information with regard to their structural, compositional and optical properties. The tools can be employed for direct observation of the actual specimen or analysis of data obtained under a given environment.

2.2.1. X-Ray Diffraction (XRD)

(i) Magnetite nanoparticles

Firstly, the structural and morphological features of the synthesized magnetite particles were studied by an X-ray diffractometer (Rigaku Mini Flex 2000). Fig.2.9 shows the typical XRD pattern and Williamson-Hall (W-H) plot of the synthesized uncoated magnetite particles. The peaks at 35.35°, 56.4°, 63.35° and 66.1° are designated as characteristic peaks of magnetite with orientation along (311), (511), (531) and (442) planes, in consistency with the other works.^[13,14] Peaks at 31° and 75.2° arise because of impurity. The sizes of the particles as well as the amount of micro-strain are calculated by the W-H method, using the equation.^[15]

$$\beta_{hkl} \cos \theta_{hkl} = \frac{0.9\lambda}{d} + 4\eta \sin \theta_{hkl} \quad (2.1)$$

where, β_{hkl} is the full width at half maxima (FWHM) in radian, θ_{hkl} is the diffraction angle in degree, λ is the wavelength of the X-rays, d is the crystallite size and η measures the micro-strain. Considering the prominent diffraction peaks, the average crystallites size was calculated to be ~ 4.1 nm and with a strain value of -17×10^{-2} . A positive micro-strain indicates interparticle contraction while a negative value represents relaxation in the system.

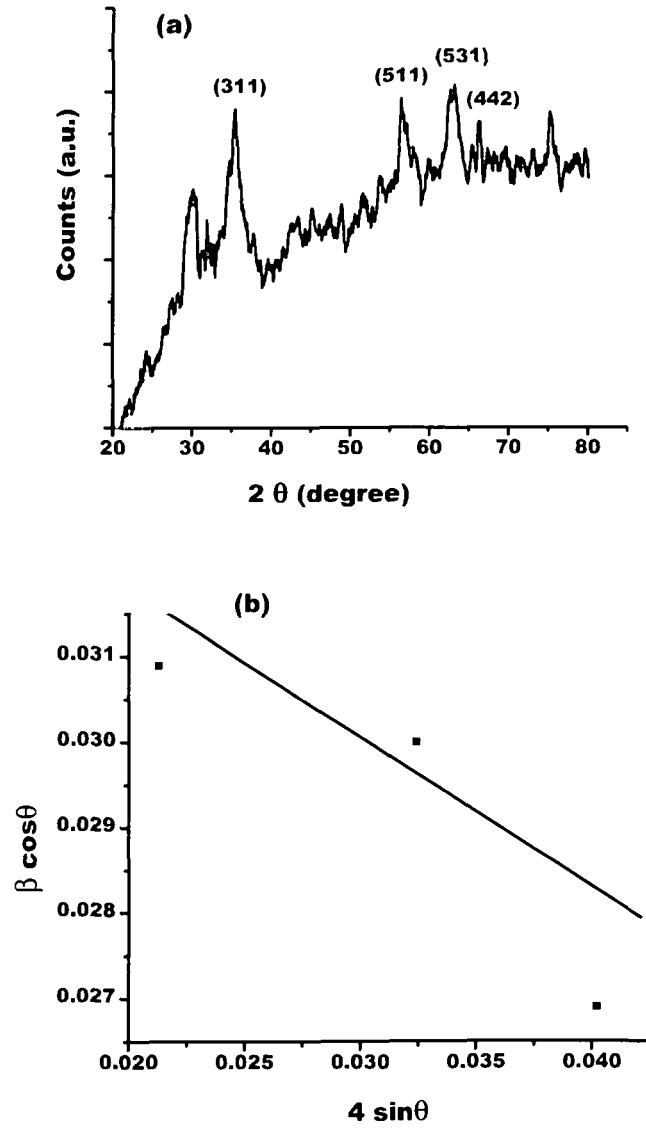


Fig. 2.9: (a) XRD pattern and (b) W-H plot of the synthesized Fe_3O_4 particle

(ii) Oleic acid coated magnetite (Fe_3O_4) nanoparticles

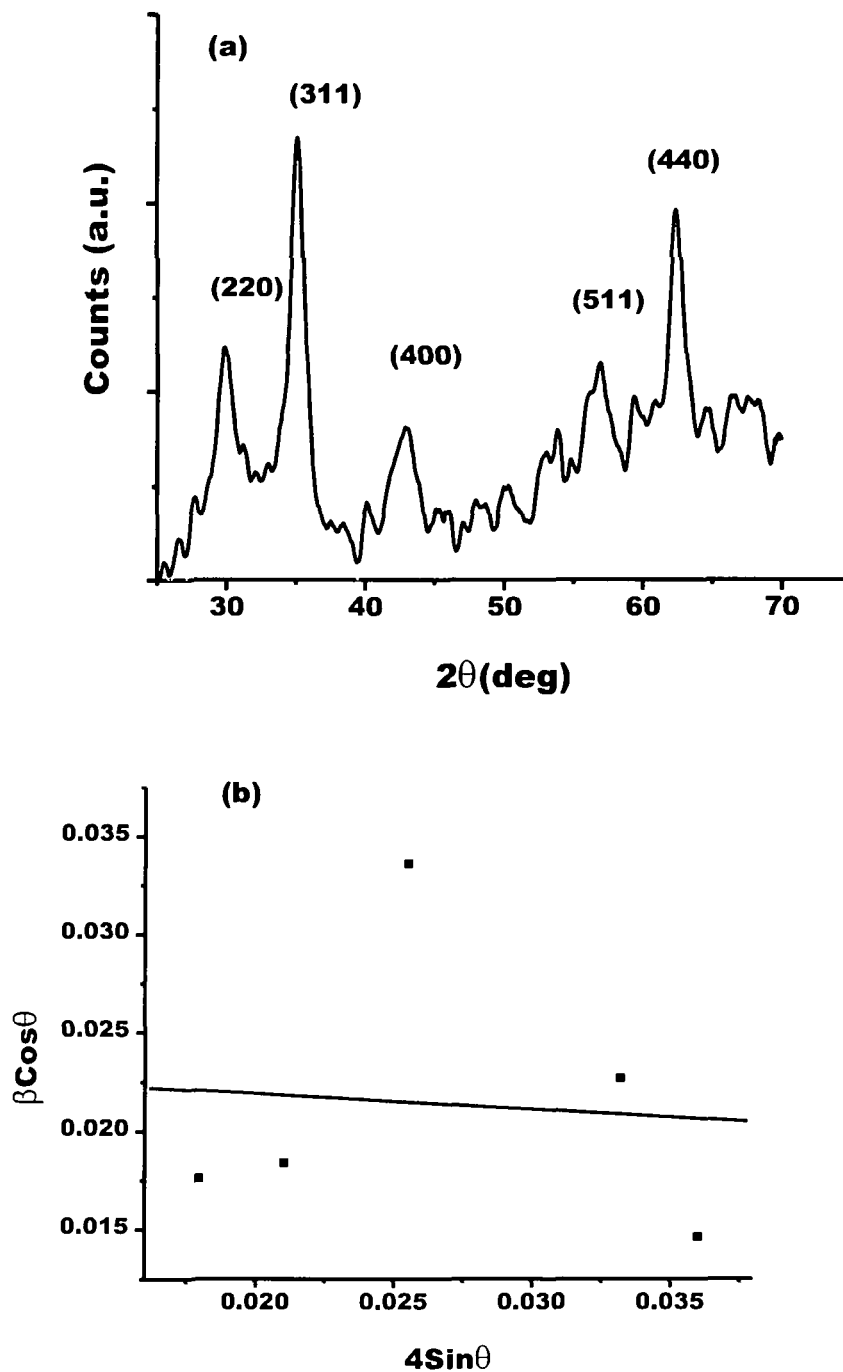


Fig.2.10: (a) XRD pattern and (b) W-H plot of oleic acid coated synthesized Fe_3O_4 nanoparticle

Fig. 2.10 (a) is a typical XRD pattern of the oleic acid coated MNPs synthesized for preparing ferrofluids FFW and FFW. The diffractogram is characterized by five distinct peaks located at 29.87° , 35.15° , 42.92° , 56.84° and 62.4° which correspond to (220), (311), (400), (511) and (440) planes of inverse spinel crystal structure of magnetite system.^[14,16] In order to estimate average crystallite size (d), we used the W-H equation. The W-H plot was drawn considering prominent XRD peaks and is shown in Fig. 2.11(b). The micro-strain was calculated from the slope, whereas crystallite size was determined from the intercept of the W-H plot. In our system, the micro strain and average crystallite size were estimated to be -7×10^{-2} , and ~ 8 nm; respectively. The negative strain indicates relaxed nature of the particles within the system.

(iii) Gadolinium oxide nanoparticles

The structural properties of the nanoscale Gd_2O_3 powder were also investigated by XRD analyses. The XRD pattern, shown in Fig. 2.11 (a), depicts six prominent peaks at respective Bragg angles (2θ) of 26.35° , 31.31° , 35.75° , 42.41° , 46.75° and 55.61° . These peaks of monoclinic (B-type) Gd_2O_3 phase corresponded to (2 0 2), (0 0 3), (2 0 3), ($\bar{3}$ 13) (2 0 4) and ($\bar{5}$ 14) planes, with preferred crystallographic orientation along (0 0 3) plane. This is also in consistency with the previous work.^[17] The average crystallite size (d) and effective micro-strain (η) can be gauged from the popular W-H method. From the W-H plot, the average crystallite size and micro-strain were estimated to be ~ 3.2 nm and -1.8×10^{-3} . Since a positive strain depicts compaction where each of the crystallites is believed to be under stress, a negative strain would represent inter-particle relaxation.

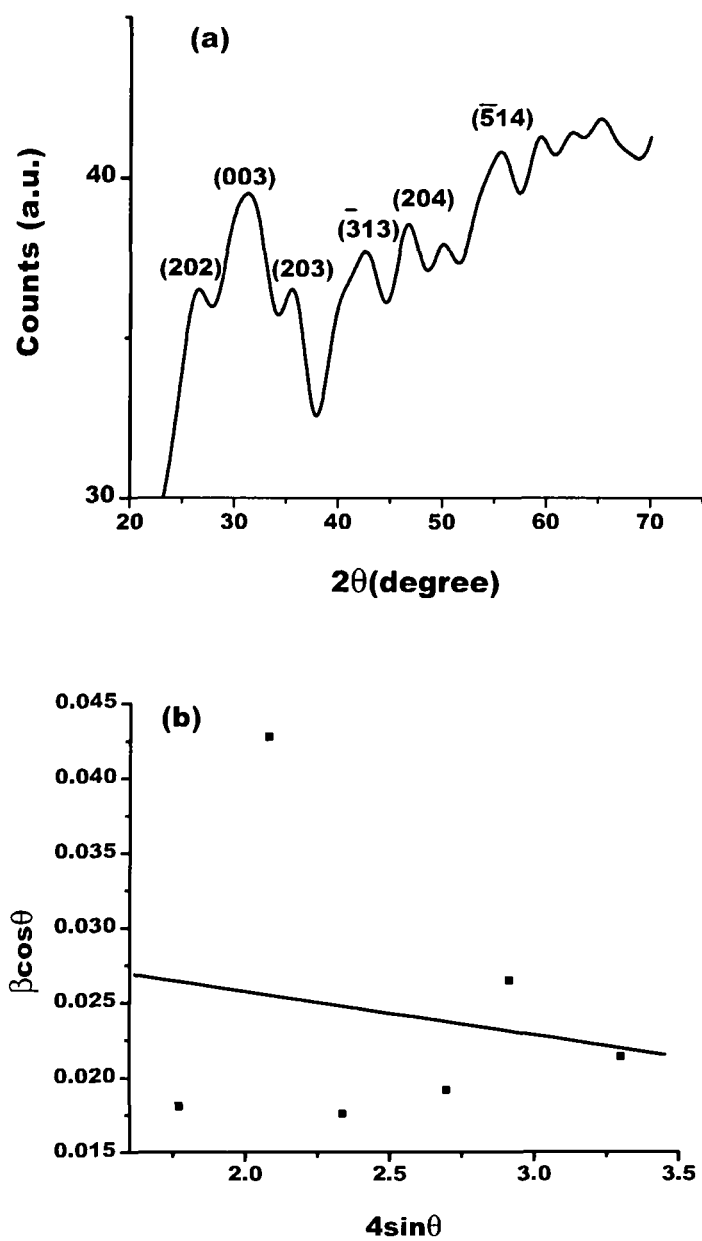


Fig. 2.11: (a) XRD pattern and (b) W-H plot of the synthesized Gd_2O_3 particle

2.2.2. Electron microscopy

Electron microscopy is regarded as the most essential tool for viewing structural and morphological features of nanostructured systems down to atomic scale resolution. It provides direct evidence of particle dimension in nanoscale regime. We have analysed our synthesized products by low as well as high resolution transmission electron microscopy (TEM).

(i) Uncoated magnetite particles, FF1 and FF2

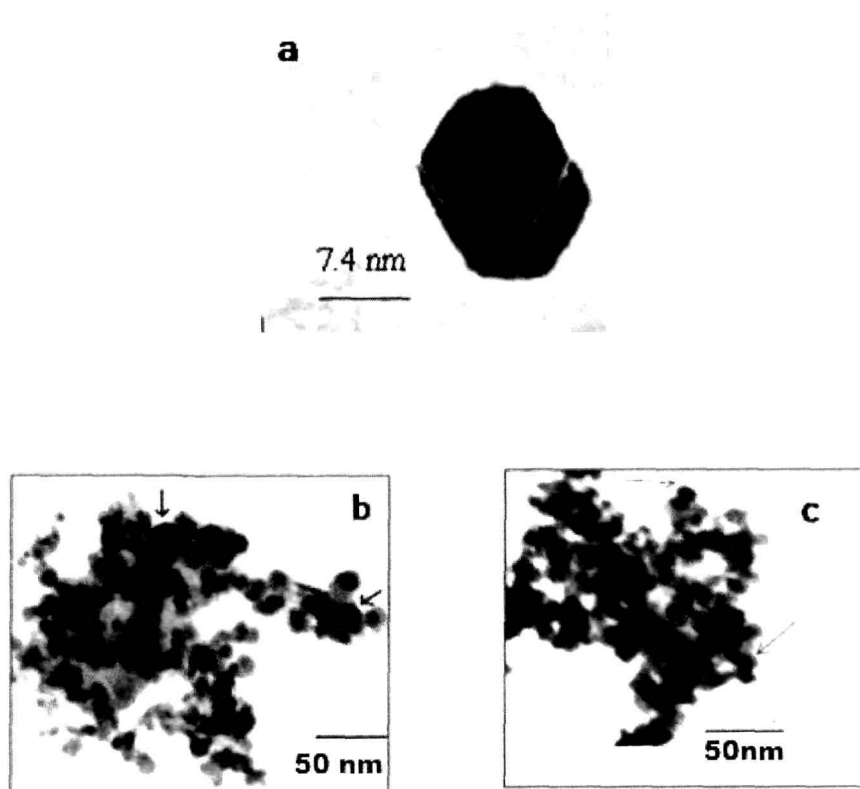


Fig. 2.12: TEM micrographs of (a) uncoated single domain magnetite nanoparticle and ferrofluids (b) FF1 and (c) FF2

Fig. 2.12 depicts the transmission electron microscopy (TEM) images (200KX magnification) of the uncoated and surfactant (TMAH, and oleic acid) coated dispersed magnetite nanoparticles (FF1 and FF2 respectively). The surfactant coated nanoparticles are seen as aggregates with a size distribution within $12\pm 2\%$. Also, it was noticed that the surfactant coated MNPs present within a given cluster have independent existence in isolation to each other. As evident from the micrographs, the samples contain substantial amount of spherical particles along with a few hexagonal particles ($\sim 5\%$, indicated by red arrow). An individual hexagonal nanoparticle (uncoated) with a major axis of 12 nm and a minor axis of 11.1 nm is shown in Fig. 2.12(a). The morphological structure of magnetite is octahedral and it could represent a hexagonal shape if viewed along [111] direction.^[18]

(ii) FFW (with oleic acid coated Fe_3O_4 particles)

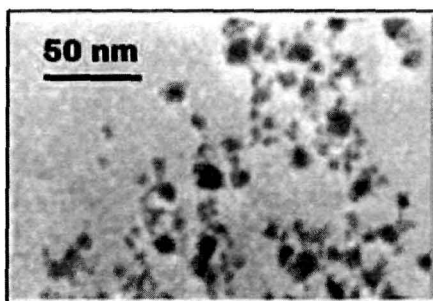


Fig. 2.13: TEM micrographs of FFW with oleic acid coated Fe_3O_4 MNPs

The TEM image of ultrasonically agitated magnetite particles of FF1 is shown in Fig.2.13. It is evident that the dispersed oleic acid coated Fe_3O_4 particles are isolated from each other. The particles are mostly spherical in shape with an average size distribution $\sim 8\pm 2\%$ nm. The presence of small cluster like structures are due to the higher

concentration of the MNPs which could not be separated out even after agitation. In this regard, dilution, vigorous ultra-sonication and high resolution of the microscope would provide a high quality image.

(iii) FFK (with oleic acid coated Fe_3O_4 particles)

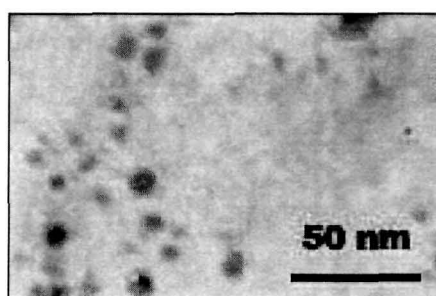


Fig. 2.14: TEM micrographs of FFK with oleic acid coated Fe_3O_4 MNPs

In order to study the morphological features of the dispersed particles, FFK was first ultrasonicated and then a few micro-drops were gently placed on a copper grid. The TEM micrograph (Fig.2.14) reveals that the particles exist in isolation from each other with minimum clustering. The particles are nearly spherical in shape. The sizes of the particles are not strictly uniform; rather it shows a distribution of $8 \pm 2\%$ nm.

(iv) FFG (with CTAB coated Gd_2O_3 particles)

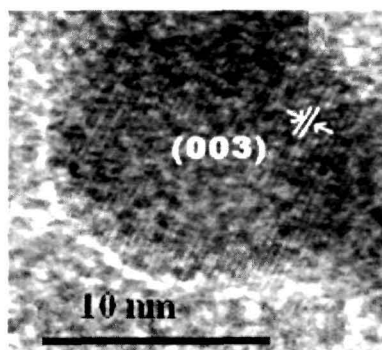


Fig. 2.15: HRTEM micrograph of a FFG particle with clear lattice planes

The structural and morphological aspects of the synthesized nanoscale Gd_2O_3 (dispersed in FFG) were investigated by HRTEM and are presented in Fig 2.15. The average size of the nanoparticles, as revealed from the micrograph is ~ 9 nm. The particles are found to be spherical along with a high degree of crystallinity and perfect lattice ordering. It reveals nearly spherical particles with distinct lattice planes and an interplanar spacing of ~ 0.28 nm. The predicted value of the interplanar spacing corresponds to the separation of (003) planes of the monoclinic Gd_2O_3 structure, ascertained from the prominent peaks of the XRD pattern [shown in fig. 2.11. (a)].

2.2.3. Dynamic light scattering (DLS)

Dynamic light scattering or, Photon Correlation Spectroscopy (PCS) or Quasi-Elastic Light Scattering (QELS), is a non-invasive, well-established technique for measuring the size distribution profile of small molecules and particles in solution or suspension. The latest technology based on DLS presents size distribution up to a few nano meter scale. In general, the DLS data gives the hydrodynamic radius of the particles, which is to some extent bigger than the actual radius measured by other direct methods like TEM.

(i) Uncoated magnetite particles

The DLS study of the uncoated Fe_3O_4 particles, prepared for the methanol based ferrofluids, is shown in fig 2.16. It gives an evidence of narrow size distribution of the particles. The Gaussian fit of the data reveals that the average size of the particles is ~ 14 nm. The observed asymmetry in the Gaussian fit was observed due to the variation of size of the particles. The asymmetry inclined towards left indicate that the concentration of smaller particles is higher than that of the bigger ones.

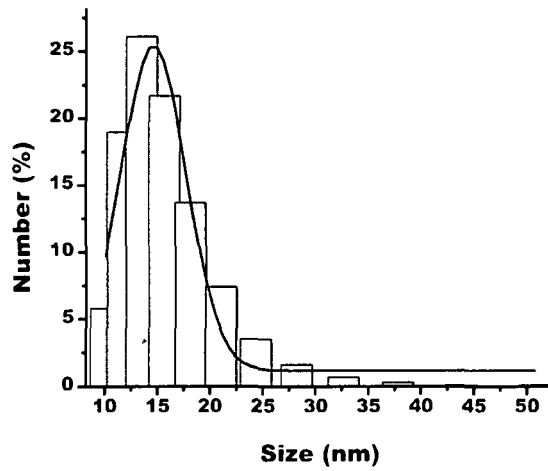


Fig. 2.16 DLS study of uncoated Fe₃O₄ nanoparticles

(ii) FFW specimen

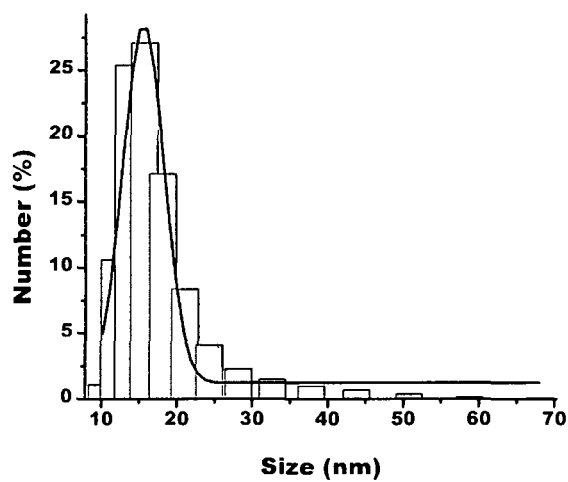


Fig. 2.17: DLS study of FFW

In order to know the actual size distribution of the dispersed particles (with hydrodynamic interaction) we have also performed DLS measurement on Fe_3O_4 based ferrofluid with water as carrier. Fig. 2.17 is the size distribution of the FF which predicts that most of the particles are having an average size of ~ 15 nm. The asymmetric nature towards left (upon Gaussian fit) reveals that the presence of smaller particles is predominantly high as compared to the case for bigger ones.

(iii) FFK specimen

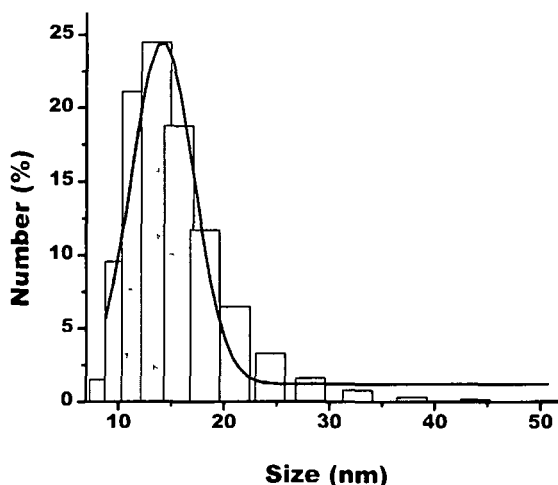


Fig. 2.18: DLS study of FFK

Fig. 2.18 exhibits particles size distribution of the ferrofluid FFK. It is evident from the figure that the most of the particles are in the size range of 10 - 20 nm. The asymmetric Gaussian distribution of the figure gives an average distribution of size ~ 14 nm.

(iv) FFG specimen

The DLS response of FFG specimen is depicted in Fig. 2.19. The Gaussian fit illustrates that the particles have a narrow size distribution in the range of 5 -10 nm with maxima at ~ 6.6 nm. It also reveals that the

Gaussian fit takes a symmetric pattern. In DLS study, symmetric nature of the curve is related with the number density of the particles. Thus, it is speculated that the percentage of smaller and bigger particles is nearly same in this particular ferrofluid.

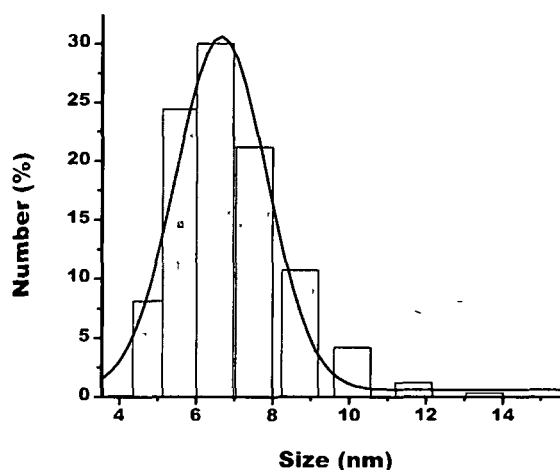


Fig. 2.19: DLS study of FFG

2.2.4. Fourier Transform Infra- Red spectroscopy

Fourier Transform Infra- Red (FT- IR) spectroscopy is an important analytical tool to analyse any varying signal of absorption, reflection, transmission, or photoacoustic spectrum into its constituent frequency components. It is a healthier access to trace the change in the vibrational features due to the presence of certain constituents in a given material system. Stretching, bonding and bending are the main vibrational modes of any component. Infra red radiations are absorbed by the molecule and the corresponding energy finally give rise to these modes.^[19] The characteristic bending, bonding or stretching modes of the IR active material corresponds to definite peaks in a FT-IR spectrum.

(i) Uncoated Fe_3O_4 , and FF1 and FF2 specimens

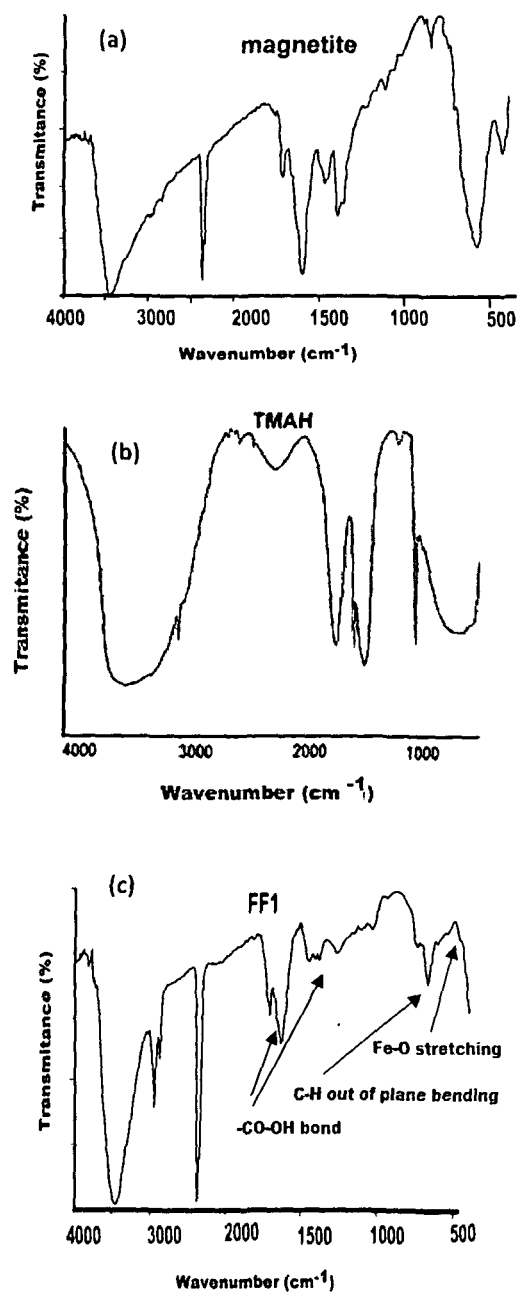


Fig. 2.20: FT-IR spectra of (a) synthesized Fe_3O_4 nanoparticle, (b) TMAH and (c) FF1

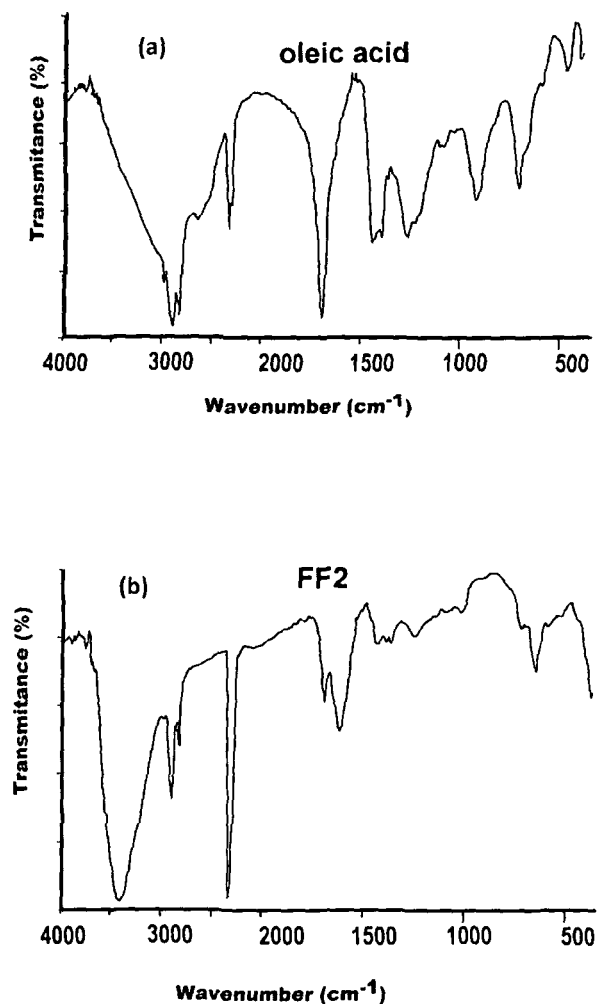


Fig. 2.21: FT-IR spectra of (a)oleic acid and (b) FF2

Fig. 2.20 and 2.21 show FT-IR spectra of the uncoated, surfactant (TMAH and Oleic acid) and surfactant-coated magnetite particles dispersed in methanol (ferrofluids: FF1 and FF2). The conventional peaks observable at $\sim 2900 - 3500 \text{ cm}^{-1}$ and 2400 cm^{-1} are the characteristics of O-H stretching of water molecules and atmospheric CO_2 , respectively.^[20,21] FT-IR characteristics of the FF1 spectrum corresponds to various

stretching and bending bands of the molecular constituents in TMAH [(CH₃)₄NOH], magnetite (Fe₃O₄) and methanol (CH₃OH). While the wavenumber range 949 -1117 cm⁻¹ depicts C-N stretching of TMAH, 464-668 cm⁻¹ correspond to Fe-O or/and Fe-OH stretching bands.^[20] A close look on the spectra of FF1, TMAH and Fe₃O₄ tells us that FF1 has a superimposed feature of TMAH and Fe₃O₄. This gives an evidence of TMAH bound to the surface MNPs at Fe-binding sites. Similarly, comparison of the FT-IR spectra of magnetite, oleic acid coatings and ferrofluid (FF2) can be made and evidence of surfactant coating could be ascertained. In case of FF2, the bands 1203.4 -1263.4 cm⁻¹, and 1719.6-1739.2 cm⁻¹ appear owing to vibrational modes related to strong -CO-OH bonding.^[19,20] The medium -CO-OH bondings are ascribed to the range 1381.1 -1449.6 cm⁻¹ and 1027.9 -1155.5 cm⁻¹ whereas, Fe - O stretching corresponds to 408.2- 669.8 cm⁻¹. Among these, the functional groups -CO-OH, C-H are possessed by oleic acid while Fe-O comes from magnetite.^[20,21]

(ii) FFW specimen

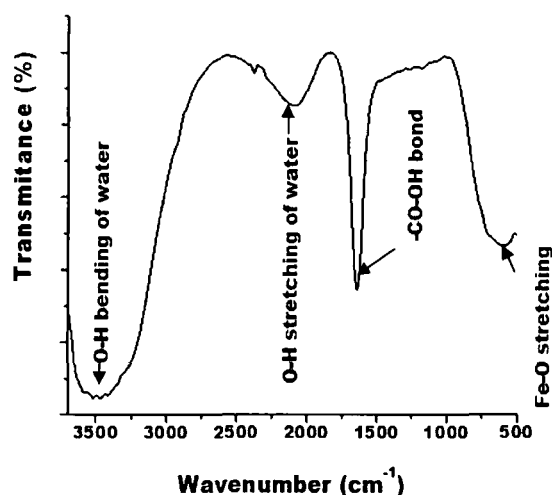


Fig. 2.22: FT-IR spectra of FFW

The room temperature FT-IR spectra of the oleic acid coated Fe_3O_4 based ferrofluid with water as carrier is shown in Fig.2.22. Apart from a peak observable at $\sim 2077 \text{ cm}^{-1}$ and identified as C-O stretching mode of the atmospheric CO_2 molecule,^[20] all other peaks corresponded to the chemical constituents available in the ferrofluid under study. The broad band at $\sim 3488.07 \text{ cm}^{-1}$ and the small peak at $\sim 2403 \text{ cm}^{-1}$ represent the characteristic O-H bending and stretching vibrational mode of the hydroxyl group of water molecule.^[20,21] The sharp peak at $\sim 1670 \text{ cm}^{-1}$ and a weak peak at $\sim 1161 \text{ cm}^{-1}$ give the respective signatures of strong and medium -CO-OH bonding of oleic acid.^[21] The typical Fe-O stretching vibrations of Fe_3O_4 are prominent in the lower wavenumber region, in the range $620\text{-}566 \text{ cm}^{-1}$ and $510\text{-}445 \text{ cm}^{-1}$.^[21]

(iii) FFK specimen

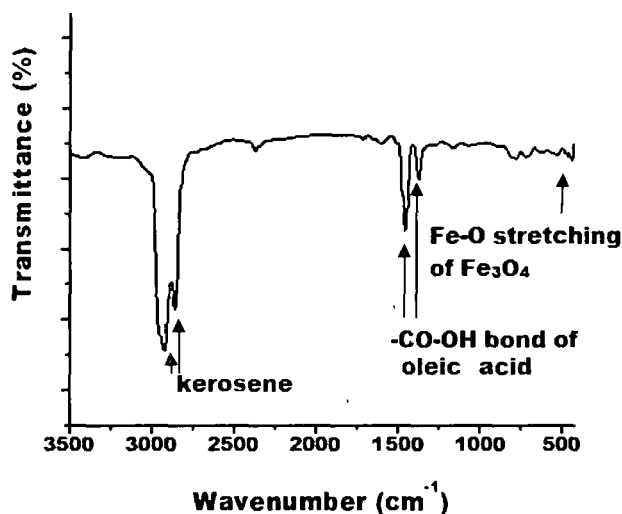


Fig. 2.23: FT-IR spectra of FFK

Fig. 2.23 is the replica of the FT-IR spectrum of oleic acid coated Fe_3O_4 based ferrofluid with kerosene as carrier fluid. Prominent characteristic peaks of the constituents are observed in the spectrum.

The sharp peaks at 2929 cm^{-1} and 2856 cm^{-1} strongly attest the presence of the carrier fluid kerosene, as the symmetric and asymmetric stretching of kerosene has witnessed the signals at these positions.^[22] The occurrence of oleic acid, which is used as surfactant, is characterized by peaks at 1453.42 cm^{-1} and 1381.9 cm^{-1} . These two peaks are assigned to medium strength -CO-OH bonding of oleic acid.^[20,21] The peaks at $440.725 - 481.155\text{ cm}^{-1}$ and 528.957 cm^{-1} were attributed to Fe-O or/and Fe-OH stretching modes of Fe_3O_4 .^[20,21]

(iv) FFG specimen

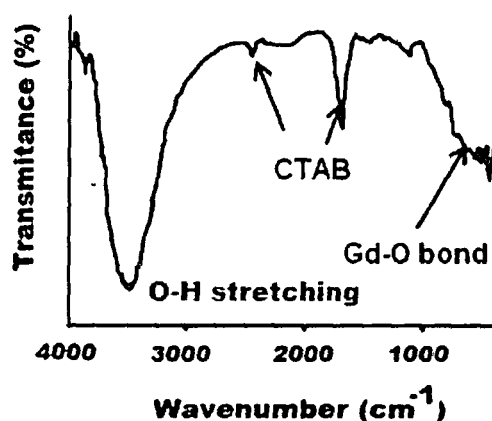


Fig. 2.24: FT-IR spectra of FFG

Fig.2.24 depicts the FT-IR spectra of the Gd_2O_3 (CTAB coated) based ferrofluid. The conventional peaks appearing at $\sim 3403\text{ cm}^{-1}$ and 2400 cm^{-1} representing the respective signatures of O-H stretching and C-O stretching of atmospheric water and CO_2 molecules.^[22,23] In case of ethanol, bending modes of CH_3 and CH_2 occur at $\sim 1392\text{ cm}^{-1}$ and 1452 cm^{-1} respectively; whereas OH, CH_2 , CH_3 and CO stretching vibrations are observable at $\sim 3679\text{ cm}^{-1}$, 2910 cm^{-1} , 2975 cm^{-1} and 1060 cm^{-1} .^[22] The weak band at 2980 cm^{-1} and the sharp band at 1550 cm^{-1} indicate the

presence of CTAB in the samples.^[24] The peaks at 536.8 cm^{-1} and 413.3 cm^{-1} are the outcome of Gd-O in- plane bonding .^[25,26]

2.2.5. Raman spectroscopy

Raman spectroscopy is based on inelastic scattering of monochromatic light, broadly used for extracting qualitative and quantitative information with respect to electron-phonon interaction. This spectroscopic technique provides a fingerprint of the specimen in terms of molecular components/functional groups. The applicability to any form of matter (solid, liquid or gaseous state) is another advantage of this technique.

The room temperature micro-Raman experiment of our samples were carried out by using $\lambda = 514.5\text{ nm}$ line of 50 mW Ar-ion laser.

(i)Oleic acid coated magnetite particles

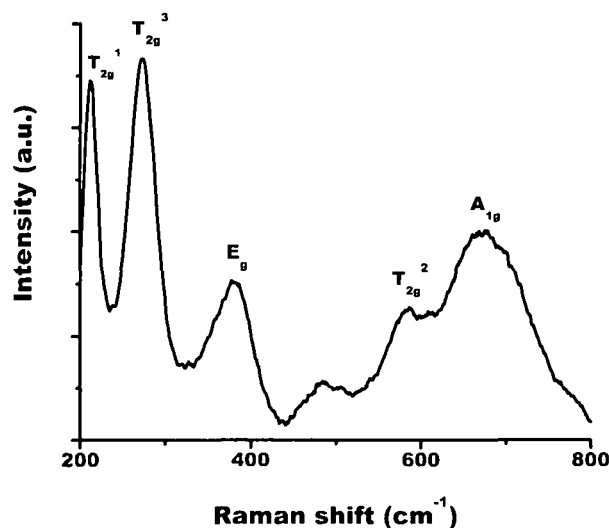


Fig. 2.25: Raman spectrum of Fe₃O₄ nanoparticles

Raman spectroscopy is a widely used, nondestructive tool to identify various iron oxides. The difficulty to distinguish magnetite (Fe_3O_4) and meghemite ($\gamma\text{-Fe}_2\text{O}_3$) can be unravelled by Raman spectroscopy. According to the space group theory, the irreducible representation at the zone centre of Fe_3O_4 above Verwey temperature predicts sixteen mode: $[A_{1g}(\text{R}) + E_g(\text{R}) + T_{1g} + 3T_{2g}(\text{R}) + 2A_{2u} + E_u + 5T_{1u}(\text{IR}) + 2T_{2u}]$.^[27] Here, R denotes Raman active and IR denote IR active modes. Fe_3O_4 exhibits total five Raman active modes at room temperature namely, A_{1g} , E_g and three T_{2g} modes while $\gamma\text{-Fe}_2\text{O}_3$ shows only three modes. Fig. 2.25 is the room temperature micro-Raman spectrum of the synthesized Fe_3O_4 nanoparticles. Here five peaks located at 211.420 cm^{-1} , 270.194 cm^{-1} , 380.222 cm^{-1} , 581.008 cm^{-1} and 659.610 cm^{-1} are recognized as T_{2g}^1 , T_{2g}^3 , E_g , T_{2g}^2 and A_{1g} Raman peaks of Fe_3O_4 .^[26,27] Table 2.1 depicts the assigned Raman modes of the sample. Note that, the slight shift in the frequency position of these peaks with respect to the reported value is attributed to the nanoscale dimension of the objects under study and adequate micro-strain in the sample.

Table 2.1: Representative data of the observed Raman peaks and assigned modes of Fe_3O_4 nanoparticles

Observed peak position (cm^{-1})	Mode assigned
211	T_{2g}^1
270	T_{2g}^3
378	E_g
581	T_{2g}^2
650	A_{1g}

(ii) CTAB coated gadolinium oxide nanoparticles

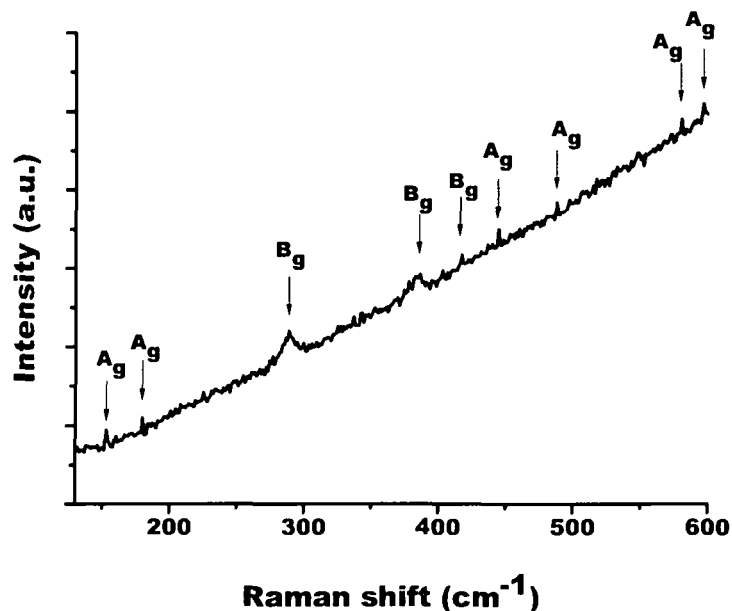


Fig. 2.26: Raman spectrum of CTAB coated Gd_2O_3 nanoparticles

The observed Raman spectrum of the nanoscale CTAB coated Gd_2O_3 is depicted in Fig. 2.26. The synthesized specimen is characterized by poorly resolved phonon modes (Table 2.1). It was known that the factor group analysis for B-type Gd_2O_3 predicts 21(14 A_g + 7 B_g) Raman active modes which signify the in-plane atomic vibration as A_g stretching mode, and out of plane vibration as B_g stretching mode with reference to (0 1 0) plane.^[29] In consistency with other reports, we have identified nine Raman bands with regard to the synthesized Gd_2O_3 sample.^[29,30] Earlier it was suggested that a competitive mechanism between the higher frequency shift due to the particle size reduction and lower frequency shift due to strain could influence the Raman spectrum appreciably.^[30] It is likely that smaller particles would experience larger strain compared to bigger ones and a typical Raman shift is characterized by the overall effect.

Table 2.2: Representative data of the observed Raman peaks and assigned modes

Observed peak position (cm ⁻¹)	Mode assigned	Reported peak position (cm ⁻¹)
153	A _g	156
180	A _g	175
289	B _g	298
385	B _g	385
417	B _g	417
445	A _g	445
486	A _g	484
579	A _g	583
596	A _g	593

2.2.6. Electron Paramagnetic Resonance spectroscopy

Electron Paramagnetic Resonance (EPR), also referred as Electron Paramagnetic Spin Resonance (ESR) is an extensively used spectroscopic practice to study paramagnetic centres of various oxide systems. Basically, these paramagnetic centres are surface defects, inorganic or organic radicals, metal cations or supported metal complexes and clusters. Different paramagnetic centres exhibit their own characteristic EPR responses.

The as synthesized nanoparticles were also analyzed by EPR spectroscopy - taken at a frequency 9.15 GHz (X band) and at a field modulation of 100 kHz. Under this experimental condition, the amplitude of the detected signal is very high.^[31] Typically, the EPR signal is presented as first derivative spectrum to locate the position corresponding to peak-maxima.

(i) Magnetite nanoparticles

The room temperature EPR spectrum of the prepared Fe_3O_4 nanoparticles is shown in Fig. 2.27. The symmetric nature of the spectrum [Fig.2.27 (a)] ensures high purity of the sample with no/minimal trace amount of other elements in the sample. The resonance field is recorded at 306.66 mT and the corresponding g (free electron g -factor) value is found to be 2.1028. It was reported that Fe_3O_4 nanoparticles with effective g value ~ 2 corresponds a phase closer to super-paramagnetic behaviour. As it moves towards ferromagnetic behaviour, the corresponding g value also increases. [32]

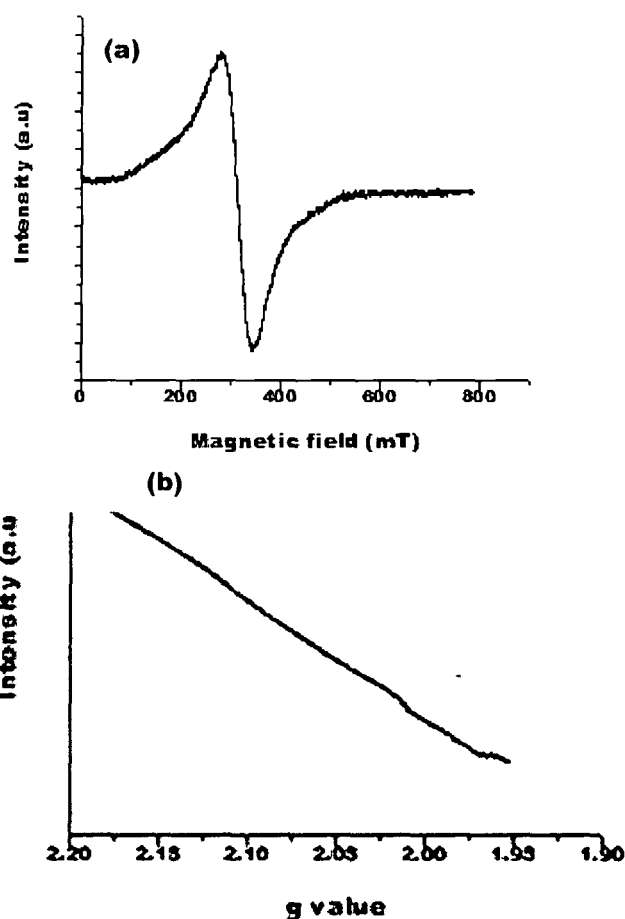


Fig. 2.27: EPR response of Fe_3O_4 system with variation of (a) magnetic field and (b) g -value

(ii) Gd_2O_3 based ferrofluid

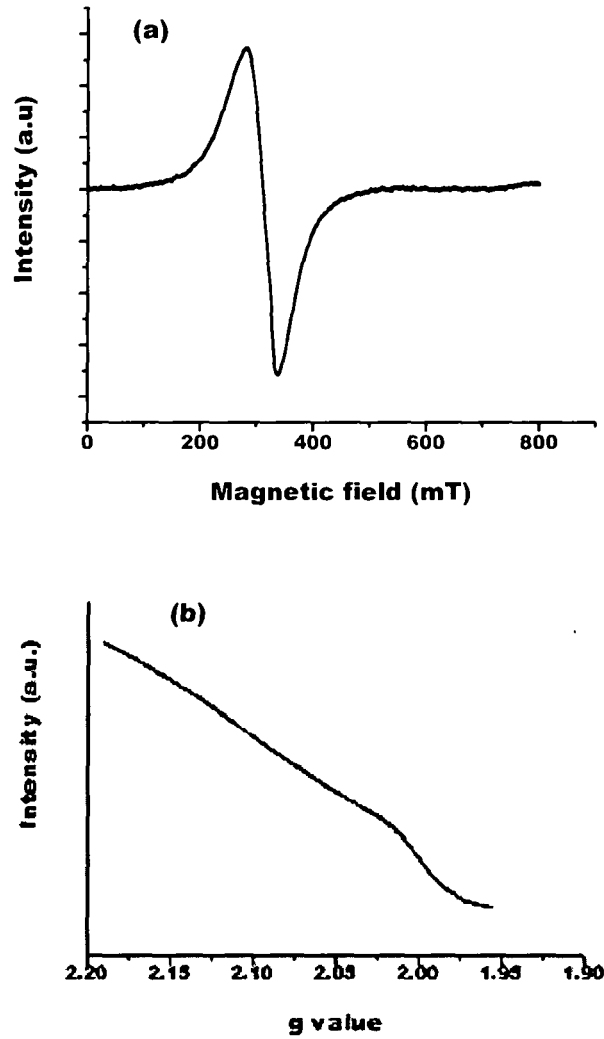


Fig. 2.28: EPR response of Gd_2O_3 system with variation of (a) magnetic field and (b) g value

Fig. 2.28 depicts room temperature EPR spectra of synthesized Gd_2O_3 nanopowder. The variation of signal intensity with magnetic field and g value are shown in Fig. 2.30(a) and (b), respectively. As can be seen from the figure the spectrum is symmetric in nature and have

resonance field centred at 310.3 mT and associated with g (free electron g -factor) values of 2.10802. In EPR study, the shape of the spectrum is a measure of the interaction of an unpaired electron with its surrounding environment. The symmetric nature of the EPR spectrum signifies high purity of the sample.

2.2.7. Photoluminescence spectroscopy

Photoluminescence (PL) spectroscopy is a versatile technique through which in-depth details related to radiative emission response can be explored. It is a contactless, nondestructive method based on either direct interband electronic relaxation events or carrier re-excitation via intermediate defect states.

(i) FFG specimen

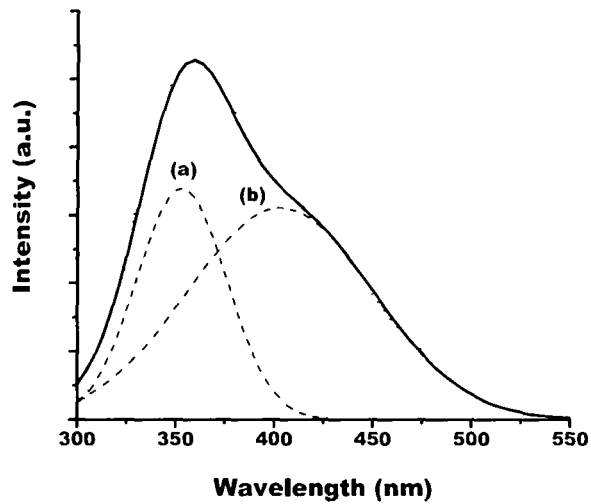


Fig. 2.29: PL spectrum of FFG specimen under excitation wavelength $\lambda_{ex}=270$ nm

The room temperature PL spectrum of Gd_2O_3 based ferrofluid is shown in Fig. 2.29. The ferrofluid has recorded an asymmetrically broadened spectrum peaking at ~ 355 nm. Earlier reports have suggested that this peak can be attributed to ${}^6P_{7/2} \leftrightarrow {}^8S_{7/2}$ transitions of $Gd(III)$.^[33] In PL spectrum, left symmetry factor (S_L) is associated with band to band transition. Here S_L is defined as $(\lambda_L - \lambda_M)/\Delta\lambda$; with λ_M representing peak-wavelength corresponding to the main peak, λ_L is the wavelength in the left hand side of the full width at half maxima (FWHM) and $\Delta\lambda = \lambda_R - \lambda_L$, λ_R being the half width wavelength on the right hand side of the FWHM. In this spectrum, the left symmetry factor is measured as 0.38. It is much expected that the nanocrystallites of Gd_2O_3 possess numerous surface defects. We speculate that the association of the defect related emission in the higher wavelength regime could have led to the remarkable asymmetry in the PL response. Upon deconvolution, the defect related emission was found to be located at ~ 415 nm, as can be observed in Fig. 2.32 (b). The overall PL spectrum is dominated by the band to band transition. The defect related transition is very weak.

2.3. Concluding remarks

A variety of ferrofluids were prepared considering two types of magnetic systems: Fe_3O_4 and Gd_2O_3 . Nanosize Fe_3O_4 was prepared by co-precipitation method. It was found that the pH and the ratio $Fe^{2+}: Fe^{3+} = 1:2$ of the precursors play important role for obtaining Fe_3O_4 phase. On the other hand, rare earth oxide system (Gd_2O_3), being highly stable, nanoparticles could not be synthesized following top down approach. Nanoscale particles of Gd_2O_3 were prepared by a select physico-chemical method. In order to achieve stable ferrofluids, the MNPs were coated with both cationic and anionic surfactants and then dispersed in carrier fluids. Different microscopic and spectroscopic characterization methods ensure the production of quality Fe_3O_4 and Gd_2O_3 based ferrofluids that are suitable for further experimentation.

References:

- [1] Vereda, F. et al. Synthesis and characterization of single-domain monocrystalline magnetite particles by oxidative aging of $\text{Fe}(\text{OH})_2$, *J. Phys. Chem. C* 112, 5843-5849, 2008.
- [2] Daou, T. J. Hydrothermal synthesis of monodisperse magnetite nanoparticles, *Chem. Mater.* 18, 4399-4404, 2006.
- [3] Weissendacher, M. *Sources of power: How energy forges human history*, Greenwood Publishing, US, 2009.
- [4] Kang, Y. S. Synthesis and characterization of nanometer-size Fe_3O_4 and $\gamma\text{-Fe}_2\text{O}_3$ particles, *Chem. Mater.* 8, 2209—2211, 1996.
- [5] Kim, D.K. et al. Synthesis and characterization of surfactant – coated superparamagnetic monodispersed iron oxide nanoparticles, *J. Magn. Mater.* 225, 30-36, 2001.
- [6] Ahrén, M. et al. Synthesis and characterization of PEGylated Gd_2O_3 Nanoparticles for MRI contrast enhancement, *Langmuir*, 26, 5753–5762, 2010.
- [7] Petoral, R. M. et al. Synthesis and characterization of Tb^{3+} doped Gd_2O_3 nanocrystals: A bifunctional material with combined fluorescent labeling and MRI contrast agent properties, *J. Phys. Chem. C.* 113, 6913–6920, 2009.
- [8] Wellenius, P. Effect of oxygen pressure on the structure and luminescence of Eu-doped Gd_2O_3 thin films, *phys. Stat. Sol. A.* 207, 1949–1953, 2010.
- [9] Răcuciu, M. Microstructural investigation of some biocompatible ferrofluids, *J. Magn. Mater.* 316, e772-e775, 2007.
- [10] Seo, S. et al. Controlled shape growth of Eu- or Tb-doped luminescent Gd_2O_3 colloidal nanocrystals, *J. Colloid Interface Sci.* 331, 236-242, 2009.

- [11] Bai, Y. et al. Aqueous dispersion of surfactant-modified multiwalled carbon nanotubes and their application as an antibacterial agent, *Carbon*. 49, 3663–3671, 2011.
- [12] Chen, H. The structural transition of Gd_2O_3 nanoparticles induced by high pressure, *J. Phys.: Condens. Matter*. 19, 425229-425233, 2007.
- [13] Hoa, L.T.M. et al. Preparation and characterization of magnetic nanoparticles coated with polyethylene glycol, *J.Phys: conf. Ser.*187, 012048-52,2009.
- [14] Hong, R. Y. Magnetic field synthesis of Fe_3O_4 nanoparticles used as a precursor of ferrofluids, *J. Magn. Mater.* 310, 37-47, 2007.
- [15] Qadri, S.B. Size-induced transition-temperature reduction in nanoparticles of ZnS, *Phys.Rev. B* 60, 9191-9193, 1999.
- [16] Zhang, L. and Zhang, Y. Fabrication and magnetic properties of Fe_3O_4 nanowire arrays in different diameters *J. Magn. Mater.* 321, L15-L20, 2009 .
- [17] Seo, S. et al. Controlled shape growth of Eu- or Tb-doped luminescent Gd_2O_3 colloidal nanocrystals *J. Colloid Interface Sci.* 331, 236-242, 2009.
- [18] Vereda, F. et al. Synthesis and characterization of single-domain monocrystalline magnetite particles by oxidative aging of $Fe(OH)_2$, *J. Phys. Chem. C.* 112 , 5843-5849, 2008.
- [19] Wilson (Jr.), Decius, J.C. and Cross, P.C. *Molecular vibrations, The theory of infrared and Raman vibrational spectra*, Dover Publications, NW, 1980.
- [20] Sahoo, Y. et al. Aqueous ferrofluid of magnetite nanoparticles: fluorescence labeling and magnetophoretic control, *J. Phys. Chem. B* 109, 3879-3855, 2005.
- [21] Maity, D. and Agrawal, D. C., Synthesis of iron oxide nanoparticles under oxidizing environment and their stabilization in aqueous and non-aqueous media, *J. Mag. Mater.* 308, 46-55, 2007.
-

- [22] Nyquist, R.A., Putzig, C.L., and Leugers, M. Anne (eds.) *Handbook of Infrared and Raman Spectra of Inorganic Compounds and Organic Salts*, Academic Press, San Diego, 1997.
- [23] Răuciu, M. et al. Room temperature synthesis of magnetic nanoparticles, *J. Optoelec. Adv. Mater.* 10, 2928-2931, 2008.
- [24] Wang, Y.D. et al. Synthesis and room temperature photoluminescence of ZnO/CTAB ordered layered nanocomposite with flake-like architecture, *J. Lumin.* 126, 661-664, 2007.
- [25] Murillo, A.G. et al. Optical properties of europium-doped Gd₂O₃ waveguiding thin films prepared by the sol-gel method, *Opt. Mater.* 19 161-168, 2002.
- [26] Guo, H. et al. Visible Upconversion in rare earth ion-doped Gd₂O₃ nanocrystals, *J. Phys. Chem. B.* 108, 19205-19209, 2004.
- [27] Gupta, R. et al. Raman study of stoichiometric and Zn-doped Fe₃O₄, *Phy. Rev. B.* 65, 104430-10442, 2002.
- [28] Tiwari, S. Oriented growth of Fe₃O₄ thin film on crystalline and amorphous substrates by pulsed laser deposition, *J. Phys. D: Appl. Phys.* 40, 4943-4947, 2007.
- [29] Gouteron, J. et al. Raman spectra of lanthanide sesquioxide single crystals: correlation between A and B-Type structures, *J. Solid State Chem.* 38, 288-296, 1981.
- [30] Luyer, C.L. et al. Waveguide Raman spectroscopy of sol-gel Gd₂O₃ thin films, *J. Raman Spectrosc.* 34, 234-239, 2003.
- [31] Eaton, G. R. et al. *Quantitative EPR*, Springer-Verlag, Berlin, Heidelberg, NY, 2010.
- [32] Salado, J. et al. Synthesis and magnetic properties of monodisperse Fe₃O₄ nanoparticles with controlled sizes, *J. Non. Crystal. sol.*, 354, 5207-5209, 2008.

3.1. Effect of static magnetic field on ferrofluids

The splendour of ferrofluid lies on two important facts: as normal liquid that flows and at the same time, it can respond to an external magnetic field. A ferrofluid, as discussed in previous chapter, would exhibit magnetic response unlike conventional fluids. It was reported that, many of its physical properties (viscosity, thermal conductivity, polarizability, velocity, droplet size-shape etc.) can be adequately controlled with applied magnetic field strength.^[1-3] The particle size distribution and number density of a FF play a crucial role in presence of an applied field. The dispersed magnetic nanoparticles of a FF constitute a colloidal model (magnetic) system due to its permanent magnetic moment.^[4] Without an external field, the dispersed particles behave as single domain magnetic particles and they are in a state of random Brownian motion. But in presence of an external field, their movement becomes streamlined as they experience an attractive force along the field direction. Referring to pp.13 of chapter-1, we can say that the dipolar interaction of these magnetic domains will also tend to increase. When these interactions become sufficiently strong, they undergo interesting structural change.^[5,6] Firstly, the randomly orientated magnetic particles join head-to- tail along the field direction forming thereby a number of chains. In fact, the chainlike structures come out as a result of competition between magnetic dipolar interaction ($U_d (ij)$) and thermal interaction ($k_B T$). The effective interaction between two ferromagnetic particles is generally expressed by a coupling constant given by:^[7]

$$L = - \frac{U_d (ij)}{k_B T} \quad (3.1)$$

Afterwards, these chains undergo secondary aggregation through lateral coalescence forming bundle of chains.^[8] This is also known as zippering effect. Two simultaneously occurring effects viz. thermal fluctuation induced interactions and hindrance in the local lateral field due to topological defect in the dipolar chains are attributed to these type of

structure formation. Consequently, many remarkable changes of ferrofluid property can be observed. In particular, magneto-optic and magneto-viscous characteristics are note-worthy that have received significant attention in recent time.

3.2. Magneto-optic effects of ferrofluid

Magneto-optic (MO) effect is a phenomenon that deals with the interaction of an electromagnetic (EM) wave with an externally applied magnetic field. In short, optical activity of a material under study changes with the application of the magnetic field. Magneto-optic effect is important in the sense that it provides information regarding the electronic and spin structure of the system.

Polarization of light describes a specific orientation of the electric vector (E) of the EM wave at a point in a period of oscillation. In circularly polarized light, the direction of propagation and the rotation of E forms either a right handed or left handed screw.^[9] When an electromagnetic wave propagates through an optically active material, the left and right polarisation vector of the EM wave move with different velocities.^[10] This difference is manifested as different MO effects. Magneto-optic effect results in the change of many optical parameters of the medium under study.^[11] The orientation of the light polarization in a medium can be studied either in the transmission mode (Faraday rotation) or in the reflection mode (Kerr effect).

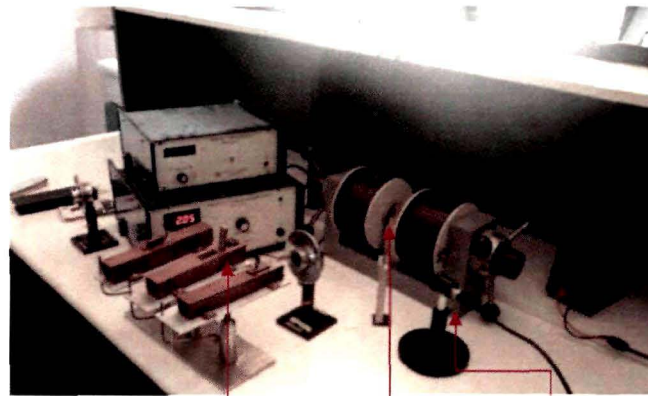
A vast number of reports are available in the literature related to the MO effects exhibited by Ferrofluids.^[12-14] The most important magneto-optic effects exhibited by FFs are Faraday rotation (FR), Faraday ellipticity, Kerr effect (for ferrofluid film), linear dichroism (LD), birefringence etc.^[12] Longitudinal MO effects in specific spectral range has been reported.^[15] Also, it was shown that FR could occur in a step- like manner. This quantization was attributed to resonant tunneling of magnetic moment in case of smaller sized quantum particles.^[16] The non-reciprocity theory

demonstrates that the rotation direction of the polarized light depends only on the magnetic field direction.^[17] A comparative study of the reciprocity of Faraday effect shown by the FF and magneto-optic glass specified that despite the reversal of the magnetic field direction, the rotation of the polarized light remained same in the former case.^[18] Many FF- based devices eg. sensor, isolator, modulator etc. can be efficiently designed by controlling the MO effects.^[19,21]

3.2.1. Faraday rotation of synthesized ferrofluids

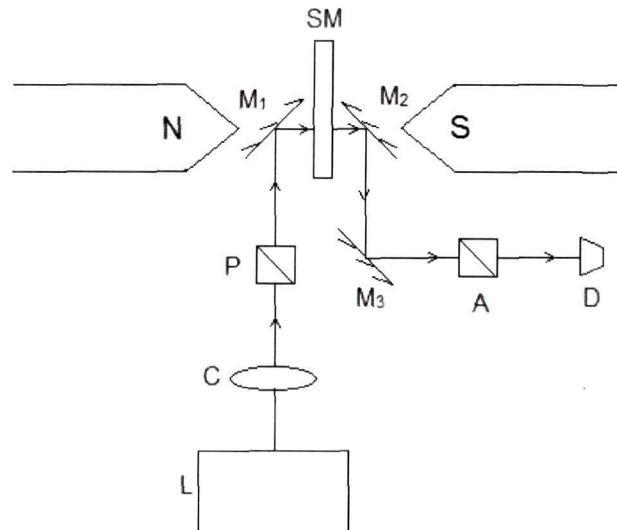
FR is a quantitative assessment of the interaction of a plane polarised light with matter in presence of an external magnetic field applied along the direction of light wave propagation. When a polarized light beam is allowed to traverse through an optically active object, it undergoes transformation into two circularly polarized light beams.^[22] Generally, ^[23] the FR is expressed as $\theta_F = VHI$, where V is the Verdet constant of the material, H is the applied magnetic field and I is the optical path length. The complete scheme of modified custom-made Faraday rotation set-up^[24] is shown in Fig. 3.1(a,b). The optical components of the set-up include solid-state lasers ($P = 20\text{mW}$, $\lambda = 632.8\text{ nm}$; $P = 50\text{ mW}$, $\lambda = 532\text{ nm}$), a plano-convex lens to collimate the laser light, a polarizer, an analyser and a Si photodiode (detector) sensitive within visible to near infra-red light. An electromagnet was used as the source of the external magnetic field. With the help of a set of surface polished mirrors (reflectance $> 99.9\%$), the incident laser light was aligned along the direction of the applied field. The FR was measured as the function of the ratio of the transmitted light intensities without and with placing the analyser in appropriate place. In order to calibrate our experimental set-up using a laser of wavelength 632.8 nm , first we measured the FR of milli-Q water (conductivity: $18.2\text{ mega } \Omega$) taken in a 1 cm cuvette with empty cuvette as reference [Fig. 3.(c)]. On linear fitting of the curve, the Verdet

constant of water was calculated to be 3.9×10^{-4} deg/ G-cm which is consistent with the previously reported value. ^[25]



Laser Specimen Detector

(a)



(b)

Fig 3.1: (a) Experimental set up and (b) schematic diagram for Faraday rotation measurement with L: laser, C: plano-convex lens, P: polarizer, SM: specimen, (M1, M2, M3): mirror, A: analyser, D: photodetector.

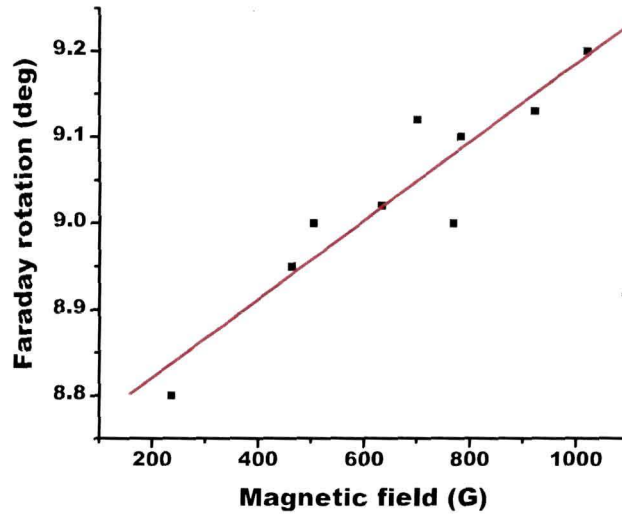


Fig 3.1(c): Faraday rotation of milli-Q water

(i) FFW specimen

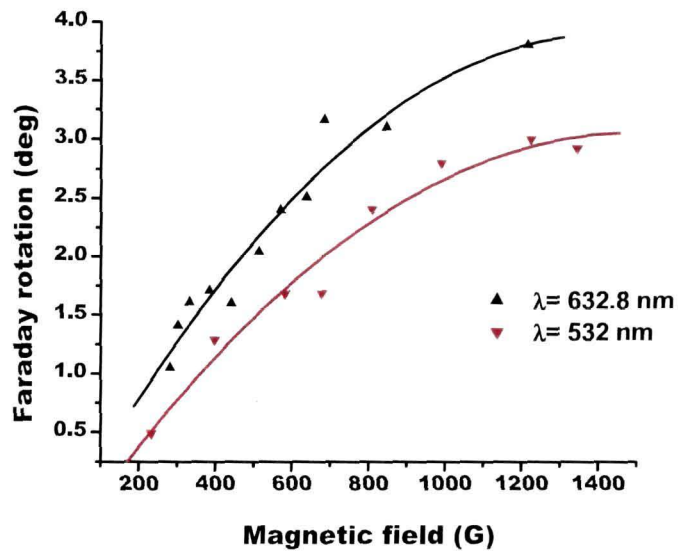


Fig 3.2: FR response of FFW at two different wavelengths

The FR characteristics of the synthesized FFW (Fe_3O_4 based ferrofluid with water as carrier) measured at two different wavelengths (532 and 632.8 nm) are shown in Fig. 3.2. For a given wavelength, the rotation gradually increases with the field and then exhibits a saturation trend. Such a Faraday response is quite obvious in FFs [26,27] and semiconductors doped with magnetic impurities.[28]

As mentioned earlier, with the application of an external field, the particles dispersed in a FF form chain or column like structures, which would otherwise exhibit independent Brownian motion in isolation from each other. In presence of the field, first the individual particles try to align themselves along the field. Later, these chains get aligned owing to zippering effect and when all the chains are aligned along the applied field, the FR would reach its saturation value. Considering chaining effect into account the FR for ferrofluids can be expressed as:[29]

$$\theta_F = C \frac{M(H)}{M_S} + V H l(H) \quad (3.2)$$

Here, C is a constant, $M(H)$ is the magnetization of the particle at an applied field H , M_S representing the saturation magnetization of the specimen and $l(H)$ being the chain length at a field H . It was also revealed that, at a definite magnetic field, the FR has a dependency on the excited wavelength [Fig 3.2]. It may be noted that larger wavelength corresponds to a lower energy value and hence it will hinder the chain formation only weakly. Consequently, an excited light with larger wavelength would result in a significant FR in comparison with a light beam of a shorter wavelength. In Fe_3O_4 system, $3d$ electronic states of iron are generally responsible for the magneto-optic effects.[30] The cations (Fe^{3+} and Fe^{2+}) are believed to occupy the tetrahedral and octahedral sites. They interact with the oxygen localized states which are already present in the vicinity of their neighbouring environment. The Faraday rotation takes place due to intervalence charge-transfer transitions (~ 0.6 eV) between neighbouring Fe^{2+} and Fe^{3+} ions. [25, 31]

(ii) FFK specimen

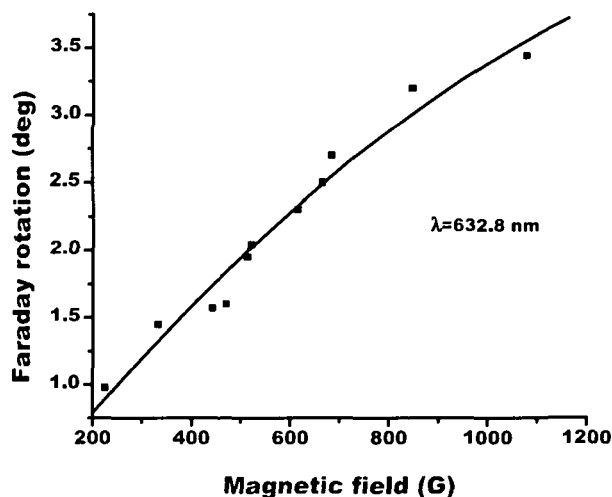


Fig 3.3: FR response of FFK

The Faraday rotation of the FFK is also measured with the above mentioned custom made set-up. The observed variation of the FR with the applied magnetic field, is depicted in Fig.3.3. The polynomial fit of the measured data illustrates a typical nature of the FF as it first increases with the increasing field and then tends to saturate. The exact saturation was expected to occur at a relatively higher external magnetic field which was beyond the limit of our current experimental arrangement. However, the rising trend towards saturation could be attributed to steady chain forming process and zippering effect of MNPs under an applied magnetic field.

Note that, the ferrofluid FFK used in this study contained dispersed magnetite nanoparticles. Thus, mainly Fe^{2+} and Fe^{3+} of magnetite systems were responsible for the observed FR. The intervalence charge transfer among these two types of ions also accounts for the FR in the system.

(iii) FFG specimen

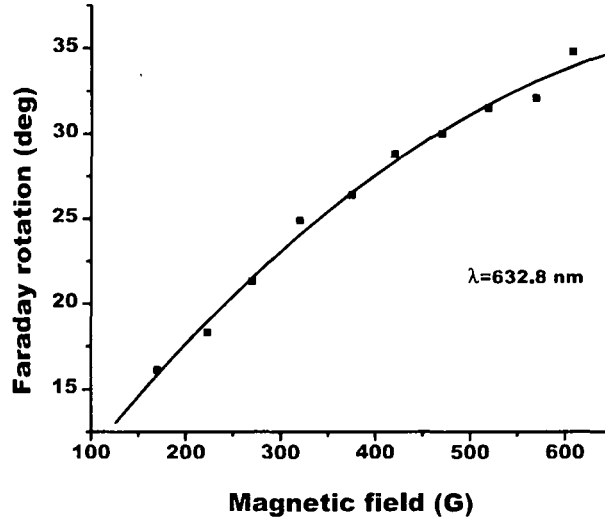


Fig 3.4: FR response of FFG

Rare earth (RE) oxides are widely used in luminescent components, permanent magnets and glass industry.^[32] They are regarded as special systems owing to combined optical and magnetic properties. The RE elements Dy, Tb, Ho as well as their oxides are optically transparent to visible light.^[33] In particular, Gd_2O_3 is a technologically important candidate which has potential in a number of fields including infra-red absorbing automotive glasses, microwave applications, colour television phosphor etc.^[34] Gd_2O_3 nanoparticle is a good candidate for magnetic resonance imaging (MRI) agent.^[35]

It was known that owing to availability of unpaired electrons in the f -sub shell of Gd, Gd_2O_3 exhibits magnetic properties both in bulk as well as in nano form.^[36] The unusual magnetic properties become prominent when the system of interest is in the nanoscale range.^[37-39] Therefore, magneto-optic phenomena like FR of Gd_2O_3 based ferrofluid is very much expected. It was suggested that, the transition between the $4f$ electrons of the RE ions could lead to modified optical response in Gd_2O_3 .^[40]

The ferrofluid FFG contained CTAB coated Gd_2O_3 nanoparticles with ethanol as carrier medium. The FR response of FFG is shown in Fig. 3.4. The Verdet constant of the synthesized Gd_2O_3 based ferrofluid in our case is calculated as $7.7 \times 10^{-2} \text{deg/G-cm}$ (positive) which is measured from the linear portion of the FR curve. A positive Verdet constant corresponds to a counter clock wise rotation when the direction of propagation is along the magnetic field. The nature of the FR response of this particular FF is similar to that of other ferrofluids. However, in case of FFG, the fluctuation response at low fields is relatively small as compared to response of FFW and FFK. This is attributed to the less scattering from the surface of Gd_2O_3 nanoparticles owing to its stability. The steady enhancement of FR that tends to saturation with the variation of the applied magnetic field, is due to structural evolution of the magnetic MNPs to chains.

3.2.2. Linear dichroism of synthesized ferrofluids

LD makes its wonder in studying the structure of a molecule or cluster of atoms. This particular electromagnetic spectroscopic phenomenon occurs as a result of unique interaction of light with matter. In general, LD is the dependence of absorption strength on the linear polarization of the light beam relative to a macroscopic laboratory axis.^[41] In case of magnetic colloidal solution the birefringence and dichroism originates from the intrinsic optical anisotropy or the shape anisotropy of the individual particles.^[42] We studied the linear dichroism response of our synthesized ferrofluids using the same experimental set-up as used for FR measurement but with modified configurations. Here, measurements were performed with the plane of polarization of light parallel and perpendicular to the applied magnetic field (100-700 G). The corresponding values of the parallel and perpendicular dichroism are defined as:^[12]

$$\Delta A_{\parallel} = -\ln\left(\frac{I_{\parallel}}{I_0}\right) \quad (3.3)$$

$$\Delta A_{\perp} = -\ln\left(\frac{I_{\perp}}{I_0}\right) \quad (3.4)$$

The transmitted light intensity when the magnetic field is switched off is referred as I_0 and that in presence of the field in a direction parallel and perpendicular to the field are written as I_{\parallel} and I_{\perp} ; respectively. The intrinsic LD of the fluid is then expressed as:^[12]

$$\Delta k = (\Delta A_{\parallel} - \Delta A_{\perp})\lambda/4\pi l \quad (3.5)$$

Here, λ is the incident light wavelength and l is the optical path length. We carried out all the dichroism measurements with a red laser of $\lambda = 632.8$ nm and power = 20 mW. As 1cm x1cm rectangular cuvette was used in the experiment, the optical path length is 1 cm.

(i) LD of synthesized FFW, FFK and FFG

The Fig.3.5, 3.6 and 3.7 exhibit the LD response of three ferrofluids: FFW, FFK and FFG; respectively. It was observed that the LD responses of the FFs generally follow Langevin-characteristics. Firstly, it increases slowly with increasing applied magnetic field. Saturation of the LD response is expected at a higher magnetic field strength. It was reported earlier that in a magnetic fluid, the LD response invariably arise from adequate optical anisotropy.^[43] According to the classical theory of interaction between light and matter, small particles (compared to the wavelength of light) behave like oscillating dipoles in presence of light. In case of two magnetic particles, the electric field produced by an individual oscillating dipole is given by:^[44]

$$E = \frac{1}{4\pi\epsilon_1|r_0|^3} \{3(\mathbf{p} \cdot \mathbf{r}_0)\mathbf{r}_0 - \mathbf{p}\} \quad (3.6)$$

where, r_0 is the position vector whose origin is at the particle or oscillating dipole centre and p is the dipole moment. The oscillating dipole interaction between particles give rise an optical anisotropy. As already mentioned, the dispersed particles of a FF form several chains along the applied

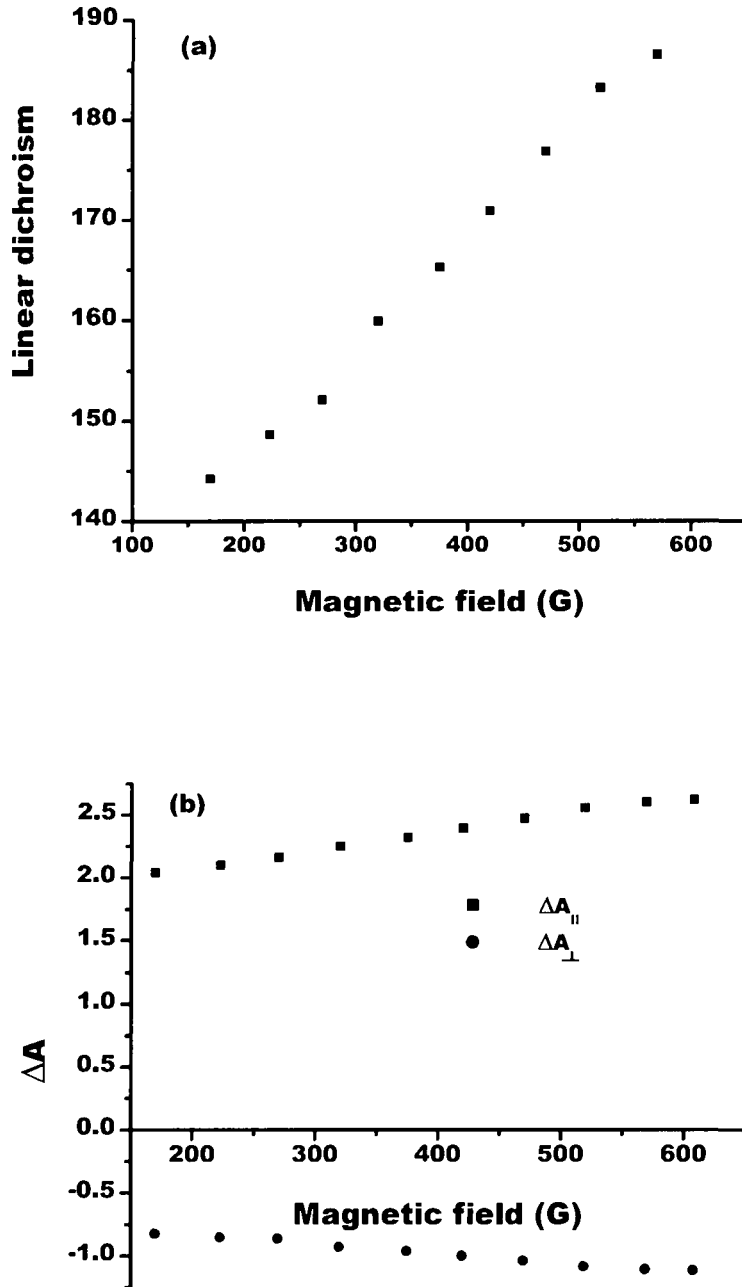


Fig 3.5:(a) LD response of FFW and (b) the parallel and perpendicular components of LD.

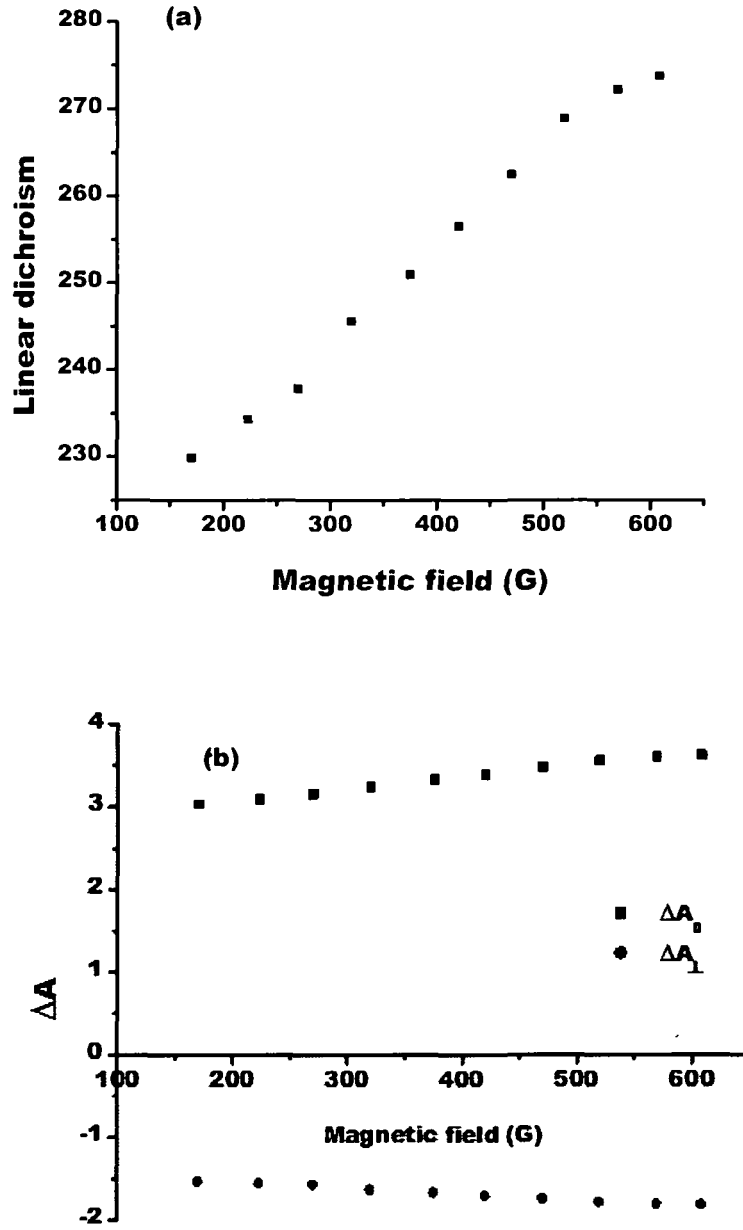


Fig 3.6: (a) LD response of FFK and (b) the parallel and perpendicular component of LD.

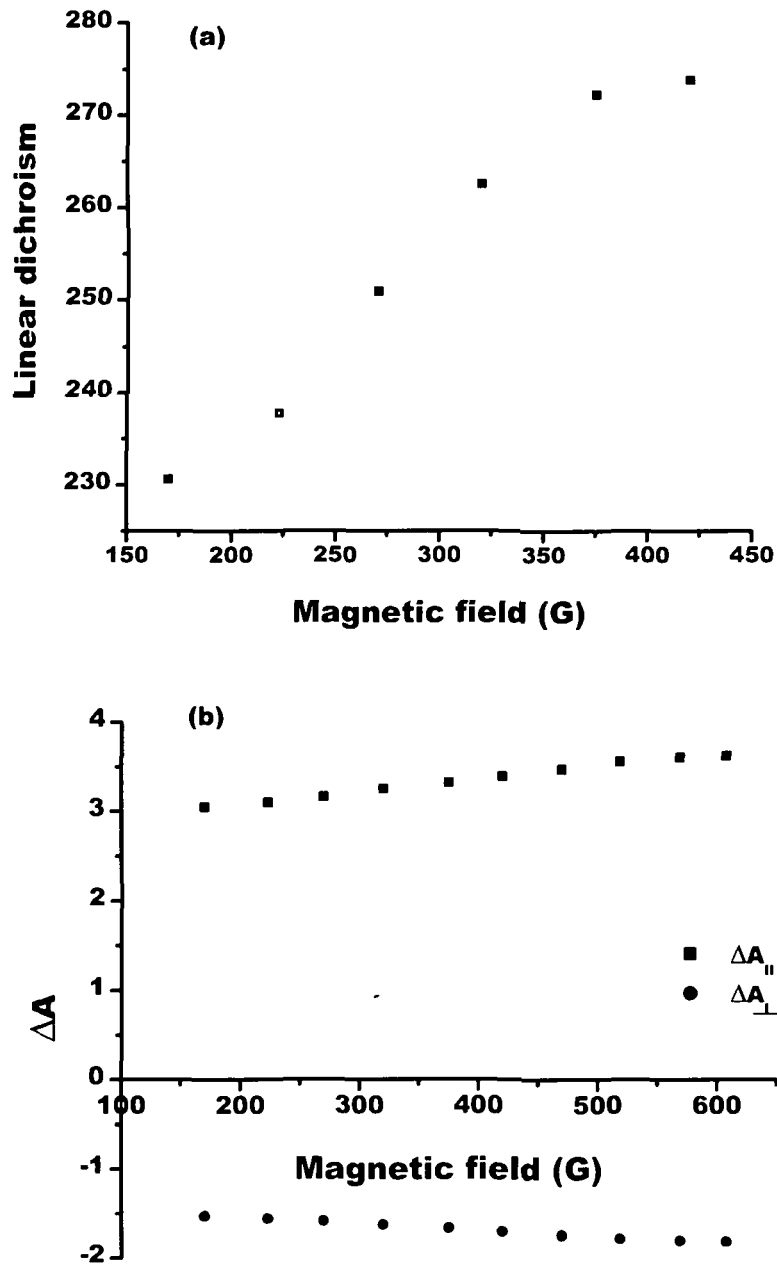


Fig 3.7: (a) LD response of FFG and (b) the parallel and perpendicular component of LD.

magnetic field. The aggregates or chains are responsible for displaying dichroism effect rather strongly than corresponding individual particles. Eq.(3.6) reveals that, the electric field or the interaction force between particles is inversely proportional to the cube of the distance between them. So in a chain, only the nearest neighbours have influence on each other, the distant particles will have only weak effect.^[44] We can speculate that the dichroism response shows enhancement with magnetic field upto the limit corresponding the rapid interaction between the particles (oscillating dipoles). As the chain length increases inter-particle interaction slows down due to the increase of the separation between distant particles. This would manifest in the saturation tendency of the dichroism effect in the region of higher magnetic field strengths.

Theory predicts that in case of a true dichroic material, the sign and magnitudes of the parallel and perpendicular components of the LD will be different for each case.^[45] The strength of the parallel component is about twice that of the perpendicular component and it is opposite in sign.^[45,46] In other words, $\Delta A_{\parallel} \cong -2\Delta A_{\perp}$. This type of variation is much expected in most of the magnetic fluids (FFs).^[12] It may be noted that, Fig.(b) of 3.5,3.6 and 3.7 corresponding to FFW, FFK and FFG specimen strictly satisfy this condition.

3.3. Magneto-rheological property of ferrofluid

Rheology is the science of deformation and flow of materials.^[47] It is based on three fundamental concepts: kinematics (study of motion), conservation laws (interchange of various energy, forces and stresses during motion) and constitutive relations (links motion and forces of special classes of bodies eg. viscous bodies).^[47] Magneto-rheology is a special branch of rheology. It is related with the variation of the rheological property of a fluid in presence of a magnetic field.^[48] The application of a magnetic field, rapidly changes the viscosity of a fluid.

Ferrofluids (being magnetic fluids) are capable of displaying exciting magneto-viscous (magneto-rheological) properties.^[49-51] When subjected to an applied magnetic field, FFs undergo notable changes in their physical properties. The change in the fluid's viscosity due to an external magnetic field is termed as magneto-viscous effect (MV). The MV effect of FFs is established as one of the most challenging and vital property for ferrofluid application/ research ^[52,53]. The viscosity of FF is invariably sensitive to the applied magnetic field. In a shear flow, the dispersed MNPs of a ferrofluid rotate themselves in such a way that their axes of rotation are parallel to the vorticity (local spinning motion of the fluid) of the flow. In case of a magnetically hard particle, the magnetic moment will be fixed within the particles. If an external magnetic field is applied perpendicular to the vorticity of the flow, then two situations will appear at the forefront simultaneously. Firstly, the magnetic field will try to align the particles along the field direction while the viscous force will tend to rotate the particles. As the moment is fixed within the particles, there will be misalignment between the field and the moment of the particles. This results in a torque. On the contrary, this torque will hinder the free rotation of the particles, thus the viscosity of the fluid changes.^[54] If the external field is applied in direction parallel to the vorticity of the fluid, there will be a resultant torque between the moment and the applied field. Thus no change will occur in the fluid's viscosity.

(i) Magneto-rheological response of FF1 and FF2

The rheological properties of the samples FF1 and FF2 were studied by a conventional Brookfield dial reading viscometer (Model: M/00-151). Fig.3.8 represents shear rate dependent variation of viscosities in the absence of a magnetic field. The nonlinear decay of viscosity with increasing shear rate confirm that the ferrofluids are likely to experience non Newtonian characteristics. The observable shear thinning i.e. decrease of viscosity with shear rate, for both the ferrofluids can be

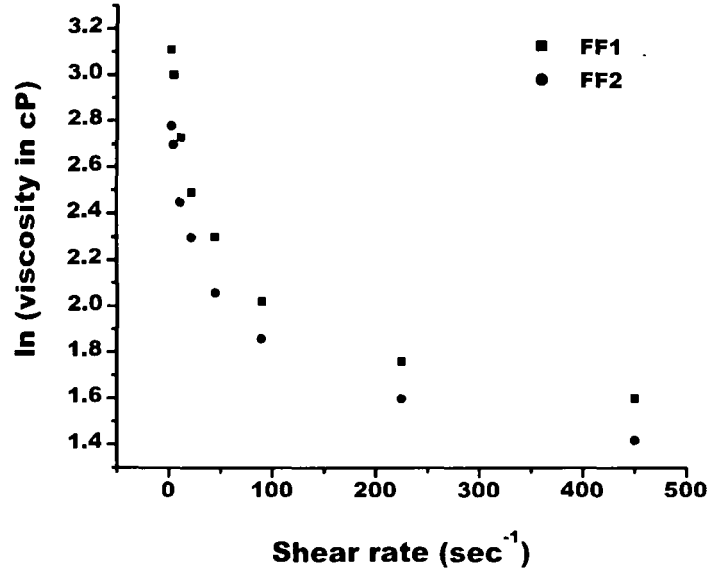


Fig 3.8: Variation of viscosity with shear rate for FF1 and FF2

expressed by:

$$y = y_0 + y_1 e^{-x/t_1} + y_2 e^{-x/t_2} \quad (3.7)$$

Here y is the viscosity in logarithmic scale, y_0 is the initial viscosity, y_1 and y_2 are the viscosities at zero shear rate for a particular trend, x is the applied shear rate while t_1 , t_2 are the decay parameters in sec^{-1} . The measured parameters are enlisted in Table 3.2. From the biexponential equation, it can be understood that the ferrofluids are undergoing two simultaneous decay equations- one of them is very fast with high decay parameter. The critical shear rate at which shear thinning has slowed down are 86.21 sec^{-1} and 118 sec^{-1} for FF1 and FF2; respectively. The overall viscous nature of the FFs can be attributed to the arrangement of small chains/clusters of the MNPs.^[55] With increasing shear rate, some kind of perturbation of these clusters occur leading to a decreasing trend of viscosity. It is evident from TEM pictures that in the absence of any external force there could be more clustering effect in FF1 than in case of FF2 [Fig.(2.14) of Chp.2]. In other words, oleic acid (anionic surfactant)

coated particles are well-dispersed than TMAH (cationic surfactant) coated particles. But with increasing shear rate, oleic acid coated clusters would respond to fragmentation more easily.

Table 3.1: Different parameters of FF1 and FF2

FF	γ_1 (cP)	γ_2 (cP)	t_1 (/s)	t_2 (/s)
FF1	0.67 ± 0.006	0.99 ± 0.003	10.99 ± 2	117.74 ± 2
FF2	0.64 ± 0.008	0.86 ± 0.01	15.36 ± 2	168.73 ± 3

In order to study the effect of applied magnetic field on the rheological property, the MV response was studied when the field was varied in the range of 0-100 G. Fig. 3.9(a) and (b) demonstrate the magneto-viscous property of FF1 and FF2. Pronounced non Newtonian behaviour was observed even in the presence of magnetic fields (H). For a particular field, viscosity decreases with increasing shear rate, similar to that in absence of applied field. Especially at a fixed shear rate, applied magnetic field could enhance the viscosity of the FFs. Other workers have argued that the formation of different field induced structures e.g. chain sequence, droplike etc. in real FFs might lead to such a variation.^[56,57] The larger the amount of such structures, the higher would be the viscosity. Particles larger than the critical size (~ 10 nm for magnetite particles) are more prone to this kind of structure formation.^[58] In a ferrofluid, the amount of such particles largely influences the magneto-viscous property. At higher shear rates these structures break down thus resulting in decreased viscosity. It was reported by Odenbach *et al* that, the interaction between the magnetic moment and mechanical torque of these particles results in high magneto viscous effect.^[59] This is attributed to the stronger orientation tendency of the dipole moments from the direction of vorticity towards the applied field. In our case, the direction of the

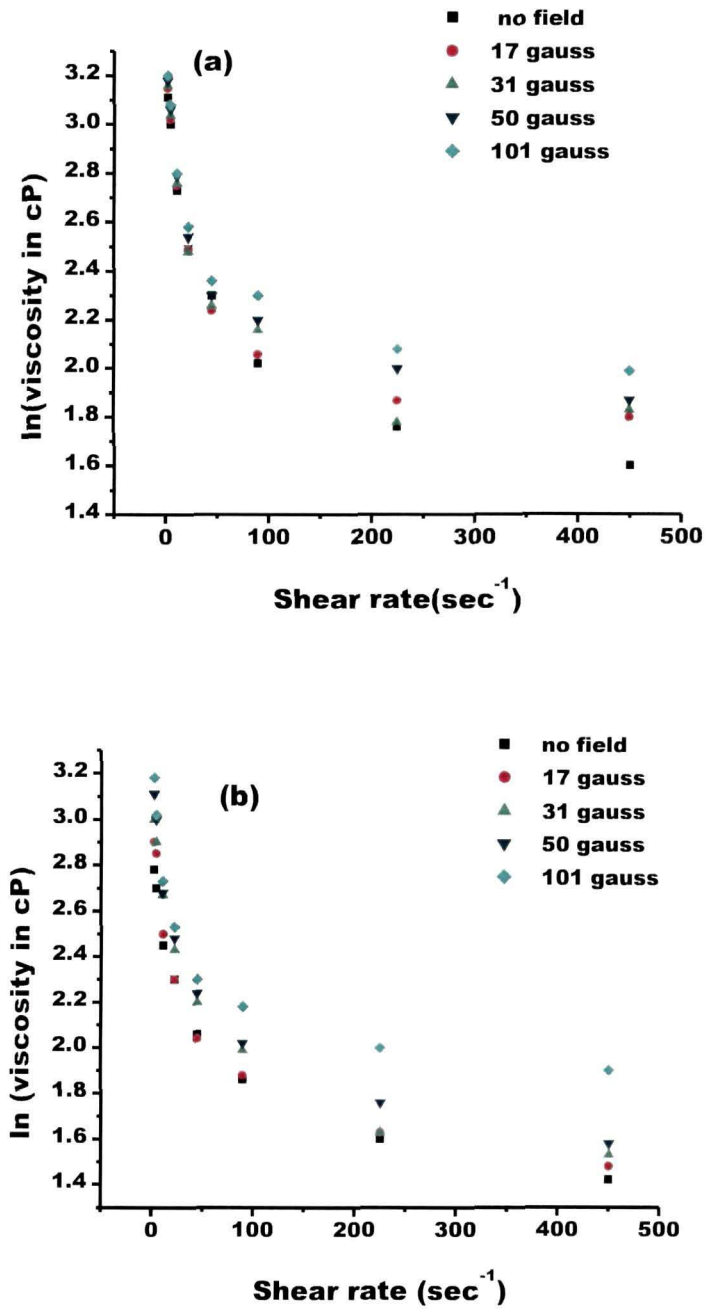


Fig 3.9: Variation of viscosity (with shear rate) of (a) FF1 and (b) FF2

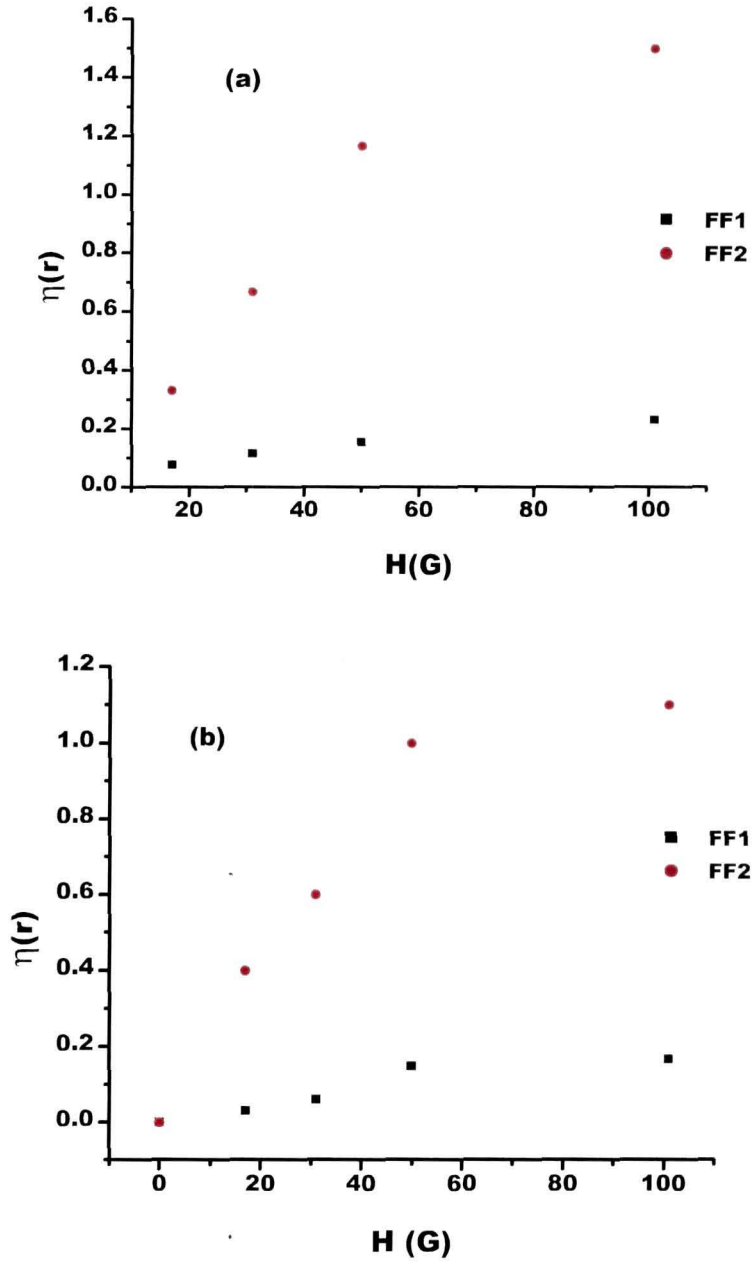


Fig 3.10: Relative change of viscosity with magnetic field at shear rate (a) 225 sec^{-1} and (b) 445 sec^{-1} .

magnetic field is perpendicular to the vorticity of the fluid. As the field increases the interaction between the field and the magnetic moments of the MNPs gets enhanced drastically. Thus, the position of the critical shear rate shifts towards lower shear rate direction with increase of field.

For the sake of better understanding and validation of the role of the two surfactants on the viscosity of the FFs, the relative change of viscosities (η_r) was also worked out. The respective change of viscosity corresponding to different magnetic fields are shown in Fig. 3.10(a) and (b). It is expressed by the equation:

$$\eta_r = \frac{\eta(H) - \eta(0)}{\eta(0)} \quad (3.8)$$

It is found that the FF2 responds more rapidly to the field than that of FF1 irrespective of shear rate. It implies that oleic acid coated particles easily interact with the field. Conversely, TMAH coated particles are more stable in ferrofluid in comparison to oleic acid coated particles. The stability of FFs with oleic acid and TMAH coated Fe_3O_4 MNPs depends on a definite surfactant environment. These two surfactants are different from each other in their respective hydrocarbon chain lengths. It is larger in TMAH $[(\text{CH}_3)_4\text{NOH}]$ than that of Oleic acid ($\text{C}_{18}\text{H}_{34}\text{O}_2$). It was reported earlier that the dispersion stability of surfactant depends on the hydrocarbon chain length.^[60] The absorption free energy increases with the increase of the hydrocarbon chain length, leading to improvement in chemical stability.^[61] Consequently, better stability can be anticipated in case of use of TMAH.

3.4. Concluding remarks

The effect of external magnetic field (static) on the synthesized FFs was studied in terms of magneto-optic and magneto-rheological response. The FR and LD responses of FFW and FFK have shown interesting results. The FR is largely dependent on the excited wavelength and exhibiting stronger response for larger wavelength. The LD of the FFs satisfied

Langevin type response with the condition $\Delta A_{\parallel} \cong -2\Delta A_{\perp}$. The rheological studies of FF1 and FF2 have revealed that the FFs were of non-Newtonian type. These FFs were also highly magneto-viscous. When the field was increased from no field to a value of ~ 100 G, the viscosity was found to get enhanced by $\sim 20\%$ when the shear rate was fixed at 4.5 sec^{-1} . Owing to the long chain length of TMAH molecules, FF2 specimen was found to be $\sim 12\%$ more viscous than FF1 (with oleic coated MNPs).

References:

- [1] Falcucci, G. et al. Rupture of a ferrofluid droplet in external magnetic fields using a single-component lattice Boltzmann model for nonideal fluids, *Phys. Rev. E*. 79, 056706-056710, 2009.

- [2] Zou, Y., Di, Z., and Chen, X. Agglomeration response of nanoparticles in magnetic fluid via monitoring of light transmission, *Appl. Opt.* 50, 1087-1090, 2011.

- [3] Lee, H. M., Horng, L. and Wu, J. C. Magnetic-field tunable transmittance in a ferrofluid-filled silicon nitride photonic crystal slab, *J. Phys. D: Appl. Phys.* 44 064016 -064020, 2011.

- [4] Rosensweig, R. E., *Ferrohydrodynamics*, 1st ed., Dover, New York, 1997.

- [5] Mendeleev, V. S. and Ivanov, A. O., Ferrofluid aggregation in chains under the influence of a magnetic field , *Phys. Rev. E*. 70, 051502-051511, 2004.

- [6] Zubarev A.Y., Iskakova L.Y., Direct and inverse domain structures in ferrofluids, *Physica A*, 367, 55–68, 2006.

- [7] Laskar, J. M., Philip, J., and Raj, B. Experimental evidence for reversible zippering of chains in magnetic nanofluids under external magnetic fields, *Phy. Rev. E*. 80, 041401-041408, 2009.

- [8] Martin, J. E., Odinek J. and Halsey, T. C. Evolution of structure in a quiescent electrorheological fluid, *Phys. Rev. Lett.* 69, 1524–1527, 1992.
- [9] Born, M. and Wolf, E. *Principles of optics*, Cambridge University Press, Cambridge, 1999.
- [10] Hopster, H. and Oepen, H.P.(eds.) *Magnetic microscopy of nanostructures*, Springer, Germany, 2005.
- [11] Iisuka, K. *Elements of photonics*, Wiley, New York, 2002.
- [12] Davies H. W. and Llewellyn J P., Magneto-optic effects in ferrofluids, *J. Phys. D: Appl. Phys.* 13, 2327-36,1980.
- [13] Kooij, E.S. et al. Versatile transmission ellipsometry to study linear ferrofluid magneto-optics, *J. Coll. Inter. Sci.* 304 261–270, 2006.
- [14] Jamon, D. Experimental investigation on the magneto-optic effects of ferrofluids via dynamic measurements, *J. Magn. Magn. Mater.* 321, 1148-1154, 2009.
- [15] Donatmi, F. et al. Experimental investigation of longitudinal magneto-optic effects in four ferrite ferrofluids in visible-near infrared spectrum, *IEEE Trans. Magn.* 35, 4311-4317, 1999.
- [16] Deb, P., Gogoi, M. and Karmakar, P. K. Anomalous magneto-optic Faraday rotation behavior due to resonant tunneling of magnetic moment, *J. Opt.* 41, 41-47, 2012.
- [17] Massard, C. et al. Hybrid sol–gel thin films for magneto-optical applications. chemical, optical and tribological study, *Surf. Coat. Technol.* 202, 1067–1072, 2007.
- [18] Wang, S. et al. Reciprocity of Faraday effect in ferrofluid: Comparison with magneto-optical Glass, *Optik.* 123, 553– 558, 2012.
- [19] Martinez, L. et al. A novel magneto-optic ferrofluid material for sensor applications, *Sens. Actuator. A.* 123–124, 438–443, 2005.
- [20] Ando, B. et al. A ferrofluidic inertial sensor exploiting the Rosensweig effect, *IEEE. Trans. Inst. Meas.* 59, 1471-1479, 2010.
-

- [21] Zu., P. et al. Magneto-optic fiber Sagnac modulator based on magnetic fluids, *Opt. Lett.* 36, 1425-1427, 2011.
- [22] Band, Y.B. *Light and Matter*, Wiley, England, 2007.
- [23] Bennette, H. S. and Stern, E. A. Faraday effects in solids, *Phy. Rev.* 137, A448-A461, 1965.
- [24] Yusuf, N. A., Rousan A. A. and Ghanem, H. M. E., Determination of Faraday rotation in ferrofluid, *J. Magn. Mater.* 65, 282-284, 1987.
- [25] Jain, P. K. et al. Surface plasmon resonance enhanced magneto-optics (SuPREMO): Faraday rotation enhancement in gold-coated iron oxide nanocrystals, *Nano Lett.* 9, 1644-1650, 2009.
- [26] Rousan, A. H. et al. Faraday rotation and chain formation in magnetic fluids *IEEE Trans. Magn.* 25, 3121-3124, 1989.
- [27] M. M. Maiorov, Faraday effect in magnetic fluids at a frequency 10 GHz *J. Magn. Mater.* 252, 111-113, 2002.
- [28] N. Misra, et al. Photochromism and magneto-optic response of ZnO: Mn semiconductor quantum dots fabricated by microemulsion route, *Cent. Eur. J. Phys.* 6, 109-115, 2008.
- [29] Yusuf, N. A. et al. On the concentration dependence of Faraday rotation in magnetic fluids, *IEEE Trans. Magn.* 26, 2852-2855, 1990.
- [30] Schlegel, A. et al. Optical properties of magnetite (Fe₃O₄), *J. Phys. C: Sol. Stat. Phys.* 12, 1157-1164, 1979.
- [31] Choi, K. H. Magnetic behavior of Fe₃O₄ nanostructure fabricated by template method, *J. Magn. Mater.* 310, e861-e863, 2007.
- [32] Adachi, G., Imanaka, N. and Kang, Z. C. (eds.) *Binary rare earth oxides*, Kluwer Academic Publishers, The Netherlands, 2004.
- [33] Morales, J. R. et al. Magneto-optical Faraday effect in nanocrystalline oxides, *J. Appl. Phys.* 109, 093110-093117, 2011.
-

- [34] Dean, J. R. *Practical Inductively coupled Plasma Spectroscopy*, Wiley, England, 2005.
- [35] Chen, X. (ed.) *Nanoplatfrom based molecular Imaging*, Wiley, New Jersey, 2011.
- [36] Kumar, C. (ed.) *Magnetic Nanomaterials*, Wiley, Germany, 2009.
- [37] Fermigier, M. et al. Structure evolution in a paramagnetic latex suspension, *J. Colloid Inter. Sci.* 154, 522-539, 1992.
- [38] Zhou, L. et al. Size-tunable synthesis of lanthanide-doped Gd₂O₃ nanoparticles and their applications for optical and magnetic resonance imaging, *J. Mater. Chem.* 22, 966-974, 2012.
- [39] Das, G.K. et al. Gadolinium oxide ultranarrow nanorods as multimodal contrast agents for optical and magnetic resonance imaging, *Langmuir*. 26, 8959–8965, 2010.
- [40] Henderson, B. and Imbusch, H. *Optical spectroscopy of inorganic solids*, Oxford, NY, 2006.
- [41] William, W. P. *Modern Optical Spectroscopy: With Exercises and Examples from Biophysics and Biochemistry*, Springer, Germany, 2009.
- [42] Blums, E. et al., *Magnetic Fluids*, de Gruyter, Berlin, 1996.
- [43] Jennings, B. R. et al. Ferrofluids structures: a magnetic dichroism study, *Proc. R. Sos. Lond. A.* 456, 891-90, 2000.
- [44] Xu, M. And Ridler, P.J., Linear dichroism and birefringence effects in magnetic fluids, *J. Appl. Phys.* 82, 326-332, 1997.
- [45] Fredericq, E. and Houssier, C. *Electric Dichroism and Electric Birefringence* Oxford University Press, UK, 1973.
- [46] Taketomi, S. et al. Magneto-optical effects of magnetic fluids, *J. Phy.Sos. Jap.*, 56, 3362-3374, 1987.
-

- [47] Tao. R. (ed.) *Electro-rheological fluids and magneto-rheological suspensions*. World Scientific, Singapore , 2011.
- [48] Tanner, R.I. and Walters, K. *Rheology: An historical perspective*, Elsevier Science B.V., the Netherlands, 1998.
- [49] Ilg, P. And Odenbach, S. Ferrofluid structure and rheology, *Colloid. Mag.Flu.*763, 1-77, 2009.
- [50] Olabi, A.G. and Grunwald, A., Design and application of magneto-rheological fluid, *Mater. Degn*, 28, 2658-2664, 2007.
- [51] Hosseini, M. S. et al. Rheological property of a γ -Fe₂O₃ paraffin based ferrofluid, *J. Magn. Magn. Mater.* 322, 3792-3796, 2010.
- [52] Shahnazian, H. et.al., Rheology of a ferrofluid based on nanodisc cobalt particles, *J. Phy. D*, 42, 205004-205009, 2009.
- [53] Ghesemi, E. et al. Magnetoviscous effect in a Maghemite ferrofluid, *J.Nanosc. Nanotech.* 11, 5285-529, 2011.
- [54] Odenbach, S. *Magnetoviscous effects in ferrofluids*, Springer- Verlag, 2002.
- [55] Pop, L. M., Microstructure and rheology of ferrofluids, *J. Magn.Magn. Mater.* 289, 303-306, 2005.
- [56] Zubarev, A. Yu. and Iskakova, L. Yu., Effect of chainlike aggregates on dynamical properties of magnetic liquids, *Phys.Rev. E.* 61, 5415-5421, 2000.
- [57] Zubarev, A. Yu. Et al. Rheological properties of dense ferrofluids. Effect of chain-like aggregates, *J. Magn. Magn. Mater.* 252, 241-243, (2002).
- [58] Odenbach, S. and Raj, K. The influence of particle agglomerates on the magnetoviscous effect in ferrofluids, *Magnetohydrodyn.* 36, 312-319, 2000.
-

[59] Odenbach, S. and Störk, H., Shear dependence of field-induced contributions to the viscosity of magnetic fluids at low shear rates, *J. Magn. Mater.* 183, 188-194, 1998.

[60] Golemanov, K. et al. Selection of surfactants for stable paraffin-in-water dispersions, undergoing solid-liquid transition of the dispersed particles, *Langmuir*, 22, 3560-3569, 2006.

[61] Hetem, M.J.J. Influence of alkyl chain length on the stability of n-alkyl-modified reversed phases. 1. chromatographic and physical analysis, *Anal. Chem.* 62, 2288-2296, 1990.

“Energy cannot be created or destroyed, it can only be changed from one form to another”-This famous quote from Einstein is unchallengeable till now. Energy transmission occurs through convection, conduction and radiation. Convection is the process of flow of heat energy via collision between atoms and molecules of a substance, while convection is related with collective movement of ensembles of molecules within fluids and rheids for transfer of energy. Radiation is the process of travel of energetic particles or waves through vacuum or through matter. Energy of radiation are of two types: ionizing and non-ionizing.

4.1. Ion irradiation

Energetic ion irradiation as well as implantation is a subject of topical interest in advanced nanoscience research. Nanomaterial fabrication, characterization and application have achieved a new dimension by the introduction of energetic ion irradiation techniques.^[1-5] The material properties can be modified by varying ion-beam related experimental conditions. Alongwith the top down and bottom up approach, ion implantation is recognized as an alternative way of processing of nanomaterial in a precise way.^[6] A number of nanostructures with extreme aspect ratios have been fabricated and tailored using the application of ion beams.^[7-8] Chemical bonds break or make during the impact of high energetic ions on the material surface and is commonly known as surface modification.^[9-10] Surface defects affect largely chemical and physical properties of a given material system. In nano scale system, defects are abundant owing to large surface to volume ratio. Irradiation induced annihilation or creation of surface defects is another aspect of ion irradiation process.^[11-12] Ion beam could be effective not only in semi conductors,^[13-15] but also capable of controlling the phase stability of alloys.^[16] Amorphization of many crystalline materials due to MeV ion irradiation have been established.^[17-18] Ion irradiation also tailors enhanced magnetic properties. Magnetic anisotropy can be modified by

energetic ion irradiation. Recently, it was reported that Ga^+ irradiation induced in-plane lattice expansion led to an enhancement in the perpendicular magnetic anisotropy (PMA) of a Pt/Co/Pt ultrathin film.^[19] Swift heavy ion (SHI) irradiation not only modified the crystal structure of magnetically frustrated thin films (BiMn_2O_5), but it also induced a weak ferrimagnetism in the polycrystalline film.^[20] Currently, topographic patterning of magnetic materials is considered as very important for magnetic data storage and magneto-logic devices. Ion irradiation or ion implantation could be useful in forming such patterning also.^[21]

In ion irradiation process, energetic ions interact with the electrons and nucleus of a target material by successive collision events.^[22] This is an inelastic collision. Energy and momentum are transferred from the energetic ion/atom to the electrons or to the nucleus of the target atom. Since the number of electrons is more than the single nucleus, the number of ion collisions with electrons is also larger than that with the nucleus. But due to smaller mass of the electrons, such collision cannot much alter the trajectory of the ion. This type of collision forms a viscous type background by taking energy from the fast moving ions. The energy loss of the ions due to the collision/excitation of the electrons is termed as electronic stopping power $S_e(E)$. Incident ions also slow down by the elastic collision between the ions and target atoms. This type of slowing down process is categorized by nuclear stopping power $S_n(E)$. Binary collision (single scattering) rather than multiple scattering of ion-matter interaction is more prominent in nanomaterial.^[23] Such elastic collisions may leads to displacement damage by the recoil of the knock-on atoms. Cascading of the recoil atoms may also occur, causing further damage of the target materials. Sputtering is another possibility of irradiation effect.^[24] The atoms present in the first or second layer of the surface may sputter into the vacuum due to the recoil energy and momentum directed away from the surface. Ion-beam mixing is also a consequence of the recoiling

atoms. In the recoiling location, several atoms may alter their lattice sites resulting atomic mixing. The mean free path between collisions in a film in the nanometre range is comparable or greater than the thickness of the film.^[23] Therefore only a small fraction of the ions get scattered from the nucleus or electrons of the atom.

The specific physical phenomenon occurring during ion irradiation is basically determined by the kinetic energy of the projectile ion and the property of the material. Approximate different regimes of the physical phenomena are classified on the basis of the kinetic energy of the ion. They are: thermal (below 1 eV), hyperthermal (1-100 eV), low energy (0.1-10 keV), medium energy (10-500 keV) and high energy (> 500keV).^[25]

4.1.1. Low energy (keV) ion irradiation

A projectile ion with low energy (in the keV range) is comparatively less energetic than the swift ions. These ions are mostly effective in the surface and near surface region of the incident material. In general, keV ions are used for ion implantation. The energy loss is due to the elastic and inelastic collision with the nucleus and the electrons respectively. The differential energy loss (dE) of a small layer of the target material with a thickness dx can be expressed as:^[26]

$$\frac{dE}{dx} = \left(\frac{dE}{dx}\right)_n + \left(\frac{dE}{dx}\right)_e \quad (4.1)$$

Here, the suffix n is for nuclear and e is for electronic process.

In keV regime, if the ion velocity is less than the orbital velocity of the electron of the target material, an approximation follows that electronic energy loss is proportional to the ion velocity (Lindhard *et.al* 1963, Firsov 1959).^[27]

The different energy losses restrict the trajectory of the ion to a finite range in the target material. The penetrating ion experiences different type of range. The average path length [$R(E)$] of an ion is derived as:^[28]

$$R(E) = \int_E^0 \frac{dE}{dE/dx} \quad (4.2)$$

The dissipated energy of the ion is transferred not only to the surface. A good portion of this energy is carried away to the reflected ion and/or to the sputtered atoms. The energy dissipation coefficient depends on many factors viz. mass, kinetic energy and angle of incidence of the ion and surface morphology.

In keV ion irradiation nuclear energy loss is dominant over electronic energy loss. In such situation, energy and momentum are transferred directly from the projectile ion to the target atoms. As a result the projectile loses large amount of energy. Consequently, the ion follows an irregular path in the material producing point defects. The target atom may also gain kinetic energy to create further atomic and electronic collisions. Thus, the interaction of a keV ion with the nucleus may produce collision cascades in the target material, which in turn results in recoiling of atoms. Sputtering is a frequent outcome of such irradiation. Kiev ions can produce point defects that can segregate to grain boundaries.^[29] In the keV scale, a light ion could produce isolated defects where as heavy ions can result in cluster of point defects. Low energy ion beams could control the defects on the surface of the nanoparticles in a precise manner without affecting its morphology and crystal structure. The dangling/unsaturated bonds, presence of foreign impurities, etc. can ideally be removed from the nanoparticles through ion beam lead surface passivation. A light ion beam can result in nanoparticles with controlled defects with reduced anisotropy and coercivity. The recoil with different energies creates different type of defects. A recoil with an energy a few times of the threshold displacement energy generate isolated Frankel pairs.^[28] Primary recoil having energy around hundreds of eV results in number of defects nearer to each other.^[28] With further increase of the energy of the recoil, extended disorder in the centre of a cascade with surrounding interstitial occur due to the more number of atoms in motion.^[28] The defect creation

and sputtering also depends on the number of atoms that take part in a collision cascade. In a cascade, the average number of moving atoms that will possess energy greater than initial energy E_0 is expressed as: ^[25]

$$\nu(E_n, E_0) \approx \Gamma \frac{E_n}{E_0} \quad (4.3)$$

Here, E_n is the fraction of the incident ion's energy spent in elastic collision and Γ is dependent on atomic collision.

Ion irradiation (keV) also leads to creation of adatoms on the surface.^[30] The impact of low energy ion irradiation on materials has been studied since decades back. In 1998, Chappert *et al* published their first paper on 'planar patterned magnetic media obtained by ion Irradiation.'^[31] They demonstrated that the easy magnetization direction of Co–Pt multilayers, which is perpendicular to the film surface, can be rotated in-plane upon He⁺ ion irradiation. Later, light ion irradiation was used to create chemical order in FePt thin layers.^[32] In thin film magnetic multilayer, symmetry breaking at the interface alter the perpendicular magnetic anisotropy (PMA).^[33] Any roughening at the surface leads to the symmetry breaking.^[33] The local environment of the atoms of a magnetic material influences its properties. Ion-beam mixing simply modifies such a local environment of a large fraction of atoms.^[34] In thermal spike regime, ion-beam mixing of thermally immiscible Ag/Fe and In/Fe layers has been reported.^[35] In one of the pioneering work of ion implantation, Ar ion was used to study the structural and magnetic property of Co/Pd multilayer.^[36] Now a days, reports are available on ion irradiation induced interfacial mixing in bilayers/multilayers and chemical ordering in alloys.^[37-39] Spherical Co nanoparticles was formed in a SiO₂ layer by implanting 160-keV Co ions (fluence: 10¹⁷ ions/ cm²) into layer.^[40] In order to reveal structural modification, the implanted samples were next irradiated with 200-MeV ion in the fluence range 10¹¹ - 10¹⁴ ions/ cm² at room temperature. Low energy ion beam (1.8-keV He ion) irradiated at an angle to the substrate was found to be an alternative way to fabricate bit

patterned media and as fabricated patterned magnetic array showed a reduced coercivity and narrow standard deviation in the switching field.^[41] Recent reports show that when ZnO nanosticks/nanorods were irradiated with low energy Ar⁻ion its magnetic as well as luminescence properties changed drastically.^[42,43] For a comparatively higher fluence (of the order of 10^{16}) Ar-ion irradiation also created intermetallic phases along with intermixing layers in a Al/Ti nanostructure.^[44] When carbon nanotubes were irradiated with 140-keV He-ion, it transformed into amorphous state with enhanced defect annealing.^[45]

4.2. Effect of 80-keV Ar ions on synthesized nanoparticles/FFS

As discussed above, low energy (~ keV) ion irradiation is mainly related with surface passivation by defect control. In view of this, we irradiated the synthesized nanoparticles with Ar-ion in a high vacuum (10^{-8} mbar) chamber at room temperature using the LEIBF facility of IUAC, New Delhi, India. Being chemically inert, Ar-ion causes less damage to the chemical composition of the irradiated surface. The energy of the ion was chosen as 80-keV based on SRIM calculation (*appendix II*). The ion fluence was chosen as 10^{13} ions cm^{-2} to create defects. For the irradiation experiments, first the synthesized nanoparticles were casted on laboratory glass slide of size 1cm x 1 cm and then subjected to the ion beam. Then FFs were prepared with the irradiated nanoparticles. The consequence of the irradiation was studied basically in the frame of magneto-optic property supported by structural and optical characterizations.

4.2.1. X-ray diffraction

The ion irradiation induced structural changes were first studied by X-ray diffraction method. Fig. 4.1 shows the XRD pattern of the unirradiated as well as the Ar-ion irradiated Fe₃O₄ nanoparticles. The unirradiated Fe₃O₄ MNP system was characterised by Bragg's reflection at 29.87°, 35.15°, 42.92°, 56.84° and 62.4° representing the crystal planes

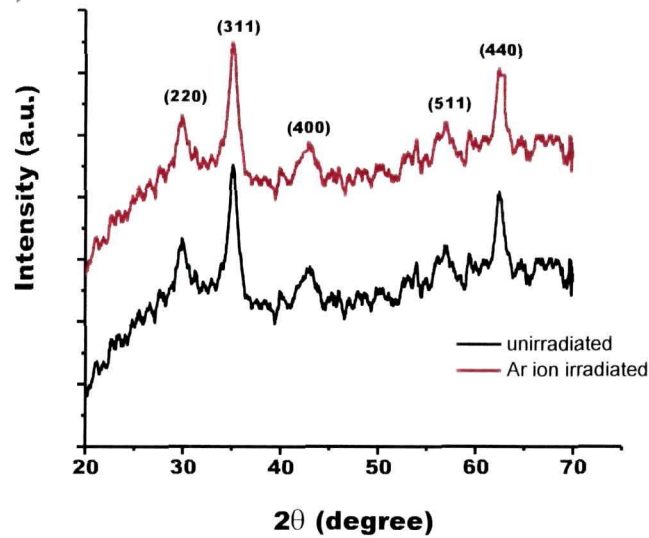


Fig.4.1: XRD pattern of unirradiated and Ar-ion irradiated Fe_3O_4

(220), (311), (400), (511) and (440) respectively. All these peaks were also evident for Ar-ion irradiated sample. The size of the particles, calculated by the Williamson–Hall equation (*referred to eq. 2.1 of chapter two*), remain same before and after irradiation (~ 8 nm). However, the same formula shows that there is a slight modification of the strain of the particle due to the irradiation. The strain for the unirradiated sample is measured as -7×10^{-2} , which changes to -7.7×10^{-2} after irradiation. The strain of a particle refers to the change viz. contraction, elongation of the atomic planes. During energetic ion irradiation point defects are created. These defects could alter the cationic distribution and produce stress/strain in the material.^[46] The observed variation in the micro strain is also attributed to the ion induced defects. In short, the basic inverse spinel structure of Fe_3O_4 and the average particles size remained practically same, although defects were formed due to the ion irradiation.

4.2.2. Transmission electron microscopy

The direct evidence of the dispersed MNPs in FFs were observed through transmission electron microscope. To perform this microscopic

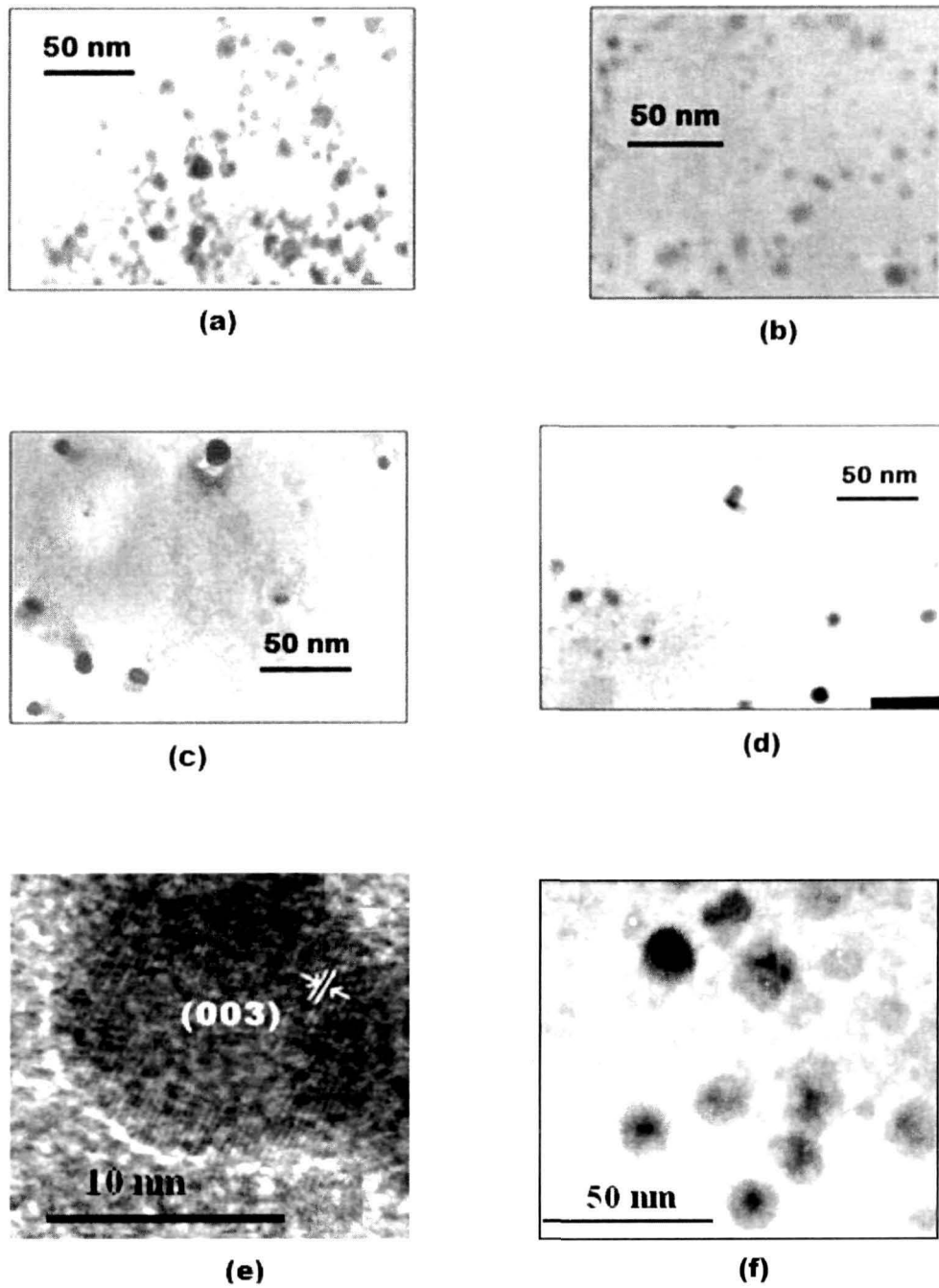


Fig.4.2: TEM micrograph of unirradiated (a) FFW, (c) FFK and (e) FFG (at high resolution). The image (b), (d) and (f) are the ferrofluids FFW, FFK and FFG respectively prepared with Ar-ion irradiated particles

study the FFs were first diluted with respective carrier fluids followed by ultra sonication. Then a drop of the sonicated ferrofluid was placed over a copper grid. The TEM micrographs of Fe_3O_4 based unirradiated ferrofluid with water (FFW) and kerosene (FFK) as carrier are shown in Fig 4.2 (a) and (c) respectively. The TEM image of the Gd_2O_3 based ferrofluid (FFG) is shown in Fig 4.2.(e). It was observed that the morphology of the particles were same before and after the irradiation. The spherical shape of the particles remains intact after the irradiation also. Similarly, the size of the dispersed particles was found $\sim 9\pm 3$ nm in the irradiated FFW and FFK and ~ 9 nm in FFG, indicating no variation in the dimension. Absence of clusters/agglomeration in the irradiated samples sustains the existence of the surfactant coating of the MNPs in spite of the energetic irradiation.

4.2.3. FT-IR spectroscopy

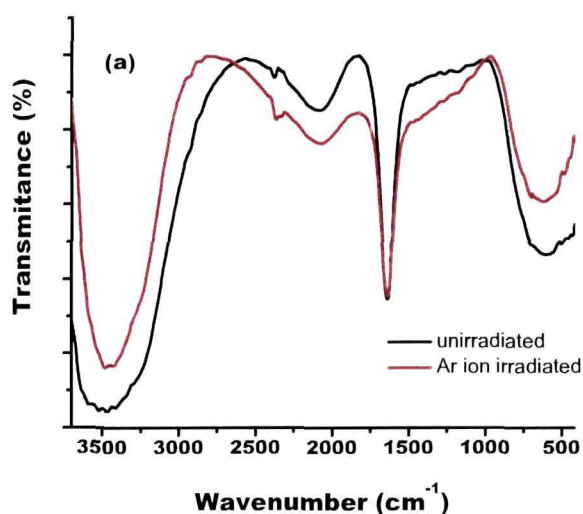


Fig.4.3(a): FT-IR spectra of FFW prepared with unirradiated and Ar ion irradiated particles

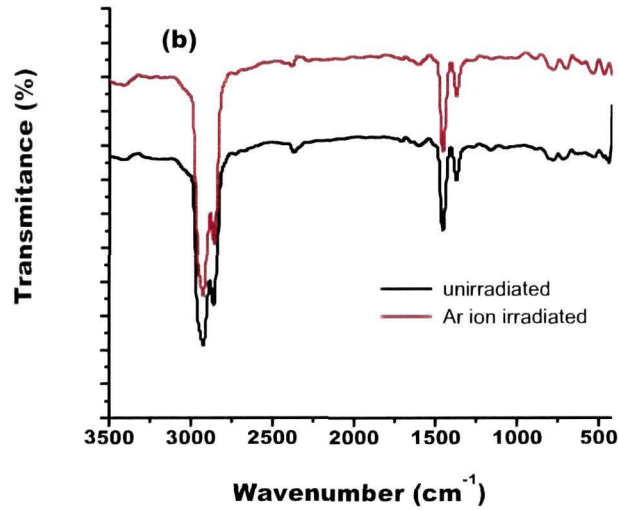


Fig.4.3 (b): FT-IR spectra of FFK prepared with unirradiated and Ar ion irradiated particles

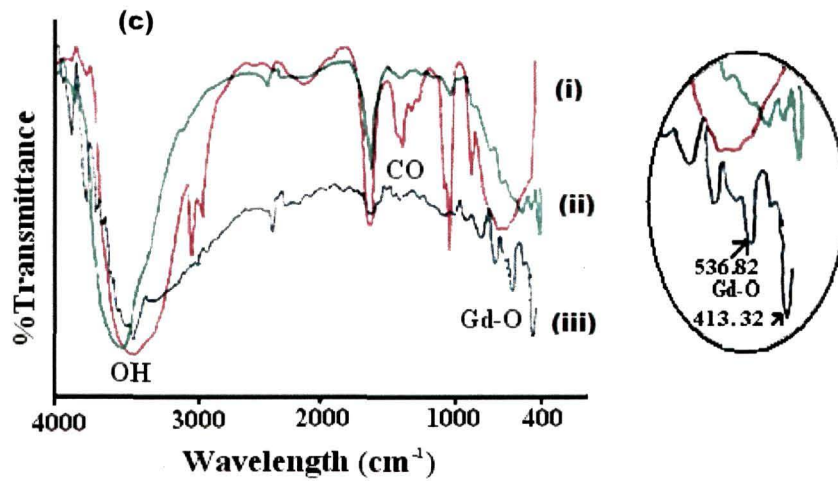


Fig.4.3.(c): FT-IR spectra of FFG [prepared with (i) unirradiated and (ii) Ar-ion irradiated particles] and (iii) ethanol as reference

An FT-IR spectrum provides information with regard to bending, bonding and stretching of molecules in a given compound. The vibrational modes generally occur at higher energies (high wavenumber) for organic compounds and at lower energies (low wavenumber) for inorganic compounds. Therefore, slight change in any aspect like the bonding energy, plane of vibration etc. due to external/internal perturbation will be traced out in the FT-IR spectrum of a compound. As shown in Fig 4.3 (a), (b) and (c) the ion irradiation to the MNPs lead to only variation in the characteristic peaks of the inorganic compounds of the respective FFs. No alteration or formation of new characteristics (e.g. Fe-O bending) peaks of all other constituent compounds in the three FFs also sustains the above statement. Absence of any peak relating Ar indicates no implantation of the ion in the MNPs. In order to study the impact of the energetic ion on the inorganic compounds of the FFs, we have to focus our attention in the lower wavenumber regions of these spectra. In case of Fe₃O₄ based FF with water as carrier [Fig. 4.3.(a)] it is noticed that though the peak representing the Fe-O stretching are present in both the unirradiated and irradiated sample, the range corresponding the vibration has changed. In the unirradiated one, the stretching vibrations are found in the wavenumber regions 620-566 cm⁻¹ and 510 – 445cm⁻¹. Instead of these, the FF after irradiation shows comparatively sharp peak in the wavenumber range 625-610 cm⁻¹ and one at 482 cm⁻¹. In the same way, in case of FFK, though the Fe-O stretching mode at 528.957 cm⁻¹ remains same, the small vibrations in between 440.725 cm⁻¹ and 481.155 cm⁻¹ appear as two distinct vibrations at 424.197 cm⁻¹ and 472.001 cm⁻¹. In the Gd₂O₃ based FF, Gd-O inplane vibrations at 536.8 and 413.3 cm⁻¹ become more prominent for irradiated Gd₂O₃ system than its unirradiated counterpart. Further, a close look on the unirradiated and irradiated FFG has revealed that apart from the prominent Gd-O vibrational peaks, splitting of peaks have also occurred in the later case. These above observations suggest that the nanoparticle surface has been modified

appreciably as a result of ion–matter interaction. It is possible that the point defects (e.g. oxygen vacancy) are created due to the energetic ion bombardment. Later, these defects can segregate to the particle surface causing some kind of distortion onto the regular lattice. The departure from the regular lattice site along with the segregated defects can result in prominent IR vibrations as evident in Fig 4.3(c). Further, a close look on the unirradiated and irradiated Gd_2O_3 nanoparticle samples has revealed that apart from the prominent Gd–O vibrational peaks, splitting of peaks have also occurred in the later case. These splitted peaks can be ascribed to the uneven distribution of surface defects, interstitials and inhomogeneties.

4.2.4. EPR spectroscopy

To substantiate further the speculation of creation of defect by the irradiation process the samples were characterized with another tool i.e. electron paramagnetic resonance technique. The room temperature EPR spectra of Fe_3O_4 and Gd_2O_3 nanoparticles recorded at X band (9.15 GHz) of the electromagnetic series and modulated at a field modulation of 100 kHz are depicted in Fig 4.4(i) and 4.4.(ii) respectively. As can be seen from Fig 4.4, though the spectra of the unirradiated and irradiated samples are symmetric in nature, have respective resonance fields centred at different positions in both the nanoparticles. The resonance fields in case of unirradiated and 80-keV Ar-ion irradiated Fe_3O_4 nanoparticle are measured as 306.66 mT and 309.06 mT respectively, whereas those for Gd_2O_3 nanoparticle are found as 310.3 and 311.6 mT. Similarly the associated g -values of Fe_3O_4 for unirradiated and irradiated are 2.1028 and 2.1096. The g -value 2.10802 of Gd_2O_3 becomes 2.09874, after ion irradiation. As the resonance shift for both the nanoparticles (2.4 mT for Fe_3O_4 and 1.3 mT for Gd_2O_3) are larger than the scanning step (0.6 mT), we predict a clear variation in the interaction parameter of the isolated

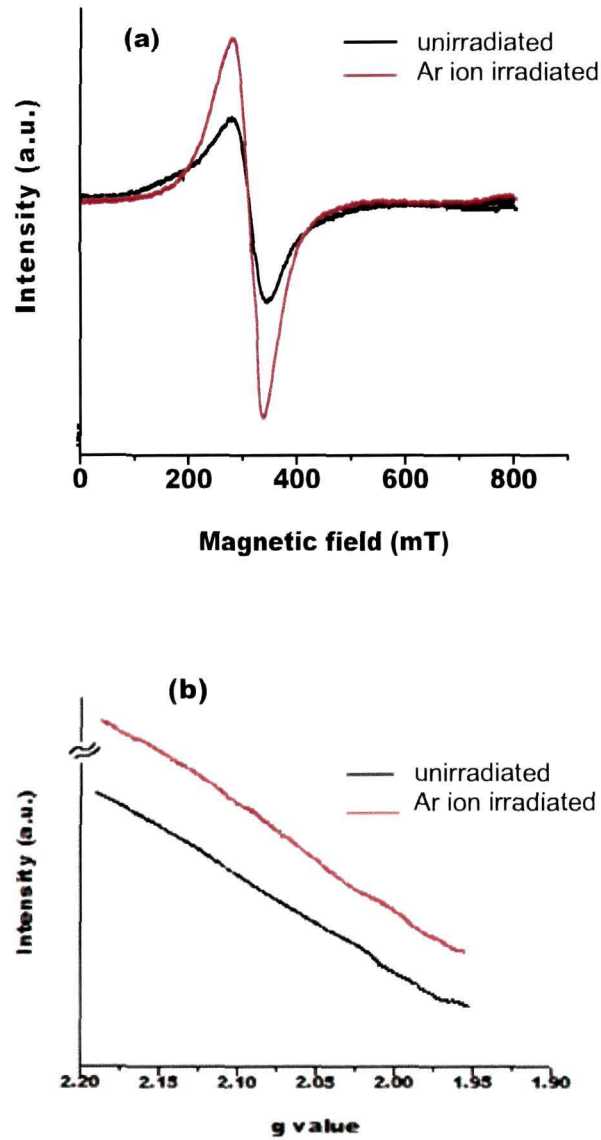


Fig.4.4(i): EPR spectra of unirradiated and irradiated Fe_3O_4 nanoparticles with respect to the variation of (a) magnetic field and (b) g -values

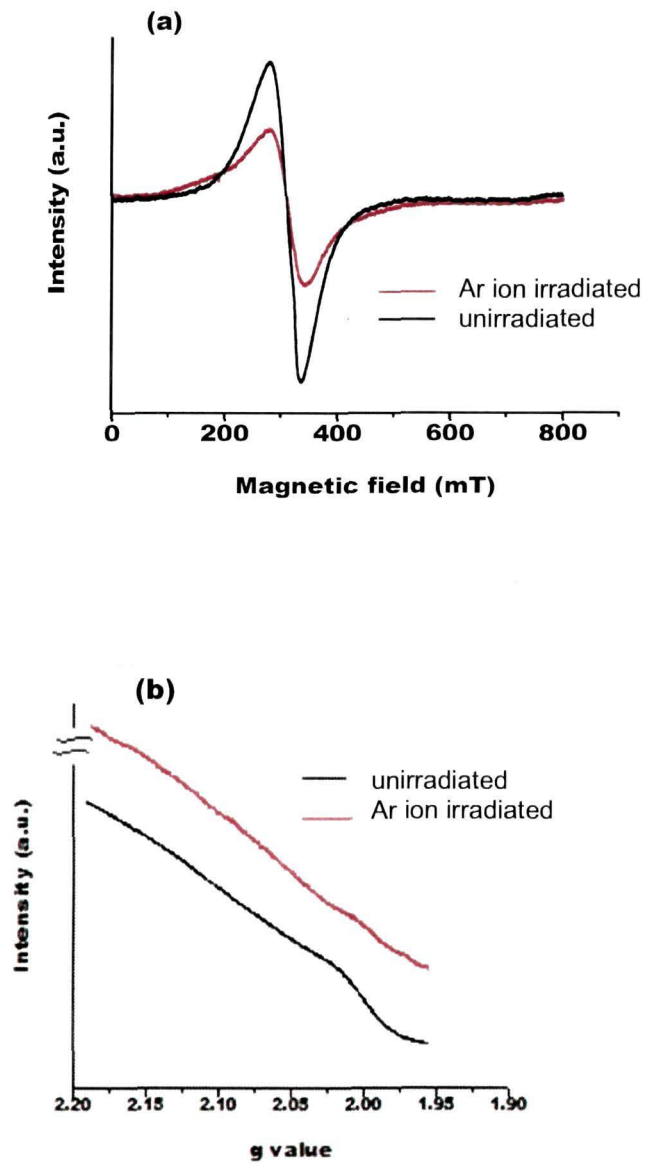


Fig.4.4(ii): EPR spectra of unirradiated and irradiated Gd_2O_3 nanoparticles with respect to the variation of (a) magnetic field and (b) g - values

electron spins arising from the prominent defect centers of the irradiated system. Generally, EPR spectra are influenced by the presence of defect centers, but the position of the defect also plays an important role in determining the physical properties of the system. If the defect is placed symmetrically surrounded by a cluster of atoms in a representative system, then it gives rise to an isotropic EPR signal around the g -value of the free electron.^[47] Previously, it was reported that location of different kinds of surface defects (edge, terrace, corner of the islands, etc.) could influence the spectra and for the point defects at the edge gives symmetric spectra with no additional doublet.^[48] EPR signal variation owing to modified electron contribution is also apparently visible in Fig.4.4.i(b) and Fig.4.4.ii(b). We attribute the symmetric spectra with the presence of surface defects (chiefly, oxygen vacancies) created as a result of keV ion impact.

4.2.5 Raman spectroscopy

The room temperature micro Raman spectra of Fe_3O_4 and Gd_2O_3 nanoparticles are shown in Fig.4.5 (a) and (b) respectively. The above figures exhibited the Raman spectra of unirradiated one and the influence of Ar ion on the nanoparticle in terms of Raman spectra. Fig.4.5(a) clearly indicate that all the five characteristic Raman peak as predicted by the space group theory (*refer to Chapter 2*) are also prominent after irradiation of the Fe_3O_4 nanoparticles. The narrowing and decrease in intensity of the peak T_{2g}^2 and A_{1g} after irradiation are observed. There is also a slight change in the peak position of the T_{2g}^3 , T_{2g}^2 and A_{1g} mode of the irradiated nanoparticle with respect to that of the unirradiated one. The T_{2g}^3 , T_{2g}^2 and A_{1g} peak shifted from 270.194 cm^{-1} , 581.008 cm^{-1} and 659.610 cm^{-1} to 271.866 cm^{-1} , 583.008 cm^{-1} and 651.253 cm^{-1} after ion irradiation. Raman spectrum is related with degree of crystallinity. Magnetite crystallizes in inverse spinel system with the Fe^{3+} and Fe^{2+} ions in the ratio 2:1. They occupy the tetrahedral and octahedral site coordinated with oxygen.

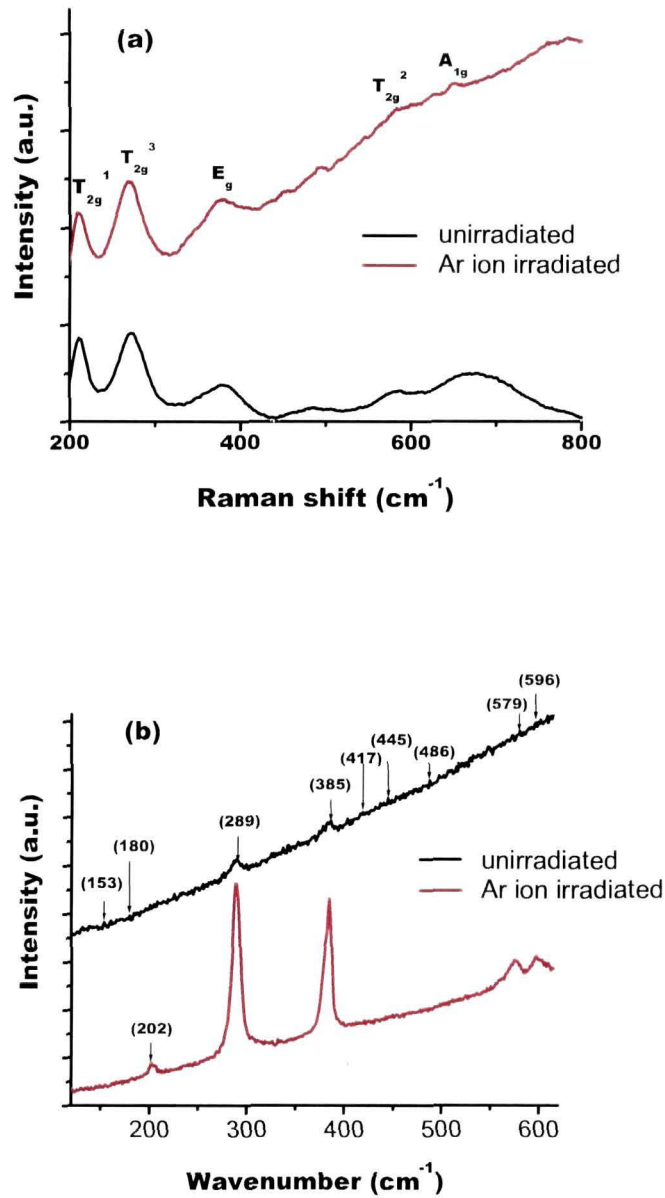


Fig.4.5: Raman spectra of unirradiated and irradiated (a) Fe₃O₄ and (b) Gd₂O₃ nanoparticles

Earlier it was reported that the variation in linewidth of the A_{1g} mode is related with the static electronic disorder due to the random arrangement of Fe^{2+} and Fe^{3+} cations in the B (octahedral) sites and the dynamic disorder due to the hopping of polarons from Fe^{2+} and Fe^{3+} sites.^[49] In our case, we speculate that the Ar ion irradiation leads to formation of defects in terms of either oxygen vacancy or dislocation. As a result, strain between the atomic planes may also altered. The newly created defects alter the iron and oxygen atom coordination along with the Fe^{3+} and Fe^{2+} environment. This is manifested as the peak broadening and slight variation in the peak positions.

As shown in Fig.4.5 (b), the irradiated sample of Gd_2O_3 has revealed a spectrum with broadened line-width, and enhanced intensity. The FWHM of the two most prominent Raman peaks (B_g modes) at 288 cm^{-1} and 384 cm^{-1} have increased from 7.68 cm^{-1} to 9.36 cm^{-1} and from 6.14 cm^{-1} to 10.41 cm^{-1} , respectively. In addition, two other A_g modes, located at 575 cm^{-1} and 595 cm^{-1} were characterized by FWHM values of 10 cm^{-1} and 8 cm^{-1} , respectively. It is expected that the energetic ion irradiation has led to the creation of point defects or, some kind of surface disorder in case of irradiated nanoscale Gd_2O_3 particles. Previously, it was advocated that the peak broadening is related with the phonon confinement and dispersion effect.^[50] Here, the minor red shift of the aforesaid (four) peaks at 288 cm^{-1} , 384 cm^{-1} , 575 cm^{-1} and 595 cm^{-1} are assigned with the weak dispersion of the phonon modes. The spectrum of the irradiated sample is also manifested by improved intensity response of these four peaks at the expense of other modes. We assign this observation to the irradiation led lattice disorder in the nanoscale system, which has also been predicted in an earlier work of oxide system.^[51] In addition, evolution of a new peak at 202 cm^{-1} in case of irradiated Gd_2O_3 system is expected to be the outcome of invariable superimposition of A_g and B_g modes in confined region. In the monoclinic phase of Gd_2O_3

(unirradiated) though this peak was not observed, for cubic structure (C-type) a weak satellite peak, observable at $\sim 198 \text{ cm}^{-1}$ is attributed to A_g mode.^[52] Another group has reported the phase transformation of $\sim 30 \text{ nm}$ Gd_2O_3 particles from C (cubic) \rightarrow B (monoclinic) by 30-keV O-ions.^[53] In contrary, in the present case, the appearance of the new peak (202 cm^{-1}) indicated a partial phase transformation from B-type to C-type. Note that, the electronic and nuclear energy losses of 30-keV O-ions in Gd_2O_3 are 0.291 eV/\AA , 0.213 eV/\AA ; respectively.^[54] Conversely, 80-KeV Ar-ions have respective energy losses limited to 0.539 eV/\AA and 0.858 eV/\AA . In other words, nuclear energy loss over electronic energy loss is more dominant in our case. We speculate that, the existence of the new peak could be due to structural reorganization leading to partial phase transformation on the nanoparticle surfaces though a complete phase-transformation was highly undesirable.

4.2.6. Magneto-optic effects

(i) Faraday rotation response

Faraday rotation (FR) is a measure of the rotation of a plane polarized light due to the field induced birefringence. As discussed in *Chapter 3*, Faraday rotation exhibited by FF is not only a measure of light matter interaction but also it gives information of the chaining effect. Basically, FR of a ferrofluid is dependent on the magnetization at a particular field, saturation magnetization and the chain length. From the figures [Fig.4.6 (a), (b) and (c)], it is clear that FR of any ferrofluid is also effected by ion irradiation. It can be seen that the FR gets enhanced for the FFs prepared with 80-keV Ar-ion irradiated nanoparticles compared to the unirradiated samples. The polynomial fit of measured rotation for the FFs indicate that similar to the respective unirradiated sample, the FR first increases with field and then tends to saturate at higher magnetic field. In case of FFG, the degree of enhancement of FR is comparatively less than that of FFW and FFK.

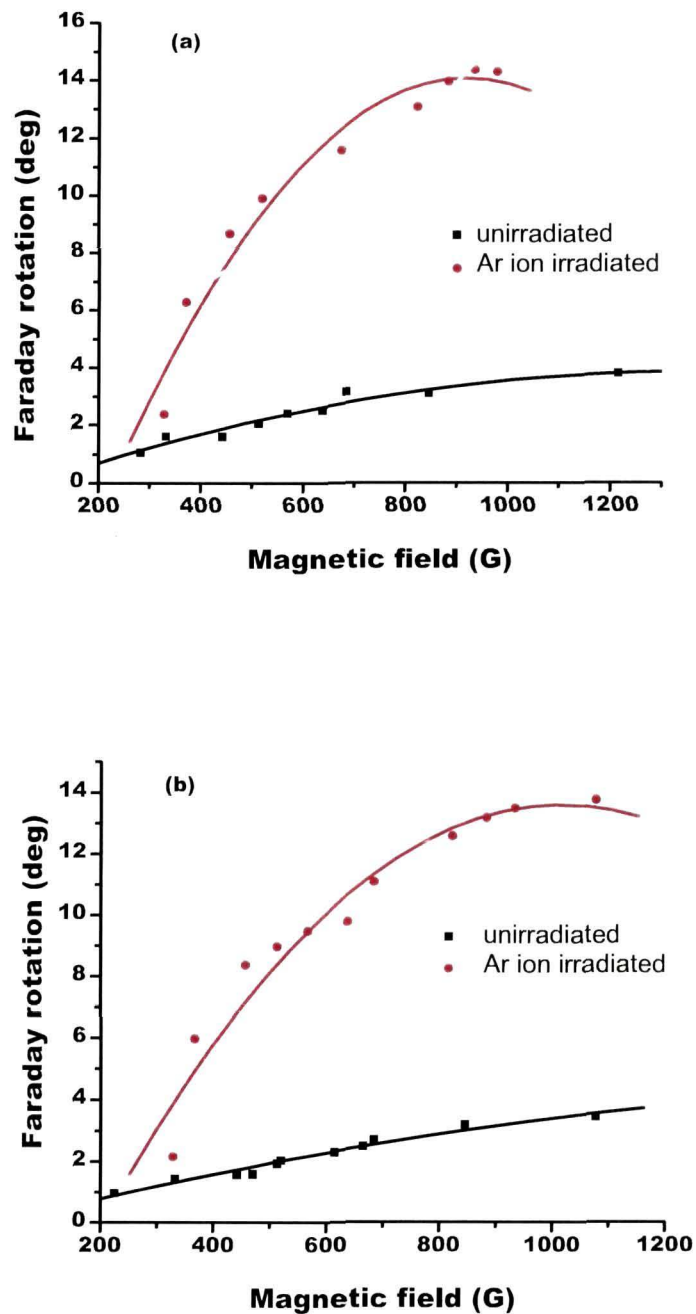


Fig.4.6: Faraday rotation of (a) FFW and (b) FFK. FFs are prepared with unirradiated and Ar-ion irradiated particles

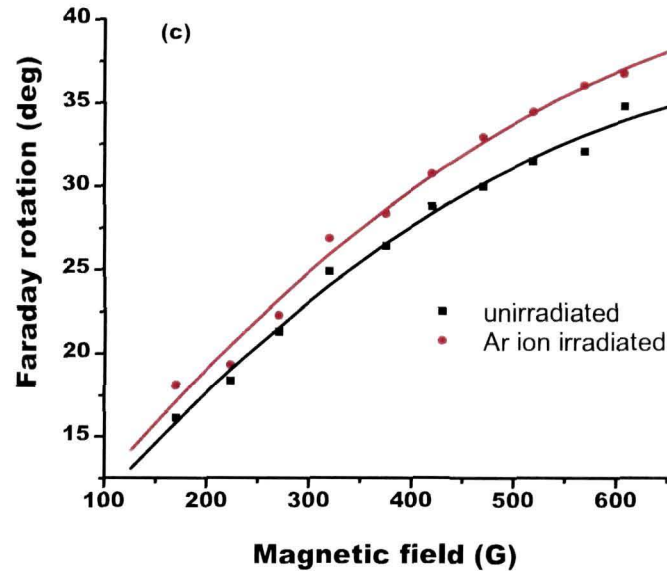


Fig.4.6(c): Faraday rotation of FFG prepared with unirradiated and Ar-ion irradiated particles

Different characterization tools e.g. XRD, TEM, FT-IR, EPR and Raman spectroscopy reveal that there is no modification in the morphological aspects of the Fe_3O_4 and Gd_2O_3 nanoparticles upon 80-keV Ar^+ irradiation. Upon irradiation, the shape and size of the nanoparticles were found to remain similar with the unirradiated ones. This fact also discards the possibility of increase of FR due to the irradiation induced growth of the nanoparticles. Irradiation induced defects formation on the nanoparticles surface is confirmed by the characterization tools. Defect segregation to the grain boundaries of the nanoparticles is also possible. Now, the ordering pattern of different ions (eg. Fe^{2+} and Fe^{3+} in magnetite) may be affected upon the formation of the defects. The oxygen stoichiometry in the oxide system is also modified by the defects. There is also possibility that newly formed defects within a nanoparticle can give rise to significant lattice strain and can affect the original strain of the particle. The lattice strain of the unirradiated and ion irradiated magnetite

nanoparticles as calculated by W-H plot supports this fact. Earlier reports reveal that the lattice strain influences the transport properties in nano/micro wires of transition metal oxide.^[55] Lattice strain can distort or enlarge the bond length or bond angles between various atoms, which in turn affects the electronic and magnetic properties of the material.^[55] We expect that the ion irradiation induced defects as well as strain are accountable for the observed enhancement in Faraday rotation of the FFs. The optical path within the nanoparticles increases due to the defects.

Rare-earth oxides are more stable than other metal or semiconductor oxide system. It is difficult to alter the internal/external structure of a stable system by any external perturbation. Thus new defects can be created in Fe_3O_4 with greater ease than Gd_2O_3 . It is contemplated that the energetic Ar-ion would create/rearrange more defects in the Fe_3O_4 nanoparticles than the Gd_2O_3 . This is manifested as the larger improvement of the FR in Fe_3O_4 based FF than that of Gd_2O_3 based FF.

(ii) Linear dichroism response

Linear dichroism is another important magneto-optic effect exhibited by FFs. As discussed in *chapter 3*, it arises from the interaction between light and matter in presence of an applied magnetic field. Figure 4.7(a), (b) and (c) show the intrinsic LD of FFW, FFK and FFG before and after 80-keV ion irradiation. It is evident the LD of the FFs were greatly influenced by the ion irradiation. Unlike the FR (got enhanced after irradiation) of the FFs, that LD decreases upon irradiation. The enhancement of FR upon irradiation can be described on the expectation ground of formation of point defects in the nanoparticles as a result of irradiation. The defect formation is anticipated from different characterization mechanisms. Hence, these defects are expected to be the origin of the variation of this magneto-optic effect of the same FFs. The

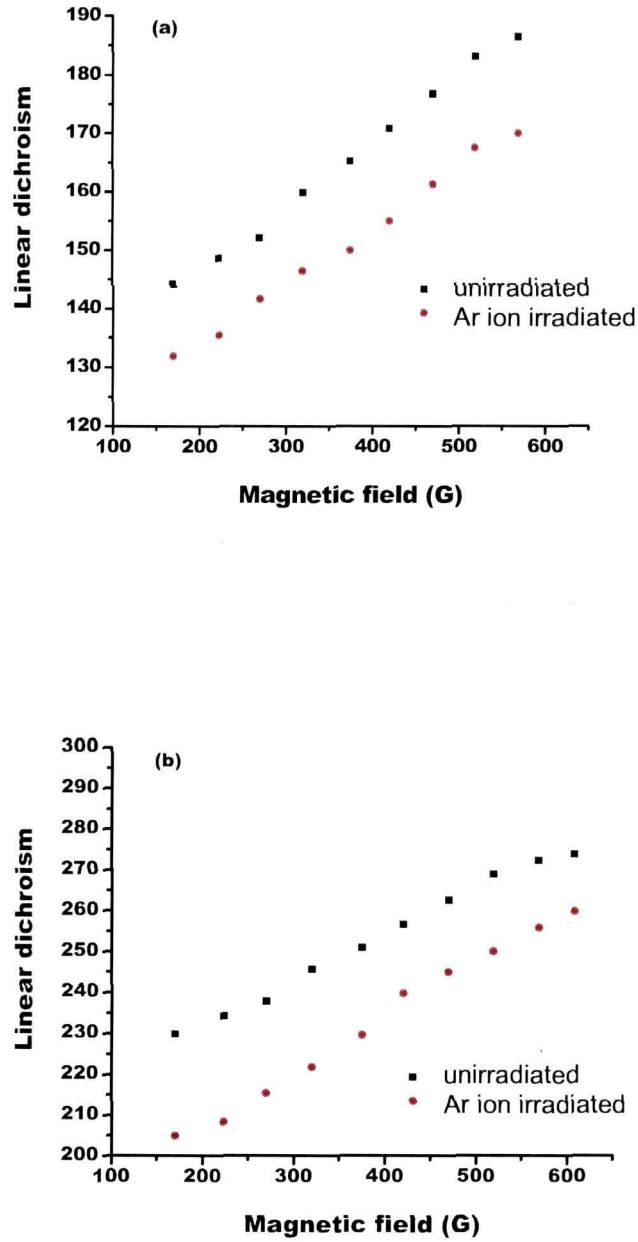


Fig.4.7: Linear dichroism of (a) FFW and (b) FFK. FFs are prepared with unirradiated and Ar-ion irradiated particles

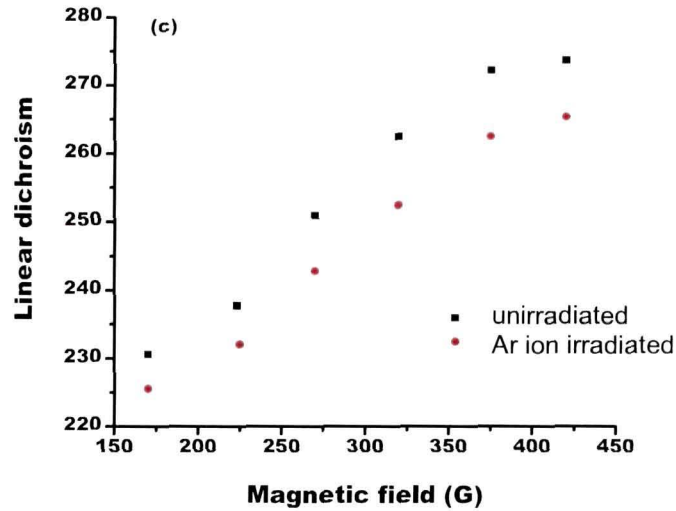


Fig.4.7(c): Linear dichroism of FFG prepared with unirradiated and Ar-ion irradiated particles

LD of FFs arises due to the optical anisotropy. The oscillating dipole interaction between particles give rise to an optical anisotropy. More precisely, the shape anisotropy caused by the chain formation directs to the LD in any FF. Earlier reports show that presence of defects influence the magnetic anisotropy of a material.^[55,56] In some instances magnetic anisotropy increases, whereas in some other occasions it is just the reverse. The enhancement or decrement of anisotropy depends on the type of defects. In general creation of vacancy defects increase anisotropy, while antisites defects leads to the decrease in anisotropy values.^[56] In the present situation, it is considered that upon irradiation led reshuffling of the ions some cationic antisites were developed within the nanoparticles. Surface magnetic anisotropy leads to optical anisotropy. Specially, in Fe_3O_4 the Fe^{3+} and Fe^{2+} interchanged their position between the A and B sites after irradiation. Magnetic anisotropy also affects the magnetic dipole moment of the particle. Due to the variation in the

magnetic anisotropy, the dipole moment may be obstructed to freely rotate along the changing direction. As a result, the electric field between oscillating dipole moment of particles is also impinged. Therefore, the LD of the FFs gets lower after irradiation.

4.3. Concluding remarks

As evident from different characterization techniques, the 80-KeV Ar-ion irradiation could induce point defects on the surfactant coated Fe_3O_4 and Gd_2O_3 nanoparticles. Further, it was observed that ion irradiation may lead to a partial transformation of Gd_2O_3 nanoparticles from B-type to A-type crystal system. The effect of low energy ion irradiation was also prominent in the MO responses of the FFs. The Verdet constant of FFs as prepared with the ion irradiated nanoparticles show a maximum enhancement upto ~10 % (in case of FFW). The observed variations in MO responses were attributed to modulation in the optical path lengths owing to irradiation led defect creation/annihilation.

References:

- [1] Dong, N. et al. Characterization of active waveguides fabricated by ultralow-fluence swift heavy ion irradiation in lithium niobate crystals, *J. Phys. D: Appl. Phys.* 44, 105103-105107, 2011.
- [2] Bayan, S. and Mohanta, D. Unusual rectifying response of nanojunctions using randomly oriented nanorods (RON) of ZnO irradiated with 80 MeV oxygen ions, *J. Electro. Mater.*, 41,1955-1961, 2012.
- [3] Som, T. and Kanjinal, D. (eds.) Nanofabrication by ion-beam sputtering: fundamentals and applications, Pan Stanford, 2012.
- [4] Fasce, L. et al. Effect of nitrogen ion irradiation on the nano-tribological and surface mechanical properties of ultra-high molecular weight polyethylene, *Surf. Coat. Technol.*204, 3887–3894, 2010.

[5] Buljan, M. et al. Generation of an ordered Ge quantum dot array in an amorphous silica matrix by ion beam irradiation: Modeling and structural characterization, *Phys. Rev. B.* 81, 085321-085330, 2010.

[6] Husinsky, W. et al. Z-scan study of nonlinear absorption of gold nanoparticles prepared by ion implantation in various types of silicate glasses, *Opt. Commun.* 285, 2729–2733, 2012.

[7] Ridgway, M.C. et al. Changes in metal nanoparticle shape and size induced by swift heavy-ion irradiation, *Nucl. Instr. & Meth. in Phys. Res.* 267, 931–935, 2009.

[8] Bayan, S. and Mohanta, D. Development of ZnO nanorods: Effect of nitrogen ion irradiation on luminescence and structural evolution, *Phys. Stat. Sol.A.* 207, 1859-1863, 2010.

[9] Tinchev, S.S. Surface modification of diamond-like carbon films to graphene under low energy ion beam irradiation, *Appl. Surf.Sci.* 258, 2931–2934, 2012.

[10] Akihiko, N. et al. Dependence of ion energy on PTFE surface modification effect by nitrogen ion irradiation, *IEEJ Tran. Fundam. Mater.* 130, 331-336, 2010.

[11] Nakajima, Y. et al. Enhancement of critical current density in Co-doped BaFe₂As₂ with columnar defects introduced by heavy-ion irradiation, *Phys. Rev. B.* 80, 012510-012513, 2009.

[12] Lehtinen, O. Effects of ion bombardment on a two-dimensional target: Atomistic simulations of graphene irradiation, *Phys. Rev. B.* 81, 153401-153403, 2010.

[13] Lehtinen, O. et al. Characterization of ion-irradiation-induced defects in multi-walled carbon nanotubes, *N.J. Phys.* 13, 073004-073013, 2011.

[14] Compagnini, G. et al. Ion irradiation and defect formation in single layer graphene, *Carbon*, 47, 3201-3207, 2009.

- [15] Ronning, C. et al. Ion beam doping of semiconductor nanowires, *Mater. Sci. Eng. R.* 70, 30–43, 2010.
- [16] Gan, J. et al. Kr ion irradiation study of the depleted-uranium alloys, *J. Nucl. Mater.* 407, 48–54, 2010.
- [17] Sprouster, D. J. Ion-irradiation-induced amorphization of cobalt nanoparticles, *Phys. Rev. B.* 81, 155414-155421, 2010.
- [18] Backman, M. , et al. Amorphization of Ge and Si nanocrystals embedded in amorphous SiO₂ by ion irradiation, *Phys. Rev. B.* 80, 144109- 144120, 2009.
- [19] Sakamaki, M. et al. Perpendicular magnetic anisotropy in a Pt/Co/Pt ultrathin film arising from a lattice distortion induced by ion irradiation, *Phys. Rev. B.* 86, 024418-024422, 2012.
- [20] Shukla, D.K. et al. Swift heavy ion irradiation induced magnetism in magnetically frustrated BiMn₂O₅ thin films, *Phys. Rev. B.* 82, 174432 - 174440, 2010.
- [21] Jaafar, M. et al. Pattern-induced magnetic anisotropy in FePt thin films by ion irradiation, *Phys. Rev. B.* 83, 094422-094428, 2011.
- [22] Bernes, H. *Material science with ion beams*, Springer-Verlag, 2010.
- [23] Hellborg R., Whitlow H.J. and Zhang Y. (eds.), *Ion beams in nanoscience and technology*, Springer, Berlin 2009.
- [24] Avasthi, D.K. and Mehta, G.K. *Swift heavy ions for materials engineering and nanostructuring*, Springer, India, 2011.
- [25] Rabalais, J.W. *Principles and Applications of Ion Scattering Spectroscopy: Surface Chemical and Structural Analysis*, Wiley InterScience: Hoboken, NJ, 2002.
- [26] Das, U. Development of Binary semiconductor elongated nanopatterns by energetic ion irradiation/photon illumination for optoelectronics/photonics application, Ph.D. thesis, 2010.
-

- [27] Sigmund, P. Elements of sputtering theory, *PSP Rev.* 9.75in x 6.5in, 1-29, 2011.
- [28] Gnaser, H. *Low energy ion irradiation of solid surface*, Springer, Verlag, Berlin, Heidelberg, 1999.
- [29] Paul, N., Devi, M. and Mohanta, D. Synthesis, characterization and effect of low energy Ar ion irradiation on gadolinium oxide nanoparticles. *Mater. Res. Bull.*46, 1296–1300, 2011.
- [30] Krasheninnikov, A. V. and Krasheninnikov, A. V. Ion and electron irradiation-induced effects in nanostructured materials, *J. Appl. Phys.* 107, 071301 – 071301, 2010.
- [31] Chappert et al. Planar Patterned Magnetic Media Obtained by Ion Irradiation, *Sci.* 280,1919-1922,1998.
- [32] Bernas, J.P. et al. Ordering Intermetallic Alloys by Ion Irradiation: A Way to Tailor Magnetic Media, *Phys. Rev. Lett.* 91, 077203-077205, 2003.
- [33] Fassbender, J. et al. Tailoring magnetism by light-ion irradiation, *J. Phys. D: Appl. Phys.* 37, R179–R196, 2004.
- [34] Prakash, J. et al., Ion beam induced interface mixing of Ni on PTFE bilayer system studied by quadrupole mass analysis and electron spectroscopy for chemical analysis, *Vacuum*,84 , 1275–1279,2010.
- [35] Neubauer, M. et al. Ion-beam mixing of Ag/Fe and In/Fe layers studied by hyperfine techniques, *Phy. Rev. B*, 53, 10237-10243,1996.
- [36] Xiao, J. Q. et al. Effect of Ar-ion implantation and annealing on structural and magnetic properties of Co/Pt multilayers, *J. Appl. Phys.* 76, 6081-6084,1994.
- [37] Chang, G. S. et al. Realization of a Large Magnetic Moment in the Ferromagnetic CoPt Bulk Phase, *Phys. Rev. Lett.* 87, 067208-0672011, 2000.
- [38] Devolder, T. Light ion irradiation of Co/Pt systems: Structural origin of the decrease in magnetic anisotropy, *Phys. Rev. B.* 62, 5794-5802, 2000.
-

- [39] Manabu, I. et al. Ion-beam-induced chemical disorder in GaN, *J. Appl. Phys.* 106, 053513 - 053513, 2009.
- [40] D'Orléans, C. et al. Anisotropy of Co nanoparticles induced by swift heavy ions, *Phys. Rev. B.* 67, 220101 (R) -220104(R), 2003.
- [41] Chang, L. V. et al. Graded bit patterned magnetic arrays fabricated via angled low-energy He ion irradiation, *Nanotechnol.* 23, 275705-275708, 2012.
- [42] S. Bayan and D. Mohanta, Interplay of native defect-related photoluminescence response of ZnO nanosticks subjected to 80 keV Ar ion irradiation, *Rad. Effect. & Def. Sol.* 166, 884–893, 2011.
- [43] Panigrahy, B. et al. Controlled optical and magnetic properties of ZnO nanorods by Ar ion irradiation, *Appl. Phys. Lett.* 98, 183109-183111, 2011.
- [44] Peruško, D. et al. Formation of intermetallics by ion implantation of multilayered Al/Ti nano-structures, *Nucl. Instr. and Method. in Phys. Res.* 282, 4–7, 2012.
- [45] Aitkaliyeva, A. and Shao, L. The production of amorphous regions in carbon nanotubes by 140 keV He ion irradiation, *Carbon*, 50, 4680–4684, 2012.
- [46] Dolia, S.N. et al. Magnetic behaviour of nanocrystalline Ni–Cu ferrite and the effect of irradiation by 100 MeV Ni ions, *Curr. Appl. Phys.* 8, 620–625, 2008.
- [47] Sterrer, M. et al. Geometric characterization of a singly charged oxygen vacancy on a single-crystalline MgO(001) film by electron paramagnetic resonance spectroscopy, *Phys. Rev. Lett.* 94, 186101-186104, 2005.
- [48] Wertz, E. et al. Electron spin resonance of *F* centers in magnesium oxide; confirmation of the spin of magnesium-25, *Phys. Rev.* 107, 1535-1537, 1957.
- [49] Gupta, R. et al. Raman study of stoichiometric and Zn-doped Fe₃O₄, *Phys. Rev. B.* 65, 104430-1044387, 2002.
-

[50] Luyer, C.L. et al. Waveguide Raman spectroscopy of sol-gel Gd₂O₃ thin films *J. Raman Spectrosc.* 34, 234-239, 2003.

[51] Ye, J.D. et al. Raman active Fröhlich optical phonon mode in arsenic implanted ZnO, *Appl. Phys. Lett.* 94, 011913-011915, 2009.

[52] Gouteron, J. et al. Raman spectra of lanthanide sesquioxide single crystals: Correlation between A and B-type structures, *J. Solid State Chem.* 38,288-296, 1981.

[53] Antic, B. et al. Effects of O²⁺ ions beam irradiation on crystal structure of rare earth sesquioxides, *Appl. Surf. Sci.* 255, 7601-7604, 2009.

[54] Ziegler, J.F., Ziegler, M.D. and Biersack, J.P. The stopping range of ions in matter, SRIM 2008.ETDEWEB ID: 21247053.

[55] Cao, J. and Wu, J. Strain effects in low-dimensional transition metal oxides, *Mater. Sci. Eng.*R71, 35–52, 2011.

[56] Shen, L. et al. The effect of introduced defects on saturation magnetization and magnetic anisotropy field of L1₀FePt, *IEEE trans. Magn.* 47, 2422-2424, 2011.

5.1. Gamma (γ) irradiation

A brainchild of NASA in 1960s, the discovery of ferrofluid was a great achievement for the scientific community related with space research. Ferrofluid gets to the bottom of many unsolved problem faced by space shuttles due to its behaviour as normal liquid without an applied field and as a magnetic liquid in presence of an applied magnetic field. With a frequency larger than the X-rays, gamma (γ) –radiation is regarded as the most energetic electromagnetic radiation. Compared to α and β rays, γ rays possess highest penetrating power without any divergence. Typically, γ -rays have energy more than 100 keV and wavelength less than 10 picometers with frequency above 10^{19} Hz. The high energetic γ - radiation is found to be abundant in the space and is believed to be major cause of the magnetic fields of many extra-terrestrial objects.

γ -radiation interacts with atoms and charged species while traversing through matter. When γ - ray falls on a surface, the total absorption of the radiation by the surface decays exponentially. The absorption probability is a function of thickness, density and absorption cross section of the surface. The intensity of the absorbed radiation at a distance x from the incident surface can be expressed as:

$$I(x) = I_0 e^{-\mu x} \quad (5.1)$$

Here, $\mu = n\sigma$ is the absorption coefficient with n as the total number of atoms per unit area of the surface and σ as the absorption coefficient.

The penetration of γ -radiation through matter is characterized by ionization through either photoelectric effect, Compton scattering or pair production.^[1] In photoelectric effect, an electron is knocked out from the surface as a result of incidence of γ -radiation. In such process, the γ -photon interaction transfer its energy to an atomic electron and ultimately the electron comes out with energy equal to the energy of the incident photon minus binding energy of the electron. In case of γ -photon with intermediate energy (~ 100 keV to 10 MeV), the ejection of electron is

accompanied by emission of a new γ -radiation. The newly emitted γ -photon possess energy less than the incident one and its emission direction is different from that of the first one. To be specific, this is called Compton scattering. γ -photon with much higher energy (exceeding 1.02 MeV) undergoes another mechanism during interaction with matter. Such a high energetic γ -photon interacts directly with the electric field of the nucleus and its energy converts into the mass of an electron-positron pair. If there still remains some extra energy beyond the equivalent rest mass of the pair produced, it appears as the kinetic energy of the pair and recoil of the emitting nucleus.

A number of reports highlighting application of γ -irradiation on matter are extensively found in literature.^[2-4] γ -irradiation has mixed impact on different materials. In material science, γ -radiation has been widely used for the creation of point defects.^[5-7] An earlier report shows that, a high dose γ -radiation could lead to the production of second order point defects.^[8] In general, Ge related defects in Ge doped SiO_2 was induced during the synthesis process. γ -irradiation could also produce such defects. These γ -ray induced defects were found to be photo-sensitive, furnishing a novel basis for photo-sensitive pattern writing through ionizing radiation.^[9] There are reports on the effect of γ -radiation on the lasing performances of Nd, Cr:GSGG (Cr^{3+} -doped gadolinium scandium gallium garnet) crystals. It was demonstrated that these crystals could retain high threshold stability for laser damage upto γ -ray doses of 1MGy.^[10] However, on exposure of such radiation, colour centres were induced and strengthening thereby fluorescence property.^[11] Previously, Mak *et al* have observed shifting of photoluminescence (PL) peak after γ -irradiation in ZnSe crystals.^[12] They have correlated the peak-shifting with the band-gap variation and ascribed it to radiation stimulated solid state recrystallization and accumulation of point defects. In RE-doped alkaline earth sulphates, the effect of γ -irradiation was shown to influence their lattice parameters

and luminescence patterns.^[13] The mechanical properties of composites fabricated from γ -radiation induced polyethylene, polypropylene and jute fabric were found to be increased significantly in comparison to their un-irradiated counterpart.^[14] Gamma irradiation is widely used in the field of medical sciences. A new approach of γ -irradiation has accelerated the concept of drug delivery from ferrofluids with great precision and control.^[15] Now a days, composites of inorganic and organic materials such as, hydroxyapatite/collagen are used in artificial bone substitutes. Common sterilization methods such as autoclave are not appropriate for hydroxyapatite/collagen composite. γ -irradiation is a comparatively new approach used for clinical sterilization. It was reported that the γ -ray irradiation of hydroxyapatite/collagen resulted in accelerated degradation by collagens.^[16] In food science, γ -irradiation is used as an alternative method of food decontamination. It is highly effective in inactivating microorganisms in foods. In ready to use tamarind juice, the antioxidant potential was shown to be improved and glucose and fructose remained unaltered after γ -irradiation.^[17]

5.2. γ -irradiation on ferrofluid (FFW, FFK and FFG) systems

Each of the as-prepared ferrofluids were taken in sealed containers and exposed in a γ -chamber with a γ -source (^{60}Co). The source is capable of emitting photons with an average energy of 1.25 MeV at a select dose rate of 1.8 Gy/s. Keeping in mind the amount of doses used by earlier workers, we have first selected five doses i.e. 32, 97, 292, 878 and 2635 Gy for irradiation purpose. On the basis of the characteristic results later, we studied the magneto-optic and other spectroscopic properties of FFW, FFK and FFG considering two specific doses of 878 Gy and 2.635 kGy.

5.2.1. Transmission electron microscopy

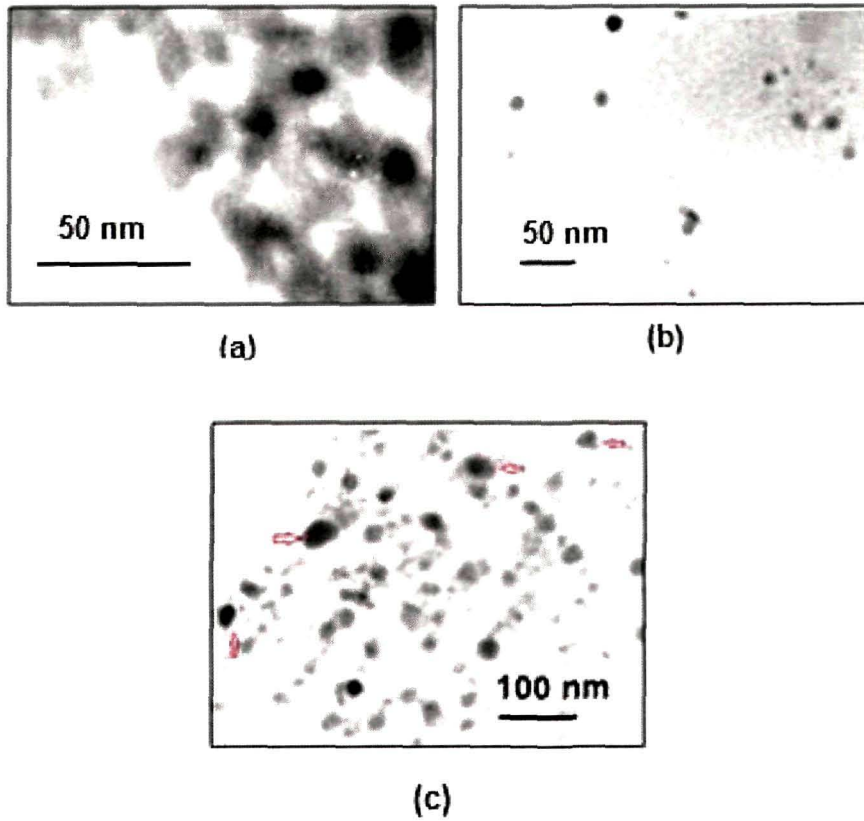


Fig.5.1(i): TEM micrograph of (a) unirradiated and irradiated FFW with dose (b) 878 Gy, (c) 2.635 kGy

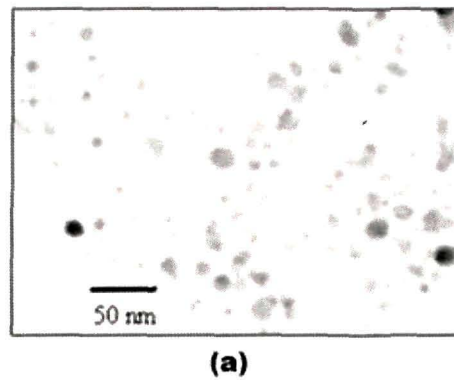


Fig.5.1(ii) (a): TEM micrograph of unirradiated FFK

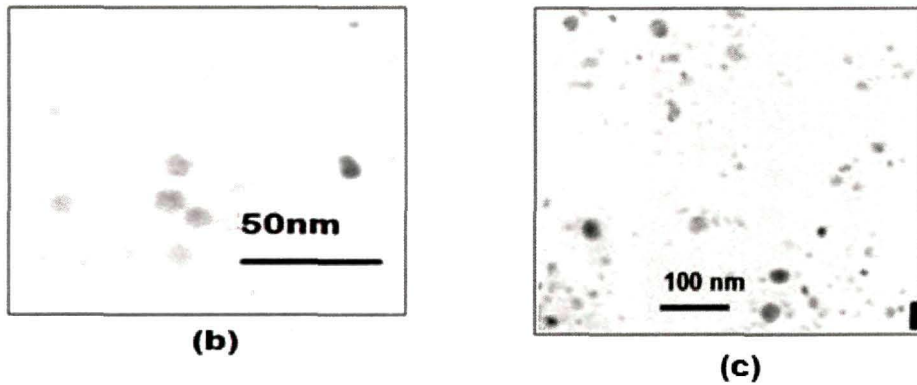


Fig.5.1(ii): TEM micrograph of irradiated FFK with dose (b) 878 Gy, (c) 2.635 kGy

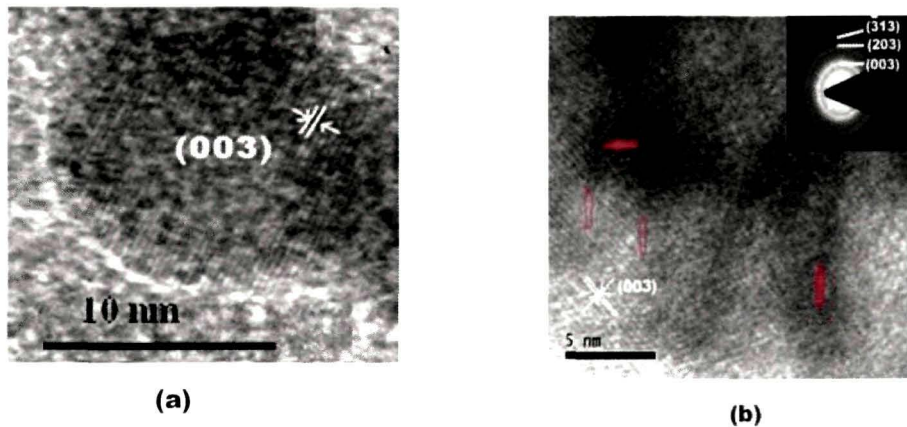


Fig.5.1(iii): HRTEM micrograph of (a) unirradiated and irradiated FFG with dose (b) 2.635 kGy. The inset of (b) is the SAED pattern

Fig.5.1.(i) and (ii) depict the TEM images of ultrasonically agitated magnetite particles of the unirradiated and γ -irradiated FFW and FFK respectively. It is evident that the particles retain their spherical shape after the irradiation of FFW, FFK and FFG with a dose of 878 Gy. When the FFs were irradiated with a comparatively higher dose (2.635 kGy), some noticeable structural changes were observed in FFW and FFK. In the unirradiated FFs, the particles were of average size ~ 9 nm. As can be

found from the micrographs, the γ -irradiated FFW and FFK contained substantial amount of large particles along with several smaller particles. In case of FFW, particles with an average size of ~ 20 and 48 nm were observed when the sample was irradiated with a dose of 878 and 2.635 kGy; respectively. On the other hand, the enlargement was comparatively low in FFK. As a consequence of the irradiation, the size of the dispersed MNPs of FFK became ~ 12 nm (dose: 878 Gy) and for the dose of 2.635 kGy the size of some nanoparticles became ~ 18 nm. Note that, when an energetic radiation, e.g. γ or, electron passes through material, it can result in fragmentation or recrystallization along with the induction of point defects. Consequently, the physical properties of the material would get modified.^[18] We speculate that the Fe_3O_4 particles, dispersed in the FFs undergo solid state recrystallization and particle growth *via* absorption of energy from γ -radiation and dissipating into the surrounding environment. Note that the density of milli-Q- water (~ 1000 kg/m³) is higher than that of kerosene (~ 817.15 kg/m³). Thus the energy dissipation during the growth process will be more in water than kerosene. Again, due to the smaller viscosity of water than kerosene, the growth process is more favourable in FFW than FFK. It is expected that the irradiation induced fragmentation or recrystallization reduces the spherical symmetry of the nanoparticles. Therefore the TEM micrograph of FFW, irradiated with a dose of 2.635 kGy, shows spherical and smaller particles along with some elongated particles.

The high resolution TEM micrograph of the irradiated (dose: 2.635 kGy) FFG [Fig. 5.1.(iii)] reveals no such structural enlargement of the particles. The size of the Gd_2O_3 nanoparticles before and after the irradiation was calculated as ~ 9 nm. Neither any deformation in the shape of the particles was also noticed upon irradiation. The chemical stability of Gd_2O_3 is attributed to this morphological stability with irradiation. Rather, it ensures the formation of nanoscale defects in the successive lattice planes (red arrows). The defects can be in the form of voids (vacancies) or

dislocations. For instance, evidence of point defect and dislocation are shown by solid and open arrows; respectively. The inset of Fig. 5.1(iii) (b) represents the selected area electron diffraction (SAED) pattern of the irradiated specimen. In that figure, the bright rings were indexed as (0 0 3), (2 0 3), ($\bar{3}$ 13) and are in conformity with the XRD analysis (refer Chapter 2).

5.2.2. Dynamic light scattering

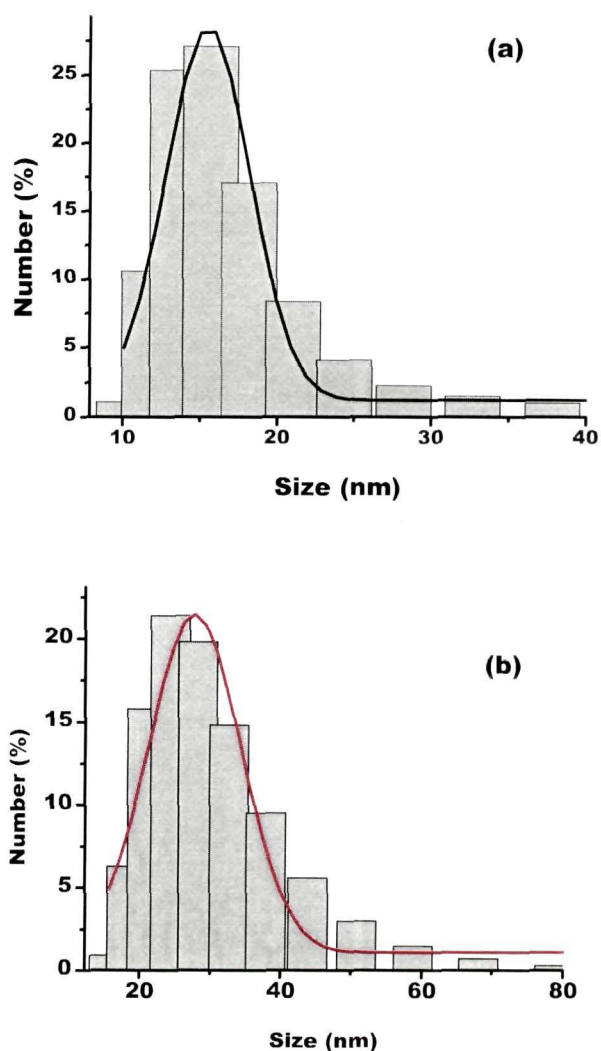


Fig.5.2(i): DLS spectra of (a) unirradiated (b) irradiated (dose:878 Gy) FFW

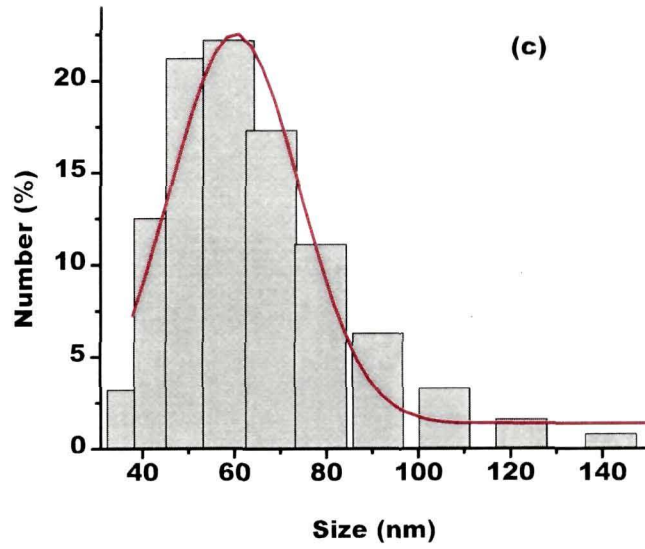


Fig.5.2 (i) (c): DLS spectra of irradiated FFW with dose 2.635 kGy

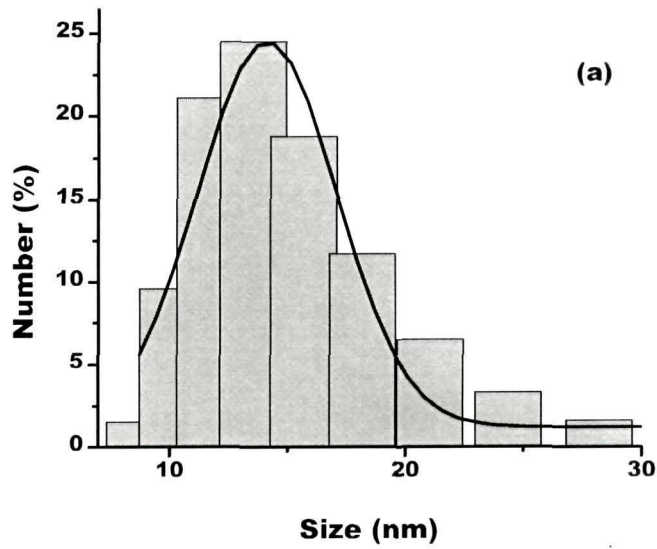


Fig. 5.2(ii)(a): DLS spectra of unirradiated FFK

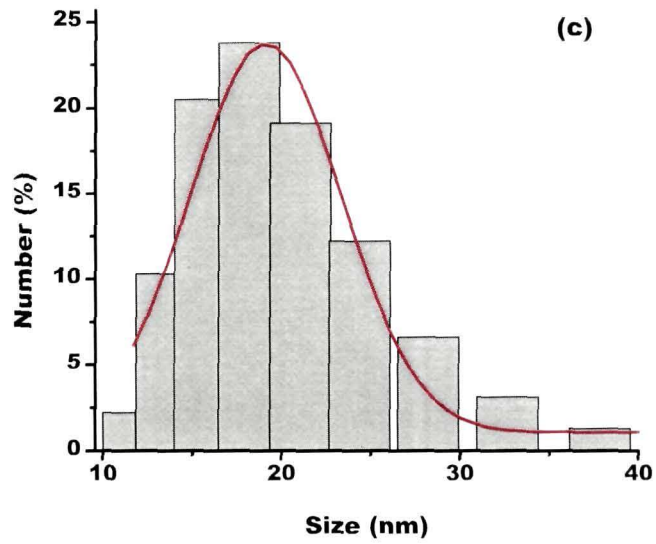
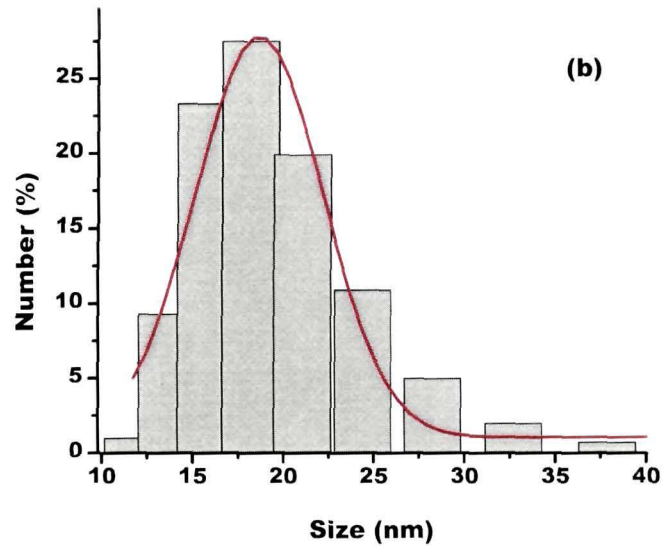


Fig.5.2(ii): DLS spectra of irradiated dose FFK with dose (b) 878 Gy and 2.635 kGy

Dynamic light scattering provides information regarding particle size distribution. Figure 5.2(i) shows a comparative analysis of the size distribution of the dispersed MNPs of the unirradiated and γ - irradiated FFW system. Similarly, Fig 5.2(ii) reveals the DLS study of the γ - irradiation effect on particle size distribution of FFK. The DLS study was performed for two γ - dose viz. 878 Gy and 2.635 kGy. In case of FFW irradiated with a dose of 878 Gy, the average size was found to be ~ 28 nm and for the higher dose (2.635 kGy) it was ~ 60 nm. The unirradiated sample showed a size distribution with average size as ~ 15 nm. Thus, adequate particle growth, as a result of γ -radiation, was also evident from the DLS studies. Note that, the predicted values are somewhat larger than the values obtained from TEM analyses owing to the fact that the DLS study which rely on scattering events actually measures the hydrodynamic diameters of the particles that are coated with surfactant layers. It was observed that the FWHM (β , in nm) of the Gaussian fitting gets increased from ~ 6.8 nm for the unirradiated to ~ 32.1 nm for the irradiated (dose: 2.635 kGy) FFW specimen. For FFW irradiated with a dose of 878 Gy, β was found to be ~ 17.02 nm. It indicates that the particle size distribution has also increased with the irradiation dose. Fig. 5.2(ii) shows that there is no adequate growth of the particles in case of γ - irradiated FFK. The average size of the particles has increased from ~ 14 nm (unirradiated) to ~ 19 nm when dose was 2.635 kGy. For FFK sample, the FWHM (β) of the DLS spectra got enhanced upon γ -irradiation. The enhancement of particle size and FWHM with dose for this FF also supports the idea of γ - irradiation induced particle modification. The observed modification in the particle growth and FWHM of the irradiated FFs highlight the role of carrier fluid. It is anticipated that in FFK, only a few particles undergo irradiation induced fragmentation and recrystallization. The random motion of the particles is affected by a comparatively large viscosity of kerosene (in FFK) than water (in FFW). Consequently, the observed variations were

much stronger in FFW than FFK the results of which are presented in Table 5.1.

Table 5.1: Analysis of DLS spectra

FFW			FFK		
Dose (Gy)	Size (nm)	β (nm)	Dose(Gy)	Size (nm)	β (nm)
0	15	6.8	0	14	5.05
878	28	17.02	878	17	8.38
2635	60	13.1	2635	19	10.31

5.2.3 FT-IR spectroscopy

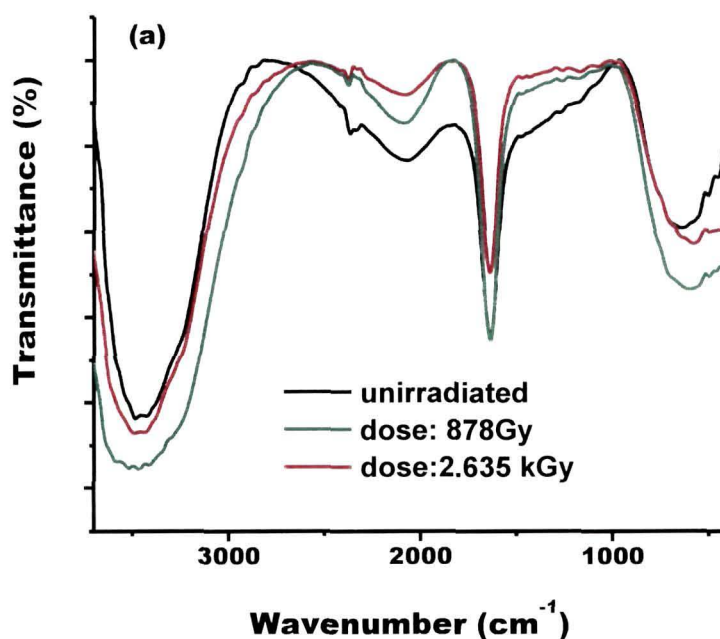


Fig. 5.3(a): FT-IR spectra of unirradiated and irradiated FFW

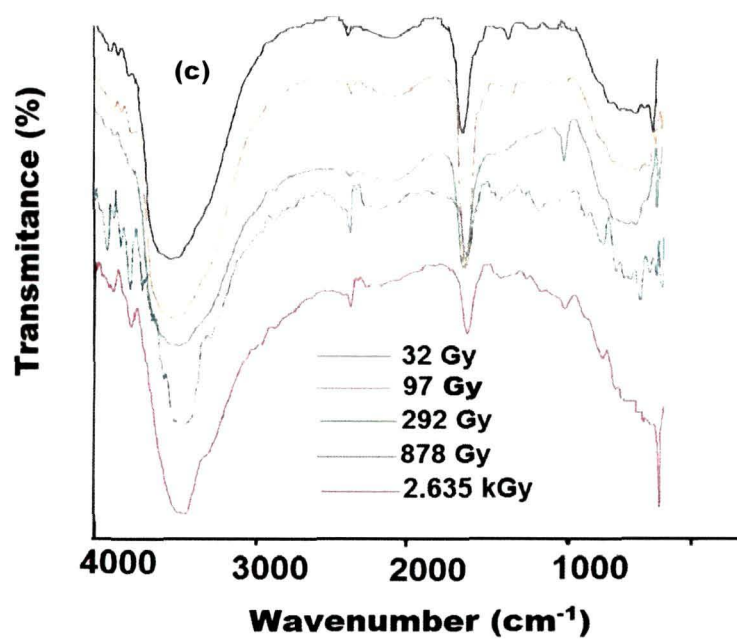
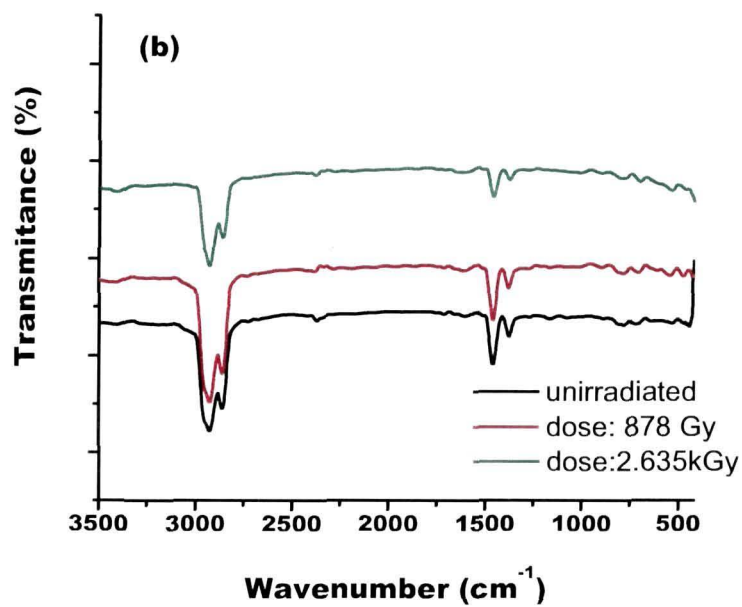


Fig.5.3: FT-IR spectra of unirradiated and irradiated (b) FFK and (c) FFG

FT-IR spectroscopy is a healthier access to evaluate the changes in the vibrational features due to the presence of certain constituents present in a given material system. Fig .5.3(a) shows the room temperature FT-IR spectra of the unirradiated and the irradiated FFW. Except a peak observable at $\sim 2077 \text{ cm}^{-1}$ and identified as C–O stretching mode of the atmospheric CO_2 molecule, all other peaks correspond to the chemical constituents available in the FF under study. The broad band at $\sim 3488.07 \text{ cm}^{-1}$ and the small peak at $\sim 2403 \text{ cm}^{-1}$ represent the characteristic O–H bending and stretching vibrational modes of the hydroxyl group of water molecule.^[19] The sharp peak at $\sim 1670 \text{ cm}^{-1}$ and a weak peak at $\sim 1161 \text{ cm}^{-1}$ give the respective signatures of strong and medium –CO–OH bonding of oleic acid.^[20] The typical Fe–O stretching vibrations of Fe_3O_4 are prominent in the lower wavenumber region, in the range $598\text{--}566 \text{ cm}^{-1}$ and $510\text{--}445 \text{ cm}^{-1}$.^[20] It is seen that after irradiation, the characteristics peak of Fe_3O_4 has shifted further towards lower wavenumber side. Molecular vibrations obey Newtonian mechanics.^[21] The actual vibrational frequency of a molecule can be calculated with the assumption that the vibration corresponds to an elastic spring problem. Again, the vibrational frequency (ν) of a molecule with mass m can be expressed as:^[21]

$$\nu = \frac{1}{2\pi} \sqrt{\frac{\kappa}{m}} \quad (5.2)$$

Here, κ is the force constant of the spring. We know that for nanoscale size, the force constant associated with bonds tends to increase. Due to the small size, a large number of bonds involving surface atoms of the nanostructures break down, resulting in a rearrangement of non-localized electrons on the surface. Consequently, the smaller the size, the larger will be the shift of the vibrational peak toward higher wavenumber side and vice versa.^[19] It may be noted that, evolution of no new peak in the spectra of the irradiated samples affirms that neither the MNP nor the surfactant (oleic acid) layer has dissociated/ transformed into new chemical species.

Fig.5.3 (b) depicts the room temperature FT-IR spectra of unirradiated and γ - irradiated FFK. No variations in the spectra are observed after the irradiation. All the characteristic peaks seen in the unirradiated FF remain in the same position even after the irradiation. The symmetric and asymmetric stretching modes of carrier fluid kerosene appear at 2929.42 cm^{-1} and 2856.9 cm^{-1} ; respectively. ^[22] The surfactant oleic acid confirms its presence by the two medium -CO-OH bonding mode at positions 1453.42 cm^{-1} and 1381.9 cm^{-1} in the unirradiated and irradiated samples.^[20] This specifies that neither the carrier fluid (kerosene) nor the surfactant (oleic acid) was dissociated by the irradiation. The peaks at $440.72 - 481.15\text{ cm}^{-1}$ and 528.96 cm^{-1} were due to Fe-O or/and Fe-OH stretching modes of Fe_3O_4 .^[20] It was seen that the FT-IR spectrum corresponding to the maximum dose (2.635 kGy) was slightly affected by the irradiation. In this spectrum, the peaks attributed to Fe_3O_4 were modified to some extent, when subjected to irradiation. Thus, TEM and DLS study indicate growth of the dispersed Fe_3O_4 particles in FFK, like that of FFW. It was also revealed that in FFK, the growth was not much as predicted in the later case. We consider that, in case of FFK the number of particles undergoing size alteration was minimal. The maximum energy of the γ -photons may have been used up in forming defects in the MNPs. Only a fewer particles could succeed in irradiation induced recrystallization and came out with bigger particle dimension. Therefore, there is no shift in the peak position corresponding to Fe_3O_4 .

Fig.5.3(c) depicts the FT-IR spectra of FFG that were irradiated with five different doses namely, 32, 97, 272, 878 and 2.635 kGy. The different vibrational modes of the constituent material of FFG were in the same position after and before the irradiation for all the applied γ - doses. The conventional peaks appearing at ~ 3403 and 2400 cm^{-1} represent the respective signatures of O-H stretching and C-O stretching of atmospheric water and CO_2 molecules.^[19] The CH_3 and CH_2 bending modes of ethanol occurred at $\sim 1384\text{-}1392\text{ cm}^{-1}$ and $1452\text{-}1569\text{ cm}^{-1}$;

respectively.^[22] The peak at $\sim 1058\text{ cm}^{-1}$ is responsible for stretching mode of functional group CO of ethanol.^[22] The weak band at 2980 cm^{-1} and the sharp band at 1550 cm^{-1} indicate the presence of CTAB in the samples.^[23] It was evident that the vibrational features corresponding to the Gd–O bonds at $\sim 536\text{ cm}^{-1}$ have been influenced by the irradiation effect.^[24] It was observed that with increasing γ -dose of radiation, the peak became more prominent. But an anomaly in the Gd–O vibration mode with discontinuities and less intensity profile was observed in sample irradiated with a dose of 878 Gy. Defects like oxygen vacancies are very common in oxide compounds. Also, some Gd vacancies produced during synthesis may also exist in the system. In fact, the creation of a large number of free electrons by the energetic γ -rays (1.25 MeV) can be associated with defect formation. The observed variation in the metal–oxygen bond vibration with increased dose can be correlated with the increased defects upto a certain dose, where the defects get saturated by distributing themselves along the grain boundaries and on the surfaces. We speculate that the uneven distribution of defects and introduction of adequate inhomogeneity could have led to the discontinuities in the vibrational features. Along with the Gd–O vibration mode, the peak corresponding to ethanol at ~ 1058 and $1452\text{--}1569\text{ cm}^{-1}$ were also getting modified in intensities due to the irradiation effect. Reports have showed that ethanol is inactive to γ -irradiation.^[25] Here, ethanol is not acting as a single identity, rather it is used as a carrier fluid of the ferrofluid. Thus the variations with respect to vibrational response can be truly conditional.

5. 3. Photoluminescence study

The influence of light on the nature of radiative transition in material systems makes PL spectroscopy an important tool for material characterisation and application. Intra- and inter-band transitions can be visualised by PL studies. The room temperature PL spectra ($\lambda_{\text{ex}} = 270\text{ nm}$) of unirradiated and irradiated FFG are shown in Fig.5.4(i). The asymmetric

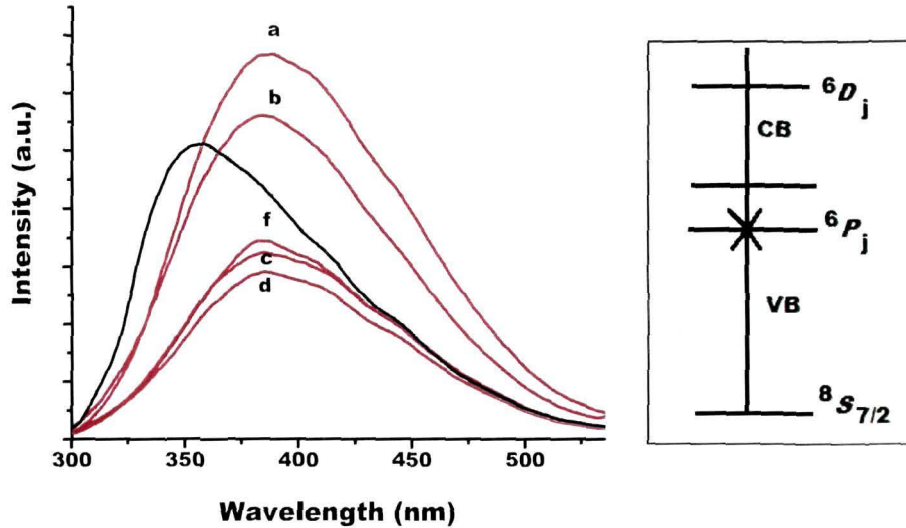


Fig.5.4: (i) PL spectra of unirradiated and irradiated FFG with dose (a) 32 Gy, (b) 97 Gy, (c) 292 Gy, (d) 878 Gy and (e) 2.635 kGy, (ii) Energy level diagram of Gd³⁺

peak at ~ 355 nm, due to the ${}^6P_{7/2} \rightarrow {}^8S_{7/2}$ transitions [Fig. 5.4 (iii)] of Gd (III) ion of the unirradiated FFG is red shifted to 390 nm after γ -irradiation. It is considered that the overall PL spectrum is a superposition of band to band and the defect related transition (discussed in Chapter 2). As discussed in Chapter 1, the photoluminescence is a consequence of transition of electrons from the excited energy level to a lower energy level. The shift of a luminescence peak either towards red or blue is related with decrease (red shift) or increase (blue shift) of the energy difference between the transition levels.^[26] In nano dimension, the red shift or blue shift of luminescence peak may occur under different conditions. The most commonly occurred shift of PL peak in nanomaterials is owing to the size variation.^[27,28] The shifting of the peak is also dependent on various experimental condition viz. temperature,^[29] pressure^[30] etc. In our case, we discard all these possibilities (variation in size, temperature or pressure). In contrast, it is considered that besides the already present vacancies in the system, plentiful metastable surface

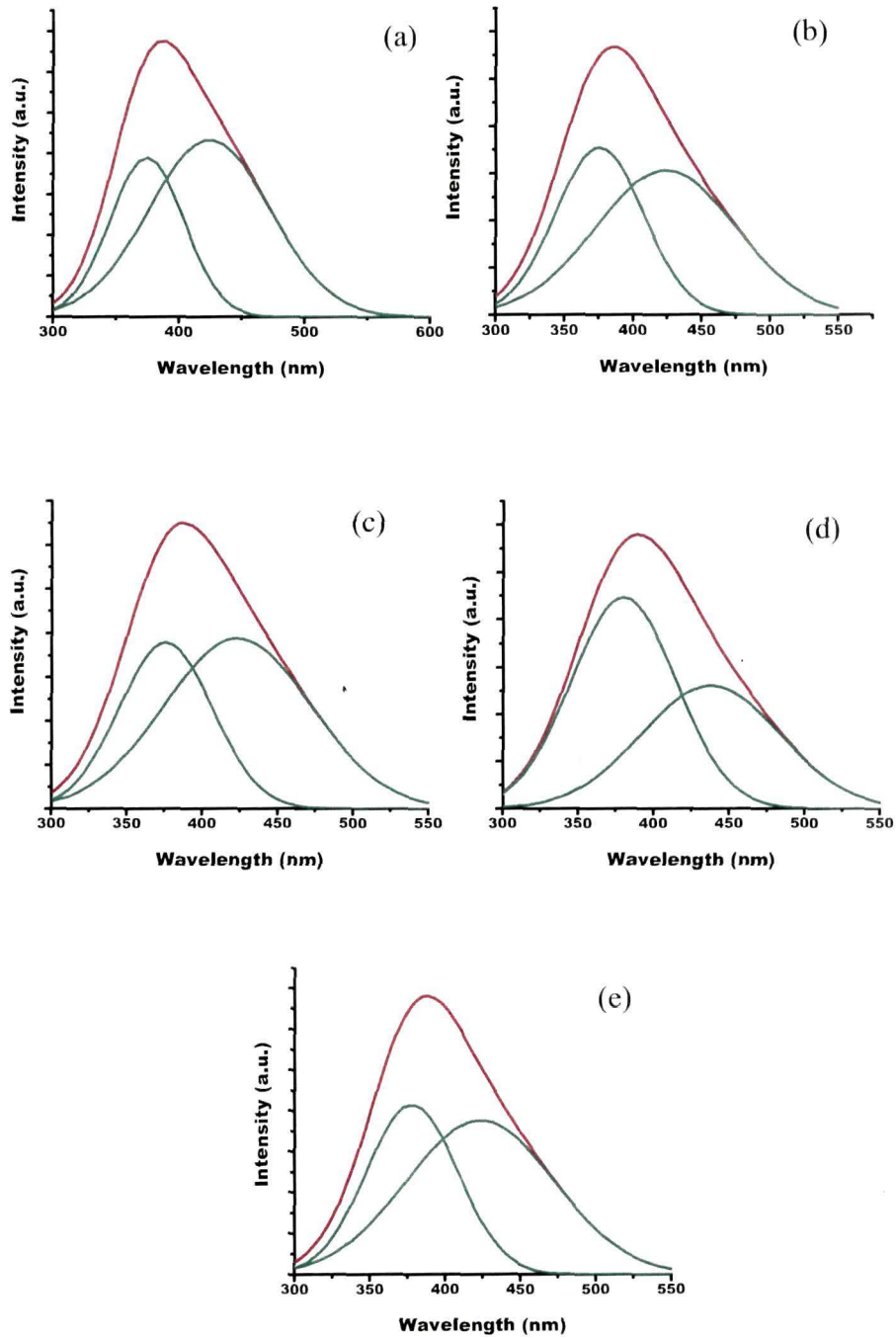


Fig. 5.4(ii): Deconvoluted PL spectra of irradiated FFG with dose (a) 32 Gy, (b) 97 Gy, (c) 292 Gy, (d) 878 Gy and (e) 2.635 kGy

states (defect states) were created due to γ -irradiation. Along with the shifting of the main peak towards higher wavelength, the abrupt change in symmetry signifies a remarkable improvement in the emission process via intermediate states, created by γ -irradiation. As mentioned earlier, during exposure of γ -radiation, electrons are emitted due to the interaction of high-energy photons with the medium through the Compton effect. These electrons can be accommodated in the pre-existing oxygen vacancies. In oxide systems, an electron in oxygen vacancy results in F^+ centres.^[31] The surface defect states are positioned well below the lower end of the upper energy level. It is the transition via these surface states that has resulted in the red-shifting of the emission peak, thus obstructing direct band-to-band transition significantly.

In order to correlate the amount of defect formation, asymmetry introduced and γ -dose, we have performed deconvolution mechanism on each of the PL spectra [Fig. 5.4(ii)]. Upon deconvolution, two distinct Gaussian peaks with variable intensities were obtained. The first peak positioned at ~ 355 nm is band-to-band (${}^6P_{7/2} \rightarrow {}^8S_{7/2}$) emission. The second peak is recognised as a defect-related peak and located at ~ 410 nm, for all the irradiated FFG samples. Irradiation dependent variation in the peak intensity would describe the nature of radiative transition undergoing in a given specimen. Emission as a result of formation/annihilation of additional defect centres manifests the definite PL intensity in a selective way. For the sake of clarity and better understanding, we have estimated symmetry factor (S) and correlated with the intensities of the deconvoluted peaks with respect to the original peak. Note that right symmetry (S_R) is related to the defect emission process whereas left symmetry (S_L) is associated with the band-to-band emission. Here, right symmetry factor is defined by $(\lambda_M - \lambda_R) / \Delta\lambda$ with λ_M representing peak-wavelength corresponding to the main peak, λ_R is the wavelength on the right-hand side of the FWHM and $\Delta\lambda = \lambda_R - \lambda_L$, λ_L being the half-width wavelength on the left-hand side of the FWHM. Fig.5.5(a) represents the

variation of relative right symmetry factor as well as relative intensity (I_2/I), I_2 being the intensity of the defect emission after deconvolution with I being the intensity

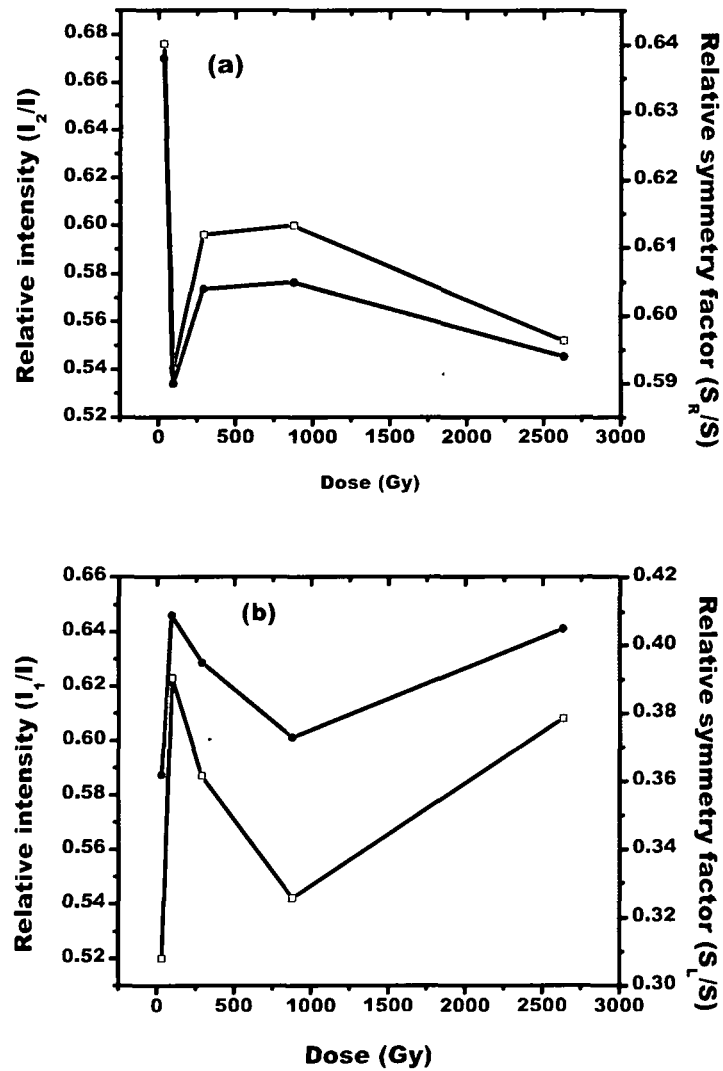


Fig.5.5: Variation of relative intensity and relative symmetry factor vs. dose corresponding to (a) defect related emission, (b) band-to-band emission

of the main peak) obtained from the deconvolution. Similarly, the respective variations for the band-to-band emission can be shown in Fig.5.5(b) with relative intensity as I_1/I (I_1 is the intensity of the deconvoluted band-to-band emission) and relative symmetry factor S_L/S (S_L is the left symmetry factor of the unirradiated sample). Interestingly, it was found that the relative intensity and symmetry factor changes in a similar fashion with increasing dose, thus indicating direct relation between these two measuring parameters. In PL spectroscopy, the intensity is a measure of the number of radiative transitions while symmetry signifies the nature of radiative centres (energy spacing, order, etc.). The non-linear nature of the curve indicates the simultaneous effect of defect formation/passivation in the irradiated system. By and large, it is expected that the formation and annihilation processes compete each other until stable energy states (defect states) are created. First, with the increase in dose from 32 to 97 Gy, we observe drastic reduction in the relative PL intensity which may be ascribed to adequate passivation of surface defects. Surprisingly, further increase in dose to 292 and 878 Gy is characterised by a significant enhancement of I_2/I ratio. At the highest dose (2.635 kGy), we notice further reduction of I_2/I . The relative symmetry factor (S_R/S) also gives a similar pattern. Reduction of defects makes the overall PL spectrum more symmetric with suppressed right symmetry factor. The γ -ray induced defect creation is not an indefinite process and we speculate that the defects get saturated after a critical dose. The defects could exist in the form of vacancies, interstitials, antisites, etc.

5.4. Magneto-optic response of gamma-irradiated ferrofluids

(i) Faraday rotation

The γ -irradiation effect on Faraday response of FFW, FFK and FFG are shown in Fig.5.6:(a),(b), and (c); respectively. The FR measurement was carried out for at a working wavelength of 632.8 nm. A quick look at

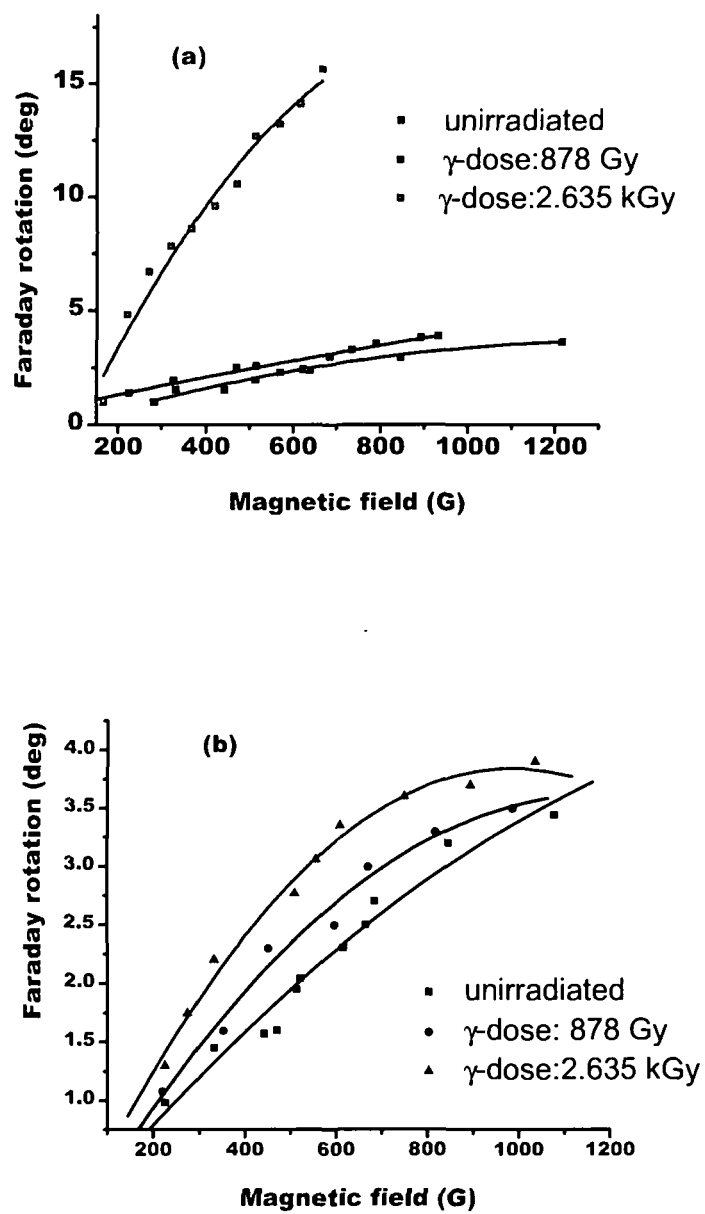


Fig.5.6: FR of unirradiated and irradiated (a) FFW and (b) FFK

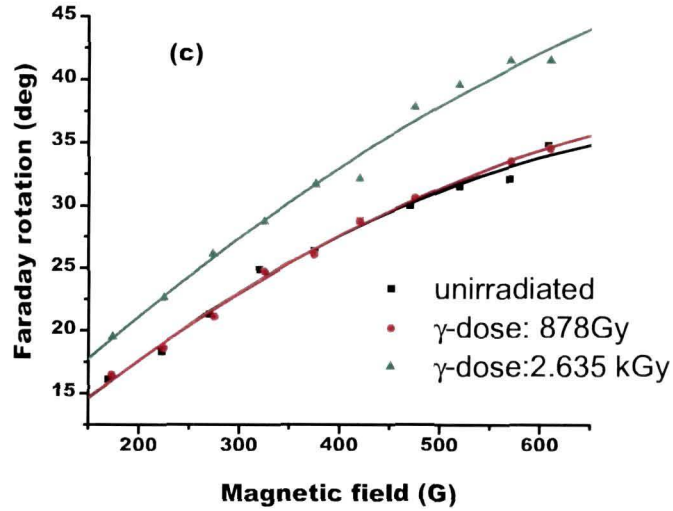


Fig.5.6(c): FR of unirradiated and irradiated FFW

the figures indicates that the FR gets enhanced with the irradiation dose, for all the FFs. As the Verdet constant is a characteristic material parameter, it could give a quantitative picture of FR response in the material. The quantitative variations of the Verdet constant (V) for each of the FF cases are shown in Table 5.2. It is apparent that the parameter showed an improved magnitude due to irradiation impact except for a given dose: 878 Gy of FFG.

Table 5.2: Verdet constant for unirradiated and irradiated ferrofluids

FFW		FFK		FFG	
Dose (Gy)	V (deg/G-cm)	Dose (Gy)	V (deg/G-cm)	Dose (Gy)	V (deg/G-cm)
0	0.64×10^{-2}	0	0.47×10^{-2}	0	7.7×10^{-2}
878	0.65×10^{-2}	878	0.49×10^{-2}	878	7.3×10^{-2}
2635	1.15×10^{-2}	2.635	0.77×10^{-2}	2.635	7.8×10^{-2}

The ninefold enhancement of FR can be attributed to the structural reorganization of the dispersed nanoparticles. In Fe_3O_4 system, $3d$ electronic states of iron are generally responsible for the magneto-optic effect.^[32] The cations (Fe^{3+} and Fe^{2+}) occupy the tetrahedral A and octahedral B sites. They interact with the oxygen localized states which are already present in the vicinity of their neighbouring environment. The FR takes place due to the intervalence charge-transfer transitions (energy order ~ 0.6 eV) between neighbouring Fe^{2+} and Fe^{3+} ions.^[33,34] Again, depending on the position of the metal ions on site A or B, the distance between them is also different. The separation between the two metal ions when they are in two B sites is smaller than if they are in A and B site. Under normal condition the electron hopping between B-B is more preferable than B-A as electron hopping depends on distance between ions involved.^[35] Further, in nanoscale dimension, the finite size effect of MNPs leads to tremendous change in the magnetic ordering.^[36] Whereas, magnetization decreases with size.^[37] So, with the reduction of size, the number of possible sites responsible for the FR would decrease. Conversely, the ratio of $\text{Fe}^{2+} / \text{Fe}^{3+}$ will be higher in a bigger particle than the case of a smaller one. In the host lattice, γ -irradiation can cause modification by annihilating/creating point defects.^[38] This is also supported by our observation revealed through different spectroscopic tools. The irradiation leads to the alteration of the total number of oxygen vacancy sites of the Fe_3O_4 system which in turn influence the charge transfer process. In addition, Eq.3.1 of *Chapter 3*, shows that chain formation plays a crucial rule in the FR of FF. The effective magnetic interaction between the two magnetic nanoparticles can be described by a coupling constant (Λ) given by:^[39]

$$\Lambda = \frac{\pi\mu_0\chi^2H^2a^3}{72k_B T} \quad (5.3)$$

The coupling constant is the ratio of the magnitude of maximum interaction energy to the thermal energy ($k_B T$) in the system. Here, a is the diameter

of the MNPs and χ is the effective susceptibility of individual MNPs. The favourable condition for chain formation of the dispersed particles is $\Lambda \gg 1$. At a specific applied field, the bigger particles are more prone to the chaining effect than the smaller ones. The higher the number of chain forming capacity, the larger would be the FR in a given FF specimen. Now, between the two Fe_3O_4 based systems (FFW and FFK), the electron microscopy and light scattering study have revealed that the specimen FFW would show substantial growth of the dispersed nanoparticle due to the γ -irradiation. The irradiation lead growth of the particles in the other FF was not that significant. It was also predicted that only a fewer particles undergo size broadening in FFK. Rather, the most of the MNPs in FFK were modified by the defect formation. As γ -irradiation is capable of creating oxygen vacancies, the enhancement of FR upon irradiation can be a combined effect of size broadening and defect creation.

In the rare earth oxide (Gd_2O_3) system, the effect of γ -irradiation on FR shows some abnormal behaviour. Though the FR get enhanced for a γ -dose of 2.635 kGy, irregularities were observed for the dose of 878 Gy. The values of the Verdet constant (table 5.2) was also found to be smaller than that of the unirradiated value for this dose. We know that magnetic properties of Gd compounds depend on the surrounding environment of the Gd^{3+} ions. It was ensured from different characterization techniques that during the γ -irradiation, some new defects were formed and some pre-existing defects get annihilated in FFG. The formation of voids and dislocation in the irradiation (dose: 2.635 kGy) induced Gd_2O_3 nanoparticles is clear from the HRTEM image. Interestingly, the FT-IR and PL study also hint irregularity in case of use of the γ -dose of 878 Gy. It was anticipated that, the limit of formation/annihilation of defects is the dose 878 Gy. The FR as well as the corresponding Verdet constant get enhanced when creation of defects supersede annihilation process. In that case, light has to traverse a longer path due to enhanced optical path

length resulted from surface defects. Owing to higher stability of Gd_2O_3 against defect modification, the enhancement of FR in case of FFG is comparatively less than the other two types of FFs.

(ii) Linear dichroism

The influence of γ -irradiation is also prominent in another type of magneto-optic effect (linear dichroism) exhibited by the FFs. As shown, Fig. 5.7(a), (b) and (c) reveals the irradiation effect on the LD response of the FFs for two doses: 878 Gy and 2.635 kGy. A close look on the figures indicate that dichroism response is adequately suppressed by γ -irradiation effect. The unirradiated samples showed a much higher LD response than the irradiated samples. Though the irradiated samples measure low LD responses, the trend with applied magnetic field is quite similar for all the cases. The LD increases with the external applied field in unirradiated as well as in γ -irradiated FFs and seems to get saturate at higher magnetic fields. As discussed earlier, the field induced optical anisotropy is the root cause of LD exhibited by FFs. The oscillating dipoles of interacting particles generate optical anisotropy. The electric field produced by an individual oscillating dipole depends on the position vector whose origin is at the particle or oscillating dipole centre and on the dipole moment (*refer to Eq.3.6 of Chapter 3*). As discussed earlier, formation and annihilation of defects (e.g. oxygen vacancy) in the oxide systems are expected during the irradiation process. The magnetic moment of any magnetic material arises due to its spin and angular momenta. In many materials, the angular momenta decreases sharply with defects.^[40] The potential associated with the defect is affected by the electrical charges of the nearby atoms. The free circulation of these electrons is hindered by the hill and valleys produced due to the electrical charge imbalance in the neighbourhood.^[40] Thus, the total angular momentum as well as the dipole moment gets quenched with the defects. The dispersed nanoparticles in FFW and FFK have also undergone size variation due to the irradiation.

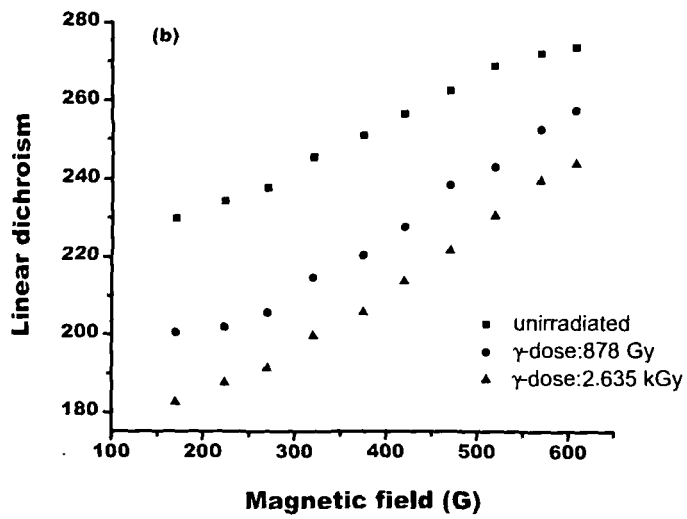
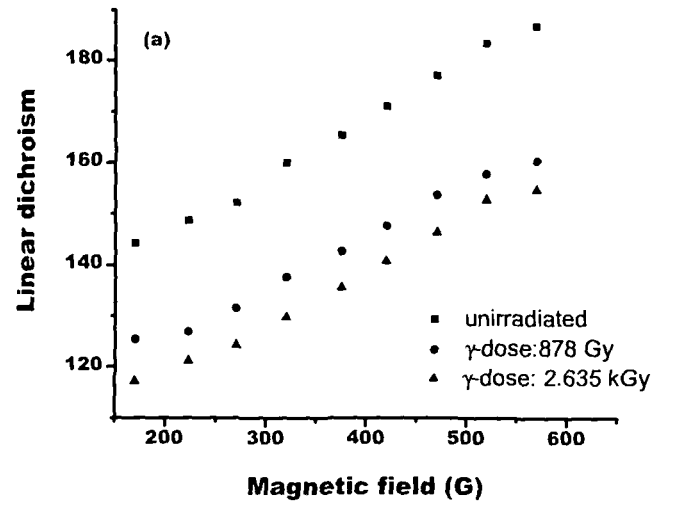


Fig.5.7: LD of unirradiated and irradiated (a) FFW and (b) FFK

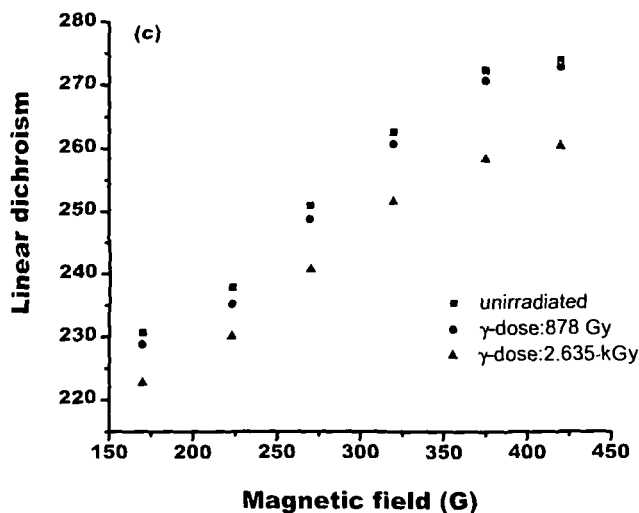


Fig.5.7(c): LD of unirradiated and irradiated FFG

The particles of these systems show substantial growth with γ -doses. Also, light had to travel a longer distance in bigger particles. The bigger particles form chains/structures with less difficulty than the smaller ones. Thus, the distance between the interacting particles of a chain also increases. In other words, the position vectors get enhanced with size variation. The electric field of the interacting particles decreases with decrease of dipole moment and increase of position vectors. This combined effect of quenching of dipole moment and enhancement in position vectors of the irradiated FFs gives an overall decrease in the LD response.

5.5. Concluding remarks

The synthesized FFs were irradiated with γ -radiation with doses 32-2635 Gy. The irradiation process has led to substantial growth of the dispersed particles, but to different extent, in different carrier media e.g., from an average size of ~ 9 to ~ 48 nm in FFW and from ~ 9 to ~ 18 nm in

FFK. Spectroscopic studies indicate that some pre existing defects were annihilated and some new defects had been created due to the γ -irradiation. To be specific, a correlation between intensity and symmetry of the PL peaks of γ -irradiated FF has been established. γ -irradiation also influences the magneto-optic effects of FFs. The enhancement of the Verdet constant (maximum $\sim 70\%$) is an important consequence of the γ -irradiation. In contrary, LD gets quenched (maximum $\sim 35\%$) due to the irradiation.

References:

- [1] L'Annunziata, M.F. *Radioactivity: Introduction and History*, Elsevier, UK, 2007.
- [2] Jagetia, G. C. et al. Evaluation of the effect of ascorbic acid treatment on wound healing in mice exposed to different doses of fractionated gamma radiation, *Rad. Res.* 159, 371-380, 2003.
- [3] Liu, Y. et al. Preparation of high-stable silver nanoparticle dispersion by using sodium alginate as a stabilizer under gamma radiation, *Rad. Phys. Chem.* 78, 251–255, 2009.
- [4] wang, J.P. et al. A chitosan-based flocculant prepared with gamma-irradiation-induced grafting, *Bioresour. Technol.* 99, 3397–3402, 2008.
- [5] Wang, L. et al. Gamma and electron beam irradiation effects on the resistance of micromachined polycrystalline silicon beams, *Sensor. Actuator. A: Phys.* 177, 99–104, 2012.
- [6] Kavetskyy, T. et al. Structural modification of chalcogenide glasses by gamma-irradiation studied with DBAL technique, *Phys. Stat. Sol. c*. DOI: 10.1002/pssc.201200252, 2012.
- [7] Gupta, S. et al. Novel nanocarbon hybrids of single-walled carbon nanotubes and dispersed nanodiamond: Structure and hierarchical defects evolution irradiated with gamma rays, *J. Appl. Phys.* 107, 104308 - 104308-15, 2010.

- [8] Pintilie, I. et al. Second-order generation of point defects in gamma-irradiated float-zone silicon, an explanation for "type inversion", *Appl. Phys. Lett.* 82, 2169-2171, 2003.
- [9] Alessi, A. Twofold co-ordinated Ge defects induced by gamma-ray irradiation in Ge-doped SiO₂, *Opt. Exp.* 16, 4895-4900, 2008.
- [10] Danileiko, Y.K. et al. Optical strength of gadolinium scandium gallium garnet active elements, *Sov. J. Quant. Elect.* 15, 286-288, 1985.
- [11] Sun, D.L. et al. Effects of annealing treatment and gamma irradiation on the absorption and fluorescence spectra of Cr:GSGG laser crystal, *Appl. Phys. B* 92, 529-533, 2008.
- [12] Mak, V.T. et al. The effect of gamma-irradiation on the bandgap width of ZnSe, *Tech. Phys. Lett.* 28, 757-758, 2002.
- [13] Gong, X. et al. Effect of γ -ray irradiation on structures and luminescent properties of nanocrystalline MSO₄:xEu³⁺ (M=Ca, Sr, Ba; x= 0.001-0.005), *J. Phys. Chem. Solids* 61, 115-121, 2000.
- [14] Haydar, U. et al. Mechanical and electrical properties of jute fabrics reinforced polyethylene/polypropylene composites: Role of gamma radiation, *Polym-Plast Technol.* 48 (7), 760-766, 2009.
- [15] Jun, L. et al. Using gamma-radiation for drug releasing from MWNT vehicle, *Chin. Phys. Lett.* 27, 038104-038106, 2010.
- [16] Kawasak, Y. et al, Effects of gamma-ray irradiation on mechanical properties, osteoconductivity, and absorption of porous hydroxyapatite/collagen, *J. Biomed. Mater. Res., Part B.* 92B(1), 161-167, 2010.
- [17] Lee, J. W. et al, Effect of gamma irradiation on microbial analysis, antioxidant activity, sugar content and color of ready-to-use tamarind juice during storage, *LWT-Food Sci. Technol.* 42,101-105, 2009.
- [18] Sayed, S.M.E. Electron beam and gamma irradiation effects on amorphous chalcogenide SbSe_{2.5} films, *Nucl. Instrum. Method. Phys. Res.* 225, 535- 543,2004.
-

- [19] Maity, D. and Agrawal, D. C. Synthesis of iron oxide nanoparticles under oxidizing environment and their stabilization in aqueous and non-aqueous media, *J. Mag. Mater.* 308, 46-55, 2007.
- [20] Nyquist, R.A., Putzig, C.L., Leungers, M.A. (Eds.), *Handbook of Infrared and Raman Spectra of Inorganic Compounds and Organic Salts*, vol. 1, Academic Press, San Diego, 1997.
- [21] Allinger, N.L., *Molecular structure*, Wiley, New Jersey, 2010.
- [22] Hong, R.Y. et al. Magnetic field synthesis of Fe_3O_4 nanoparticles used as a precursor of ferrofluids, *J. Magn. Mater.* 310, 37-47, 2007.
- [23] Wang, Y.D. et al. Synthesis and room temperature photoluminescence of ZnO/CTAB ordered layered nanocomposite with flake-like architecture, *J. Lumin.* 126, 661–664, 1997.
- [24] Murillo, A.G. et al. Optical properties of europium-doped Gd_2O_3 wave guiding thin films prepared by the sol-gel method, *Opt. Mater.* 19, 161-168, 2002.
- [25] Seymour, C.B. et al. The effect of ethanol on the radiation response of CHO-K1 cells, *Br. J. Radiol.* 60, 577–581, 1987.
- [26] Schroder, D. K. *Semiconductor Material And Device Characterization*, Wiley, New Jersey, 2006.
- [27] Gerasimos, S. et al. Size Dependence in Hexagonal Mesoporous Germanium: Pore Wall Thickness versus Energy Gap and Photoluminescence, *Nano Lett.* 10, 3330-3336, 2010.
- [28] Zhang, L. et al. Origin of Visible Photoluminescence of ZnO Quantum Dots: Defect-Dependent and Size-Dependent, *J. Phys. Chem. C* 114 (21), 9651–9658, 2010.
- [29] Pan, X. H. et al. Temperature-dependent Hall and photoluminescence evidence for conduction-band edge shift induced by alloying ZnO with magnesium, *Appl. Phys. Lett.* 95, 152105-152109, 2009.

- [30] Staszczak, G. et al. Different behavior of semipolar and polar InGaN/GaN quantum wells: Pressure studies of photoluminescence, *Phys. Stat. Sol.* 208, 1526–1528, 2011.
- [31] Vij, D.R. *Hand Book of Applied Solid State Spectroscopy*, Springer, Germany, 2006.
- [32] Schlegel, A. et al. Optical properties of magnetite (Fe_3O_4), *J. Phys. C: Solid State Phys.* 12, 1157-1165, 1979.
- [33] Jain, P.K. et al. Surface plasmon resonance enhanced magneto-optics (SuPREMO): Faraday rotation enhancement in gold-coated iron oxide nanocrystals, *Nano Lett.* 9 (4), 1644-1650, 2009.
- [34] Choi, K.H. et al. Magnetic behavior of Fe_3O_4 nanostructure fabricated by template method, *J. Magn. Magn. Mater.* 310, 861-863, 2007.
- [35] Pant, R.P. et al Anomalous enhancement in the optical scattered radiation in magnetite base ferrofluid , *J. Magn. Magn. Mater.* 252, 107-110, 2002.
- [36] Demortier, A. et al. Size-dependent properties of magnetic iron oxide nanocrystals, *Nanoscale*, , 3, 225-232,2011.
- [37] Shi, D. B. Aktas, L. Pust, F.Mikail ov (eds.), *Nanostructured Magnetic Materials and Their Applications* , Springer, Berlin, 2002.
- [38] Caruntu, D. et al. Magnetic properties of variable-sized Fe_3O_4 nanoparticles synthesized from non-aqueous homogeneous solutions of polyols, *J. Phys. D, Appl. Phys.*40, 5801-5810, 2007.
- [39] Laskar, J.M., Philip, J. and Raj, B. Experimental evidence for reversible zippering of chains in magnetic nanofluids under external magnetic fields, *Phys. Rev. E.* 80, 041401-041408, 2009.
- [40] Stavola, M. *Identification of defects in semiconductors*, Academic Press, San Diego, USA, 1998.

FFs are basically colloidal systems comprising of surfactant coated magnetic nanoparticles suspended in an appropriate carrier fluid.^[1,2] Different properties viz. physical, chemical, magnetic etc. can be adequately governed by the constituents of a FF. The morphology (shape and size) and structure of the MNPs play a crucial role in determining the overall properties of a FF.^[3,4,5] The selection of an appropriate surfactant for coating the MNPs is definitely not an easy job while stability of FF is largely controlled by the surfactants.^[6] The role of surfactant in the FF synthesis is also one of the frontline areas of research. Additionally, the carrier fluid could influence the flow property of the dispersed particles of a FF.^[7]

6.1. Comparison of magneto-optic responses

It is known that different irradiation (photons, charged particles etc.) events/processes may lead to adequate surface passivation of the nanoparticles in ferrofluids.^[8,9] Consequently, the overall FF properties get modified by the creation and annihilation of defects on the MNPs due to irradiation impact. Nanoscale defects are created/ annihilated at the cost of energy loss of the incident radiation. The radiation-matter interaction process is specific to the type of the radiation and the material surface. The energy of the radiation plays a crucial role in this regard. The present chapter highlights a comparative analysis of MO responses exhibited by different unirradiated as well as irradiated FFs for the excited wavelength 632.8 nm. Two types of irradiation process namely, low energy ion irradiation (80- keV Ar-ion) and γ -irradiation (dose: 2.635 kGy) were considered in this context. For better understanding on the role of the constituents, FFs viz. FFW and FFK were selected for this study. These are oleic acid coated Fe₃O₄ based FF. They differ in their respective carrier fluids. Milli-Q-water is the carrier of FFW whereas, MNPs were dispersed in kerosene in case of FFK.

6.1.1. Faraday rotation of Fe_3O_4 based ferrofluids

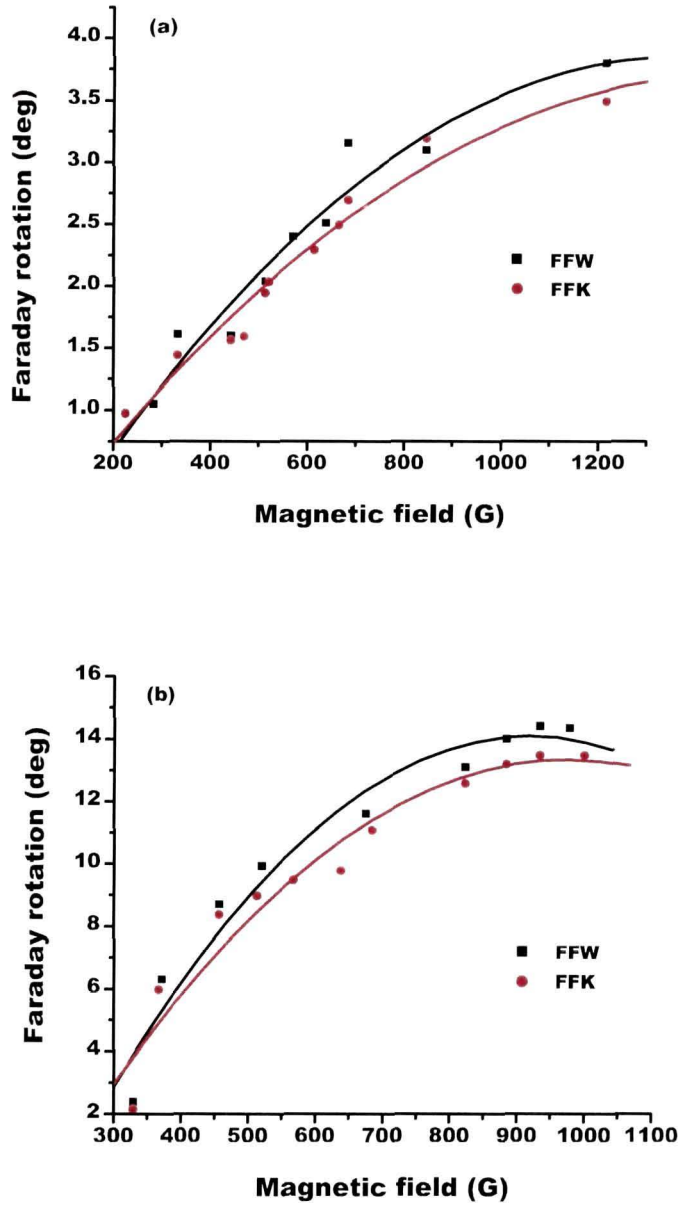


Fig 6.1: FR of (a) unirradiated and (b) 80-keV Ar-ion irradiated MNPs based FFW and FFK

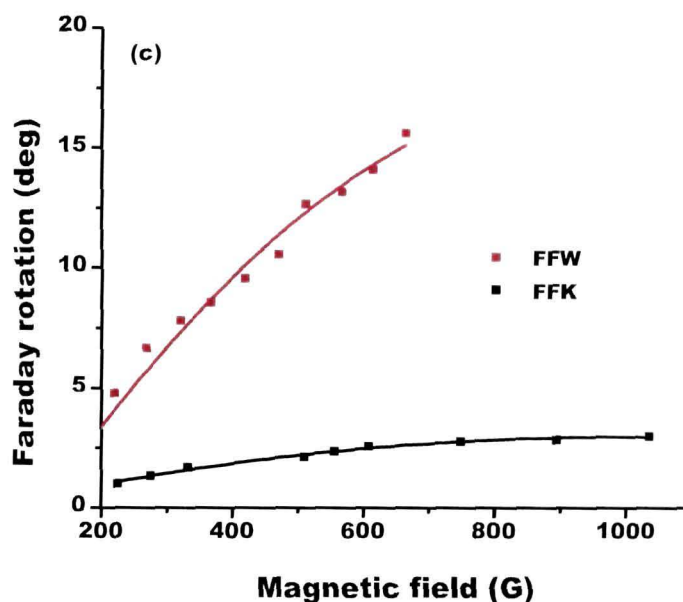


Fig 6.1.(c): FR of γ -irradiated FFW and FFK

The Fig. 6.1(a), (b) and (c) reveal the comparison of the FR response for unirradiated, Ar-ion irradiated MNPs based and γ -irradiated FFW and FFK. The excited wavelength is considered as 632.8 nm for all the cases. As can be observed, both the samples have followed a typical increasing trend of the FR response before attaining saturation. But the response is comparatively large at a definite field in case of FFW. The FR responses in both the FFs are attributed to the Fe^{2+} and Fe^{3+} charge transfer in Fe_3O_4 particles. It is mentioned in Eq. (3.1) (*refer to Chapter 3*) that, the FR of a FF is dependent on the magnetization, saturation magnetization of the MNPs and therefore, on the formation of chains at a definite magnetic field. All these properties are dependent on the size of the colloidal particles. In our case, the size of the dispersed particles of FFW and FFK in both the unirradiated and Ar-ion irradiated systems is quite similar as predicted from different characterization tools (*viz.* XRD,

TEM analysis of *Chapter 4*). Hence, size is not an effective parameter in these cases. Secondly, the role of carrier fluid on the FR cannot be ignored. The concerned FFs contain milli- Q water and kerosene as carrier fluid. These two liquids differ in many aspects as far as physical properties are concerned (*appendix II*). A theory of hydrodynamics predicts that the viscosity of a carrier fluid influences the overall magnetization of the FF.^[10] Again, as the dispersed MNPs move along the field direction through the carrier fluid, they experience a viscous drag force (F_v). This viscous force hinders the structure evolution in the FF. This force can be expressed as:^[11]

$$F_v = \eta u C_v \quad (6.1)$$

Here, η is the viscosity of the carrier fluid, u is the drift velocity and C_v is a size dependent drift coefficient. Thus, assuming the size of the MNPs fixed, the drift velocity is mainly controlled by the carrier fluid viscosity. The larger the viscosity of the carrier fluid, the smaller will be the orientation of the dispersed particles towards the applied field direction. In other words, the particles can pile up constructively and align along the field direction more easily in a less viscous fluid and vice versa. In our case, the viscosity of kerosene is about 1.5 times larger than that of milli- Q water. Therefore, corresponding to a given field, the chain formation will be more effective in FFW than the case of FFK. The FR is thus more sensitive in the former case for a chosen wavelength of light. Eq. (3.1) suggests that FR of FF is directly dependent on the chain length of the dispersed particles. This also supports our experimental results i.e., noticeable lagging of FR of FF with kerosene as carrier than that of FF with carrier fluid water, at a particular magnetic field.

Moreover, the difference between the two FFs in the FR response is quite large when the FFs were irradiated with the γ rays [Fig.6.1(c)]. Note that there was substantial growth of the nanoparticles (*refer to Chapter 5*) due to the γ -irradiation. The enhancement was comparatively more in FFW than that of FFK. With increase of size, the magnetization of the particles

also increases.^[12] It is expected that the bigger particles would form chains more rapidly. Thus, the enhanced FR response of γ -irradiated FFW than FFK is attributed to the bigger size of the MNPs as well as the larger viscosity of the carrier. Table 6.1 shows the enhancement of the Verdet constant of the two FF for different condition.

Table 6.1: Verdet constant (deg/G-cm) of FFW and FFK for different conditions

condition	FFW	FFK
unirradiated	0.64×10^{-2}	0.47×10^{-2}
Ion irradiation	0.7×10^{-2}	0.5×10^{-2}
γ -irradiation	1.15×10^{-2}	0.77×10^{-2}

6.1.2. Linear dichroism of Fe₃O₄ based ferrofluids

Fig. 6.2 shows the comparative linear dichroism response of two Fe₃O₄ based FF namely FFW and FFK. It is observed that the LD response of both the FFs in all the cases [(a)unirradiated, (b) ferrofluid prepared ion irradiated particles and (c) γ -irradiated] follow the same trend with increasing magnetic field. But it is quite higher in case of FFK than that of FFW. As discussed in earlier chapter (*Chapter 3*), the LD response is due to the field induced optical anisotropy in FFs. In a FF, with increase of the applied field, the dispersed particles undergo structural transformation from separated particles to chains and then bundles of chains. As the number/length of chains increases, the optical path within the nanoparticles also increases.

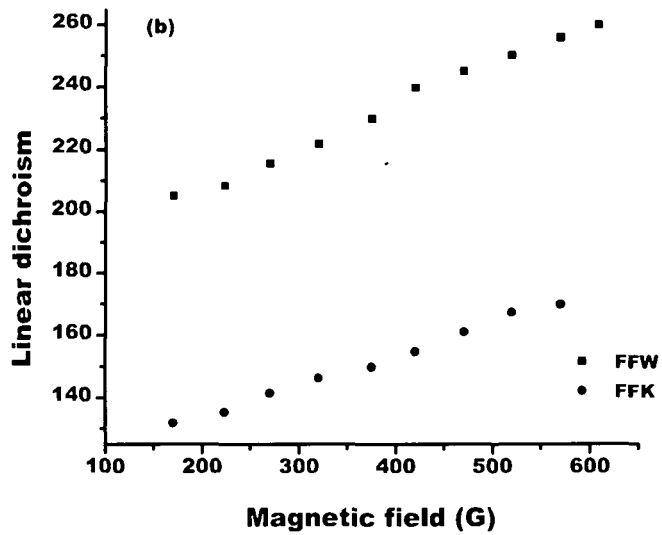
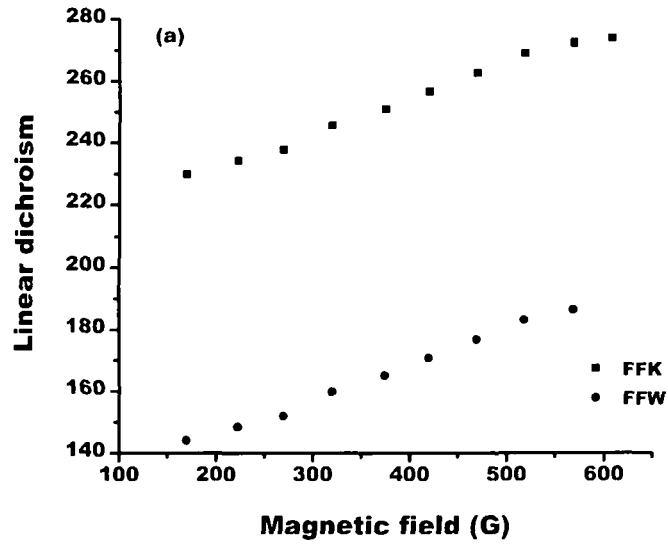


Fig 6.2: LD of (a) unirradiated and (b) 80-keV Ar-ion irradiated MNPs based

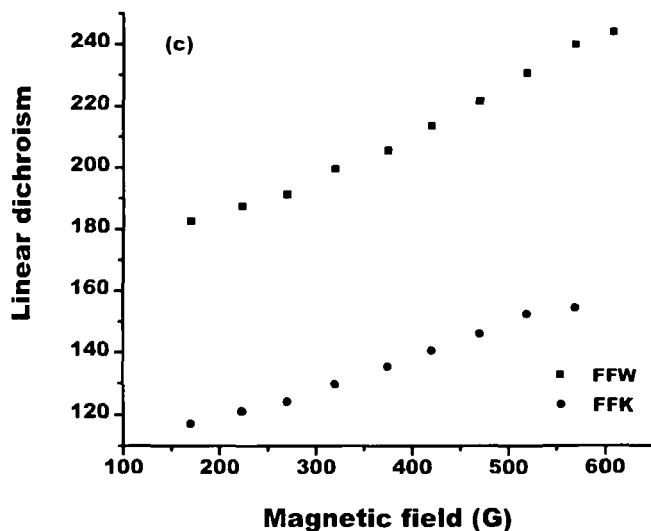


Fig 6.2.(c): LD of γ -irradiated FFW and FFK

increases. Light scatters more from a comparatively longer chain than single particles or shorter chains. Referring to Eq. 6.1, it is considered that the number/length of chains will be more in FFW than that in the case of FFK. Owing to the less viscosity of water, the dispersed particles in FFW can easily move in the carrier than in FFK with kerosene as carrier. In FFW, the particles align themselves toward the direction of the applied magnetic field with less difficulty than in the other concerned FF. Thus, the reduced LD response of FFW is attributed to the longer chains formed by the dispersed particles. Viscosity of the carrier plays an important role in determining the LD response of FF.

6.1.2. Irradiation effect on Faraday rotation of FFW

The FR response of FF varies with different irradiation processes. Fig. 6.2 shows the normalized FR response of FFW and its variation with Ar-ion and γ -irradiation. As discussed earlier, both keV scale energy ion irradiation and γ -irradiation induce numerous defects in nanoparticle

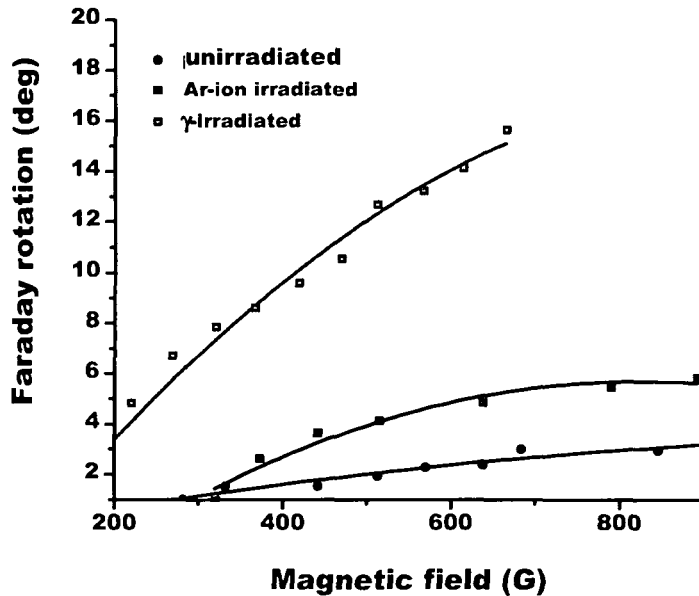


Fig 6.3: FR response of unirradiated, Ar-ion irradiated MNPs based and γ -irradiated FFW.

systems. In general, nanosystems contain plentiful defects^[12], particularly oxygen vacancies^[13, 14] are dominant in oxide nanostructured systems. Interaction between an oxide surface and energetic radiation (keV ion and γ -irradiation) is capable of forming and annihilating oxygen vacancies.^[15, 16] The creation of large number of free electrons during irradiation process also take part in the formation of charged defects like oxygen vacancy. The number of defect formation during irradiation process depends on the energy loss during irradiation process. It is the energy release to the external surrounding within the specimen that decides defect manifestation and structural evolution. γ -radiation is the most energetic electromagnetic radiation with energy scale greater than 100 keV. Thus, γ -radiation is capable of forming more defects than 80-keV Ar-ions. Secondly, in case of former type of irradiation the defect creation is expected to be

homogeneous as the FF specimen as a whole was subjected to irradiation in a closed chamber. In the later case, however, since the particles were first irradiated prior to making FFs, the defects may have been restricted to surface only.

Different characterization techniques have revealed no significant change in morphology and chemical composition of FFW prepared with Ar-ion irradiated Fe_3O_4 nanoparticles. Thus, the only possibility of the modified FR of Ar-irradiated FFW as compared to the unirradiated one is due to the defect formation in the MNPs. The newly formed defects could alter the mechanical strain as well as optical path length of the particles. The optical path of the incident light has to travel a larger distance due to the formation of charged defect sites in the irradiated sample. On the other hand, substantial particle growth was observed in case of γ -irradiated FFW. Due to the particle growth, the number of Fe^{2+} and Fe^{3+} ions will also be more in the irradiated FFW. The chain formation also takes place more easily in case of bigger particles. In addition to the particle growth, newly formed defects have resulted in the improved FR of γ -irradiated FFW.

6.2. Concluding remarks

The comparative analysis of different Fe_3O_4 system based FFs namely; FFW and FFG reveal that the viscosity of the carrier is an important parameter in determining MO responses (FR rotation and LD) of FFs. It is less significant in case of highly viscous carrier fluid. The Verdet constant is ~25% more in case of FFW than the former one owing to the large viscosity of kerosene. The keV scale-energetic ion irradiation and γ -irradiation also affect the FR of the FF appreciably. The irradiation lead modification of the FR response of FFW depends on the energy loss of the incident radiation during exposure. To be specific, irradiation induced defects and growth of the MNPs have caused enhanced FR response. As compared to the pristine FFW, the Verdet constant is enhanced by ~ 70% and ~10% in case of γ -irradiated and ion irradiated samples respectively.

References:

- [1] Miller, F.P., Vandome, A.F. and McBrewster, J. *Ferofluid*, VDM Publishing, Verlag, 2010,
- [2] Odenbach, S. (ed.) *Colloidal Magnetic Fluid*, Springer, Verlag, Berlin, Heidelberg, 2009.
- [3] Liu, A. P. et al. Study of Fe_3O_4 nano-magnetic ferrofluid by atomic force microscope, *J. Superconduct. Novel Magn.*, 23, 967-970,2010.
- [4] Cabuil, V. et al. Ionic magnetic fluid based on cobalt ferrite nanoparticles: Influence of hydrothermal treatment on the nanoparticle size, *J. Magn.Magn. Mater.*323, 1238–1241, 2011.
- [5] Chen, C. H. et al. Microfluidic assembly of magnetic hydrogel particles with uniformly anisotropic structure, *Adv.Mater.* 21, 3201–3204, 2009.
- [6] Arco. L. R. et al. Steric repulsion as a way to achieve the required stability for the preparation of ionic liquid-based ferrofluids, *J. Coll. Inter. Sci.* 357, 252–254, 2011.
- [7] Morales, M. B. et al. Particle blocking and carrier fluid freezing effects on the magnetic properties of Fe_3O_4 -based ferrofluids, *J.Appl. Phys.* 105, 07B511-07B511-3, 2009.
- [8] Rawat, S. et al. Study of ferrofluids in confined geometry, *J. Coll.Inter. Sci.*350, 51–57, 2010.
- [9] Ping, C. K. et al. Photon irradiation and modification of chitosan-coated ferrofluid, *Adv. Sci. Lett.*, 19, 516-518,2013.
- [10] Rosensweig, R. E. *Ferrohydrodynamics*. Cambridge University Press, Cambridge, New York 1985.
- [11] Fermigier, M. and Alice, P. Gast A. G. Structure evolution in a paramagnetic latex suspension, *J.Colloid Inter.Sci.* 154, 522-539,1992.
- [12] Hosokawa, M. and Nogi, K.(eds.) *Nano Technology Handbook*, Elsevier, UK,2012.
-

[13] Rodriguez, J. A. and Garcia, M. F. (eds.) *Synthesis, properties and applications of oxide nanomaterials*, Wiley, New Jersey, 2007.

[14] Wu, P. et al. Correlation between photoluminescence and oxygen vacancies in In_2O_3 , SnO_2 and ZnO metal oxide nanostructures, *J. Phys.: Conf. Ser.* 188, 012054-012062, 2009.

[15] N. Paul, M. Devi, D. Mohanta, Synthesis, characterization and effect of low energy Ar ion irradiation on gadolinium oxide nanoparticles, *Mater. Res. Bull.* 46, 1296–1300, 2011.

[16] Devi, M., Paul, N., Mohanta, D. and Saha, A. characteristic spectroscopic properties of γ -irradiated rare-earth oxide-based ferrofluids, *J. Exp. Nanosci.* 7, 586-595, 2012.

7.1. Structure transition in ferrofluid

Ferrofluids or magnetic fluids are very rich in structure formation. As mentioned in previous chapters, FFs exhibit unusual property of particle-chain formation.^[1,2] We have showed (supported by literatures) that the most effective MO and MV effect of FFs come into reality due to the particle chaining effect. The underlying mechanisms of chain formation, kinetics as well as the dynamics of these chains are demanding both in the field of experimental and theoretical research. The mystery of chains continues to be an interesting problem since the discovery of FF till date. In the past, the evidence of field induced aggregations/structures of FF were found in many studies e.g. dichroism,^[3] Raman scattering,^[4] electron microscopy,^[5] small angle neutron scattering (SANS),^[6] atomic force microscopy (AFM),^[7] light scattering^[8] etc. Popplewell *et al* observed a chainlike structure in tin and copper FFs while studying the dichroism in the microwave region. They presented an image of linear arrangement of particles under an external magnetic field applied parallel to the slit containing the particles.^[9] Decades ago, it was seen that magnetic nanoparticles (Co) in a colloidal solution under goes a reversible process of different structures.^[10] First, as the external magnetic field was switched on, the particles form linear chains along the field direction. These chains became floppy after the removal of the field and then folded into three dimensional coiled like structure with gentle agitation. Under vigorous agitation the coiled broke down into smaller units and then turned into homogeneous colloidal solution upon ultra sonication. Some better attestation of magnetic field induced structural evolution of Fe₃O₄ based FF emulsion is also presented in another report.^[11] The detailed structural evolution of the dispersed particles of a FF was found in a light scattering study^[12] in which time-dependent intensity and scattered pattern of particles were recorded. Intensity variation and patterns formed by the scattered light indicated several critical fields. The zippering effect of chains was correlated with these pattern formations.

The phase diagram of chaining effect is also regarded as an important topic in many theoretical and simulated studies. Long back, Krueger attempted to estimate the equilibrium chain lengths in magnetic colloids.^[13] Assuming the grains of identical size, the average number of grains per agglomerate was calculated in that report. A similar effort was also made in a recent study of FF with large but finite aggregates of magnetic dipoles.^[14] It was seen that with increase of size, the aggregates form chains and rings to multi chains and multi rings due to the competition among various energy terms. To unfold this phase diagram different models viz. Monte Carlo modelling,^[15] molecular dynamics,^[16] Brownian dynamics^[17] etc. were employed. Now-a-days, most of the reports on chains are based on computer simulation.^[18-20] Combining nuclear magnetic resonance and molecular simulations, Heinrich *et.al* have elaborated the structure formation in magnetic colloid with strong dipole-dipole interaction.^[21] They reported that the aggregation dynamics of ionic magnetic colloids (like, FF) endure subsequent stages of evolution in a *homogeneous magnetic field*. The different subsequent structural stages were characterized by increasing hierarchical ordering. Researchers also study the chaining mechanism using a two particle theory,^[22] instead of that all particle are strongly interacting (check the correctness). Recently, a statistical-mechanics and computer simulation based dipolar hard sphere model is reported for construction of the pair distribution function (PDF).^[23] This report stipulates that the PDF depends not only on the length of the pair separation vector, but its orientation with respect to field is also equally important.

Besides these stated reports, research is still on so as to evaluate the exact saturation value of the chain length in on/off mode in an external magnetic field. Basically, chain aggregates in magnetic colloid is treated with two approaches. First one is termed as dynamic method.^[22,24] In this method, the recombination of particle is considered as a reversible chemical reaction. The other approach is free energy minimization.^[25] In

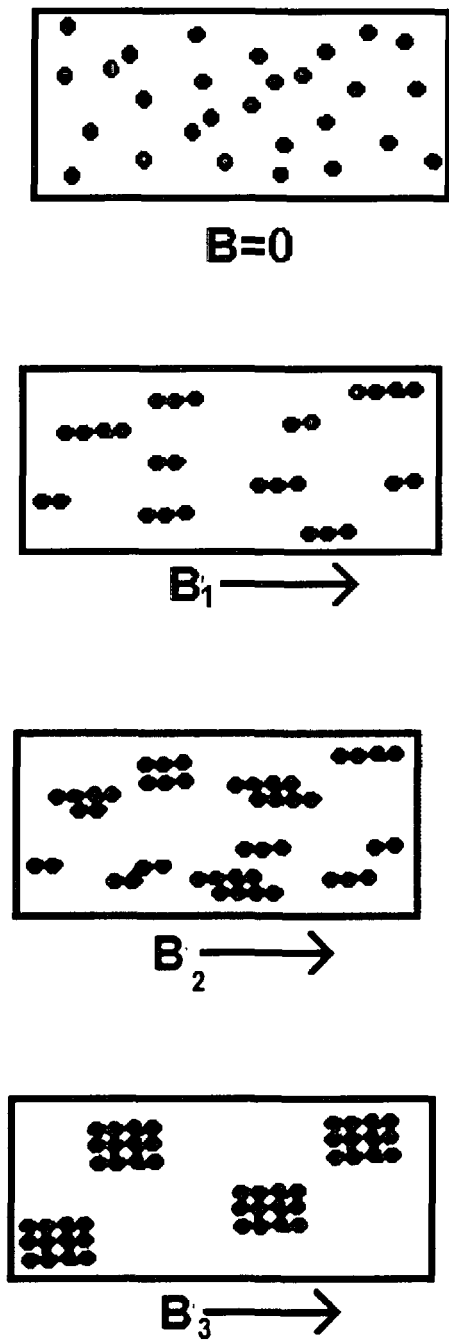


Fig.7.1: Schematic of structural evolution in a FF with increasing magnetic field

the later case, the free energy is considered as a function of chain distribution density. Unfortunately, the problem of structural transition of magnetic fluid/FF brings in cumbersome task. The actual FFs are mostly poly-disperse. For the sake of convenience and ease of modelling only mono-disperse or bi-disperse cases are considered.

Here, an alternative method is endeavoured in perspective of estimation of chain length in FFs under study. The importance of MO /MV effect and its correlation with chain length is elaborated in previous chapters. Here, we associate these effects analytically so as to correlate the chain length with different physical parameters in the light of fluid mechanics. The respective parameters have been obtained from the FR response or/and MV effect studied under a select wavelength and shear flow condition.

7.2. Dimensional analysis

Dimensional analysis is a widely employed technique in science. It is used for design, ordering and performance of model tests. More precisely, dimensional analysis clarifies and explains relationship among different physical quantities by their dimensions.^[26] Though it does not give an absolute analysis; it is a better tool for complete understanding of a problem. Dimensional analysis can also be used to accumulate the results of experiments in a concise, easily reached forms so that the broadly applicable general form can be attained from a small test. It is a general process of removal of units which ultimately removes the conversion factors.

7.2.1. Methods of dimensional analysis

If the number of variables associated with a physical phenomenon is known, then dimensional analysis can be done with the help of the following methods:

(i) Rayleigh's methods

This method is used to determine the expression of a quantity which depends up to a maximum of three to four variables. If the number of independent variables are more than four, it is very difficult to find the expression for the dependent variable by this method. The main drawback of this method is that it does not provide any information regarding the number of dimensionless groups to be obtained as a result of dimensional analysis.^[27]

In Rayleigh's method, a variable is expressed in the form of an exponential equation which must be dimensionally homogeneous. Suppose X is a variable which depends on X_1 , X_2 and X_3 . Then according to the Rayleigh's method:

$$X = f(X_1, X_2, X_3) \quad (7.1)$$

Eq. No.7.1 can be written as:

$$X = C(X_1^a, X_2^b, X_3^c) \quad (7.2)$$

Here, C is a constant and a , b and c are arbitrary exponents. By comparing the powers of the fundamental dimensions of both sides, the values of the arbitrary powers can be calculated.

(ii) Buckingham's π - theorem

The Buckingham π - theorem is an extensively used theorem in dimensional analysis. It is an improvement over the Rayleigh's theorem. The problem of facing more number variables in Rayleigh's theorem can be overcome by this theorem. It gives a relation between a function expressed in terms of dimensional parameters and a related function in terms of non-dimensional parameters. The Buckingham's π - theorem states that in any physical problem where there are "q" quantities (e.g. velocity, pressure etc.) involving "d" basic dimensions (e.g. mass, time, length etc.) needed to describe the problem, these quantities can be

rearranged into at most (q-d) independent dimensionless parameters.^[28] These dimensionless terms are called π -terms.

Mathematically, if a variable X_1 , depends on independent variables $X_2, X_3, X_4, \dots, X_n$, then X_1 can be written as:

$$X_1 = f(X_2, X_3, X_4, \dots, X_n) \quad (7.3)$$

Or, $f_1(X_1, X_2, X_3, X_4, \dots, X_n) = 0 \quad (7.4)$

If there are m fundamental dimensions, then according to the Buckingham's π -theorem Eq.7.4 can be written in terms of π - terms in which number of π - terms is equal to $(n - m)$. Hence Eq.7.4 becomes:

$$f_1(\pi_1, \pi_2, \pi_3, \dots, \pi_{n-m}) = 0 \quad (7.5)$$

Each π -term contains $(m + 1)$ variables. The m variables that appear repeatedly in each π -term are called repeating variables. The repeating variables must be such that they themselves should not form any dimensionless quantity and must contain jointly all the fundamental dimensions present in the problem. If X_2, X_3, X_4 are considered as repeating variables and if there are three fundamental dimensions (say M, L, T), then each π -term will be in the form:

$$\pi_1 = X_2^{a_1} \cdot X_3^{b_1} \cdot X_4^{c_1} \cdot X_1$$

$$\pi_2 = X_2^{a_2} \cdot X_3^{b_2} \cdot X_4^{c_2} \cdot X_5$$

.

.

.

$$\pi_{n-m} = X_2^{a_{n-m}} \cdot X_3^{b_{n-m}} \cdot X_4^{c_{n-m}} \cdot X_n$$

where $a_1, b_1, c_1; a_2, b_2, c_2$ etc. are constants. These constants are determined by considering dimensional homogeneity. The final general equation for the phenomenon may be obtained as follows,

$$\begin{aligned}\pi_1 &= \varphi(\pi_2, \pi_3, \pi_4 \dots \dots \pi_{n-m}) \\ \pi_2 &= \varphi(\pi_1, \pi_3, \pi_4 \dots \dots \pi_{n-m})\end{aligned}$$

7.2.2. Error analysis

The error/uncertainty creeps into all experimental data in spite of adequate care is extended to calibration and data acquisition process. Analysis must be performed on all experimental results to ease out uncertainty and restrict into minimal errors. The accuracy of an experiment is limited unless it is scrutinized by error analysis. While performing an experiment, errors come out due to various reasons, viz. the faulty design of the experimental setup, insufficient data, lack of calibration etc. The errors can be of different origin and nature. They may be random errors, fixed errors (appear in repeated reading by the same amount but for unknown reasons) etc.^[29]

(i) Uncertainty analysis

The errors in the experimental data lead to some extent of uncertainty in the results. Thus, the amount of uncertainty has to be calculated in a definite way. Based on specification of the uncertainty in the various primary experimental measurements, Kline and McClintock proposed a method to estimate the uncertainty in experimental results, given by:^[30]

$$W_r = \left[\left(\frac{\partial R}{\partial x_1} W_1 \right)^2 + \left(\frac{\partial R}{\partial x_2} W_2 \right)^2 + \dots \dots \dots \right]^{1/2} \quad (7.6)$$

Here, R is an experimental result and function of independent variables $x_1, x_2, x_3 \dots$, the uncertainty in the result is W_r and that in the independent variables are $w_1, w_2, w_3 \dots$

7.3. Analytical calculation of chain length in ferrofluid

We have studied the FR response of the synthesized FF as well as of irradiated FFs. The experimental observations intimate enhanced FR as a result of low energy ion and γ -ray irradiation. A significant modification of

the value of the Verdet constant due to the irradiation effect is also observed. Basically, the chaining effect is responsible for the observed magneto-optic effect in FF. It is seen that the FR first increases with field and then tends to saturate. On the other hand, the saturation indicates the limit of a chain. Zippering or bundle of chains starts from the saturation point. The magnetic property of FF also governs the Faraday response. Eq.3.1 (*Chapter 3*) evidently signifies the dependence of FR on magnetization and chain length. Again, the chaining effect is expected to be controlled by the particle size, magnetization and other parameters (*coupling constant, Eq.5.1 of Chapter 5*). We have measured the magnetization of our samples in a hysteresis loop tracer kit (Model HLT-111).

During the course of study of the FR of different FFs, it was noticed that the viscosity of carrier fluid plays an important role (*Chapter 3*). The larger the viscosity of the carrier fluid, the smaller is the response. As discussed in the previous chapter, the viscous force acts as a hindrance to the chain formation. Thus, the FR as well as the Verdet constant decreases with increase in viscosity of the fluid.

FR of FF has been studied under different conditions till date. Report shows that it also depends on the concentration of FF (*reference 22 of Chapter 3*). The chain length at a given field is found to be linear with concentration. This linearity in turn, makes the FR dependent of concentration dependant. The concentration of any ferrofluid is expressed in terms of v/v or wt/v. It mainly signifies the density of the dispersed particles with surfactant coating.

In a FF the dispersed nanoparticles experience translational motion under a magnetic field. The translational motion is characterized by both translational and rotational motion. In other words, the particles endure magnetic force driven diffusion process. The overall change of the particle concentration is more important than the individual velocity and trajectory of the particle in such condition. In a FF flow, the velocity gradient plays a

crucial role in chaining effect. The gradient of velocity in any flowing material can be expressed by one term, i.e. shear rate. It has been reported earlier (*Ref. 59 of Chapter 3*) that shear rate has a significant influence on the particles' chain in a definite FF. With increasing shear rate, the agglomerations or the chains break down resulting in non Newtonian nature of FF. Thus the transformation of the optical property of FF with shear rate is much expected like MV effect.

On the basis of the above discussion, we try to find an empirical correlation of FR response in terms of different factors. For the convenience of dimensional analysis by Buckingham's π – theorem, we consider the Verdet constant, rather than the rotation itself. First it is supposed that, the Verdet constant (V) of a FF is a function of: chain length (l), particle diameter (D), viscosity of the carrier fluid (η), particle density (ρ), magnetization (m), shear rate ($\dot{\gamma}$).

Mathematically, it can be expressed as:

$$V = f(l, D, \eta^{-1}, \rho, m, \dot{\gamma}) \quad (7.7)$$

$$\text{Or,} \quad f_1(V, l, D, \eta^{-1}, \rho, m, \dot{\gamma}) = 0 \quad (7.8)$$

Thus, the total number of variables = 7.

In order to find the total number of fundamental dimensions, we express each of the variables in terms of their dimensions as follows,

$$V = M^{-1}L^{-1}Q \text{ (rad/T-m)}$$

$$l = L \text{ (m)}$$

$$D = L \text{ (m)}$$

$$\eta^{-1} = M^{-1}LT \text{ (Pa.s)}^{-1}$$

$$\rho = ML^{-3} \text{ (kg/m}^3\text{)}$$

$$m = L^{-1}T^{-1}Q \text{ (A/m)}$$

$$\dot{\gamma} = T^{-1} \text{ (s}^{-1}\text{)}$$

The total number of fundamental dimensions = 4 (M, L, T and Q)

According to the Buckingham's π - theorem, total number of π terms= 3. Consequently, three π - terms (say, π_1, π_2 and π_3) are formed. Now, equation 7.7 can be rewritten as:

$$f_1(\pi_1, \pi_2, \pi_3) = 0 \quad (7.9)$$

Selection of repeating variables

In this problem, we find that total number of fundamental dimensions is four. Therefore, out of the seven quantities ($V, l, d, \mu^{-1}, \rho, m, u$), four variables must be chosen as repeating variables. Being the dependent variable, V is discarded from selecting as repeating variable. We consider $l, \rho, m, \dot{\gamma}$ as repeating variables as the fundamental dimensions M, L, T and Q are present in them and they do not form any dimensionless term.

Now, the three π terms are selected as follows:

$$\pi_1 = l^{a_1} \dot{\gamma}^{b_1} \rho^{c_1} m^{d_1} V$$

$$\pi_2 = l^{a_2} \dot{\gamma}^{b_2} \rho^{c_2} m^{d_2} \eta^{-1}$$

$$\pi_3 = l^{a_3} \dot{\gamma}^{b_3} \rho^{c_3} m^{d_3} D$$

Each π term is solved by the principle of dimensional homogeneity as follows:

π_1 - term:

$$M^0 L^0 T^0 Q^0 = L^{a_1} \cdot (T^{-1})^{b_1} \cdot (ML^{-3})^{c_1} \cdot (L^{-1}T^{-1}Q)^{d_1} \cdot (M^{-1}L^{-1}Q)$$

Comparing the exponents of M, L, T and Q respectively,

$$\text{For } M: 0 = c_1 - 1$$

$$\text{For } L: 0 = a_1 - 3c_1 - d_1 - 1$$

$$\text{For } T: 0 = -b_1 - d_1$$

For Q : $0 = d_1 + 1$

Solving these, we get, $a_1 = 3$, $b_1 = 1$, $c_1 = 1$ and $d_1 = -1$

$$\therefore \pi_1 = l^3 \dot{\gamma} \rho m^{-1} V$$

π_2 -term:

$$M^\circ L^\circ T^\circ Q^\circ = L^{a_2} \cdot (T^{-1})^{b_2} \cdot (ML^{-3})^{c_2} \cdot (L^{-1}T^{-1}Q)^{d_2} \cdot (M^{-1}LT)$$

Comparing the exponents of M, L, T and Q respectively,

For M : $0 = c_2 - 1$

For L : $0 = a_2 - 3c_2 - d_2 + 1$

For T : $0 = -b_2 - d_2 + 1$

For Q : $0 = d_2$

Solving these on equal footing, we get, $a_2 = 2$, $b_2 = 1$, $c_2 = 1$ and $d_2 = 0$

$$\therefore \pi_2 = l^2 \dot{\gamma} \rho \eta^{-1}$$

π_3 - term:

$$M^\circ L^\circ T^\circ Q^\circ = L^{a_3} \cdot (T^{-1})^{b_3} \cdot (ML^{-3})^{c_3} \cdot (L^{-1}T^{-1}Q)^{d_3} \cdot L$$

Comparing the exponents of M, L, T and Q respectively,

For M : $0 = c_3$

For L : $0 = a_3 - 3c_3 - d_3 + 1$

For T : $0 = -b_3 - d_3$

For Q : $0 = -d_3$

Solving these, we obtain, $a_3 = -1$, $b_3 = 0$, $c_3 = 0$ and $d_3 = 0$

$$\therefore \pi_3 = l^{-1} D$$

Substituting the value of π_1, π_2 and π_3 in Eqn. 7.8 we get,

$$f_1(l^3 \dot{\gamma} \rho m^{-1} V, l^2 \dot{\gamma} \rho \eta^{-1}, l^{-1} D) \quad (7.10)$$

Or,
$$l^3 \dot{\gamma} \rho m^{-1} V = c (l^2 \dot{\gamma} \rho \eta^{-1})^p (l^{-1} D)^q \quad (7.11)$$

Here, c is a material specific constant. Now, taking \ln on both the sides,

$$\ln (l^3 \dot{\gamma} \rho m^{-1} V) = \ln [c (l^2 \dot{\gamma} \rho \eta^{-1})^p (l^{-1} D)^q] \quad (7.12)$$

$$(3 - 2p + q) \ln l = \ln c + (p - 1) \ln \dot{\gamma} + (p - 1) \ln \rho - p \ln \eta + \ln m - \ln V + q \ln D \quad (7.13)$$

The p and q values were determined with the help of the experimental results. The values of different parameters corresponding to a field ~ 100 G used in this calculation are highlighted in Table 7.1.

Table 7.1: Different parameters obtained from experimental results.

FF	V (rad/T-m)	$\dot{\gamma}$ (s ⁻¹)	η (Pa-s)	m (A/m)	D (m)	ρ (kg/m ³)
FFW	0.11x10 ³	4	0.0073	3529	8x10 ⁻⁹	0.175
FFK	0.081x10 ³	5.1	0.0082	3508	10x10 ⁻⁹	0.175
FF1	0.05x10 ³	44.3	0.009	2400	12x10 ⁻⁹	0.66
FF2	0.052x10 ³	22.8	0.013	2400	12x10 ⁻⁹	0.66

Using Eq. 7.13 for different sets of data as shown in table 7.1, the values of p and q are found to be ~ 0.67 and ~ 2 . Putting the value of p and q in Eq.7.13, we get:

$$3.7 \ln l = \ln c - 0.31 \ln \dot{\gamma} - 0.31 \ln \rho - 0.68 \ln \eta + \ln m - \ln V + 2 \ln D \quad (7.14)$$

$$\text{Or, } \ln l = 0.27 \ln c - 0.09 \ln \dot{\gamma} - 0.09 \ln \rho - 0.18 \ln \eta + 0.27 \ln m - 0.27 \ln V + 0.56 \ln D \quad (7.15)$$

The eqn. (7.15) gives an empirical formula for obtaining chain length of nanoparticles in a given FF. The values of all the variables/measurable parameters in the above equation can be evaluated experimentally. The value of the constant c is determined from the initial condition that, in the absence of an applied magnetic field the particles are in random motion. In that case, the length of the field induced chain is considered as zero. Consequently, the value of the Verdet constant is also discarded. Under high shear rate condition, the few pre-existing aggregates break down resulting in a uniformly dispersed FF with comparatively low viscosity. The initial parameters corresponding to zero chain length and calculated value of the constant c for each data set are shown in Table 7.2.

Table 7.2: Different initial parameters.

FF	$\dot{\gamma}$ (s ⁻¹)	η (Pa-s)	m (A/m)	D (m)	ρ (kg/m ³)	$\ln c$
FFW	90	0.005	3529	8x10 ⁻⁹	0.175	9.81
FFK	110	0.0059	3508	10x10 ⁻⁹	0.175	9.48
FF1	100	0.0064	2400	12x10 ⁻⁹	0.66	10.88
FF2	105	0.011	2400	12x10 ⁻⁹	0.66	10.96

Finally, the predicted chain lengths of different FFs for a static field strength ~ 100 G are shown in Table 7.3:

Table 7.3: Calculated chain length for different FFs.

FF	Chain length (μm)
FFW	400
FFK	500
FF1	600
FF2	700

It was found that, the MNPs of the FFs are capable of forming chains of length in the micrometre range when subjected to an applied field of ~ 100 G. This is supported by an earlier report that, a Fe_3O_4 magnetic fluid with polymer acrylic resin forms chains of length in the micrometre scale ($>200 \mu\text{m}$) in response to a moderate magnetic field strength (281-1030) Oe [31]. With reference to eqn. (3.1) of *Chapter 3*, it can be said that the bigger particles have a better chain forming capability than the smaller ones. The calculated smaller chain length in FFW than in FFK is mainly attributed to the smaller particle size in the former FF. Furthermore, the magneto-rheological response (*page 84 of Chapter 3*) shows that, the FF2 responds more promptly to the field than that of FF1. In fact, the dispersion stability of surfactant depends on the hydrocarbon chain length. Due to the longer hydrocarbon chain, the absorption free energy in TMAH (surfactant of FF1) is higher than that of oleic acid (surfactant of FF2).^[32] Consequently, the chaining effect can be adequately suppressed owing to better chemical stability of FF1 over its FF2 counterpart. In addition, a larger value of the shear rate in FF1 in the calculation part, could also contribute to the shorter chain length. Not surprisingly, the chains or aligned aggregates could break down at an increased shear rate.

Uncertainty calculation

The uncertainty in the above calculation is determined by the following the method as described in *section 7.2.2(i)* of this chapter. The uncertainty in each data set is calculated by the Eq.(7.6). The errors in individual data and overall uncertainty corresponding to the chain length of a FF are described in Table 7.4.

7.3. Concluding remarks

The dimensional analysis of the Verdet constant and its dependency on various parameters, following the Buckingham's π – theorem, gives an empirical formula to calculate the chain length of FF. It is calculated for four

different FF systems with varying MO and MV conditions. The chain length for all the four FFs is found in the micrometre range and with nominal uncertainty.

Table 7.4: Error analysis and overall uncertainty.

FF	V (rad/T-m)	η (Pa-s)	m (A/m)	D (m)	ρ (kg/m ³)	W_r
FFW	± 0.0014	± 0.05	± 3	$\pm 2 \times 10^{-9}$	± 0.007	~ 0.5
FFK	± 0.0018	± 0.0821	± 1	$\pm 2 \times 10^{-9}$	± 0.007	~ 0.75
FF1	± 0.0098	± 0.0637	± 2	$\pm 2 \times 10^{-9}$	± 0.002	~ 0.54
FF2	± 0.0052	± 0.03	± 2	$\pm 2 \times 10^{-9}$	± 0.002	~ 0.002

References:

- [1] Zubarev, A.Y. and Iskakova, L.Y. Theory of structural transformations in ferrofluids: chains and "gas-liquid" phase transitions, *Phys Rev E*. 65, 061406-061409, 2002.
- [2] Odenbach, S. *Colloidal Magnetic fluids*, Springer, Verlag, 2009.
- [3] Davies H. W. and Llewellyn J P., Magneto-optic effects in ferrofluids, *J. Phys. D: Appl. Phys.* 13, 2327-36, 1980.
- [4] Mendeleev, V. S. and Ivanov, A. O. Ferrofluid aggregation in chains under the influence of a magnetic field, *Phys. Rev. E*. 70, 051502-051512, 2004.
- [5] Butter, K. et al. Direct observation of dipolar chains in iron ferrofluids by cryogenic electron microscopy, *Nat Mater*. 2, 88-91, 2003.
- [6] Pyanzina, E. et al. Structure factor of ferrofluids with chain aggregates: Theory and computer simulations, *J. Magn. Magn. Mater.* 323, 1263-1268, 2011.
- [7] Groß, C. et al. Characterization of a ferrofluid by atomic force microscopy and photon correlation spectroscopy after magnetic fractionation, *Euro. Cell. Mater.* 3, 163-166, 2002.
- [8] Laskar, J.M. et al. Comparison of light scattering from self assembled array of nanoparticle chains with cylinders, *Opt. Commun.* 285, 1242-1247, 2012.

- [9] Popplewell, J. et al. Microwave properties of ferrofluid composites, *J. Magn. Magn. Mater.* 54-57, 761-762, 1986.
- [10] Guangjun, C. et al. Magnetic-field-induced assemblies of cobalt nanoparticles, *Langmuir* 21, 12055-12059, 2005. .
- [11] Ivey, M. et al. Magnetic-field-induced structural transitions in a ferrofluid emulsion, *Phys. Rev. E.*, 63, 011403-011413, 2003.
- [12] Laskar, J. M. et al. Experimental evidence for reversible zippering of chains in magnetic nanofluids under external magnetic fields, *Phys. Rev. E.* 80, 041401-041408, 2009.
- [13] Krueger D. A. Theoretical Estimates of Equilibrium Chain Lengths in Magnetic Colloids, *J Coll. Inter. Sci.* 70, 558-563, 1979.
- [14] Yoon, M. and Tomanek D. Equilibrium structure of ferrofluid Aggregates, *J. Phys.: Condens. Matter* 22 , 455105-455110, 2010.
- [15] Tran, N.L. and Tran, H.H. Role of the poly-dispersity and the dipolar interaction in magnetic nanoparticle systems: Monte Carlo study, *J. Non-Crystal. Sol.*357, 996–999, 2011.
- [16] Tanygin, B.M. et al. Molecular dynamics study of the primary ferrofluid aggregate formation, *J. Magn. Magn. Mater.* 324, 4006–4010, 2012.
- [17] Aquino, D. S., Rosso, D. and Rinaldi, C. Oscillatory shear response of dilute ferrofluids: Predictions from rotational Brownian dynamics simulations and ferrohydrodynamics modelling, *Phys. Rev. E* .84, 056306 - 0563115, 2011.
- [18] Kantorovich, S. et al. Microstructure analysis of monodisperse ferrofluid monolayers: theory and simulation, *Phys. Chem. Chem. Phys.*, 10, 1883-1895, 2008 .
- [19] Pyanzina, E. S. and Kantorovich, S. S. Structure factor of ferrofluids with chain aggregates: Influence of an external magnetic field, *Phy. Particle. Nucl. Lett.* 8, 051-1053, 2011.

- [20] Jian, Y. C. et al. Structure of polydisperse inverse ferrofluids: Theory and computer simulation, *J. Phys. Chem. B.* 112, 715–721, 2008.
- [21] Heinrich, D. et al. Dynamics of the field-induced formation of hexagonal zipped-chain superstructures in magnetic colloids, *Phys. Rev.Lett.* 106, 208301-208304, 2011.
- [22] Jordan, P. Association phenomena in a ferromagnetic colloid, *Mol. Phys.* 25, 961-973, 1973.
- [23] Ekaterina, A. Theory and simulation of anisotropic pair correlations in ferrofluids in magnetic fields, *J. Chem. Phys* 136, 194502-194513, 2012.
- [24] Jordan, P. Field dependent chain formation by ferromagnetic colloids, *Mol. Phys.* 38, 769-780, 1979.
- [25] A. Yu. Zubarev and L. Yu. Iskakova, Theory of physical properties of magnetic liquids with chain aggregates, *J. Exp. Theor. Phys.* 80, 857-866, 1995.
- [26] Palmer, A.C. *Dimensional analysis and intelligent experimentation*, World Scientific Publishing, Singapore, 2008.
- [27] Rajput, R.K. *Heat and mass transfer*, S. Chand & company, New Delhi, 2004.
- [28] Graebel, W.P. *Engineering fluid Mechanics*, Taylor and Francis, New York, 2001.
- [29] Holman, J.P. *Experimental methods for engineers*, Tata McGraw Hill, New Delhi, 2007.
- [30] Kline, S. J. and McClintok, F. A., *Describing Uncertainties in single sample experiments*, *Mech. Eng.* 75, 3-8, 1953.
- [31] Fang, W.-X. et al. Magnetic-field-induced chain-like assembly structures of Fe₃O₄ nanoparticles, *Euro. Phys. Lett.* 77, 68004-68009, 2007.
- [32] Hetem, M.J.J. Influence of alkyl chain length on the stability of n-alkyl-modified reversed phases. 1. chromatographic and physical analysis, *Anal. Chem.* 62, 2288-2296, 1990.

The importance of ferrofluids is not only customary to the material scientists but also to the technologists to benefit the society at large. The FF based devices are not only limited to day to day components but also useful to the space crafts and submarine parts. The role of MNPs, surfactant and carrier fluid is inevitable in determining the technologically important MO and MV properties of the FF. In this context, this work is an endeavor to synthesize diverse FF systems, both conventional and novel kinds, followed by characterization by different microscopic and spectroscopic tools. To be specific, magnetite (Fe_3O_4) and gadolinium oxide (Gd_2O_3) based FFs were prepared. The nanoparticles of the FFs were spherical in shape and ~ 9 nm in size. The role of surfactants as well as carrier fluids were also studied by synthesizing FF with anionic surfactant (*oleic acid*) and cationic surfactant (*TMAH*) coated Fe_3O_4 MNPs in different kinds of carrier fluids (water, kerosene and methanol). Various analytical tools have revealed that the particles were well functionalized by the respective surfactants to form suitable, stable FFs.

The MO effects of the synthesized FFs were studied in a custom made experimental set-up. The FR and LD response of the ferrofluids FFW and FFK are noteworthy, seems to saturate beyond an applied field. The magneto-rheological study of the synthesized FFs namely, FF1 and FF2 showed improved viscoelastic response with the increasing applied field. In other words, FFs are highly magneto-viscous in nature. In fact, these FFs exhibited the non Newtonian nature. A comparative study of the magneto-viscous properties of FF1 and FF2 for various shear rates ($2\text{-}450 \text{ sec}^{-1}$) and applied magnetic fields ($0\text{-}100 \text{ G}$) have showed that, in case of no field and under no shear, the FF prepared with the oleic acid coated particle (FF1) tends to be $\sim 12\%$ more viscous as compared to its TMAH coated counterpart (FF2). Furthermore, it was observed that, the particles in FF2 were more dispersed than FF1. The better stability of FF2 was attributed to the longer hydrocarbon chain length of TMAH than that of oleic acid.

In order to study the effect of energetic ion irradiation, FFs were also prepared with 80-keV Ar-ion irradiated MNPs. The creation of point defects on the nano particles by 80 keV Ar-ion irradiation were predicted by in-depth spectroscopic analyses. The signature of partial phase transformation from B-type to A-type crystal system of Gd_2O_3 nanoparticles (reveals from the Raman analysis) is an important consequence of the ion irradiation.

For comparative analysis, FFs were also irradiated with γ -radiation and of doses: 32 to 2.635 kGy. Different characterizations of the irradiated FFs illustrate that γ -irradiation could lead to substantial growth of the MNPs in case of FFW and FFK. The optical microscopy and spectroscopic tools have probed that, in case of FFW, the particle growth was from ~ 9 nm to ~ 48 nm whereas, in the latter case (FFK), it was from ~ 9 nm to ~ 18 nm for pristine and irradiated (dose: 2.635 kGy) samples; respectively. The creation of new defects (e.g. oxygen vacancy) and annihilation of some pre-existing defects in particles of FFW, FFK and FFG were also manifested in analytical tools such as, HRTEM, FT-IR spectroscopy, Raman spectroscopy and EPR spectroscopy. Moreover, γ -irradiation was shown to alter the luminescence property of the FFs. The room temperature photoluminescence study of FFG gave an evidence of red-shift of the PL peak. It is considered that the shift is due to the irradiation induced defects. It also reveals the impact of γ -irradiation on improving the PL symmetry factor of Gd_2O_3 by $\sim 20\%$. On administering the deconvolution process so as to study asymmetric nature of PL spectra of γ -irradiated FFG, it was seen that intensity and symmetry of the PL spectra can be tuned with the irradiation dose.

The effect of the two above mentioned irradiation processes on the MO responses of the FFs were also prominent in the Faraday rotation and linear dichroism study. The modified FR and LD responses were attributed

to the defect formation due to the low energy (80-keV) Ar-ion and γ -irradiation process. The optical path within the nanoparticles gets enhanced due to the newly formed defects. Further, the growth of the MNPs due to the solid state recrystallization during γ -irradiation also results in the modification of the MO responses. As mentioned in Chapter 5, larger particles rapidly form chains in response to the applied field and consequently, the FR and LD response become significant. The Verdet constant of the FFs were also changed by the irradiation impact. In case of γ -irradiated (dose: 2.635 kGy) FFW, the enhancement was as high as ~70%.

Lastly, as an alternative but innovative approach, the calculation of chain length of particles in FF was established with the help of dimensional analysis. Following Buckingham's π – theorem, the chain length was expressed empirically in terms of various measurable quantity viz. magnetization, density, particle size, Verdet constant, shear rate, viscosity. The accuracy of the calculated value of the chain length was tested by the uncertainty analysis.

During this course of study, adequate care was taken to minimize the time gap between the synthesis process and characterization of the nanoparticles as well as the FFs. Due to the high mechanical and chemical stability of RE element; it was difficult to synthesize Gd_2O_3 nanoparticles from their bulk counterpart. In this context, a physico-chemical method was followed to prepare the same. But the adopted procedure for the synthesis of Gd_2O_3 nanoparticles needs to be improved further to get sufficient amount of MNPs. We have studied the low energy ion irradiation and γ -irradiation effect. As the MO responses show significant improvement of the irradiated samples, there is a scope of a detailed study using other radiation sources and doses. In this regard, UV-radiation and high energetic ion (a few MeV) would give a complete picture of the radiation

induced changes of FFs. It may be noted, however, in order to ensure precise control over FF properties, better techniques may be opted considering possibility of irradiation on FF films -rather than on MNPs meant for making FFs.

In our case, a custom made setup was employed to study the magneto-optic response of the FFs. This initial set-up comprised of manual devices which had to be calibrated prior to data acquisition process. In this regard, modification with computer interfacing can provide ample scope for fast data processing with improved accuracy.

The beauty of FF is much devoted to its chain forming effect. We have predicted an empirical formula to calculate the chain length of FF. In the present study only the structural evolution to linear chains is considered. But the actual evolution process is much more complicated. Further investigation with regard to linear chain, multi-chain formation, zippering effect or combination of these needs to be worked out, based on the influence of different parameters/forces acting on the particles. Towards this end, computer simulation is highly acceptable. However, the present work is an attempt to provide wealth of technologically important information with regard to ferrofluids both iron based and rare earth based ones. The following device and design concepts could be applicable to the investigated systems of topical interest.

(i) Rare-earth oxide based FF sealing/shielding: FF based sealing and shielding devices are widely used in space craft, loud speaker cooling etc. RE system is chemically inert. In this present investigation, it was seen that RE oxide (Gd_2O_3) based FF provide stable dispersion with controlled MO feature. Thus, such a system will be more promising over the conventional type FFs ensuring suitable candidate in sealing and electromagnetic shielding devices.

(ii) Radiation detector: The MO study of the different irradiated FF sample reveals that the MO responses get modified by the irradiation. It also changes with the energy of the incident radiation. Further study on this perception would be beneficial to prior design of a prototype radiation detector.

(iii) Ferrofluid based MRI contrast agent: MRI (Magnetic resonance imaging) is a widely used technique in medical diagnosis process. It is used to visualize the internal structure of a body in detail. In this process, magnetic particles are injected to the vein of a patient and the patient lies inside a powerful magnetic field. The magnetic particles could enhance the contrast of the blood vessels, tumors etc. Ferrofluid can be used as a normal liquid as well as a magnetic liquid in presence of a field. FFs are also used in targeted drug delivery process. Thus, ferrofluid (with drug) would be a better option as MRI contrast agent. FF based simultaneous preliminary drug injection and contrast agent would be an uprising process in the field of medical science and diagnosis.

Appendix I

Tensile strain and compressive strain: In dynamics of rigid body, the changes occurred in a body are describes by the terms: stress, strain and modulus of elasticity. Stress is a measurement of the strength of a material, strain is a measure of the change in the shape of the object that is undergoing stress whereas elastic modulus measures the amount of stress needed to change the shape of the object.

In the Fig. 1(a), a body of cross sectional area A is subjected to a tensile force P . Then the tensile stress is expressed as:

$$\sigma = P/A$$

If the original length of the body is L and it becomes $(L + \Delta L)$ after the force applied, the term strain measures the deformation of the body. It is define as:

$$\text{Strain} = \Delta L/L$$

The compressive strain [(Fig. 1(b))] is related with a compressive force. In such case the strain is negative as the length decreases due to the force applied [Fig. 1(b)]

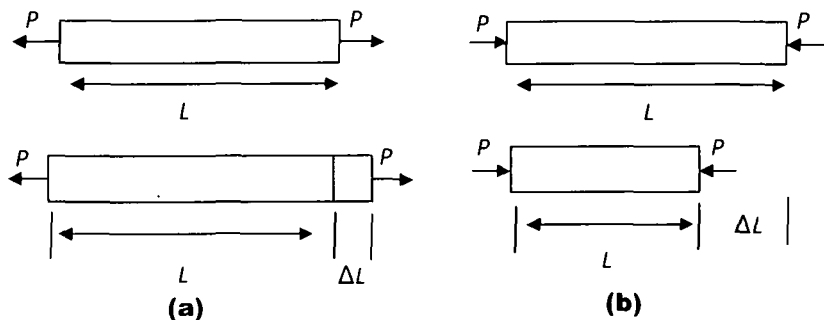


Fig. 1: (a) Tensile and (b) compressive strain

Appendix II

Physical properties of host materials

Properties of oleic acid	
Molar mass	282.4614 g mol ⁻¹
Appearance	Pale yellow or brownish yellow oily liquid with lard-like odor
Density	0.895 g mL ⁻¹
Melting point	(13-14) °C
Boiling point	360 °C

Properties of ethanol	
Molar mass	46.07 g mol ⁻¹
Appearance	Colorless liquid
Density	0.789 g cm ⁻³
Melting point	-114 °C, 159 K, -173 °F
Boiling point	78 °C, 351 K, 172 °F
Vapor pressure	5.95 kPa (at 20 °C)
Acidity (pK _a)	15.9
Basicity (pK _b)	-1.9
Refractive index (n _D)	1.36
Viscosity	0.0012 Pa s (at 20 °C)

Properties of TMAH	
Molar mass	91.15 g mol ⁻¹
Appearance & Odor	Clear, colorless. Slight amine odor
Boiling Point	>100°C
Melting Point	< 0°C
Physical State	Liquid
pH	>12.5
Specific Gravity	1.0-1.1

Properties of methanol

Molar mass	32.04 g mol ⁻¹
Appearance	Colorless liquid
Density	0.7918 g cm ⁻³
Melting point	-98--97 °C
Boiling point	65 °C
Viscosity	5.9×10 ⁻⁴ Pa s (at 20 °C)
Dipole moment	1.69 D

Appendix III

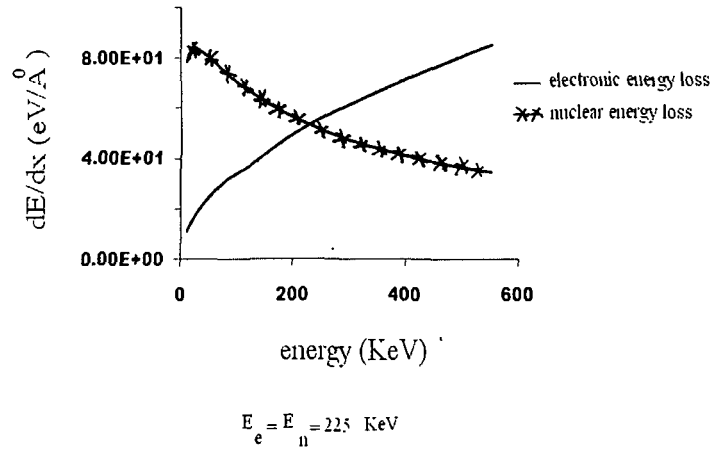


Fig: SRIM calculation for Ar ion irradiation on Fe_3O_4

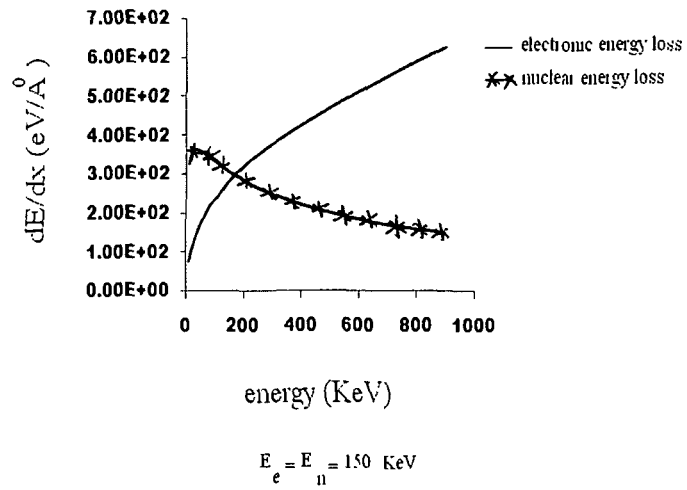


Fig: SRIM calculation for Ar ion irradiation on Gd_2O_3

Publications

1. Devi, M. and Mohanta, D. Rheological properties of iron oxide based ferrofluids, *AIP Conf. Proc.* CP1147,495-501, 2009.
2. Paul, N., Devi, M. and Mohanta, D. Synthesis, characterization and effect of low energy Ar ion irradiation on gadolinium oxide nanoparticles, *Mat. Res. Bull.* 46, 1296-1300, 2011
3. Devi, M., Das, R., Mohanta, D. ,Saha, A. and Baruah, K.K. Enhanced magneto-optic activity of magnetite-based ferrofluids subjected to gamma irradiation, *Appl. Phy. A*, 106,765-771, 2012
4. Devi, M., Paul, N., Mohanta, D. and Saha, A. Characteristic spectroscopic properties of γ -irradiated rare-earth oxide-based ferrofluids, *J. Exp. Nanosci.*, 7,586-595, 2012.
5. Paul, N., Devi, M., Mohanta, D. and Saha, A. Magnetically induced optical activity and dichroism of gadolinium oxide nanoparticle-based ferrofluids, *J. Appl. Phys.* 111, 044904-044909, 2012.

ADDENDA

Rheological Properties of Iron Oxide Based Ferrofluids

M. Devi^a and D. Mohanta^b

Nanoscience Laboratory, Department of Physics, Tezpur University, Tezpur 784028, Assam, India

^a manasidevi25@gmail.com; ^b best@tezu.ernet.in

Abstract. In the present work, we report synthesis and magneto-viscous properties of cationic and anionic surfactant coated, iron oxide nanoparticles based ferrofluids. Structural and morphological aspects are revealed by x-ray diffraction (XRD) and transmission electron microscopy (TEM) studies. We compare the rheological/magneto-viscous properties of different ferrofluids for various shear rates (2- 450 sec⁻¹) and applied magnetic fields (0-100 gauss) In the absence of a magnetic field, and under no shear case, the ferrofluid prepared with TMAH coated particle is found to be 12% more viscous compared to its counterpart. The rheological properties are governed by non-Newtonian features, and for a definite shear rate, viscosity of a given ferrofluid is found to be strongly dependent on the applied magnetic field as well as nature of the surfactant.

Keywords: Ferrofluids, surfactant; rheological properties.

PACS: 81.07.-b, 66.20.Ej, 75.75.+a

INTRODUCTION

In recent years, ferrofluid systems have emerged as technologically important candidates with prospective applications in magneto-sealing, magneto-shielding, biomedicine etc. [1-4]. These technological attractions are basically due to their unique magneto-viscous properties (magnetic control of their flow). Ferrofluid is a colloidal solution of magnetic nanoparticles (MNPs) and therefore, a ferrofluid can exhibit magneto-viscous effect [5-7]. In ferrofluid synthesis method, the most commonly used nanoparticles are magnetite (Fe₃O₄) and maghemite (γ -Fe₂O₃) and oil, water, kerosene etc. are used as dispersing media. In this kind of fluid, different long and short range forces result in sedimentation and agglomeration of the particles. The stability of this kind of fluid can be attained either by steric repulsion or by charging the particles electrically [8]. In case of steric repulsion, the MNPs are coated with a surfactant layer (anionic, cationic, zwitterionic etc). The surfactant molecule gets attached to the surface of the nanoparticles and helps in gaining the stability of the fluid by stopping agglomeration. Generally, particles of size 4 - 20 nm with a surfactant layer of thickness \sim 2 nm result in a good quality ferrofluid [9]. In a ferrofluid flow, the magnetic moment of the particles is aligned with the vorticity of the flow and in presence of a magnetic field the MNPs would try to reorient themselves. This is very important in deciding the rheological properties of the fluid and crucial for many devices.

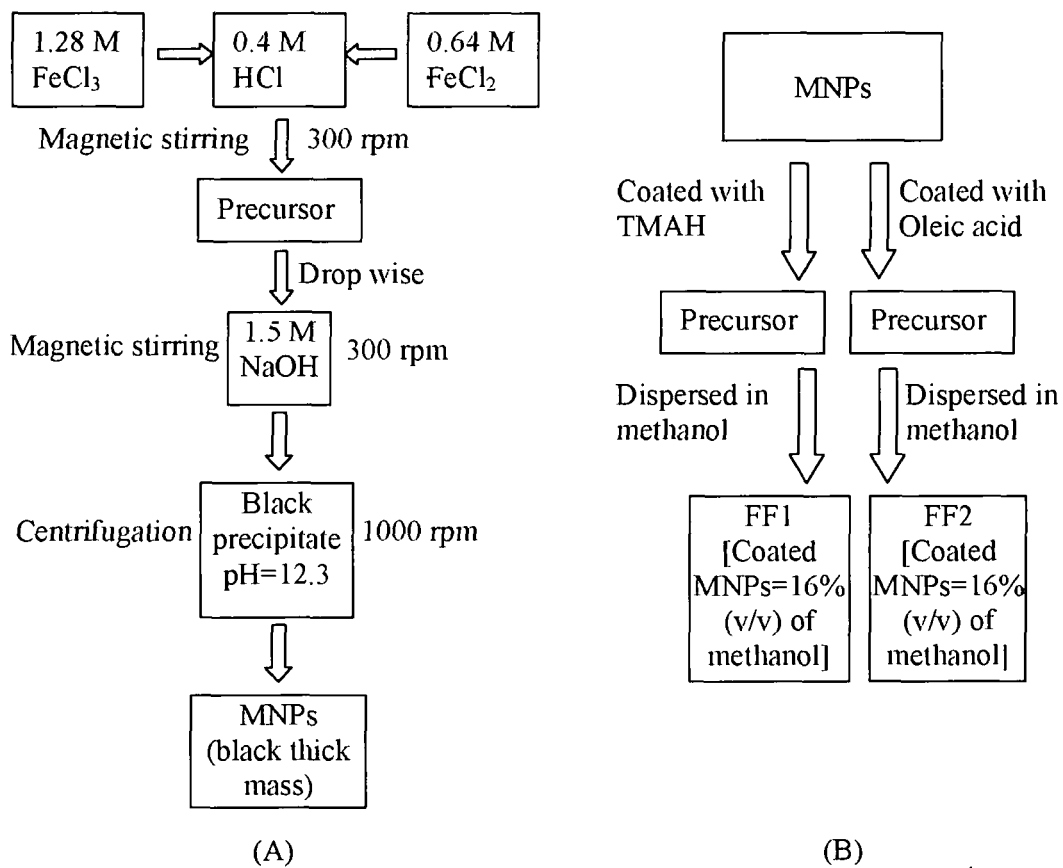
Here, we report the synthesis of anionic and cationic surfactant coated two iron oxide (Fe₃O₄) based ferrofluids and compare their magneto-viscous characteristics for various shear rates, with and without application of magnetic fields.

EXPERIMENTAL DETAILS

As a prime step of ferrofluid preparation, first MNPs were synthesized. We have followed an inexpensive co-precipitation method for producing nano-sized Fe_3O_4 . The chemical equation is as follows:



In the second step, the synthesized nanoparticles are coated with two kinds of surfactants namely, tetra methyl ammonium hydroxide (TMAH) and oleic acid. The former one is cationic and the latter one is anionic surfactant. In this work we take methanol as carrier fluid. The schematic synthesis procedure is presented below.



(A) (B)
 FIGURE 1. Block diagram of synthesis procedure of ferrofluid (A) 1st step (B) 2nd step

RESULTS AND DISCUSSION

Structural Studies

First, the synthesized magnetite particles are characterized by x-ray diffractometer (model. Rigaku Mini Flex 200). Fig.2 shows the typical XRD pattern of the synthesized uncoated magnetite particles. The peaks at 35.35°, 56.4°, 63.35° and 66.1° are designated as characteristics peaks of magnetite with preferred orientation along (311), (511), (531) and (442) planes, in consistency with the other works [10-11]. Peaks at 31° and 75.2° arise because of impurity. The size of the particles is calculated by the Scherrer's formula:

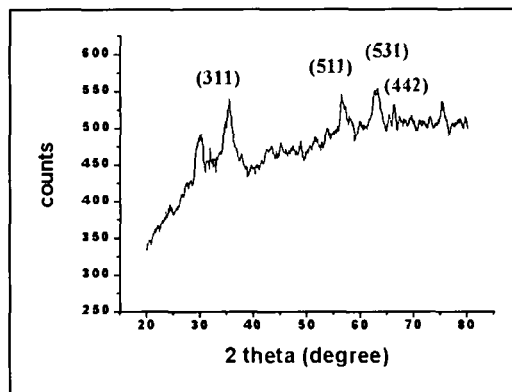


FIGURE 2. XRD pattern of uncoated magnetite sample

$$d = \frac{0.9\lambda}{\beta \cos \theta} \quad (1)$$

where d is the particle size, λ is the wavelength of the x-rays, β is the full width at half maxima in radian and θ being the diffraction angle. Considering the most prominent peak, the average size of the MNPs was calculated to be ~ 4.7 nm and with a strain value of -0.0012 . The negative value of strain reflects contraction of atomic planes within a given nanoparticle. The formula exploited to calculate the strain of the particle is [12]

$$\frac{\beta \cos \theta}{d} = \frac{1}{d} + \frac{s \sin \theta}{\lambda} \quad (2)$$

(s is the strain and other symbols are the same as in the Scherrer's formula)

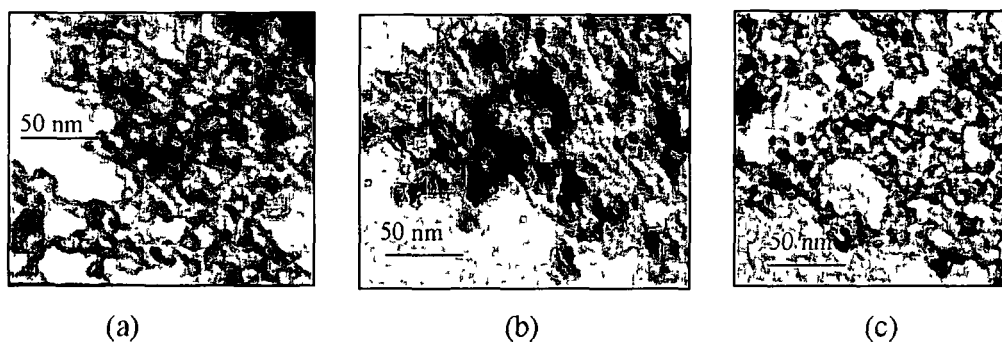


FIGURE 3. (a) Uncoated magnetite particles, particles coated with (b) TMAH and (c) oleic acid dispersed in methanol

Further, the samples are analyzed by transmission electron microscopy (TEM) Fig 3 depicts the TEM micrograph of uncoated, TMAH and oleic acid coated magnetite samples. It is found that the particles have an average size of 5 ± 0.2 nm and are of nonspherical nature. Most of the structures include oblate, hexagonal and rhombohedral features.

Rheological properties

Rheological properties of the prepared samples are studied in a Brookfield dial reading viscometer (Model M/00-151). Fig 4 (a) represents shear rate dependent variation of viscosities in the absence of a magnetic field. The non-linear decay of viscosity with increasing shear rate confirms that the ferrofluids possess non-Newtonian characteristics. The substantial amounts of shear thinning, i.e. decrease of viscosity with shear rate, for both the ferrofluids can be expressed as

$$y = y_1 e^{-x/t_1} + y_2 e^{-x/t_2} \quad (3)$$

Here y is the $\log(\text{viscosity})$, y_1 and y_2 are viscosities at zero shear rate, x is the shear rate and t_1, t_2 are the decay parameters in sec^{-1} . These parameters correspond differently to FF1 and FF2 (Table 1). From the exponential equation, it can be understood that the ferrofluids are undergoing two simultaneous decay equations - one of them is very fast with a high decay parameter. The critical shear rates at which shear thinning slows down are 86.21 sec^{-1} and 118 sec^{-1} for FF1 and FF2 respectively. The overall viscous nature of the ferrofluids can be attributed to the arrangement of small dispersed chains of the MNPs [13]. With increasing shear rate, some kind of perturbation of these clusters occurs, leading to a decreasing trend of viscosity. It is evident that in the absence of any external force, there are more numbers of clusters in FF1 than that of FF2 (Fig 3(a)). In other words, oleic acid (anionic surfactant) coated particles are more dispersed than TMAH (anionic surfactant) coated particles in the ferrofluids. But with increasing shear rate, oleic acid coated clusters respond to fragmentation more rapidly.

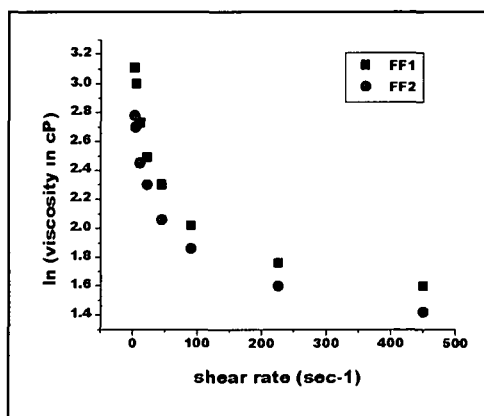


FIGURE 4(a). Variation of viscosity with shear rate for FF1 and FF2.

TABLE 1: Different parameters of FF1 and FF2

FF1		FF2	
y_1	0.67	y_1	0.64
y_2	0.99	y_2	0.86
t_1	10.99	t_1	15.36
t_2	117.74	t_2	168.73

Fig 4 (b) and Fig 4 (c) demonstrate the magneto-viscous property of the as prepared ferrofluids. Pronounced non Newtonian behavior was observed even in the presence of magnetic fields (H). For a fixed shear rate, applied magnetic field could enhance the viscosity of the ferrofluids. But for a particular field, viscosity decreases with increasing shear rate. Other workers have argued that the formation of different field induced structures e.g. chain sequence, droplike etc. in real ferrofluids [14-15] might lead to such a variation. Particles larger than the critical size (~ 10 nm for magnetite particle) are more prone to this kind of structure formation [6]. In a ferrofluid the amount of such particles greatly influences the magneto-viscous property. With high shear rate these structures break down, which results in decreased viscosity. It is reported by Odenbach et al. that the interaction between the magnetic moment and mechanical torque of the particles results in high magneto viscous effect. This is substantially owing to stronger orientation tendency of dipole moments from the direction of vorticity towards applied field [16]. In our case, the direction of the magnetic field is perpendicular to the vorticity of the fluid. As the field increases, the strength of the interaction between the field and the magnetic moments of the MNPs also increases, which results in shifting of the critical shear rate toward lower shear rate direction. The relative changes of viscosity (η_r) for both FF1 and FF2 at different

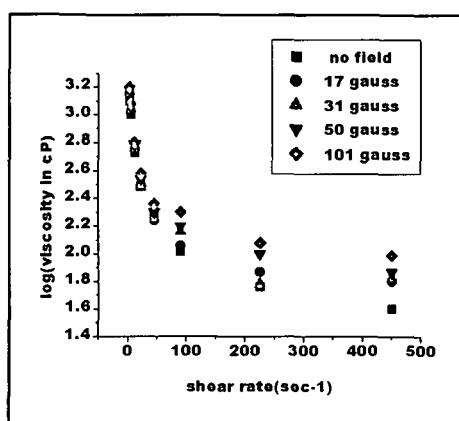


FIGURE 4(b). Variation of viscosity of FF1 with shear rate

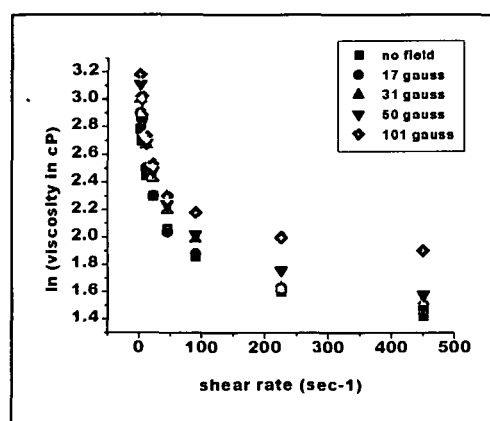


FIGURE 4(c) Variation of viscosity of FF2 with shear rate

magnetic fields are shown in Fig 4 (d) and Fig 4(e). It is expressed by the equation

$$\eta_{FF1} = \frac{\eta_s(\dot{\gamma}) - \eta_s(\dot{\gamma}_c)}{\eta_s(\dot{\gamma}_c)} \quad (4)$$

It is seen that the FF2 responds more rapidly to the field than that of FF1 irrespective of shear rate. It implies that oleic acid coated particles easily interact with the field. TMAH coated particles are more stable in ferrofluid in comparison to oleic acid coated particles.

CONCLUSIONS

We prepared two chemically synthesized magnetite based ferrofluids. The ferrofluids differ from each other depending on the surfactant type used to stabilize the MNPs. The rheological study gives hints about the role played by the surfactants in deciding the viscous property of the ferrofluids. In consistent with other report, it is found that the magneto-viscous property of the ferrofluid exhibits shear thinning. Oleic acid coated particles in ferrofluid (FF2) are found to be more disperse in the absence of field and more rapidly responding to the applied magnetic field than that of TMAH coated particles (FF1). Understanding magneto-viscous properties in terms of role of surfactants, shear dependency, and size dispersity would find various application e.g., sealing, switching and lubricating agents etc.

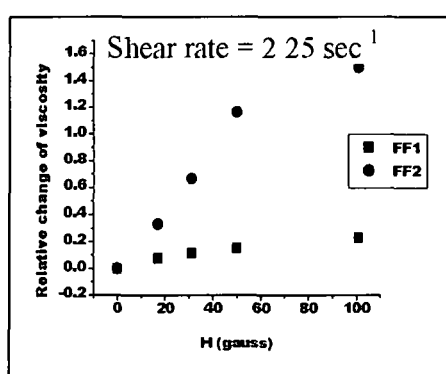


FIGURE 4(d). Relative change of viscosity with magnetic field

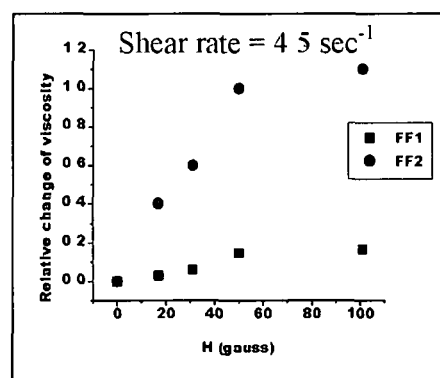


FIGURE 4(e). Relative change of viscosity with magnetic field

ACKNOWLEDGMENTS

The authors thank the Sophisticated Analytical Instrument Facility (SAIF), NEHU-Shillong, Dr R. Dutta and Mr H. Deka of Department of Chemical Sciences, TU

REFERENCES

- 1 J Popplewell, *Phys Technol* **15**, (1984)
- 2 Li-Ying Zhang, H. Chen Gu and Xu-Man Wang *J Magn Magn Mater* **311**, 228 (2007)
- 3 X. Mao, L. Yang, X.-Li Su and Y. Li *Biosens Bioelectron* **21**, 1178 (2006)
- 4 M. Stromberg, K. Gunnarsson, S. Valizadeh, P. Svedlindh and M. Stromme, *J Appl Phys* **101**, 023911 (2007)
- 5 S. Odenbach, *J Phys Condens Matter* **16**, R1135 - R1150 (2004)
- 6 S. Odenbach and K. Raj *Magneto hydrodynamics* **36**, 312 (2000)
- 7 S. Thurm and S. Odenbach, *Phys Fluids* **15**, 1658 (2003)
- 8 C. Scherrer and A. M. Figueiredo Neto, *Braz J Phys* **35**, 718 (2005)
- 9 S. Odenbach, *Magneto viscous effect in ferrofluid -Lecture Notes in Physics*, Springer, 2002
- 10 R. Y. Hong, T. T. Pan, Y. P. Han, H. Z. Li, J. Ding and Sijun Han, *J Magn Magn Mater* **310**, 37 (2007)
- 11 D. K. Kim, Y. Zhang, W. Voit, K. V. Rao and M. Muhammed, *J Magn Magn Mater* **225**, 30 (2001)
- 12 S. B. Qadri, E. F. Skelton, D. Hsu, A. D. Dinsmore, J. Yang, H. F. Gray and B. R. Ratna, *Phys*

- Rev. B* **60**, 9191(1999)
13. L. Mirela Pop, S. Odenbach, A. Wiedenmaan, N. Matoussevitch and H. Bönnemann, *J. Magn. Mater.* **289**, 303 (2005).
 14. A. Yu. Zubarev and L. Yu. Iskakova, *Phys.Rev. E* **61**, 5415 (2000).
 15. A. Yu. Zubarev, S. Odenbach and J. Fleischer, *J. Magn. Mater.* **252**, 241 (2002).
 16. S. Odenbach and H. Störk, *J. Magn. Mater.* **183**, 188 (1998).



Contents lists available at ScienceDirect

Materials Research Bulletin

journal homepage www.elsevier.com/locate/matresbu

Synthesis, characterization and effect of low energy Ar ion irradiation on gadolinium oxide nanoparticles

N. Paul, M. Devi, D. Mohanta*

Nanoscience Laboratory Department of Physics Tezpur University Assam 784028 India

ARTICLE INFO

Article history

Received 12 May 2010

Received in revised form 2 February 2011

Accepted 28 March 2011

Available online 6 April 2011

PACS

No 61 80 Jh

71 20 Eh

76 30 Kg

M 78 30 -j

S 78 55 -m

ABSTRACT

In this work we report on the surfactant assisted synthesis of gadolinium oxide (Gd_2O_3) nanoparticles and their characterization through various microscopic and spectroscopic tools. Exhibiting a monoclinic phase, the nanoscale Gd_2O_3 particles are believed to be comprising of crystallites with an average size of ~ 3.2 nm as revealed from the X-ray diffraction analysis. The transmission electron microscopy has predicted a particle size of ~ 9 nm and an interplanar spacing of ~ 0.28 nm. Fourier transform infrared spectroscopy studies show that Gd–O inplane vibrations at 536.8 and 413.3 cm^{-1} were more prominent for 80-keV Ar-ion irradiated Gd_2O_3 nanosystem than unirradiated system. The photoluminescence (PL) spectra of irradiated specimen have revealed an improvement in the symmetry factor owing to significant enhancement of surface-trap emission, compared to the band-edge counterpart. Irradiation induced creation of point defects (oxygen vacancies) were predicted both from PL and electron paramagnetic resonance (EPR) studies. Further the Raman spectra of the irradiated sample have exhibited notable vibrational features along with the evolution of a new peak at ~ 202 cm^{-1} . This can be ascribed to an additional Raman active vibrational response owing to considerable modification of the nanostructure surface as a result of ion bombardment. Probing nanoscale defects through prime spectroscopy tools would find a new avenue for precise tuning of physical properties with generation and annihilation of defects.

© 2011 Elsevier Ltd. All rights reserved.

1. Introduction

Magnetic nanostructured systems, especially paramagnetic or superparamagnetic nanoparticles have emerged as technologically important candidates owing to their potential application in diverse areas of nanoscience and nanotechnology. The ferrofluids, which are prepared by dispersing nanosized iron oxide particles in a carrier fluid are being used in magnetic drug targeting and hyperthermia [1,2]. There has been an explosion of research in the development of memory devices and quantum architecture that primarily make use of magnetic nanoparticles as building blocks [3,4]. Rare earth (RE) sesquioxides having unpaired *d* or *f* electrons have also imperative role for their unique magnetic response to device fabrication. Recently, high-quality RE functional nanocrystals have drawn a great deal of attention because of their novel physical and chemical properties along with characteristic magnetic features. Gadolinium-containing complexes and nanocrystalline gadolinium oxide (Gd_2O_3) are being used in examining magnetoresonance imaging (MRI) of patients. The signals are achieved owing to the paramagnetic properties of gadolinium (III)

ions stemming from the seven unpaired *f* electrons [5,6]. Similarly, RE-doped Gd_2O_3 is one of the most promising systems that has immense application in solid-state lasers and display devices [7,8]. In general, Gd_2O_3 occurs in two crystal forms cubic and monoclinic. Monoclinic gadolinium sesquioxide is used as a catalyst for the dimerization of methane, 1-butene isomerization, hydrogenation of 1,3-butadiene, acetone aldol addition as a selective catalyst and as a support for metals that catalyze methanol formation from CO_2 and H_2 [9]. Earlier, it was shown that the intense narrow emission response of doped Gd_2O_3 particles can be attractive for efficient fluorescent labelling which could replace the use of conventional organic fluorophores [10]. Therefore the lanthanide system can act as an alternative candidate that can help in the quantitative analysis of immobilized proteins and small molecules in micro immunoassays with very high specificity.

On the other hand, another important field of research is the effect of energetic ion irradiation on nanostructured systems. For MeV ion irradiation the electronic energy loss is dominant over nuclear energy loss where as for ions carrying keV scale energy the situation is reverse. When materials are irradiated by swift heavy ions (SHI) the incident energy is mainly transferred to the electrons of the target material within a time scale of 10^{-15} s and then released to the lattice in 10^{-12} s. As a result of fast quenching the energetic ions (MeV scale) are capable of producing typical

* Corresponding author. Tel: +91 3712 267007/8/9x5558; fax: +91 3712 267005; E-mail address: best@tezu.ernet.in (D. Mohanta).

columnar defects (amorphized zones). Usually, MeV ion irradiation is used for structural and morphological modification [11,12]. In contrast, keV ions are widely used for ion implantation [13–15]. In keV scale, heavy ions can create cluster of point defects where as light ions are capable of generating isolated point defects. It is expected that keV ions would produce point defects that can segregate to grain boundaries. The dangling/unsaturated bonds, presence of foreign impurities, etc. can ideally be removed from the nanoparticles through ion beam lead surface passivation. A light ion beam could be useful in realizing controlled defects along with reduced anisotropy in the system [16,17]. We report here the fabrication of monoclinic nanoscale Gd_2O_3 particles by a user-friendly physico-chemical route. The synthesized and 80 keV Ar ion irradiated products were characterized by advanced microscopic and spectroscopic techniques. Probing of nanoscale defects is also encountered through radiative emission and vibrational characteristics.

2. Experimental

We have prepared nanoscale Gd_2O_3 powders by adopting a simple physico-chemical route. Note that mechanical grinding/crushing of bulk Gd_2O_3 would not result in nanopowder owing to very high thermal and environmental stability of the RE system. At first, 100 mmol of bulk Gd_2O_3 (99%, Otto) was added to 50 ml of double distilled water. Then, an appropriate amount of HNO_3 (69%GR, Merck) was mixed to this solution under vigorous stirring until a clear solution of $Gd(NO_3)_3$ is obtained. The solution was diluted to 100 ml in a volumetric conical flask by adding more distilled water and 3.3 g of N-Cetyl-N,N,N-trimethylammonium bromide (CTAB, a cationic surfactant) was subsequently added at 65 °C resulting in a yellow colored precursor. The yellowish solution was allowed to cool down to the room temperature, which is then followed by addition of 10 ml of aq. NaOH (6×10^{-3} M) at once. Upon stirring for 30 min and subsequent centrifugation, one could separate out white precipitate of $Gd(OH)_3$ from the brownish one. In order to obtain finest quality precipitate, the as-received product was subjected to repeated washing with hot distilled water and centrifugation. The precipitate was dried in air and then heated at ~ 800 °C for 1 h till an off-white powder of Gd_2O_3 is achieved.

The dry Gd_2O_3 powder was sprinkled on a hydraulic-pressed teflon-pellet and then it was irradiated with 80 keV Ar ions (fluence: 10^{13} ions cm^{-2}) in a high vacuum (10^{-8} mbar) chamber at room temperature. The Gd_2O_3 samples were characterized by Rigaku Mini Flex 200 X-ray diffractometer (XRD), high resolution transmission electron microscopy (HRTEM) (Tecnai S twin), Fourier transform infrared (FT-IR) spectroscopy (Nicolet Impact 410), photoluminescence (PL) spectroscopy (PerkinElmer LS 55), electron paramagnetic resonance (EPR) spectrometer (JEOL: JES-FA200) and Raman spectroscopy (Renishaw, UK).

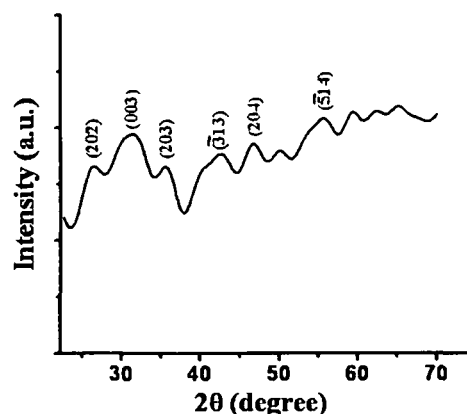


Fig. 1. XRD pattern of the synthesized nanoscale Gd_2O_3 system.

3. Results and discussion

The characteristic properties of the synthesized and irradiated nanoscale Gd_2O_3 products are as discussed below.

3.1. Diffraction and microscopic studies

The structural and morphological characteristics of the nanoscale powder are studied by XRD and HRTEM analysis. The XRD pattern, shown in Fig. 1, depicts six prominent peaks at respective Bragg angles (2θ) of 26.35°, 31.31°, 35.75°, 42.41°, 46.75° and 55.61°. These peaks of monoclinic (*B*-type) Gd_2O_3 phase corresponded to (2 0 2), (0 0 3), (2 0 3), ($\bar{3}$ 1 3), (2 0 4) and ($\bar{5}$ 1 4) planes, with preferred crystallographic orientation along (0 0 3) plane. This is also in consistency with the previous work [7]. The average crystallite size (d) and effective microstrain (η) can be gauged from the popular Williamson–Hall (W–H) expression [18]:

$$\beta_{hkl} \cos \theta_{hkl} = 0.9 \frac{\lambda}{d} + 4\eta \sin \theta_{hkl} \quad (1)$$

where, β_{hkl} is the full width at half maxima in radian, θ_{hkl} is the diffraction angle in degree, λ is the wavelength of the X-rays (1.53 Å). From the W–H plot (not shown), the average crystallite size and microstrain are estimated to be ~ 3.2 nm and -1.8×10^{-3} . Since a positive strain depicts compaction where each of the crystallites is believed to be under stress, a negative strain would represent relaxation. On the other hand, the average size of the Gd_2O_3 nanoparticles as estimated from HRTEM micrograph is ~ 9 nm (Fig. 2a). The particles are found to be nearly spherical and possessing high degree of crystallinity. Note that, a particle may comprise of several crystallites and the crystallite and particle sizes are generally not same in polycrystalline systems and that is why we observe a visible difference in the size estimation performed

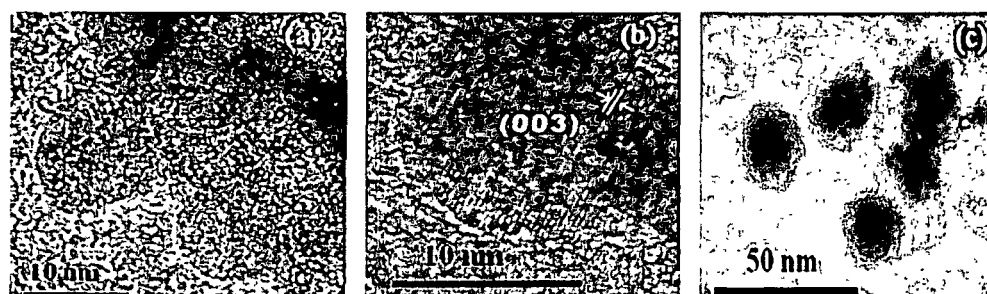


Fig. 2. HRTEM micrographs of synthesized Gd_2O_3 at (a) lower, (b) higher magnification and (c) Ar irradiated Gd_2O_3 system.

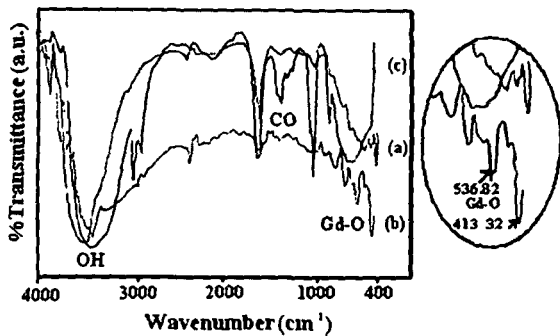


Fig 3 FT-IR spectra of (a) synthesized Gd_2O_3 (b) Ar ion irradiated Gd_2O_3 (fluence 10^{13} ions cm^{-2}) and (c) ethanol as reference

through XRD and TEM analyses Fig 2b shows an isolated spherical particle, which depicts distinct, equispaced lattice planes (shown by short parallel lines) having an interplanar spacing of 0.28 nm. The magnitude of the interplanar spacing between successive (003) planes of the monoclinic Gd_2O_3 structure can also be estimated from the Bragg's law ($2d_{hkl} \sin \theta_{hkl} = n\lambda$, considering 1st order diffraction). The TEM micrograph of the 80 keV Ar ion irradiated specimen (Fig 2c) reveals no variation with regard to size and morphological shape evolution. Upon irradiation the nanoparticles still appear in unclustered form while keeping spherical nature intact.

3.2 Spectroscopic studies

The spectroscopic response of unirradiated and irradiated nanoscale Gd_2O_3 system was investigated through FT-IR, PL, EPR and Raman spectroscopy.

An FT-IR spectrum provides information with regard to bending, bonding and stretching of molecules in a given compound. The vibrational modes generally occur at higher energies (high wavenumber) for organic compounds and at lower

energies (low wavenumber) for inorganic compounds. As shown in Fig 3, the characteristic FT-IR spectra show independent vibrational features for three kinds of specimens namely ethanol (red label), Gd_2O_3 dissolved in ethanol (green label) and irradiated Gd_2O_3 dissolved in ethanol (blue label). In case of ethanol, CH_3 and CH_2 bending modes occurred at 1392 and 1452 cm^{-1} whereas CH_2 , CH_3 , CO and OH stretching vibrations are observable at 2910, 2975, 1060 and 3679 cm^{-1} , respectively [19]. In the present case, we assign the band 1384–1392 cm^{-1} and 1452–1469 cm^{-1} to symmetric CH_3 and CH_2 vibrations (Fig 3a). For all the spectra, the broad peaks located at 3449.46 cm^{-1} and at 1637.7 cm^{-1} are assigned to the characteristic O–H stretching of atmospheric water and due to the atmospheric CO_2 , respectively (Fig 3a–c). In order to understand the vibrational response of inorganic Gd_2O_3 particles in organic media, we now focus our attention on the highlighted area. It clearly depicts the absence of Gd–O bonding feature in pure ethanol sample. On the other hand, Gd–O vibrational response is evident both for unirradiated and Ar ion irradiated sample [20,21]. Moreover, Gd–O inplane vibrations at 536.8 and 413.3 cm^{-1} become more prominent for irradiated Gd_2O_3 system than its unirradiated counterpart. This suggests that the nanoparticle surface has been modified appreciably as a result of ion–matter interaction. It is possible that the point defects (e.g. oxygen vacancy) are created due to energetic ion bombardment. Later, these defects can segregate to the particle surface causing some kind of distortion onto the regular Gd–O lattice. The departure from the regular lattice site along with the segregated defects can result in prominent IR vibrations as evident in Fig 3c. Further, a close look on the unirradiated and irradiated Gd_2O_3 nanoparticle samples has revealed that apart from the prominent Gd–O vibrational peaks, splitting of peaks has also occurred in the later case. These splitted peaks can be ascribed to the uneven distribution of surface defects, interstitials and inhomogeneities.

A PL spectrum, essentially provides information with regard to interband and intraband carrier transitions. The room temperature luminescence spectra of both unirradiated and irradiated Gd_2O_3 nanoparticles ($\lambda_{ex} = 270$ nm) are shown in Fig 4A. In consistency

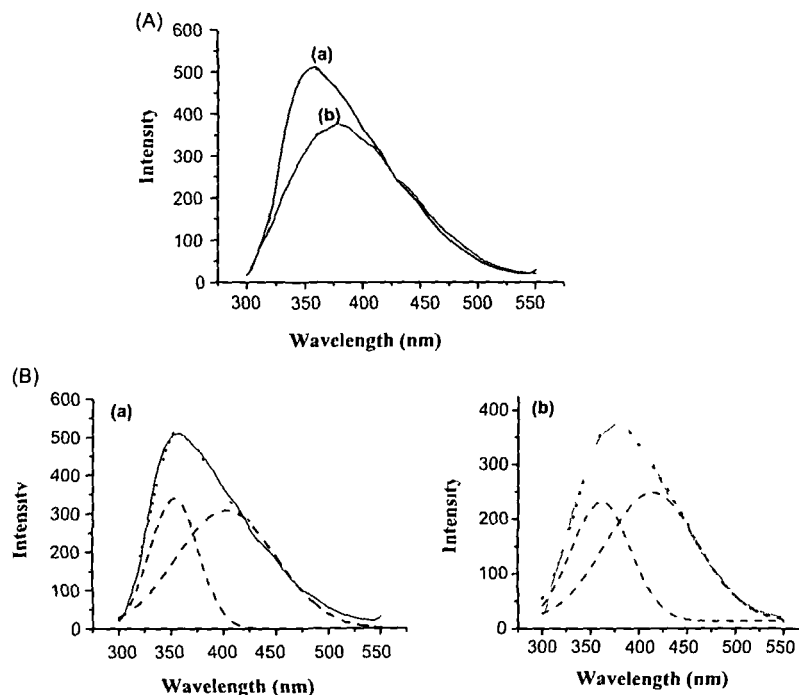


Fig 4 (A) PL spectra of (a) synthesized Gd_2O_3 (b) Ar ion irradiated Gd_2O_3 and (B) deconvolution of PL spectra of (a) unirradiated and (b) irradiated Gd_2O_3 nanosystems

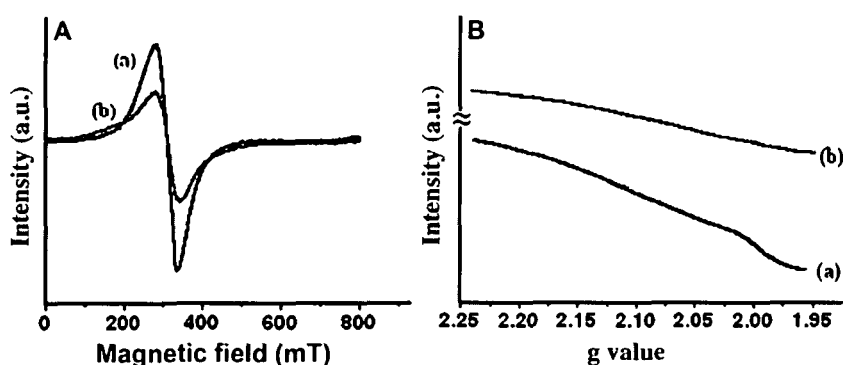


Fig. 5 EPR response of nanoscale Gd_2O_3 system (A) with respect to magnetic field variation and (B) with g varying between 1.95 and 2.2. The as-synthesized and Ar ion irradiated samples are labeled by (a) and (b) respectively.

with the earlier report, an asymmetrically broadened peak at ~ 355 nm was noticed which is ascribed to ${}^6P_{7/2} \leftrightarrow {}^8S_{7/2}$ transition of Gd(III) [22]. We speculate that the association of a defect related emission in the higher wavelength regime could have led to the remarkable asymmetry in the PL response. Upon deconvolution, the defect related emission was found to be located at ~ 415 nm, as can be observed in Fig. 4B. For the irradiated sample, a significant increase of symmetry factor (parts of full width at half maxima (FWHM) around the main peak) suggests that the defect related emission is drastically enhanced over the band-to-band emission. Recently, we have also witnessed a substantial improvement in the symmetry factor in case of Gd_2O_3 nanoparticle system subjected to gamma-irradiation, up to a certain dose [23]. In the present case, the left symmetry factor has increased from 0.38 (unirradiated case) to 0.46 (irradiated system). From the deconvoluted peak analysis, the band to band vs defect related emission intensity ratio is found to decrease from 1.12 to 0.93. Effectively, the competitive defect related emission as a result of development and participation of nonradiative defect centers owing to low energy irradiation has been established.

EPR is a very special technique to probe paramagnetic centers, charged point defects, organic and inorganic radicals etc. Keeping the electromagnetic frequency band fixed, magnetic field is generally varied to achieve resonance. Fig. 5 depicts room temperature EPR spectra of (a) unirradiated and (b) 80-keV ion irradiated (10^{13} ions cm^{-2}) Gd_2O_3 nanopowder samples recorded in the X-band (9.15 GHz) of the electromagnetic spectrum and at a field modulation of 100 kHz. The variation of signal intensity with magnetic field and g value are shown in Fig. 5A and B, respectively. As can be seen from Fig. 5A, though the spectra of the unirradiated and irradiated samples are symmetric in nature, have respective resonance fields centered at 310.3 and 311.6 mT and associated with g -values of 2.10802 and 2.09874, respectively. As the resonance shift (~ 1.3 mT) is larger than the scanning step (0.6 mT), we predict a clear variation in the interaction parameter of the isolated electron spins arising from the prominent defect centers of the irradiated system. Generally, EPR spectra are influenced by the presence of defect centers, but the position of the defect also plays an important role in determining the physical properties of the system. If the defect is placed symmetrically surrounded by a cluster of atoms in a representative system, then it gives rise to an isotropic EPR signal around the g -value of the free electron [24]. Previously, it was reported that location of different kinds of surface defects (edge, terrace, corner of the islands, etc.) could influence the spectra and for the point defects at the edge gives symmetric spectra with no additional doublet [25]. EPR signal variation owing to modified electron contribution is also apparently visible in Fig. 5B. We attribute the symmetric spectra

with the presence of surface defects (chiefly oxygen vacancies) created as a result of keV ion impact.

Raman spectroscopy deals with the inelastic scattering of light and is widely used as nondestructive tool to identify various Raman active vibrational (phonon) modes. The room temperature micro-Raman experiment was carried out by using $\lambda = 514.5$ nm line of 50 mW Ar-ion laser. The observed Raman spectrum of the nanoscale Gd_2O_3 is depicted in Fig. 6. The unirradiated specimen is characterized by poorly resolved phonon modes (Table 1). It was known that the factor group analysis for B -type Gd_2O_3 predicts 21 ($14 A_g + 7 B_g$) Raman active modes which signify the inplane atomic vibration as A_g stretching mode, and out of plane vibration as B_g stretching mode with reference to (010) plane [22]. In consistency with other reports, referring to Fig. 6A, we have identified nine Raman bands with regard to unirradiated Gd_2O_3 sample [22,26]. Earlier it was suggested that a competitive mechanism between the higher frequency shift due to the particle size reduction and lower frequency shift due to strain could influence the Raman spectrum appreciably [26]. It is likely that smaller particles would experience larger strain compared to bigger ones and a typical Raman shift is characterized by the overall effect.

As shown in Fig. 6B, the irradiated sample has revealed a spectrum with broadened line-width, and enhanced intensity. The FWHM of the two most prominent Raman peaks (B_g modes) at 288 cm^{-1} and 384 cm^{-1} have increased from 7.68 cm^{-1} to

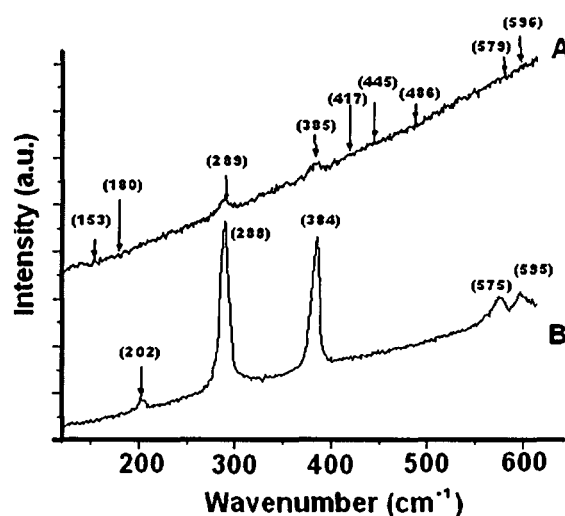


Fig. 6 Raman spectra of (A) unirradiated and (B) irradiated Gd_2O_3 nanosystems.

Table 1
Representative data of the observed Raman bands and assigned modes

Observed (cm^{-1})	wavenumber	Mode assignment	Reported wavenumber (cm^{-1})
Unirradiated Gd_2O_3	Irradiated Gd_2O_3		
153	–	A_g	156
180	–	A_g	175
289	288	B_g	298
385	384	B_g	385
417	–	B_g	417
445	–	A_g	445
486	–	A_g	484
579	575	A_g	583
596	595	A_g	593

9.36 cm^{-1} and from 6.14 cm^{-1} to 10.41 cm^{-1} , respectively. In addition, two other A_g modes, located at 575 cm^{-1} and 595 cm^{-1} were characterized by FWHM values of 10 cm^{-1} and 8 cm^{-1} , respectively. It is expected that the energetic ion irradiation has led to the creation of point defects or, some kind of surface disorder in case of irradiated nanoscale Gd_2O_3 particles. Previously, it was advocated that the peak broadening is related with the phonon confinement and dispersion effect [26]. Here, the minor red shift of the aforesaid (four) peaks at 288 cm^{-1} , 384 cm^{-1} , 575 cm^{-1} and 595 cm^{-1} are assigned with the weak dispersion of the phonon modes. The spectrum of the irradiated sample is also manifested by improved intensity response of these four peaks at the expense of other modes. We assign this observation to the irradiation led lattice disorder in the nanoscale system, which has also been predicted in an earlier work of oxide system [27]. In addition, evolution of a new peak at 202 cm^{-1} in case of irradiated Gd_2O_3 system is expected to be the outcome of invariable superimposition of A_g and B_g modes in confined region. In the monoclinic phase of Gd_2O_3 (unirradiated) though this peak was not observed, for cubic structure (C-type) a weak satellite peak, observable at $\sim 198 \text{ cm}^{-1}$ is attributed to A_g mode [22]. Another group has reported the phase transformation of $\sim 30 \text{ nm}$ Gd_2O_3 particles from C (cubic) \rightarrow B (monoclinic) by 30 keV O ions [28]. In contrary, in the present case, the appearance of the new peak (202 cm^{-1}) indicated a partial phase transformation from B-type to C-type. Note that, the electronic and nuclear energy losses of 30 keV O ions in Gd_2O_3 are 0.291 eV/\AA , 0.213 eV/\AA ; respectively [29]. Conversely, 80 keV Ar ions have respective energy losses limited to 0.539 eV/\AA and 0.858 eV/\AA . In other words, nuclear energy loss over electronic energy loss is more dominant in our case. We speculate that, the existence of the new peak could be due to structural reorganization leading to partial phase transformation on the nanoparticle surfaces though a complete phase-transformation is highly undesirable.

4. Conclusion

We have synthesized nanocrystalline Gd_2O_3 particles by adopting a simple physico-chemical route and then irradiated with energetic 80 keV Ar ions at fluence of $10^{13} \text{ ions cm}^{-2}$. Referring to (003) plane, the interplanar spacing as calculated through diffraction and electron microscopy studies is $\sim 0.28 \text{ nm}$. The creation of point defects and signature of partial phase transformation are predicted by in-depth spectroscopic analysis

As revealed in the PL spectra, the effect of low energy Ar ion irradiation is found to improve the symmetry factor of the overall emission response. The EPR spectra have also hinted the formation/annihilation of nanoscale point defects. The indication of partial phase transformation from monoclinic to cubic (as observed in Raman spectrum) with ion irradiation would open up an important avenue for further study as the cubic phase of this RE oxide has some additional advantage over the monoclinic phase for suitable deployment in luminescent device applications.

Acknowledgements

The authors thank Dr. A. Saha of UGC-DAE CSR, Kolkata, and SINP, Kolkata, for HRTEM measurements. Dr. D. Kanjilal, Dr. P. Kumar and Dr. F. Singh of IUAC, New Delhi are acknowledged for their help in performing ion irradiation experiment and Raman studies. We also thank NEHU, Shillong for TEM measurement and University of Hyderabad for EPR measurements.

References

- [1] T.Y. Liu, S.H. Hu, S.H. Hu, S.P. Tsai, S.Y. Chen, *J. Magn. Magn. Mater.* 310 (2007) 2850.
- [2] H. Rahn, I.G. Morilla, R. Jurgons, C. Alexiou, S. Odenbach, *J. Phys. Condens. Matter* 20 (2008) 204152.
- [3] M. Mannini, F. Pineider, P. Saintavrit, C. Danieli, E. Otero, C. Sciancalepore, A.M. Talarico, M.A. Arrio, A. Cornia, D. Gatteschi, R. Sessoli, *Nat. Mater.* 8 (2009) 194.
- [4] J. Qiu, H. Peng, R. Liang, *Electrochem. Commun.* 9 (2007) 2734.
- [5] P. Sanchez, E. Valero, N. Galvez, J.M. Dominguez-Vera, M. Marinone, G. Poletti, M. Corti, A. Lascialfari, *Dalton Trans.* 5 (2009) 800.
- [6] Y. Gossuin, A. Hocq, Q.L. Vuong, S. Disch, R.P. Hermann, P. Gillis, *Nanotechnology* 19 (2008) 475102.
- [7] S. Seo, H. Yang, P.H. Holloway, *J. Colloid Interface Sci.* 331 (2009) 236.
- [8] E.M. Goldys, K.D. Tomsia, S. Jinjun, D. Dosev, I.M. Kennedy, S. Yatsunencko, M. Godlewski, *J. Am. Chem. Soc.* 128 (2006) 14498.
- [9] G.A.M. Hussein, *J. Phys. Chem.* 98 (1994) 9657.
- [10] M. Nichkova, D. Dosev, R. Perron, S.J. Gee, B.D. Hammock, I.M. Kennedy, *Anal. Bioanal. Chem.* 384 (2006) 631.
- [11] S. Bayan, U. Das, D. Mohanta, *Phys. Stat. Sol. A* 207 (2010) 1859.
- [12] S. Bayan, D. Mohanta, *Nucl. Instrum. Meth. B* 269 (2011) 374.
- [13] J. Mangency, H. Choumane, G. Patriarche, G. Leroux, G. Aubin, J.C. Harmand, J.L. Ouder, H. Bernas, *Appl. Phys. Lett.* 79 (2001) 2722.
- [14] P. Partzka, Y. Zhong, K. Nordlund, R.S. Averback, I.M. Robinson, P. Ehrhart, *Phys. Rev. B* 64 (2001) 235207.
- [15] M.L. Sharma, P.K. Ashwini Kumar, S.K. Sarkar, G.S. Virdi, R. Rup, *Supercond. Sci. Technol.* 7 (1994) 210.
- [16] A.V. Krasheninnikov, K. Nordlund, *J. Appl. Phys.* 107 (2010) 071301.
- [17] S.O. Kucheyev, J.S. Williams, J. Zou, C. Jagadish, G. Li, *Appl. Phys. Lett.* 78 (2001) 1373.
- [18] S.B. Qadri, E.F. Skelton, D. Hsu, A.D. Dinsmore, J. Yang, H.F. Gray, B.R. Ratna, *Phys. Rev. B* 60 (1999) 9191.
- [19] R.A. Nyquist, C.L. Putzig, M.A. Leurgers (Eds.), *Handbook of Infrared and Raman Spectra of Inorganic Compounds and Organic Salts*, vol. 1, Academic Press, San Diego, 1997.
- [20] A.G. Munillo, C.L. Luyer, C. Garapon, C. Dujardin, E. Bernstein, C. Pedrini, *J. Mugnier, Opt. Mater.* 19 (2002) 161.
- [21] H. Guo, N. Dong, M. Yin, W. Zhang, L. Lou, S. Xia, *J. Phys. Chem. B* 108 (2004) 19205.
- [22] J. Gouteron, D. Michel, A.M. Lejus, J. Zarembovitch, *J. Solid State Chem.* 38 (1981) 288.
- [23] M. Devi, N. Paul, D. Mohanta, A. Saha, *J. Exp. Nanosci.* (2011), doi:10.1080/17458080.2010.548408.
- [24] M. Sterrer, E. Fischbach, T. Risse, H.J. Freund, *Phys. Rev. Lett.* 94 (2005) 186101.
- [25] E. Wertz, P. Auzins, R.A. Weeks, R.H. Silsbee, *Phys. Rev.* 107 (1957) 1535.
- [26] C.L. Luyer, A.G. Munillo, E. Bernstein, J. Mugnier, *J. Raman Spectrosc.* 34 (2003) 234.
- [27] J.D. Ye, S.T. Tripathy, F.F. Ren, X.W. Sun, G.Q. Lo, K.L. Teo, *Appl. Phys. Lett.* 94 (2009), 011913.
- [28] B. Antic, A. Kremenovic, I. Draganic, Ph. Colombari, D. Vasiljevic-Radovic, J. Blanus, M. Tadic, M. Mitric, *Appl. Surf. Sci.* 255 (2009) 7601.
- [29] J.F. Ziegler, M.D. Ziegler, J.P. Biersack, *The stopping range of ions in matter* (2008) www.srim.org.

Enhanced magneto-optic activity of magnetite-based ferrofluids subjected to gamma irradiation

Manasi Devi · Rupali Das · Dambarudhar Mohanta ·
Kishor Kumar Baruah · Abhijit Saha

Received 14 March 2011 / Accepted 7 November 2011
© Springer-Verlag 2011

Abstract We report here the effect of γ -irradiation on the particle size and size distribution dependent spectroscopic and magneto-optic properties of ferrofluids, synthesized by a co-precipitation method. The X-ray diffraction (XRD) study exhibits magnetite (Fe_3O_4) phase of the particles while electron microscopic and dynamic light scattering (DLS) studies have predicted particle growth upon γ -irradiation. Further, Fourier transform infrared (FT-IR) spectroscopy studies ensured that no dissociation has occurred due to irradiation effect. As a consequence of magneto-optic behavior reflected in the Faraday rotation (FR) measurement, the Verdet constant increased from a value of 0.64×10^{-2} for the pristine sample to 5.6×10^{-2} deg/Gauss-cm for the sample irradiated with the highest dose (2.635 kGy). The substantial enhancement in the FR is assigned to the improvement in associated chaining effect owing to adequate particle growth where an increased stoichiometry variation of $\text{Fe}^{2+}/\text{Fe}^{3+}$ is assured.

1 Introduction

A brainchild of NASA in 1960s, the discovery of ferrofluid, was a great achievement for the scientific community for its easy preparation method and immense applicability in

diverse fields. This mysterious ferrofluid is a colloidal suspension of magnetic nanoparticles (MNPs) in an appropriate carrier fluid-like oil, water, kerosene, etc. Magnetite and maghemite are the two most prominent candidates used in the preparation of ferrofluid. The magnetic particles are suspended in such a way that they remain dispersed indefinitely in the carrier fluid in spite of long range magnetic forces and short range van der Waals forces of attraction. Stability of any ferrofluid plays a key role for all application purposes. The stability can be achieved either by coating the magnetic particles with surfactant molecules or by electrically charging the particles [1]. In recent times, magnetic fluids/ferrofluids are extensively used in drug targeting mechanism [2–4]. The growing interest on ferrofluid in other applications (e.g., sealing [5], shielding [6], optical limiting devices [7], etc.) is owing to its magnetically tunable properties. Especially, magneto-optic (MO) study has posed immense scientific interest as it relies on user-friendly and non-invasive principles. Strategically, Faraday rotation, birefringence, dichroism, etc. are among the widely investigated MO effects [8, 9]. The dependence of FR on the concentration of the MNPs has also been reported [10]. Plenty works highlighting MO effect under different conditions exist in the literature [11–13], however, FR studies on samples exposed to energetic radiation are rarely found.

With a frequency larger than the X-rays, γ -irradiation is regarded as the most energetic electromagnetic radiation. The high energetic γ -radiation is found to be abundant in the space and is believed to be major cause of the magnetic fields of many extra-terrestrial objects. The FR effect has been considered a powerful tool for estimating magnetic field strengths in Galactic and extra-galactic sources [14]. In the field of medical sciences, the new approach of γ -irradiation has accelerated the concept of drug delivery from ferrofluids with great precision and control [15].

M. Devi, R. Das, D. Mohanta (✉), K. K. Baruah
Nanoscience and Soft Matter Laboratory, Department of Physics,
Tezpur University, PO Napaam, Assam 784028, India
e-mail: best@tezu.ernet.in
Fax: +91-3712-267005/6

A. Saha
UGC-DAE Consortium for Scientific Research, Kolkata Centre,
III/LB 8 Bidhannagar, Kolkata 700 098, India

In this report, we present the effect of γ -irradiation on the water-dispersed Fe_3O_4 based ferrofluids. The size-dependent optical and magneto-optical changes as a result of irradiation are also highlighted.

2 Experimental: materials and methods

The preparation of a stable water-based ferrofluid requires that the MNPs are coated with two layers of surfactant. First, we synthesized magnetite (Fe_3O_4) particles by a coprecipitation method following an earlier method [16] with some modification. At constant stirring (~ 200 rpm), FeCl_3 and FeCl_2 (in the molar ratio $\text{Fe}^{+2}/\text{Fe}^{+3} = 0.5$) were transferred simultaneously to a conical flask containing 25 ml of 0.4 N HCl. Then, 200 μl of oleic acid ($\text{C}_{18}\text{H}_{34}\text{O}_2$, 99% pure, Otto) was mixed with 3 ml of AR-grade acetone and then transferred to the above precursor. The resulting solution was added drop-wise to 250 ml of 1.5 N NaOH solution under vigorous stirring. To facilitate the reaction, 100 μl of oleic acid was added in steps, in 10 min interval. This has resulted in a dark black coloration. In the precursor, the nanoparticle growth was allowed to proceed for 30 min at 30°C with constant stirring. Finally, it was allowed to cool down to room temperature and by performing repeated washing, centrifugation and decantation, we obtained impurity-free surfactant-coated magnetite powder.

In order to prepare a water-based ferrofluid, ~ 2 g of oleic acid coated MNPs were added to 40 ml of milli-Q water and then heated to 60°C under vigorous stirring, for 1 h. Simultaneously, a separate solution of oleic acid, milli-Q water and a few drops of NH_4OH was prepared and added to it to get a stable solution ($\text{pH} = 10.2$).

The as-prepared ferrofluid was irradiated with a γ -source (^{60}Co chamber) that is capable of emitting photons with average energy of 1.25 MeV and at a dose rate of 1.8 Gy/sec. For making a comparative analysis with reference to the pristine sample, we have selected two doses, i.e., 878 Gy and 2.635 kGy. The synthesized Fe_3O_4 particles were characterized by an X-ray diffractometer (Rigaku Mini Flex 200). Microscopic characterization of the pristine and irradiated ferrofluid was performed by transmission electron microscopy (TEM, JEOL-JEM CX II model). The specimen was first diluted and then subjected to ultrasonication for 45 min, and then a microdrop was placed gently on a carbon-coated copper grid. The size and size distribution of the particles, before and after irradiation, were also deliberated through dynamic light scattering (DLS nanoZS, Malvern Instruments) experiments. Further, in order to examine the nature of radiation-induced changes in the molecular vibration and binding, the samples were analyzed by Fourier transform infrared (FT-IR, Nicolet Impact 410) spectroscopy. Faraday rotation was measured in a custom made experimen-

tal set-up following an earlier work [9]. The optical components of the set-up include solid-state lasers ($P = 20$ mW, $\lambda = 632.8$ nm, $P = 50$ mW, $\lambda = 532$ nm), a plano-convex lens to collimate the laser light, a polarizer, an analyser and a Si photodiode (detector) sensitive within visible to red light. An electromagnet was used as the source of external magnetic field. With the help of a set of surface polished mirrors (reflectance $> 99.9\%$), the incident laser light was aligned along the direction of the applied field. The FR was measured as the function of the ratio of the transmitted light intensities without and with placement of analyser as discussed in the literature [9].

3 Results and discussion

3.1 XRD analysis

The synthesized MNPs were first characterized by XRD. Figure 1(a) is a typical XRD pattern of the synthesized product which is characterized by five distinct peaks located at 29.87°, 35.15°, 42.92°, 56.84° and 62.4° and corresponding to (220), (311), (400), (511) and (440) planes of inverse spinel crystal structure of magnetite system [17, 18]. In order to estimate average crystallite size (d), we used the Williamson–Hall (W-H) equation given by [19]

$$\beta_{hkl} \cos \theta_{hkl} = \frac{0.9\lambda}{d} + 4\eta \sin \theta_{hkl} \quad (1)$$

where β_{hkl} is the full width at half-maxima (FWHM) in radian, θ_{hkl} is the diffraction angle in degrees, λ is the wavelength of the X-rays (~ 1.54 Å), and η represents a dimensionless quantity, termed as microstrain. A positive microstrain indicates interparticle contraction while a negative value represents relaxation in the system. The W-H plot was drawn considering prominent XRD peaks (Fig. 1(b)). The microstrain was calculated from the slope, whereas crystallite size was determined from the intercept of the W-H plot. In our system, the microstrain and average crystallite size are estimated to be -7×10^{-2} , and ~ 7 nm, respectively.

3.2 TEM analysis

The direct proof of evidence on the formation of nanoparticles can be assessed from TEM studies. Figure 2 depicts the TEM images of ultrasonically agitated magnetite particles of the pristine and γ -irradiated ferrofluids. It is evident that the particles retain their spherical shape both in case of the pristine ferrofluid and the one which was irradiated with a dose of 878 Gy (Fig. 2(b)) except the fact that particles existed in unclustered form in the later case. When the ferrofluid was irradiated with a comparatively higher dose (2.635 kGy), some noticeable structural changes were observed. In the pristine ferrofluid, the particles are of average

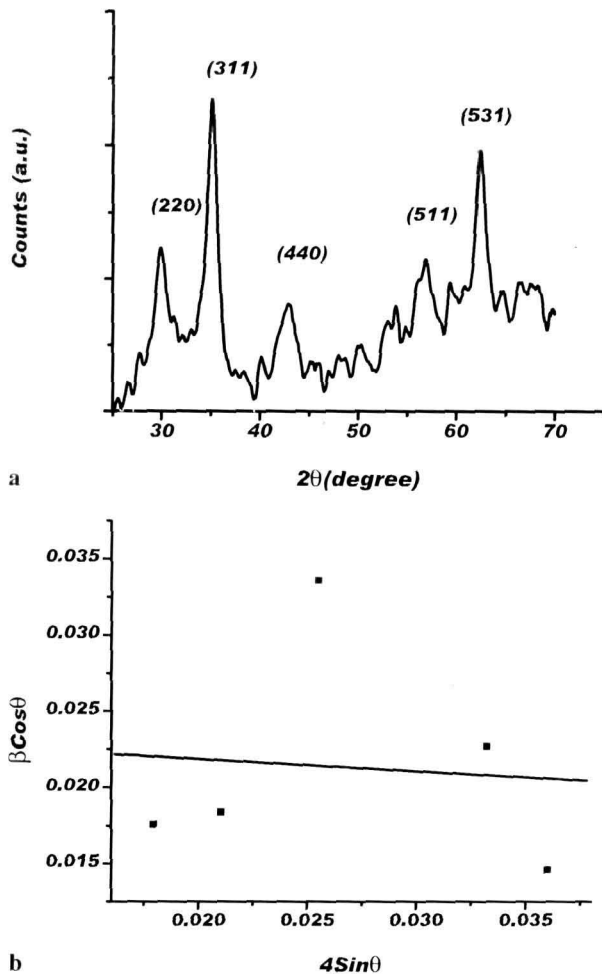


Fig. 1 (a) XRD pattern of the synthesized magnetite (Fe_3O_4) particles, and (b) W-H plot obtained using major diffraction peaks from (a)

size ~ 8 nm. As can be found from the micrographs, the γ -irradiated ferrofluids contained substantial amount of larger particles along with several smaller particles. Particles with an average size of ~ 20 , and 48 nm are observed in case of the ferrofluids irradiated with a dose of 878, and 2.635 kGy, respectively. If an energetic radiation, e.g. γ or electron radiation, passes through material, it can result in fragmentation or recrystallization along with the induction of point defects. Consequently, the physical properties of the material would get modified [20]. We speculate that the Fe_3O_4 particles, dispersed in the ferrofluids undergo solid state recrystallization and particle growth *via* absorption of energy from γ -radiation and dissipating into the surrounding environment. It is expected that the smaller particles will be more spherically symmetric than the larger ones.

3.3 DLS studies

In order to know the particle size distribution under hydrodynamic interactions, the pristine and irradiated ferrofluids

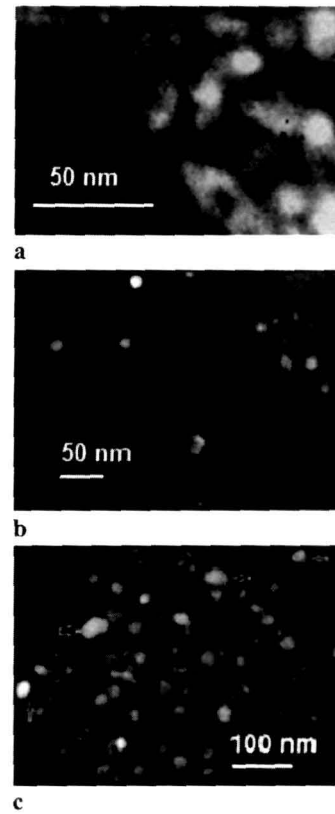


Fig. 2 TEM micrograph of (a) pristine and irradiated ferrofluids with dose (b) 878 Gy, (c) 2.635 kGy

are also analyzed by dynamic light scattering studies. Figure 3(a) is the size distribution of the unirradiated ferrofluid, which predicts that most of the particles are having an average size of ~ 15 nm. In case of the ferrofluid irradiated with a dose of 878 Gy, the average size is increased (~ 28 nm) and for the higher dose (2.635 kGy) it is ~ 60 nm. Thus, adequate particle growth, as a result of γ -radiation, is also evident from the DLS studies. Note that the predicted values are somewhat larger than the values obtained from TEM analyses owing to the fact that the DLS study which relies on scattering events depends on the hydrodynamic diameters of the particles that are coated with surfactant layers. It was also observed that the FWHM (β , in nm) of the Gaussian fitting gets increased from 6.8 for the pristine to 32.1 nm for the irradiated (dose: 2.635 kGy) ferrofluids. For the ferrofluid irradiated with a dose of 878 Gy, β is found to be 17.02. It indicates that the particle size distribution has increased with irradiation dose.

3.4 FT-IR analysis

FT-IR spectroscopy is a healthier access to trace the change in the vibrational features due to the presence of certain constituents in a given material system. The characteristic bend-

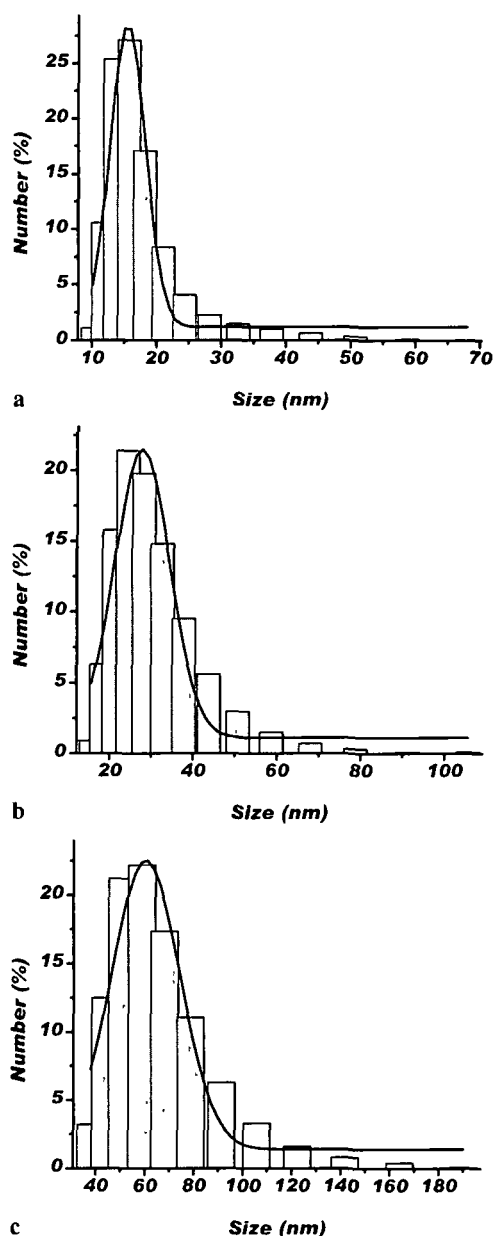


Fig. 3 DLS study of the (a) pristine and irradiated ferrofluid with doses (b) 878 Gy and (c) 2.635 kGy

ing, bonding or stretching modes of the IR active material corresponds to specific peaks in an FT-IR spectrum. Figure 4 shows the room temperature FT-IR spectra of the pristine and the irradiated ferrofluids. Except a peak observable at $\sim 2077\text{ cm}^{-1}$ and identified as C–O stretching mode of the atmospheric CO_2 molecule, all other peaks correspond to the chemical constituents available in the ferrofluid under study. The broad band at $\sim 3488.07\text{ cm}^{-1}$ and the small peak at $\sim 2403\text{ cm}^{-1}$ represent the characteristic O–H bending and stretching vibrational modes of the hydroxyl group

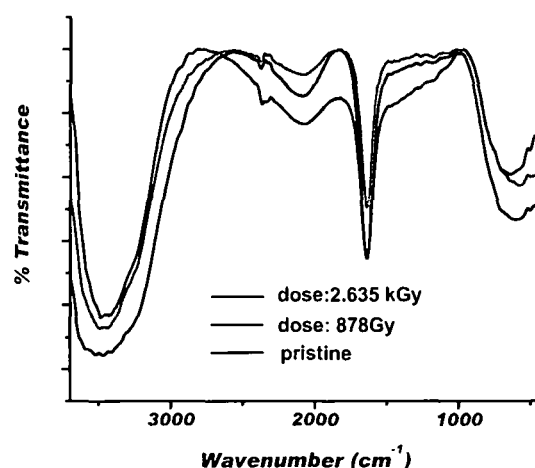


Fig. 4 FT-IR spectra of pristine and irradiated ferrofluids

of water molecule. The sharp peak at $\sim 1670\text{ cm}^{-1}$ and a weak peak at $\sim 1161\text{ cm}^{-1}$ give the respective signatures of strong and medium –CO–OH bonding of oleic acid. The typical Fe–O stretching vibrations of Fe_3O_4 are prominent in the lower wavenumber region, in the range $598\text{--}566\text{ cm}^{-1}$ and $510\text{--}445\text{ cm}^{-1}$. It is seen that after irradiation, the characteristic peak of Fe_3O_4 has shifted further toward lower wavenumber side. We know that for nanoscale size, the force constant associated with bonds tends to increase. Due to the small size, a large number of bonds involving surface atoms of the nanostructures break down, resulting in a rearrangement of non-localized electrons on the surface. Consequently, the smaller the size, the larger will be the shift of vibrational peak toward higher wavenumber side and vice versa [21]. It may be noted that evolution of no new peak in the spectra of the irradiated samples affirms that neither the MNP nor the surfactant (oleic acid) layer has dissociated/transformed into new chemical species.

3.5 Magneto-optic Faraday effect

When optical activity of a material under study changes with the application of a magnetic field, the corresponding effect is called as magneto-optic effect. Magneto-optic effect is important in the sense that it provides information regarding the electronic and the spin structure of the system. The orientation of the light polarization in a medium can be studied either in the transmission mode (Faraday rotation) or in the reflection mode (Kerr effect). FR is a measure of the interaction of a plane polarized light with matter in the presence of an external magnetic field applied along the direction of light wave propagation. When a polarized light beam is transmitted through an optically active matter, it undergoes transformation into two circularly polarized light beams. Generally [22], FR (θ_F) is expressed as $\theta_F = VHI$, where V is the Verdet constant of the material,

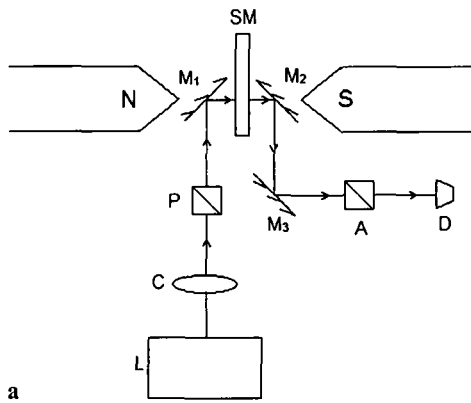


Fig. 5a Schematic experimental set-up for Faraday rotation measurement with *L* laser, *C* collimator (lens), *P* polarizer, *SM* specimen, (*M*₁, *M*₂, *M*₃) mirror, *A* analyser, *D* photodetector

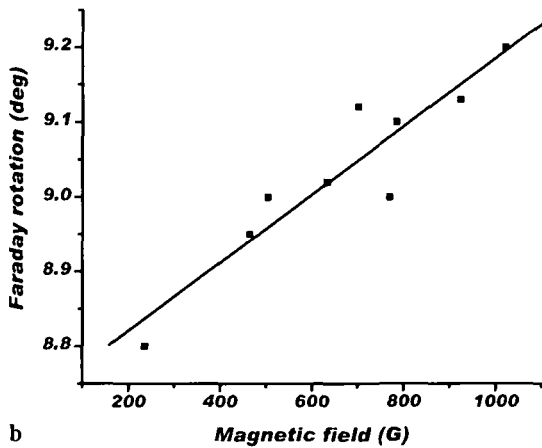


Fig. 5b Faraday rotation of milli-Q water

H is the applied magnetic field and *l* is the optical path length. A custom-made Faraday rotation set-up is shown schematically in Fig. 5a. In order to calibrate our set-up using a wavelength of 632.8 nm, first we measured the FR of milli-Q water taken in a 1 cm cuvette with empty cuvette as reference (Fig. 5b). On linear fitting of the curve, the Verdet constant of water was calculated to be 3.9×10^{-4} deg/G-cm and is found to be consistent with the reported value [23].

The FR responses of the pristine ferrofluid measured for two different wavelengths (532 and 632 nm) are shown in Fig. 5c. For a given wavelength, the rotation gradually increases with the field and then exhibits a saturation trend. Such a Faraday response is quite obvious in ferrofluids [24, 25] and semiconductor doped with magnetic impurities [26]. With the application of an external field, the particles dispersed in a ferrofluid form chain or column-like structures, which would otherwise exhibit independent Brownian motion in isolation from each other. In the presence of a field, first the individual particles try to align them-

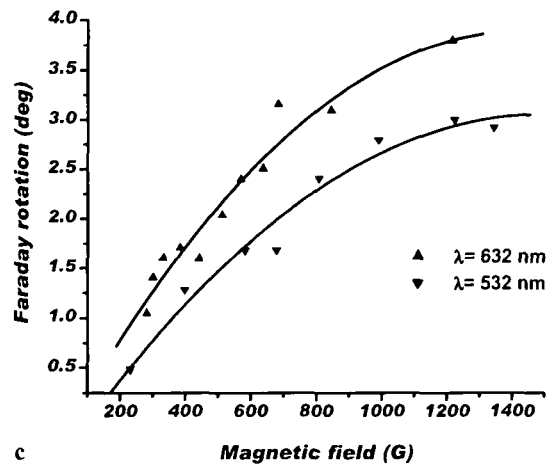


Fig. 5c Faraday rotation response of unirradiated ferrofluid at two different wavelengths

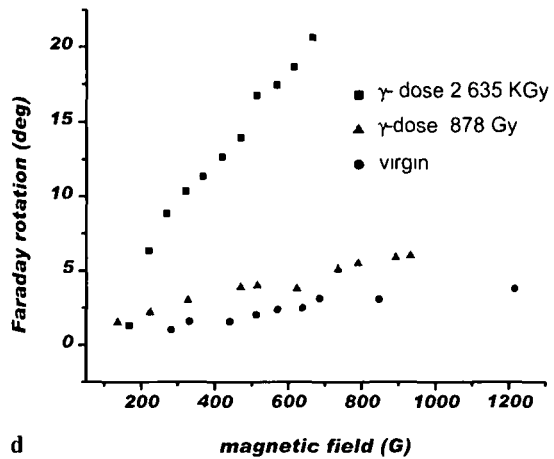


Fig. 5d Faraday rotation response of pristine and irradiated

selves along the field. Later, these chains get aligned owing to the zipper effect, and when all the chains are aligned along the applied field, FR reaches its saturation value. Considering the chaining effect into account, the FR for ferrofluids can be expressed as [27]

$$\theta_F = C \frac{M(H)}{M_S} + VHI(H) \tag{2}$$

Here, *C* is a constant, *M*(*H*) is the magnetization of the particle at an applied field *H*, where *M*_S represents the saturation magnetization of the specimen, and finally, *l*(*H*) represents the chain length at a field *H*. It was also revealed that at a definite magnetic field, the FR has a dependency on the excited wavelength (Fig. 5c). It may be noted that a larger wavelength corresponds to a lower energy, and hence, it will hinder the chain formation only weakly. Consequently, an excited light with a larger wavelength would result in a significant FR in comparison with a light beam

possessing a shorter wavelength. The Faraday response of the irradiated and pristine ferrofluids (working wavelength 632 nm) is shown in Fig. 5d. It was observed that the FR gets enhanced with the irradiation dose. Quantitatively, the Verdet constant, as calculated from the linear part, was found to improve from 0.64×10^{-2} to 5.9×10^{-2} deg/G-cm for pristine ferrofluid and the one subjected to irradiation (dose 2.635 kGy). The ninefold enhancement of FR can be attributed to the structural reorganization of the dispersed nanoparticles. In Fe_3O_4 system, 3d electronic states of iron are generally responsible for the magneto-optic effect [28]. The cations (Fe^{3+} and Fe^{2+}) are believed to occupy the tetrahedral and octahedral sites. They interact with the oxygen localized states which are already present in the vicinity of their neighboring environment. The FR takes place due to the intervalence charge-transfer transitions (0.6 eV) between neighboring Fe^{2+} and Fe^{3+} ions [23, 29]. Further, in nanoscale dimension, the finite size effect of MNPs leads to tremendous change in the magnetic ordering [30], whereas magnetization decreases with size [31]. So, with the reduction of size, the number of possible sites responsible for the FR would decrease. Conversely, the ratio of $\text{Fe}^{2+}/\text{Fe}^{3+}$ will be more in a bigger sized particle than that of a smaller one. In the host lattice, γ -irradiation can cause modification by annihilating/creating point defects [32]. The irradiation leads to the alteration of the total number of oxygen vacancy sites of the Fe_3O_4 system which in turn influence the charge transfer process. In addition, (2) shows that chain formation plays a crucial role in the FR of ferrofluid. The effective magnetic interaction between two magnetic nanoparticles can be described by a coupling constant (Λ) given by [33]

$$\Lambda = \frac{\pi \mu_0 \chi^2 H^2 a^3}{72 K_B T} \quad (3)$$

The coupling constant is the ratio of the maximum magnitude interaction energy to the thermal energy ($k_B T$) in the system. Here, a is the diameter of the MNPs and χ is the effective susceptibility of individual MNPs. The favourable condition for chain formation of the dispersed particles is $\Lambda \gg 1$. At a specific applied field, the bigger particles are more prone to the chaining effect than the smaller ones. The higher the number of chain forming capacity, the larger would be the FR in a given ferrofluid specimen. It is because of this that the irradiated ferrofluids record substantial FR in comparison with the pristine one.

4 Conclusion

We have synthesized oleic acid coated Fe_3O_4 based ferrofluid taking water as carrier medium. The prepared ferrofluids were irradiated with γ -irradiation at two selected

doses of 878 Gy and 2.635 kGy. The TEM and DLS studies illustrate particle growth with radiation dose. The FT-IR study ensures protective bonding of surfactant-coated MNPs and the possibility of dissociation as a result of irradiation was discarded. Consistently with other reports, we found that the FR of our ferrofluids (both pristine and irradiated) gradually increase with the applied magnetic field and then tend to saturate. The irradiation effect on the FR is manifested as enhanced rotation with dose. We assign this enhancement with the particle growth, increased charge-transfer capacity and more chain-forming capacity. Enhanced magneto-optic activity would find application in Faraday isolator, rotator and dichroic optical components.

Acknowledgements We acknowledge UGC, New Delhi, for the financial support received under major project scheme No. 37-367/2009 (SR). The association of Ms. Nibedita Paul, RS, is acknowledged. We extend our sincere thanks to Dr. A. Dutta, UGC-DAE, CSR, Kolkata, for her help during γ -irradiation and DLS study. We are also thankful to SAIF, NEHU, Shillong, for extending TEM Facility. The FT-IR facility provided by the Department of Chemical Sciences, TU, is gratefully acknowledged.

References

- 1 C. Scherrer, A. M. F. Neto, Braz. J. Phys. **35**, 718 (2005)
- 2 H. Rahn, I. G. Morilla, R. Jurgons, C. Alexiou, S. Odenbach, J. Phys.: Condens. Matter **20**, 204152 (2008)
- 3 E. Munnier, S. C. Jonathan, C. Linossier, L. D. Eyrolles, H. Marchais, M. Soucé, K. Hervé, P. Dubois, I. Chourpa, Int. J. Pharmacol. **363**, 170 (2008)
- 4 D. Y. Ju, P. Bian, M. Nakano, H. Matsuura, K. Makino, N. Noda, K. Koide, T. Nemoto, Mater. Sci. Forum **614**, 229 (2009)
- 5 R. Ravaut, M. Pinho, G. Lemarquand, N. Dauchez, J. M. Genevaux, V. Lemarquand, B. Brouard, IEEE Trans. Magn. **45**, 4388 (2009)
- 6 T. H. Mihail, US Patent Application 20100084586 Kind Code A1, 2010
- 7 S. S. Nair, J. Thomas, C. S. S. Sandeep, M. R. Anantharaman, R. Philip, Appl. Phys. Lett. **92**, 171908 (2008)
- 8 H. W. Davies, J. P. Llewellyn, J. Phys. D, Appl. Phys. **13**, 2327 (1980)
- 9 N. A. Yusuf, A. A. Rousan, H. M. E. Ghanem, J. Magn. Magn. Mater. **65**, 282 (1987)
- 10 N. A. Yusuf, I. Abu-Aljarayesh, A. A. Rousan, H. M. El-Ghanem, IEEE Trans. Magn. **36**, 2852 (1990)
- 11 C. P. Pang, C. T. Hsieh, J. T. Lue, J. Phys. D, Appl. Phys. **36**, 1764 (2003)
- 12 D. Jamon, F. Donatini, A. Siblani, F. Royer, R. Perzynski, V. Cabuil, S. Neveu, J. Magn. Magn. Mater. **321**, 1148 (2009)
- 13 E. S. Kooij, A. C. Gálci, B. Poelsema, J. Colloid Interface Sci. **304**, 261 (2006)
- 14 E. D. López, Astrophys. J. **641**, 710 (2006)
- 15 L. Jun, S. Hao, D. Y. Dong, Chin. Phys. Lett. **27**, 038104 (2010)
- 16 Y. S. Kang, S. Risbud, J. F. Rabolt, P. Stroeve, Chem. Mater. **8**, 2209 (1996)
- 17 L. Zhang, Y. Zhang, J. Magn. Magn. Mater. **321**, L15 (2009)
- 18 R. Y. Hong, T. T. Pan, Y. P. Han, H. Z. Li, J. Ding, S. Han, J. Magn. Magn. Mater. **310**, 37 (2007)
- 19 X. D. Zhou, W. Huebner, Appl. Phys. Lett. **79**, 3512 (2001)
- 20 S. M. E. Sayed, Nucl. Instrum. Methods Phys. Res., Sect. B, Beam Interact. Mater. Atoms **225**, 535 (2004)

- 21 U Schwertmann, R M Cornell, *Iron Oxide in the Laboratory Preparation and Characterization* (Cambridge University Press, New York, 1991)
- 22 H S Bennett, E A Stern, *Phys Rev* **137**, A448 (1965)
- 23 P K Jain, Y Xiao, R Walsworth, A E Cohen, *Nano Lett* **9**, 1644 (2009)
- 24 A A Rousan, H M El-Ghanem, N A Yusuf, *IEEE Trans Magn* **24**, 1653 (1988)
- 25 M M Maierov, *J Magn Magn Mater* **252**, 111 (2002)
- 26 N Misra, M Roy, D Mohanta, K K Baruah, A Choudhury, *Cent Eur J Phys* **6**, 109 (2008)
- 27 A A Rousan, H M El-Ghanem, N A Yusuf, *IEEE Trans Magn* **25**, 3121 (1989)
- 28 A Schlegel, S F Alvarado, P Wachter, *J Phys C, Solid State Phys* **12**, 1157 (1979)
- 29 K H Choi, S H Lee, Y R Kim, L Malkinski, A Vovk, Y Barnakov, J H Park, Y K Jung, J S Jung, *J Magn Magn Mater* **310**, e861 (2007)
- 30 D Shi, B Aktas, L Pust, F Mikailov (eds), *Nanostructured Magnetic Materials and Their Applications* (Springer, Berlin, 2002)
- 31 D Caruntu, G Caruntu, C J O'Connor, *J Phys D, Appl Phys* **40**, 5801 (2007)
- 32 M Devi, N Paul, D Mohanta, A Saha, *J Exp Nanosci* (2011) doi 10.1080/17458080.2010.548408
- 33 J M Laskar, J Philip, B Raj, *Phys Rev E* **80**, 041401 (2009)

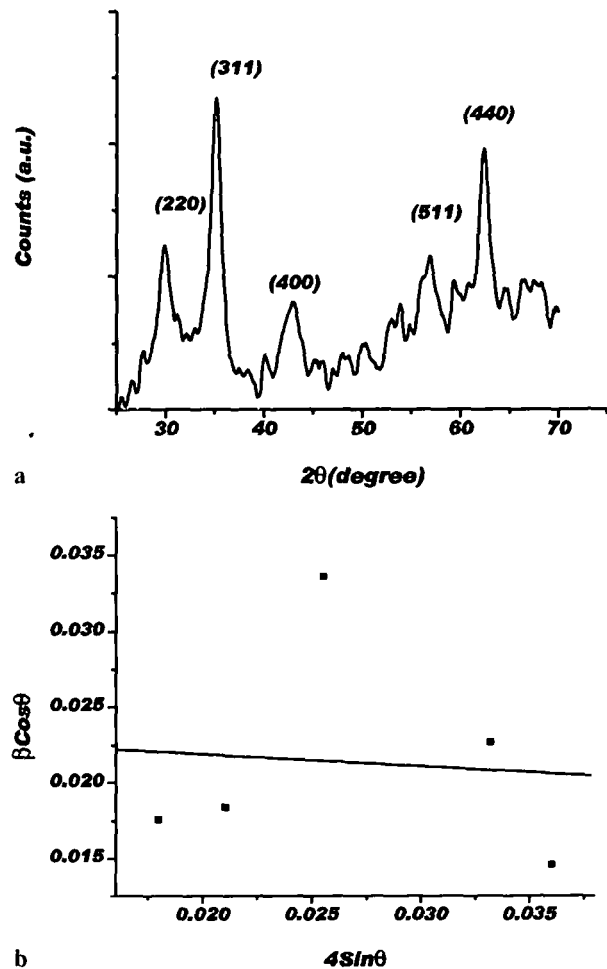
Erratum to: Enhanced magneto-optic activity of magnetite-based ferrofluids subjected to gamma irradiation

Manasi Devi · Rupali Das · Dambarudhar Mohanta ·
Kishor Kumar Baruah · Abhijit Saha

Published online: 14 December 2011
© Springer-Verlag 2011

Erratum to: *Appl Phys A*
DOI 10.1007/s00339-011-6678-4

Due to a processing error, the presentation of Fig. 1a was incorrect. The corrected Fig. 1 is given below.



The online version of the original article can be found under
doi:10.1007/s00339-011-6678-4.

M. Devi · R. Das · D. Mohanta (✉) · K.K. Baruah
Nanoscience and Soft Matter Laboratory, Department of Physics,
Tezpur University, PO Napaam, Assam 784028, India
e-mail: best@tezu.ernet.in
Fax: +91-3712-267005/6

A. Saha
UGC-DAE Consortium for Scientific Research, Kolkata Centre,
III/LB-8 Bidhannagar, Kolkata 700 098, India

Fig. 1 (a) XRD pattern of the synthesized magnetite (Fe_3O_4) particles, and (b) W-H plot obtained using major diffraction peaks from (a)

Characteristic spectroscopic properties of γ -irradiated rare-earth oxide-based ferrofluids

Manasi Devi^a, Nibedita Paul^a, Dambarudhar Mohanta^{a*} and Abhijit Saha^b

^aNanoscience Laboratory, Department of Physics, Tezpur University, PO Napaam, Assam 784028, India; ^bUGC-DAE Consortium for Scientific Research, Kolkata Centre, III/LB-8 Bidhannagar, Kolkata 700098, India

(Received 11 October 2010; final version received 12 December 2010)

Ferrofluids are being considered as potential candidates both in basic and applied research owing to their novel optical and magneto-optical properties. We have synthesised surfactant (N-Cetyl-N,N,N-trimethylammonium bromide, CTAB)-coated nanoscale gadolinium oxide (Gd_2O_3) based ferrofluids and then irradiated by gamma (γ -) rays with doses in the range of 32 Gy–2.635 kGy. High-resolution transmission electron microscope (HRTEM) analysis shows that the particles have developed intragranular defects owing to γ -ray irradiation. Fourier transform infrared (FT-IR) and photoluminescence (PL) studies also support the formation of defect ordering upon irradiation. Further, PL study indicates abrupt change of the symmetry factor with increase in γ -dose. By viewing the nature of variation between relative intensity of the defect-related emission and dose-dependent symmetry factor, one can predict the tunability of PL response. A proper understanding of the PL response of the irradiated nanoscale rare-earth oxides would find new avenues for lasing and other optoelectronic/photonic devices.

Keywords: ferrofluid; gamma irradiation; photoluminescence; defect

1. Introduction

The growing interest of low-dimensional materials with respect to their bulk counterparts dwells on their unique electronic, magnetic, optical and mechanical properties. In the recent decades, nanoscience and nanotechnology have emerged as a thrilling trend both in the field of basic research and industrial application [1,2]. Magnetic nanoparticle (MNP) systems have attracted a great deal of attention for their size-dependent functionality and applicability in making integrated/hybrid structures. Ferrofluid, a colloidal dispersion of MNPs, has several advantages as it displays tunable viscoelastic and optical properties in the presence of a static magnetic field (SMF) [3]. The most commonly used ferrofluids generally comprise superparamagnetic magnetite (Fe_3O_4) or, maghemite ($\gamma\text{-Fe}_2\text{O}_3$) particles which are dispersed in a suitable carrier fluid (oil, water, etc.). Ferrofluids have potential in the area of drug targeting [4], sealing [5], shielding [6], optical limiting devices

*Corresponding author. Email: best@tezu.ernet.in

[7], etc. Also, ferrofluids are widely used in aircrafts and space shuttles. It has been found that the rare-earth (RE) oxide materials exhibit lower toxicity in comparison to several types of quantum dots (Cd, Se, Tb, Hg, etc.) [8]. There exists ample scope for the deployment of RE oxide-based ferrofluids as imperative fluorescent/drug targeting agents. Further, owing to better environmental stability and durability, RE oxide-based ferrofluids emerge as alternative candidate with immense technological relevance in sealing and shielding applications.

Gamma (γ) rays are energetic electromagnetic radiations like X-rays. They are the most energetic form of electromagnetic radiation. γ -radiation is most common in outer space environment. This type of radiation has mixed impact on different materials. There are reports on the effect of this type of radiation on the lasing performance of Nd, Cr: GSGG (Cr^{3+} -doped gadolinium scandium gallium garnet) crystals. It was found that these crystals retain high threshold for laser damage up to γ -ray doses of 1 MGy [9]. However, on exposure of such radiation, colour centres are induced which strengthen the fluorescence property [10]. Previously, Mak et al. [11] have observed shifting of photoluminescence (PL) peak after γ -irradiation in ZnSe crystals. They correlated the peak-shifting with the band-gap variation and ascribed it to radiation stimulated solid-state recrystallisation and accumulation of point defects. In RE-doped alkaline earth sulphates, the effect of γ -irradiation was shown to influence their lattice parameters and luminescence patterns [12].

In this context, there is hardly any work that describes spectroscopic and light-emitting properties of γ -irradiated RE-based ferrofluids. In this report, we highlight the synthesis and impact of γ -radiation on the molecular vibrational features and asymmetric emission response of gadolinium oxide (Gd_2O_3)-based ferrofluids.

2. Experimental: materials and methods

The bulk Gd_2O_3 is a very stable RE compound against high-pressure, high-temperature and environmental degeneration. It is very difficult to synthesise it in nanoscale form following top-down approach. In order to prepare nano-sized Gd_2O_3 powders, we have followed a low-cost physico-chemical route as proposed by Chen et al. [13] with little modification. In this method, bulk Gd_2O_3 is converted first into a nitrate compound followed by subsequent reduction to get hydroxide and oxide products. At first, 1 mmol of bulk Gd_2O_3 (99%, Otto) was added to 50 mL of double-distilled water. Then, an appropriate amount of HNO_3 (69%GR, Merck) was mixed to this solution under vigorous stirring until a clear solution of $\text{Gd}(\text{NO}_3)_3$ is obtained. The solution was diluted to 100 mL in a volumetric conical flask by adding more distilled water and then 3.3 g of N-Cetyl-N,N,N-trimethylammonium bromide (CTAB) was subsequently added at 65°C resulting in a yellow coloured precursor. After the yellowish solution was cooled down to the room temperature, 10 mL of freshly prepared 0.006 M aqueous NaOH was transferred to it. As a result, a white precipitate of $\text{Gd}(\text{OH})_3$ is formed which is then followed by continuous stirring (30 min), and centrifugation (30 min). In order to obtain finest quality precipitate, the as-received product was subjected to repeated washing with hot distilled water and centrifugation. The precipitate was dried in air and then heated at 800°C for 1 h till an off-white powder of Gd_2O_3 is received. For preparing a ferrofluid system, surfactant-coated particles were required to get dispersed in a carrier fluid. We have chosen

ethanol as a carrier medium as CTAB is chemically inert in ethanol. The CTAB-coated Gd_2O_3 nanoscale powder was dissolved in ethanol followed by stirring overnight which has resulted in a well-dispersed Gd_2O_3 ferrofluid. The prepared ferrofluid was then divided into six equal parts for carrying out irradiation experiment independently.

The as-prepared ferrofluid was irradiated with a γ -source (^{60}Co chamber) that is capable of emitting photons with an average energy of 1.25 MeV at a dose rate of 1.8 Gy/s. Keeping in mind the amount of doses used by earlier workers, we have selected five doses i.e. 32, 97, 292, 878 Gy and 2.635 kGy. The crystal structure of the synthesised Gd_2O_3 powder was first investigated by an X-ray diffractometer (XRD, Rigaku Mini Flex 200). Microscopic characterisation of the pristine and irradiated ferrofluid was performed by a high-resolution transmission electron microscope (HRTEM, FEI, Tecnai S-twin) operating at an accelerating voltage of 200 kV. For this purpose, the specimen was first subjected to ultrasonication and then a microdrop was gently placed on a carbon-coated copper grid (no. of meshes: 400 cm^{-2}). The spectroscopic and luminescence properties of the ferrofluids were characterised by different tools, namely Fourier transform infra-red spectroscopy (FT-IR, Nicolet Impact 410) and PL spectroscopy (Perkin Elmer LS 55).

3. Results and discussion

The structural and morphological aspects were revealed by HRTEM and XRD analyses. In contrast, the nature of molecular vibration and radiative light emission characteristics were explored by FT-IR and PL measurements, respectively.

3.1. Microscopic and diffraction studies

The structural and morphological aspects of the synthesised nanoscale Gd_2O_3 were investigated by HRTEM and are shown in Figure 1. The average size of the nanoparticles as revealed from the micrograph is $\sim 9\text{ nm}$. The particles are found to be nearly spherical along with a high degree of crystallinity and perfect lattice ordering. Figure 1(a) and inset reveal nearly spherical particles with distinct lattice planes and an interplanar spacing of 0.28 nm. The predicted value of the interplanar spacing corresponds to the separation of (003) planes of the monoclinic Gd_2O_3 structure, ascertained from the prominent peaks of the XRD pattern (shown in Figure 1b). A close look on the micrograph of the irradiated (dose: 2.635 kGy) sample, shown in Figure 1(c), ensures the formation of nanoscale defects in the successive lattice planes (red arrows). The defects can be in the form of voids (vacancies) or dislocations. For instance, evidence of point defect and dislocation are shown by solid and open arrows, respectively. The inset of Figure 1(c) represents the selected area electron diffraction (SAED) pattern of the irradiated specimen. The bright rings are indexed as (0 0 3), (2 0 3), ($\bar{3}$ 13) and are in conformity with the earlier XRD analysis of monoclinic Gd_2O_3 system [14].

3.2. FT-IR analysis

Fourier spectroscopy is an important tool to describe the analysis of a varying signal into its constituent frequency components. FT-IR is a powerful method that helps in revealing bending, bonding and stretching modes of various IR active molecular vibrations.

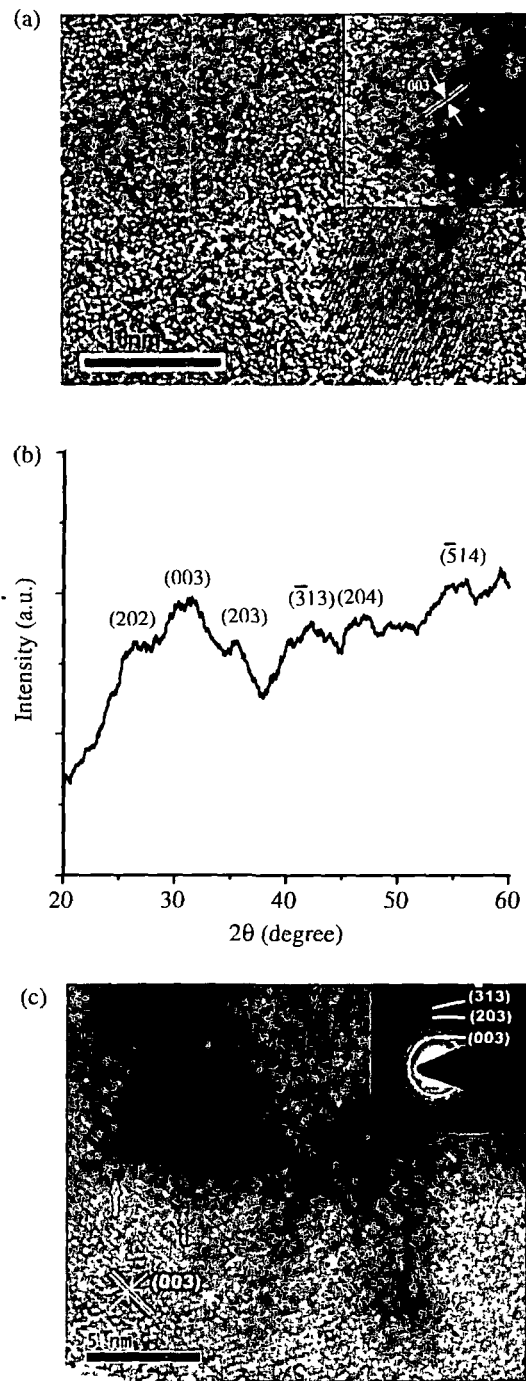


Figure 1. (a) HRTEM and (b) XRD patterns of synthesised nanoscale Gd_2O_3 particles and (c) HRTEM image of the particles of the prepared ferrofluid subjected to γ -irradiation (dose: 2.635 kGy). Inset of (a) is the (0 0 3) plane and inset of (c) is the SAED image.

Figure 2 depicts the FT-IR spectra of the ferrofluids that were irradiated with different doses. The conventional peaks appearing at ~ 3403 and 2400 cm^{-1} represent the respective signatures of O–H stretching and C–O stretching of atmospheric water and CO_2 molecules. In the case of ethanol, bending modes of CH_3 and CH_2 occur at ~ 1392 and 1452 cm^{-1} , respectively; whereas CH_2 , CH_3 , CO and OH stretching vibrations are

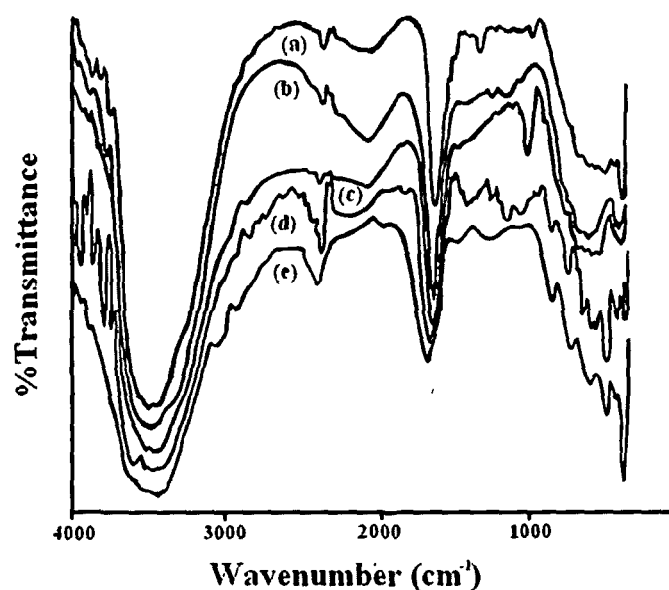


Figure 2. FT-IR spectra of the ferrofluids irradiated with different doses: (a) 32 Gy, (b) 97 Gy, (c) 292 Gy (d) 878 Gy and (e) 2.635 kGy.

Table 1. Assigned modes in the FT-IR spectra.

Peak position (cm^{-1})	Assigned mode
2980	C-CH ₃ asymmetric stretching and N-CH ₃ symmetric stretching of CTAB
1550	-CH ₂ - and -CH ₃ stretching of CTAB
1384-1392	CH ₃ vibration of ethanol
1452-1469	CH ₂ vibration of ethanol
1058	C-O vibration of ethanol
536	In-plane Gd-O vibration

observable at ~ 2910 , 2975 , 1060 and 3679 cm^{-1} [15]. The weak band at 2980 cm^{-1} and the sharp band at 1550 cm^{-1} indicate the presence of CTAB in the samples [16]. Different peaks that are assigned to various components of Gd₂O₃-based ferrofluids are listed in Table 1. It was evident that the vibrational features corresponding to the Gd-O bonds have been influenced by the irradiation effect. A close look on the spectra reveals that with increasing dose of γ -radiation, the peak becomes more prominent. But an anomaly in the Gd-O vibration mode with discontinuities and less intensity profile is observed in sample irradiated with a dose of 878 Gy. Defects like oxygen vacancies are very common in oxide compounds. Some Gd vacancies produced during synthesis may also exist in the system. In fact, the creation of large number of free electrons by the energetic γ -rays (1.25 MeV) can take part in defect formation. The observed variation in the metal-oxygen bond vibration with increased dose can be correlated with the increased defects up to a certain dose, where the defects get saturated by distributing along the grain boundaries and the surface. We speculate that the uneven distribution of defects and inhomogeneities have led to the discontinuities in the vibrational patterns. It was reported that ethanol (the carrier fluid of

the ferrofluid) is less reactive in γ -radiation [17]. But the nanoparticle-dispersed ethanol is characterised by an appreciable modification in the characteristic peaks observable at 1058 and 1459–1469 cm^{-1} .

3.3. PL studies

The influence of light on the nature of radiative transition in material systems makes PL spectroscopy an important tool for material characterisation. Intra- and inter-band transitions can be visualised by PL studies. The room temperature PL spectra ($\lambda_{\text{ex}} = 270 \text{ nm}$) of unirradiated and irradiated ferrofluids are shown in Figure 3(A). The unirradiated ferrofluid has recorded an asymmetrically broadened spectrum peaking at $\sim 355 \text{ nm}$. Earlier reports have suggested that this peak can be attributed to ${}^6\text{P}_{7/2} \leftrightarrow {}^8\text{S}_{7/2}$ transitions of Gd(III) [18]. Also the observed asymmetry in the PL response (pristine sample) is assigned to the existence of surface defects on the nanoscale Gd_2O_3 crystallites. In the pristine sample, the defect-related transition is very weak. Consequently, the overall PL spectrum of the pristine sample is dominated by the band-to-band transition. Upon γ -irradiation, the above-mentioned peak is red-shifted to 390 nm (we speculate that this is a superimposed peak due to band-to-band and defect emission). In this system, besides the already present vacancies, plentiful metastable surface states (defect states) are created due to γ -irradiation. Along with the shifting of the main peak towards higher wavelength, the abrupt change in symmetry signifies a remarkable improvement in the emission process via intermediate states, created by γ -irradiation. Note that, during exposure of γ -radiation, electrons are emitted due to the interaction of high-energy photons with the medium through the Compton effect. These electrons can be accommodated in the pre-existing oxygen vacancies. In oxide systems, an electron in oxygen vacancy results in F^+ centre [19]. The surface defect states are positioned well below the lower end of the upper energy level. It is the transition via these surface states that has resulted in the red-shifting of the emission peak, thus obstructing direct band-to-band transition significantly.

In order to correlate the amount of defect formation, asymmetry introduced and γ -dose, we have performed deconvolution mechanism on each of the PL spectra (Figure 3B). Upon deconvolution, two distinct Gaussian peaks with variable intensities are obtained. The first peak positioned at $\sim 355 \text{ nm}$ is band-to-band (${}^6\text{P}_{7/2} \leftrightarrow {}^8\text{S}_{7/2}$) emission. The second peak is recognised as a defect-related peak and located at $\sim 410 \text{ nm}$, for all the irradiated ferrofluid samples. Irradiation-dependent variation in the peak intensity of these two peaks would describe the nature of radiative transition undergoing in a given specimen. Emission as a result of formation/annihilation of additional defect centres manifests the definite PL intensity in a selective way.

For the sake of clarity and better understanding, we have estimated symmetry factor (S) and correlated with the intensities of the deconvoluted peaks with respect to the original peak. Note that right symmetry (S_R) is related to the defect emission process whereas left symmetry (S_L) is associated with the band-to-band emission. Here, right symmetry factor is defined by $(\lambda_M - \lambda_R)/\Delta\lambda$ with λ_M representing peak-wavelength corresponding to the main peak, λ_R is the wavelength on the right-hand side of the full width at half maxima (FWHM) and $\Delta\lambda = \lambda_R - \lambda_L$, λ_L being the half-width wavelength on the left-hand side of the FWHM. Figure 4(a) represents the variation of relative right

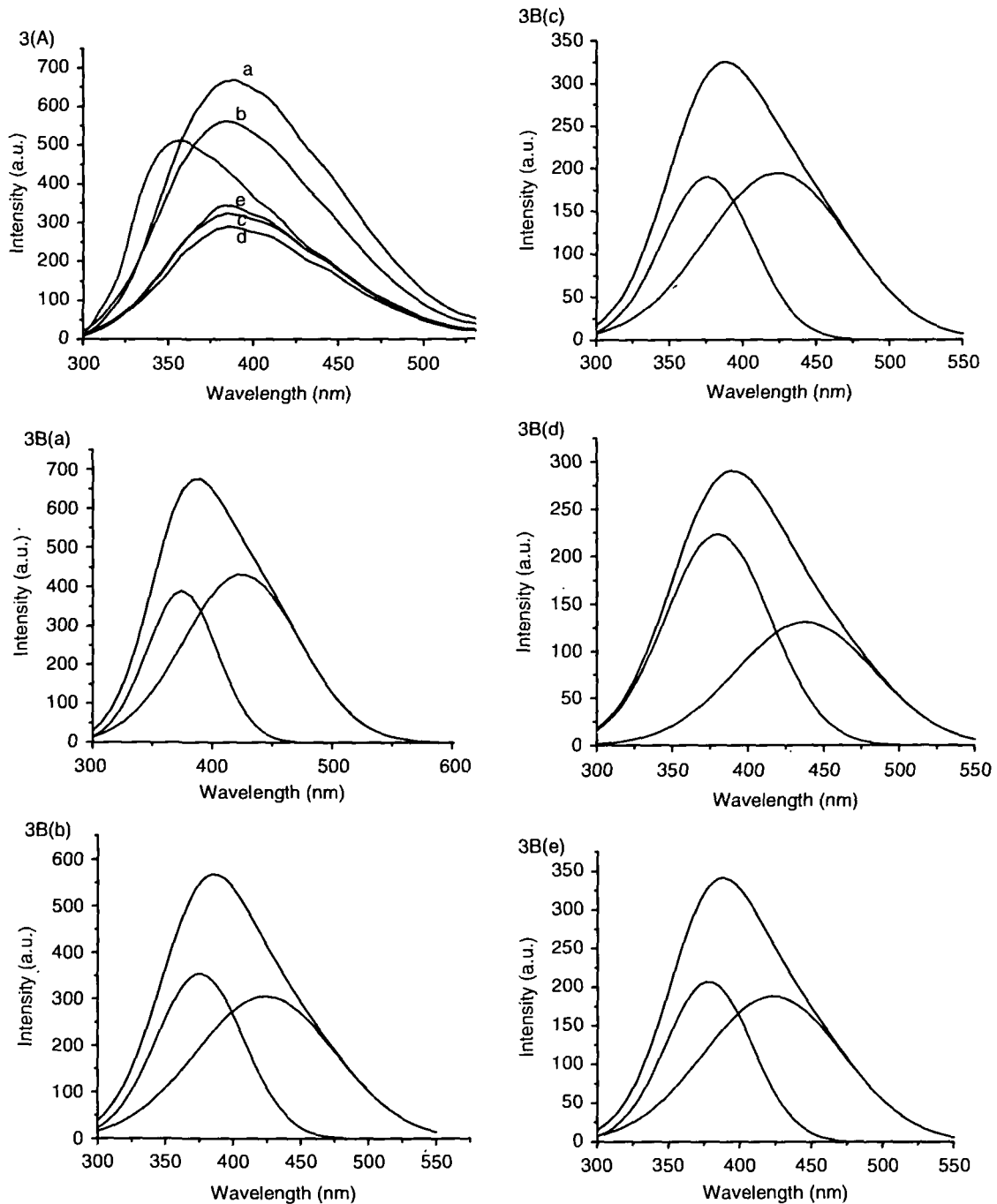


Figure 3. Room temperature PL response of (A) unirradiated and γ -irradiated Gd_2O_3 ferrofluids with doses (a) 32 Gy, (b) 97 Gy, (c) 292 Gy, (d) 878 Gy and (e) 2.635 kGy. (B) (a)–(e) representing respective deconvolution of individual PL peaks of the irradiated samples.

symmetry factor as well as relative intensity (I_2/I , I_2 being the intensity of the defect emission after deconvolution and I is the intensity of the main peak) obtained from the deconvolution. Similarly, the respective variations for the band-to-band emission can be shown in Figure 4(b) with relative intensity as I_1/I (I_1 is the intensity of the deconvoluted band-to-band emission) and relative symmetry factor S_L/S (S_L is the left symmetry factor

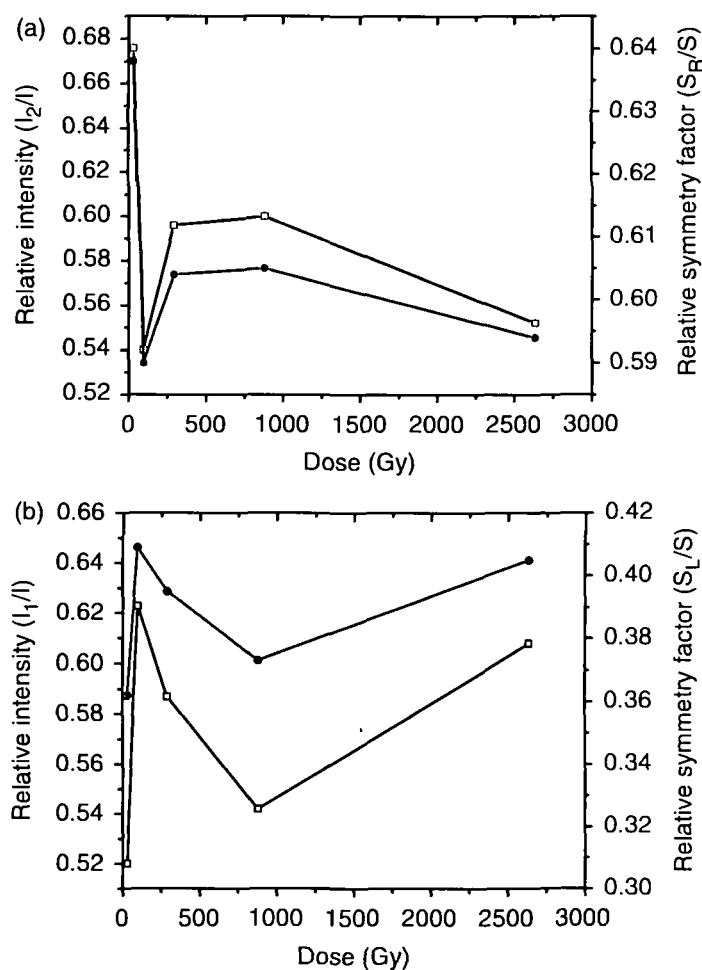


Figure 4. Variation of relative intensity and relative symmetry factor vs. dose corresponding to (a) defect-related emission and (b) band-to-band emission.

of the pristine sample). Interestingly, it was found that the relative intensity and symmetry factor changes in a similar fashion with increasing dose, thus indicating direct relation between these two measuring parameters. In PL spectroscopy, the intensity is a measure of the number of radiative transitions while symmetry signifies the nature of radiative centres (energy spacing, order, etc.). The non-linear nature of the curve indicates the simultaneous effect of defect formation/passivation in the irradiated system. By and large, it is expected that the formation and annihilation processes compete each other until stable energy states (defect states) are created. First, with the increase in dose from 32 to 97 Gy, we observe drastic reduction in the relative PL intensity which may be ascribed to adequate passivation of surface defects. Surprisingly, further increase in dose to 292 and 878 Gy is characterised by significant enhancement of I_2/I ratio. At the highest dose (2.635 kGy), we notice further reduction of I_2/I . The relative symmetry factor (S_R/S) also gives a similar pattern. Reduction of defects makes the overall PL spectrum more symmetric with suppressed right symmetry factor. The γ -ray induced defect creation is not an indefinite process and we speculate that the defects get saturated after a critical dose. The defects could exist in the form of vacancies, interstitials, antisites, etc.

4. Conclusions

We have synthesised RE oxide (Gd_2O_3)-based ferrofluid taking ethanol as carrier fluid and CTAB as surfactant for coating the nanoparticles. The as-prepared ferrofluid was irradiated with five different doses of γ -radiation starting from 32 Gy to 2.635 kGy. In HRTEM study, it was found that though there is no change in the interplanar spacing of atoms that make-up the nanoparticle, numerous defects, such as vacancies and dislocations are created with γ -radiation. Its impact was also observed in FT-IR study. Room temperature luminescence study has exhibited shifting and change in the intensity of the PL peak after irradiation with respect to that of the pristine one. We correlate this observable change with the creation/annihilation and saturation of defects along the grain boundaries. Also, on administering deconvolution process, it was revealed that the intensity and symmetry of the PL spectra can be changed with irradiation doses. We have predicted a direct linkage between the relative intensity and relative symmetry factor and suggest that, beyond a critical dose, defects would tend to saturate for the irradiated samples. A more careful investigation followed by theoretical justification is in progress.

Acknowledgements

We acknowledge UGC, New Delhi for the financial support received under major project scheme no. 37-367/2009 (SR). The authors thank Dr A. Datta for the help received while performing irradiation experiment with gamma irradiation facility available at UGC-DAE Consortium for Scientific Research, Kolkata. The authors are also grateful to the Electron Microscope Facility Centre of SINP, Kolkata for carrying out HRTEM measurements.

References

- [1] M.C. Newton, S.J. Leake, R. Harder, and I.K. Robinson, *Three-dimensional imaging of strain in a single ZnO nanorod*, Nat. Mater. 9 (2010), pp. 120–124.
- [2] S. Sanchez and M. Pumera, *Nanorobots: The ultimate wireless self-propelled sensing and actuating devices*, Chem.: Asian J. 4 (2009), pp. 1402–1410.
- [3] T.Y. Liu, S.H. Hu, S.H. Hu, S.P. Tsai, and S.Y. Chen, *Preparation and characterization of thermal-sensitive ferrofluids for drug delivery application*, J. Magn. Magn. Mater. 310 (2007), pp. 2850–2852.
- [4] E. Munnier, S. Cohen-Jonathan, C. Linassier, L. Douziech-Eyrolles, H. Marchais, M. Soucé, K. Hervé, P. Dubois, and I. Chourpa, *Novel method of doxorubicin–SPION reversible association for magnetic drug targeting*, Int. J. Pharm. 363 (2008), pp. 170–176.
- [5] R. Ravaud and G. Lemarquand, *Design of ironless loudspeakers with ferrofluid seals: Analytical study based on the Coulombian model*, Prog. Electromagn. Res. B 14 (2009), pp. 285–309.
- [6] T.H. Mihail, United States Patent Application 20100084586 Kind Code: A1.
- [7] S.S. Nair, J. Thomas, C.S.S. Sandeep, M.R. Anantharaman, and R. Philip, *An optical limiter based on ferrofluids*, Appl. Phys. Lett. 92 (2008), pp. 171908-1–171908-3.
- [8] J.L. Bridot, A.C. Faure, S. Laurent, C. Rivière, C. Billotey, B. Hiba, M. Janier, V. Jossierand, J.-L. Coll, L.V. Elst, R. Muller, S. Roux, P. Perria, and O. Tillement, *Hybrid gadolinium oxide nanoparticles: Multimodal contrast agents for in vivo imaging*, J. Am. Chem. Soc. 129 (2007), pp. 5076–5084.
- [9] Y.K. Danileiko, E.V. Zharikov, V.V. Laptev, Yu.P. Minaev, V.N. Nikolaev, A.V. Nikolaev, A.V. Sidoren, G.N. Toropkin, and I.A. Shcherbakov, *Optical strength of gadolinium scandium gallium garnet active elements*, Sov. J. Quantum Electron. 15 (1985), pp. 286–288.

- [10] D.L. Sun, J.Q. Luo, J.Z. Xiao, Q.L. Zhang, H.H. Jiang, S.T. Yin, Y.F. Wang, and X.W. Ge, *Effects of annealing treatment and gamma irradiation on the absorption and fluorescence spectra of Cr:GSGG laser crystal*, Appl. Phys. B 92 (2008), pp. 529–533.
- [11] V.T. Mak, V.S. Manzharova, V.I. Beizym, and V.I. Khivrich, *The effect of gamma-irradiation on the bandgap width of ZnSe*, Tech. Phys. Lett. 28 (2002), pp. 757–758.
- [12] X. Gong, P. Wu, W.K. Chan, and W. Chen, *Effect of γ -ray irradiation on structures and luminescent properties of nanocrystalline $MSO_4 \cdot xEu^{3+}$ ($M=Ca, Sr, Ba$; $x=0.001-0.005$)*, J. Phys. Chem. Solids 61 (2000), pp. 115–121.
- [13] H. Chen, C. He, C. Gao, Y. Ma, J. Zhang, X. Wang, S. Gao, D. Li, S. Kan, and G. Zou, *The structural transition of Gd_2O_3 nanoparticles induced by high pressure*, J. Phys.: Condens. Matter 19 (2007), pp. 425229-1–425229-5.
- [14] S. Seo, H. Yang, and P.H. Holloway, *Controlled shape growth of Eu- or Tb-doped luminescent Gd_2O_3 colloidal nanocrystals*, J. Colloid Interface Sci. 331 (2009), pp. 236–242.
- [15] R.A. Nyquist, C.L. Putzig, and M.A. Leugers (eds.), *The Handbook of Infrared and Raman Spectra of Inorganic Compounds and Organic Salts*, Vol. 1, Academic Press, San Diego, 1996.
- [16] Y.D. Wang, S. Zhang, C.L. Ma, and H.D. Li, *Synthesis and room temperature photoluminescence of ZnO/CTAB ordered layered nanocomposite with flake-like architecture*, J. Lumin. 126 (1997), pp. 661–664.
- [17] C.B. Seymour, C. Mothersill, M.J. Moriarty, and F. Tipton, *The effect of ethanol on the radiation response of CHO-K1 cells*, Br. J. Radiol. 60 (1987), pp. 577–581.
- [18] D.L. Rogow, C.H. Swanson, A.G. Oliver, and S.R.J. Oliver, *Two related gadolinium aquo carbonate 2-D and 3-D structures and their thermal, spectroscopic and paramagnetic properties*, Inorg. Chem. 48 (2009), pp. 1533–1541.
- [19] D.R. Vij (ed.), *Hand Book of Applied Solid State Spectroscopy*, Springer, Germany, 2006.

Magnetically induced optical activity and dichroism of gadolinium oxide nanoparticle-based ferrofluids

Nibedita Paul,¹ Manasi Devi,¹ Dambarudhar Mohanta,^{1 a)} and Abhijit Saha²

¹Nanoscience and Soft Matter Laboratory Department of Physics Tezpur University PO Napaam Tezpur 784 028 Assam India

²UGC DAE Consortium for Scientific Research Kolkata Centre IIIILB 8 Bidhannaagar Kolkata 700 098 India

(Received 3 November 2011, accepted 5 January 2012, published online 22 February 2012)

The present work reports on magnetically induced optical activity (such as Faraday rotation and linear dichroism) of pristine and gamma-irradiated gadolinium oxide (Gd_2O_3) nanoparticle-based ferrofluids. The ferrofluids were produced by dispersing N-cetyl-N,N,N-trimethyl ammonium bromide (CTAB)-coated ~ 9 -nm-sized Gd_2O_3 particles in a carrier fluid of ethanol. The ferrofluids were then irradiated with 1.25 MeV energetic gamma rays (dose 868 Gy and 2.635 kGy). Irradiation-induced formation of a number of point defects was revealed through high resolution electron microscopy. The interaction of light with the ionized point defects is believed to have caused substantial improvement in the magneto-optic response of irradiated magnetic fluids. © 2012 American Institute of Physics [doi:10.1063/1.3682765]

I. INTRODUCTION

Among various kinds of nanostructured systems, dispersion of magnetic nanoparticles (MNPs) in a carrier fluid is considered as one of the most promising areas of investigation, both from the point of view of fundamental understanding as well as applied research. Ferrofluids (FF) are basically stable suspension of MNPs (e.g., Fe_3O_4 , $CoFe_2O_4$, Gd_2O_3)¹⁻³ in select carrier fluids, such as water, oil, ethanol, etc. To prevent agglomeration, the MNPs are generally coated with surfactants of either anionic or cationic types.^{4,5} The FF, popularly called magnetic fluids, have a wide range of potential application that includes drug targeting,⁶ sealing,⁷ shielding,⁸ and optical limiting⁹ devices. Further, FFs find a prominent role in the aircraft industry and technology associated with space applications. Compared to other nanoscale systems (Cd, Tb, Hg, etc.), rare-earth (RE) oxides were found to be less toxic.¹⁰ Owing to higher chemical and environmental stability over conventional FF, RE oxide nanostructure-based FF can emerge as an alternative candidate for use, particularly when stability is a major concern. Very recently, we have found that radiation could result in particle-aggregation in the case of the Fe_3O_4 nanosystem,¹¹ whereas no particle-coalescence was observed for the nanoscale Gd_2O_3 system.³

Earlier, it was known that, with the application of an external field, MNPs or their moments orient along the direction of the field. The nature of orientation is largely dependent on the size of the MNPs as well as on the field strength. Consequently, anisotropy would build up in the magnetically induced optical absorption of the FF, giving rise to orientational birefringence or dichroism.^{12,13} Numerous reports were also available in the literature with regard to the magneto-optic response of magnetite- and ferrite-based FFs.^{9,12,13} However, there exists hardly any report that

highlights magneto-optic features of nanoscale RE oxide-based FFs.

In this work, we present the results of magneto-optic characteristics of novel FFs, which were based on pristine and gamma-irradiated Gd_2O_3 nanoscale systems. Essentially, the nature of Faraday rotation (FR) and linear dichroism (LD) is discussed in conjunction with the γ -irradiation exposure and defect manifestation.

II. EXPERIMENTAL DETAILS

RE oxide materials are very stable against high-temperature, high-pressure, and environmental degeneration. That is why synthesis of nanoscale RE oxides is extremely difficult following the top-down approach. The nano-sized Gd_2O_3 powders were synthesized by adopting a low-cost, two-step physico-chemical route reported elsewhere¹⁴ and introducing partial modification to it. In this method, bulk gadolinium oxide is first converted to gadolinium nitrate [$Gd(NO_3)_3$], followed by subsequent reduction to yield hydroxide and oxide products. At first 1 mmol of bulk Gd_2O_3 (99%, Otto) was added to 50 mL of double-distilled water. Then, an appropriate amount (~ 2.5 mL) of HNO_3 (69% GR, Merck) was mixed to this solution under vigorous stirring (~ 250 rpm) until a clear solution of $Gd(NO_3)_3$ was obtained. The solution was then diluted to 100 mL in a volumetric conical flask, and, subsequently, 3.3 g of N-Cetyl-N,N,N-trimethylammonium bromide (CTAB) was added at 65°C, which has resulted in a yellow-colored precursor. On cooling down to room temperature, 10 mL of freshly prepared 0.006 M aqueous NaOH was transferred all at once. Consequently, a white precipitate of $Gd(OH)_3$ is formed, which is then subjected to vigorous stirring (30 min) and centrifugation (30 min). In order to obtain the finest quality precipitate, the as-received product was subjected to repeated washing with hot distilled water and centrifugation. Later, the white precipitate was dried in air and sintered at 800°C.

^{a)}Author to whom correspondence should be addressed. Electronic mail: best@tezu.ernet.in Fax: +91 3712 267005

for 1 h, so as to obtain an off-white product of Gd_2O_3 nanopowder

In order to prepare a FF system, surfactant-coated particles need to be dispersed in a carrier fluid. Since CTAB is chemically inert in ethanol, we preferred to choose ethanol as the carrier medium. The CTAB-coated Gd_2O_3 nanoscale particles were first transferred to ethanol medium, and, in order to achieve uniform dispersion, the sample was followed by stirring overnight. The prepared FF was then divided into three equal parts for carrying out an independent irradiation experiment. The as-prepared FF was irradiated with a γ -source (^{60}Co chamber) that is capable of emitting photons with an average energy of 1.25 MeV and at a dose rate of 1.8 Gy/s. Two doses of 868 Gy and 2.635 kGy were selected for the irradiation studies. Microscopic characterization of the pristine and irradiated FF was performed by high-resolution transmission electron microscopy (HRTEM, FEI, Tecnai S-twin) operating at an accelerating voltage of 200 kV. For this purpose, the specimen was sonicated properly and then a microdrop was placed gently on a carbon-coated copper grid (no. of meshes 400 cm^{-2}).

Magneto-optic properties were explored using a monochromatic laser source, an electromagnet, a set of polarizer and analyzer, a sample cuvette, and photodetector.

III. RESULTS AND DISCUSSION

The details of morphological and magneto-optic characteristics are as discussed below.

A. Structural and microscopic analysis

The structural and morphological aspects of the synthesized nanoscale Gd_2O_3 were assessed by HRTEM, and the images of which are shown in Fig. 1. The average size of the nanoparticles, as revealed from the micrograph, is ~ 9 nm. The particles are found to be nearly spherical with distinct lattice planes and an interplanar spacing of ~ 0.28 nm (Fig. 1(a)). The predicted value of the interplanar spacing corresponds to the separation of (0 0 3) planes of the monoclinic Gd_2O_3 structure and also ascertained from the prominent peaks of the XRD pattern (not shown). Figure 1(b) represents the HRTEM image of the irradiated (dose 2.635 kGy) sample. Formation of nanoscale defects can be easily

visualized from the micrograph. A close look at the micrograph has revealed the presence of nanoscale defects in the consecutive lattice planes (shown by arrow marks). The defects could be in the form of voids (vacancies) or dislocations. For instance, the evidence of point defect and dislocations is shown by solid and open arrows, respectively. The inset of Fig. 1(b) represents the selected area electron diffraction (SAED) pattern of the irradiated specimen. Diffused but distinguishable rings were indexed as (0 0 3), (2 0 3), and ($\bar{3}$ 1 3), which are found to conform with the XRD patterns of monoclinic Gd_2O_3 .¹⁵ The absence of sharp, bright rings implies that the specimen is mostly polycrystalline in nature.

B. Magneto-optic activity and Faraday rotation

Figure 2 depicts a scheme of Faraday rotation (FR) measurement setup. The magneto-optic setup was comprising of a laser source (L), a polarizer (P), a set of mirrors fixed at 45° (M_1 and M_2), a sample cell (S) placed between the poles of an electromagnet, an analyzer (A), a detector (D), a power meter, and a digital Gauss meter. A beam of unpolarized light (obtained from a 5 mW laser source) is focused by a plano-convex lens prior to getting polarized while making its way through the polarizer. The linearly polarized light is then allowed to traverse through a 10 mm sample cell placed within the poles of an electromagnet. The field strength was measured by means of a quality InAs Hall probe with the inhomogeneity of the field distribution over the optical path length (the specimen cell) estimated to be less than 1%. The field was varied within 0-700 G. The analyzer was set at an angle of 45° with respect to the polarizer. Thus, an appreciable change in the intensity of light due to orientation of the plane of polarization caused by the optical activity of the sample could be recorded. The intensities of the transmitted light were measured at zero and different magnetic field strengths. The FR was estimated by the amount of rotation the analyzer required to compensate the intensity of the zero-field case.

The FR deals with the rotation of a plane polarized light due to the field-induced birefringence in the material when the direction of light propagation is parallel to the applied magnetic field.¹⁶ Classically, for a uniform dispersion of single domain ferromagnetic particles, the FR is given by¹⁷

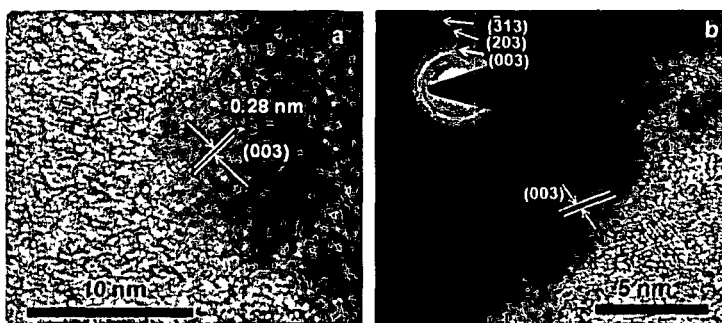


FIG. 1 (Color online) HRTEM image of (a) pristine and (b) irradiated Gd_2O_3 nanoparticles (dose 2.635 kGy). Inset of (b) is the SAED image.

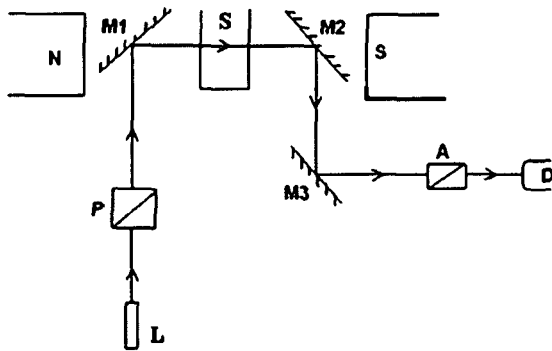


FIG 2 (Color online) Block diagram of magneto-optic set-up L laser, P polarizer, M₁, M₂, M₃ mirrors, S sample, A analyzer, D photodetector

$$\theta = C(M/M_s) \quad (1)$$

where θ is the FR at magnetic field that gives magnetization M , whereas M_s is the saturation magnetization. Here, C is a proportionality constant which depends on the nature of the system under investigation.

With the application of an external magnetic field, particle dispersion gets affected, owing to agglomeration and

chain formation along the direction of the field. Taking into consideration quantum treatment, which accounts for the chain formation, Eq (1) can be rewritten as

$$\theta = V H l, \quad (2a)$$

where V is the Verdet constant, l is the optical path length, and H is the applied magnetic flux density. For irradiated samples, manifestation in the optical path length may occur, owing to the formation of defects, and Eq (2a) then be re-expressed in differential form,

$$\frac{d\theta}{dH} = V(l + \delta l), \quad (2b)$$

with δl being variation in the optical length. Note that our samples are magnetic fluids of surfactant (CTAB)-coated Gd_2O_3 nanoparticles that are suspended in a carrier fluid. Figure 3(a) shows the FR response of pristine (G_0) and gamma-irradiated (G_1 , 868 Gy, G_2 , 2.635 kGy) samples. The figure inset depicts the FR response of specimen G_0 while using a 532 and 632.8 nm laser source. As the FR has exhibited better sensitivity for $\lambda = 632.8$ nm, the source was considered for further experiments. It was also revealed earlier

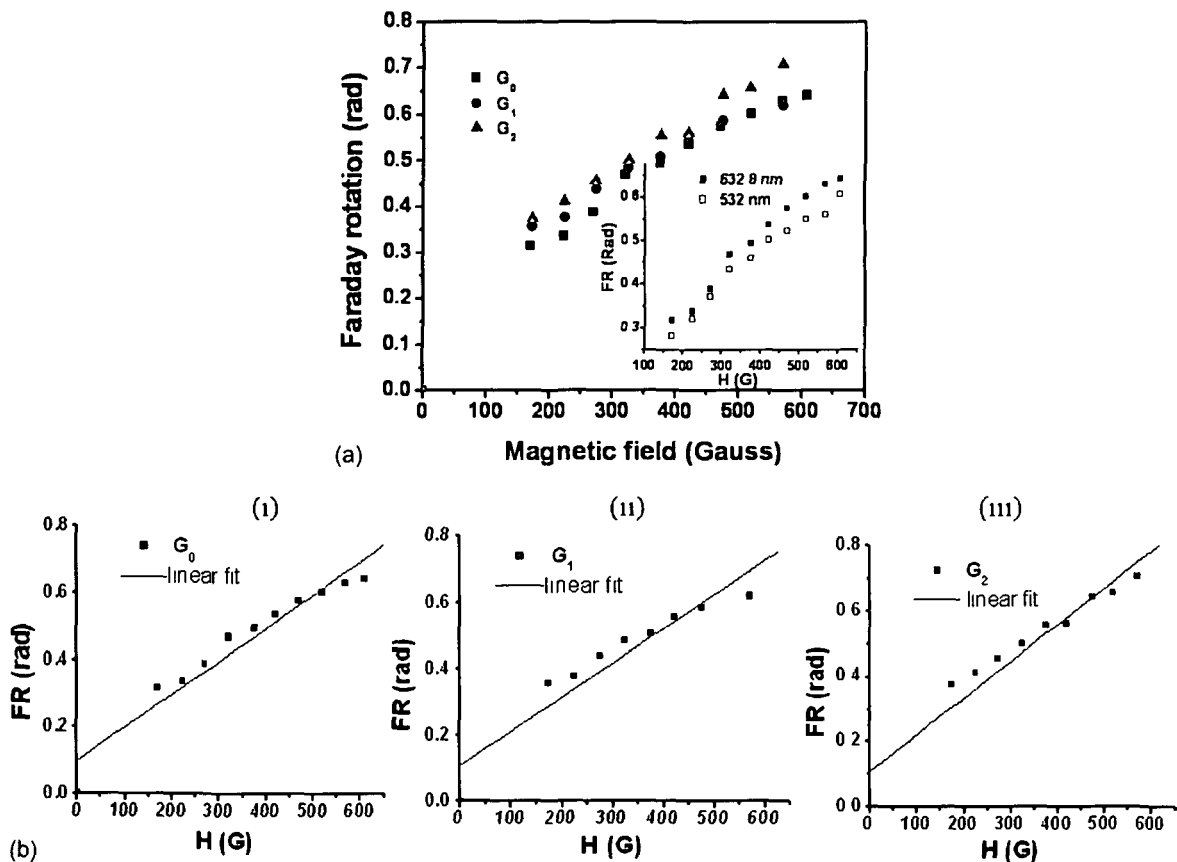


FIG 3 (Color online) (a) Field-dependent Faraday rotation for samples G_0 , G_1 , and G_2 ferrofluids using 632.8 nm laser source. Inset shows response of G_0 using 532 and 632.8 nm lasers. (b) Individual cases with linear fits for (i) G_0 , (ii) G_1 , and (iii) G_2 ferrofluids

that, for a finite field, the FR has a wavelength dependency with the supposition that longer wavelength (low energy) would hinder the chain formation weakly.¹¹ The calibration and measurements were made as per the procedure reported elsewhere.¹⁸ Effectively, the results are characterized by a monotonic increase of θ , with the field followed by a saturation trend in the region of higher field strength. In the presence of an external field, the magnetic moments of the MNPs in the fluid tend to orient along the field direction, forming, thereby, long chains through dipole-dipole interaction. As the interaction energy is a function of magnetization, which has a saturation trend at higher fields, the chain formation also tends to saturate. Earlier, the chain length was shown to be correlated with the FR.¹⁹

For gamma-irradiated FF samples, a substantial improvement of the FR can be found, as evident from the plots shown in Fig. 3(a). In reference to G_0 and G_1 , the response of the specimen G_2 has revealed that the saturation trend could be realized at a relatively higher magnetic field. In other words, saturation magnetization has not yet been reached and so is the case for chain formation. Previous works also demonstrate that, without saturation of a particular length of chain, a new chain length would not be formed.¹⁹ Since RE oxides are very stable against γ -radiation, the observed variation in the FR can be correlated with the interplay of point defects/vacancies. Defects, like oxygen vacancies, are very common in oxide compounds. In fact, the creation of a large number of free electrons by the energetic γ -rays can take part in the defect formation. It was reported that ethanol (the carrier fluid of our FF) is less reactive under γ -radiation.²⁰ In order to evaluate the corresponding effect of radiation on the FF containing nanoscale Gd_2O_3 , we have used Eq. (2). The results of individual cases are shown in Fig. 3(b), and the linear fitting of each of the cases gives the manifested optical length δ/l . The estimated values for G_1 and G_2 specimens are 0.04 and 0.132 cm, respectively. As radiation-induced point defects are charged/ionized ones, the incident light would experience larger path lengths during its passage under the applied field.

C. Magneto-optic response and dichroism

Linear magneto-optic dichroism is defined in terms of the preferential absorption by the material of linearly polarized light along parallel and perpendicular directions of the applied magnetic field. This polarization predilection differentiates dichroism from general absorption and very often relates to the alignment of anisotropic structural elements.²¹

The linear dichroism (LD) was measured using the same setup as used for the FR measurements, but with different configuration. Measurements were made with the plane-polarized light parallel and perpendicular to the applied magnetic field and corresponding values of parallel and perpendicular dichroisms, ΔA_{\parallel} and ΔA_{\perp} , are defined as the changes in the absorbance of the sample caused by turning on the magnetic field. We write²¹

$$\Delta A_{\parallel} = \ln(I_{\parallel}/I_0) \quad (3a)$$

$$\Delta A_{\perp} = \ln(I_{\perp}/I_0) \quad (3b)$$

where I_{\parallel} and I_{\perp} depict transmitted light intensities in the direction parallel and perpendicular to the magnetic field and I_0 is the intensity of the incident light when it was turned off. The dichroism is also the difference in the extinction indices k_{\perp} and k_{\parallel} . Expressing transmitted light intensity in terms of extinction indices,²¹

$$I_{\parallel} = I_0 \alpha_{\parallel} = I_0 \exp[-(4\pi)lk_{\parallel}/\lambda], \quad (4a)$$

$$I_{\perp} = I_0 \alpha_{\perp} = I_0 \exp[-(4\pi)lk_{\perp}/\lambda] \quad (4b)$$

Here, α_{\parallel} and α_{\perp} are respective transmission coefficients of the FF in the direction parallel and perpendicular to the field direction, λ is the wavelength of the incident light, and l is the thickness of the sample. The orientation of the particles by an external field is offset by the Brownian motion. The magnetic dipole moment, m , of the particle makes an angle, θ , with the applied external field, H , and, hence, the orientation energy is given by

$$U = mH \cos \theta \quad (5)$$

In the magnetic fluid, the chain formation occurs when orientation energy overcomes the thermal energy ($k_B T$). Both Neel-type and Brownian-type relaxation responses are at work.¹⁷ The differential absorption (for both parallel and perpendicular polarized light) with respect to the applied magnetic field is depicted in Fig. 4. The fluids exhibit the exact intrinsic dichroism as reported earlier,^{13,21}

$$\Delta A_{\parallel} = -2 \Delta A_{\perp} \quad (6)$$

Figure 4(a) represents the field-dependent LD spectra of the pristine and γ -irradiated specimens. Typically, the absorbance of light parallel to the applied magnetic field increases, while, along the perpendicular polarization direction, it has a decreasing trend. The differential absorption increases with the applied magnetic field, while fluid follows the Langevin-type behavior without pre-existing aggregates.²² The anisotropy vanishes rapidly as soon as the field is removed. As RE oxides are very stable against radiation, defects have been created without any structural modification. For γ -irradiated specimen, there exists a noticeable change (about 10% for G_2 than G_0) in the absorbance along the parallel polarization direction as compared to its counterpart. This could be attributed to the collective role of the point defects in field-induced one-dimensional chains. Nevertheless, as can be evident from Fig. 4(b), the differential plots of the LD are found to be almost uniform for all the specimens. The optical activity and the LD response of nanoscale Gd_2O_3 -based FFs will be promising, while designing field-induced transient optical rotators and other such components where the interaction of the particles with the applied field plays a dominant role over the inter-particle interaction.

IV. CONCLUSION

Magneto-optic features of the un-irradiated and γ -irradiated Gd_2O_3 nanostructure-based FFs have been demonstrated. The HRTEM images of the γ -irradiated (2.635 kGy)

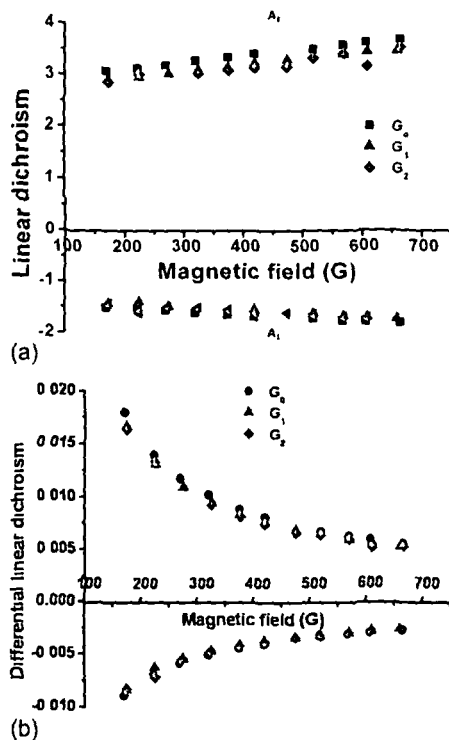


FIG 4. (Color online) (a) LD response of pristine and γ -irradiated sample using 632.8 nm laser, and (b) the differential change of LD with the applied field.

specimen has shown the evidence of point defects and dislocations mostly along the grain boundaries. Magneto-optic characteristics have exhibited an enhanced FR in the case of use of 632.8 nm laser light, and the effective optical length was found to be increased with the creation of point defects. The LD spectral response, though, gives similar trend for pristine and irradiated samples, the absorbance along the parallel direction is suppressed for the later cases. Interrelating the number of chains and defects with the typical magnitude of optical activity would find scope in magneto-optic and nonlinear optical elements.

ACKNOWLEDGMENTS

We acknowledge UGC, New Delhi for the financial support received under major project scheme No 37-367/2009 (SR). One of the authors (NP) acknowledges DST, New Delhi for providing fellowship through INSPIRE scheme. The authors thank Dr. K. K. Baruah for assisting in the magneto-optic setup. The authors are also grateful to the Electron Microscope Facility Centre of SINP, Kolkata for carrying out HRTEM measurements.

- ¹E. Ghazemi, A. Mirhabibi, and M. Edrissi, *J. Magn. Magn. Mater.* **320**, 2635 (2008).
- ²P. Didukh, J. M. Greneche, A. Slawska-Waniewska, P. C. Fannin, and L. Casas, *J. Magn. Magn. Mater.* **242–245**, 613 (2002).
- ³M. Devi, N. Paul, D. Mohanta, and A. Saha, "Characteristic spectroscopic properties of gamma-irradiated rare-earth oxide-based ferrofluids," *J. Exp. Nanosci.* (to be published).
- ⁴S. W. Charles, "The preparation of magnetic fluids," in *Ferrofluids: Magnetically Controllable Fluids and Their Applications*, edited by S. Odenbach (Springer-Verlag, Berlin, 2002), pp. 3–18.
- ⁵D. Maity and D. C. Agrawal, *J. Magn. Magn. Mater.* **308**, 46 (2007).
- ⁶E. Munier, S. Cohen-Jonathan, C. Linossier, L. Douzrech-Eyrolles, H. Marchais, M. Souce, K. Hervé, P. Dubois, and I. Chourpa, *Int. J. Pharm.* **363**, 170 (2008).
- ⁷R. Ravaut and G. Lemarquand, *Prog. Electromagn. Res.* **14**, 285 (2009).
- ⁸A. Yamamura, H. Ishizaki, and H. Unozaawa, U.S. patent 6,290,233 B1 (18 September 2001).
- ⁹S. S. Nair, J. Thomas, C. S. S. Sandeep, M. R. Anantharaman, and R. Philip, *Appl. Phys. Lett.* **92**, 171908 (2008).
- ¹⁰J. L. Brndot, A. C. Faure, S. Laurent, C. Rivière, C. Billotey, B. Hiba, M. Janier, V. Jossierand, J. L. Coll, L. V. Elsi, R. Muller, S. Roux, P. Perria, and O. Tillement, *J. Am. Chem. Soc.* **129**, 5076 (2007).
- ¹¹M. Devi, R. Das, D. Mohanta, K. K. Baruah, and A. Saha, *Appl. Phys. A* **106**, 757 (2012).
- ¹²H. W. Davies and J. P. Llewellyn, *J. Phys. D: Appl. Phys.* **12**, 1357 (1979).
- ¹³H. W. Davies and J. P. Llewellyn, *J. Phys. D: Appl. Phys.* **13**, 2327 (1980).
- ¹⁴H. Chen, C. He, C. Gao, Y. Ma, J. Zhang, X. Wang, S. Gao, D. Li, S. Kan, and G. Zou, *J. Phys. Condens. Matter* **19**, 425229 (2007).
- ¹⁵S. Seo, H. Yang, and P. H. Holloway, *J. Colloid Interface Sci.* **331**, 236 (2009).
- ¹⁶K. Miyamoto, K. Isai, M. Suwa, and H. Watarai, *J. Am. Chem. Soc.* **131**, 6328 (2009).
- ¹⁷A. A. Rousan, H. M. El-Ghanem, and N. A. Yusuf, *IEEE Trans. Magn.* **25**(4), 3121 (1989).
- ¹⁸N. A. Yusuf, A. A. Rousan, and H. M. El-Ghanem, *J. Magn. Magn. Mater.* **65**, 282 (1987).
- ¹⁹N. A. Yusuf, *J. Phys. D: Appl. Phys.* **22**, 1916 (1989).
- ²⁰C. B. Seymour, C. Mothersill, M. J. Moriarty, and F. Tipton, *J. Radiat.* **60**, 577 (1987).
- ²¹B. R. Jennings, M. Xu, and P. J. Ridler, *Proc. R. Soc. London, Ser. A* **456**, 891 (2000).
- ²²Q. Zhang, J. Wang, and H. Zhu, *J. Appl. Phys.* **78**, 3999 (1995).